# UV/Vis, MCD and EPR Spectra of Mononuclear Manganese and Molybdenum Complexes

Dissertation

zur Erlangung des Doktorgrades

der Mathematisch-Naturwissenschaftlichen Fakultät

der Christian-Albrechts-Universität zu Kiel

vorgelegt von

**Anne Westphal**

Kiel

Januar 2012

Referent: Prof. Dr. Felix Tuczek

Koreferent: Prof. Dr. Bernd Hartke

Prof. Dr. Martin L. Kirk, University of New Mexico, Albuquerque

Tag der mündlichen Prüfung: 20.03.2012

Zum Druck genehmigt: 20.03.2012

Dekan: Prof. Dr. L. Kipp

Ideas that have great results are always simple ones.

*Es sind immer die einfachsten Ideen, die außergewöhnliche Erfolge haben.*

Lew N. Tolstoi, „Krieg und Frieden“ (1869)

## Abstract

This PhD thesis deals with the spectroscopic characterization of the electronic structures of mononuclear manganese and molybdenum complexes. At this, in addition to UV/Vis spectroscopy absorption, electron paramagnetic resonance (EPR) and magnetic circular dichroism (MCD) spectroscopy were applied in this work. Additionally, new procedures for the general analysis of MCD *C*-term intensities were developed within the scope of this thesis. It is divided into four parts.

Following a general procedure for the determination of MCD intensities and signs, the MCD spectrum of a molybdenum(V) complex was analyzed in the first part. Theoretical expressions were derived for the observed transitions.

In the second part, a series of manganese(III) complexes was studied by UV/Vis, EPR and MCD spectroscopy. Here, especially the influence of the variation of the ligand field strength was analyzed.

The electronic transitions of a series of molybdenum(III) halogenido complexes were analyzed by UV/Vis spectroscopy in the third part. Molecular orbitals and electronic transition were computed by (time-dependent) DFT.

In the last part, the EPR spectra of molybdenum(III) and -(V) complexes were used as test spectra for spectral simulations using the XSophe simulation software suite.[1]

## Kurzdarstellung

Die vorliegende Arbeit beschäftigt sich mit der Charakterisierung der elektronischen Struktur einkerniger Mangan- und Molybdän-Komplexe mit Hilfe der UV/Vis-, der Elektronenspinresonanz- (ESR) sowie der Magnetischen Zirkulardichroismus-Spektroskopie (MCD). Ziel der Arbeit war es außerdem, weiterführende Methoden für die Auswertung von MCD-Spektren zu entwickeln. Die Arbeit gliedert sich in vier Teile.

Aufbauend auf bereits etablierten Methoden zur Bestimmung der MCD-*C*-Term-Intensität, wurde im ersten Teil zunächst das MCD-Spektrum eines Molybdän(V)-Komplexes analysiert. Die beobachteten Übergänge wurden theoretisch beschrieben.

Im Anschluss daran wurden die UV/Vis-, EPR- und MCD-Spektren einer Serie von Mangan(III)-Komplexen analysiert. Hierbei wurde insbesondere der Einfluss des Ligandenfeldes untersucht.

Im dritten Teil wurden die elektronischen Übergänge einer Reihe von Molybdän(III)-Komplexen mit Hilfe der UV/Vis-Spektroskopie untersucht. Molekülorbitale und elektronische Übergänge wurden mit Hilfe von (TD)DFT-Rechnungen berechnet.

Im letzten Teil der Arbeit dienten die ESR-Spektren von Molybdän(III) und Molybdän(V)-Komplexen als Testspektren für die Spektren-Simulation mit Hilfe der XSophe-Simulationssoftware.[1]

# Content

# Motivation

Structural and mechanistic details of enzymatic reactions are generally rather studied on biomimetic molecular model systems than on the natural enzymes. In the Tuczek and Kurz groups, molybdenum and manganese complexes are studied as model systems for the biological redox enzymes nitrogenase (reductive nitrogen fixation) and the *oxygen-evolving complex* of photosystem II (photoinduced water-oxidation), respectively.[2-7] The redox properties of these molybdenum and manganese model compounds are generally adjusted by the design of specific complex geometries and appropriate ligands. However, to predict and explain the reactivity of potential catalytic model complexes, a thorough characterization of the electronic structure is absolutely essential.

Being interested in the oxidation and spin states as well as the energies of electronic transitions, the most obvious and common spectroscopic techniques to characterize the electronic structures of transition metal complexes are UV/Visible absorption (UV/Vis) and electron paramagnetic resonance (EPR) spectroscopy. Another powerful tool to gain insight into the electronic structure of transition metal complexes is magnetic circular dichroism (MCD) spectroscopy. By means of this technique the differential absorption $\Delta\varepsilon$ between left (lcp) and right (rcp) circular polarized light of a sample is measured in the presence of a longitudinal magnetic field. The observed MCD bands thus by definition have positive or negative signs. Considering individual electronic transitions, the determination of the absolute MCD intensities and signs is not trivial and therefore has often been neglected in the interpretation of MCD spectra so far. However, this lack of theoretical understanding definitely leads to an incomplete utilization of the potential of this method, a loss of spectral information with respect to the manifold of excited states and to the possibility of erroneous band assignments. The aim of this thesis therefore is to establish a more general approach how to completely analyze MCD spectra including the signs of the considered electronic transitions.

For this purpose, relatively simple mononuclear manganese and molybdenum model complexes showing a clear molecular symmetry were studied to broaden the empirical basis for the analysis of MCD signs. Low-temperature MCD spectra of paramagnetic transition metal complexes are dominated by the so-called *C*-term intensity. A general quantum-

mechanical method to calculate the MCD *C*-term intensities and signs for spins $S \geq ½$ has already been described by Neese and Solomon.[8] To demonstrate how this protocol can be applied, the low-temperature MCD spectrum of the $C_S$ symmetric molybdenum(V) complex [Mo(O)$Cl_3$*dppe*] (*dppe* = 1,2-bis(diphenylphosphino)ethane) which only has a single unpaired electron ($d^1$, S = 1/2) has been analyzed first (chapter 3).

Subsequently, the procedure of MCD band assignment and determination of the MCD signs has been transferred to a multi-electron system, a series of the five-coordinate manganese(III) complexes [Mn(*acen*)X] (*acen* = *N,N'*-ethylenebis(acetylacetone)imine, $X = I^-$, $Br^-$, $Cl^-$ and *N*$CS^-$) with S = 2 which show (pseudo-)$C_S$ symmetry as well. The series allowed to also analyze the impact of small variations of the ligand field within a given coordination geometry on the MCD spectra of by the variation of the axial co-ligand X (chapter 4).

Considering the electronic transitions of the facially coordinated molybdenum(III) *tripod* complexes [$MoX_3P_3$] ($P_3$ = 1,1,1-tris(diphenylphosphinomethyl)ethan, $X = Br^-$, $Cl^-$) and [$MoCl_3SiP_3$] ($SiP_3$ = tris(dimethylphosphinomethyl)methylsilane) an assignment of the observed bands was also suggested based on a combined UV/Vis and MCD study (chapter 5).

Both V/Vis and EPR spectroscopy are already well-established to characterize transition metal compounds and are discussed as complementary techniques on the example of the various paramagnetic manganese and molybdenum complexes as well.

Additionally, a pure EPR spectroelectrochemistry study is presented within this work as the EPR spectra which were recorded after the reduction and oxidation of [Mo(NCMe)(NEt)*depe*$_2$]$^{2+}$ (*depe* = 1,2-bis(diethylphosphino)ethane) turned out be excellent spectra to test the XSophe spectral simulation software[1] (chapter 6).

In general, most of these studies on the electronic transitions of the considered molybdenum and manganese complexes are accompanied by quantum chemical calculations of molecular orbitals and electronic transitions by using (time-dependent) density functional theory, (TD)DFT as well as by ligand field calculations based on the *angular overlap model* (AOM).

# 1 Catalysis of Biological Redox Processes by Manganese and Molybdenum Metalloenzymes

Manganese and molybdenum metalloenzymes are involved in very important biological redox processes. Bio-inspired manganese and molybdenum complexes are therefore studied by the Tuczek and Kurz groups as model systems of these enzymes with respect to their structural, spectroscopic and redox properties as well as to their potential catalytic activities.[2-7] Within the scope of this thesis, the considered spectroscopic and theoretical methods were to be developed relevant to the current projects of both groups, so it was obvious to also chose molybdenum and manganese complexes for this work.

The most important manganese and molybdenum metalloenzymes as well as various bioinorganic model systems are shortly presented in the following.

## 1.1 Manganese Containing Metalloenzymes

### 1.1.1 Manganese Containing Superoxide Dismutase and Catalase

High concentrations of reactive oxygen species (ROS) like superoxide ($O_2^{\cdot-}$), peroxide ($O_2^{2-}$) or peroxynitrite ($ONOO^-$) are toxic for cells. Their presence can account for oxidative stress, which accelerates cellular aging and inflammatory processes and might be associated with fatal diseases like diabetes, Parkinson's disease, Alzheimer's disease or cancer.[9, 10] Superoxide and hydrogen peroxide is constantly generated in cellular respiratory processes due to incomplete reduction of $O_2$. To keep their levels low, they have to be disposed of efficiently. This is managed by superoxide dismutases and catalases, which are not surprisingly two of the most efficient of all natural enzymes and show $O_2^{\cdot-}$ and $H_2O_2$ dismutation rates approaching that of a diffusion controlled reaction ($10^8 – 10^9$ $mol^{-1}s^{-1}$).

*Superoxide Dismutase (SOD)*

Superoxide radicals are both strong oxidants and reductants for various targets. For example, they oxidize sulphur containing amino acids and soluble proteins containing [Fe-S] clusters or reduce *cytochrome c*.[11] They may easily be formed if an excess of electrons is generated in

mitochondrial redox processes in the presence of oxygen. To protect cells from oxidative damage, $O_2^{\cdot-}$ is catalytically decomposed to $O_2$ and $H_2O_2$ by superoxide dismutases (SOD),[11] which are ubiquituous metalloenzymes classified after the metal centers in their active sites into CuZnSOD, FeSOD, NiSOD and MnSOD.[12]

$$2\ O_2^{\cdot-} + 2\ H^+ \rightarrow H_2O_2 + O_2$$

CuZnSODs are the most common SODs. They are found in the chloroplasts, in the outer mitochondrial space and in the cytoplasm of eukaryotic cells, while FeSODs are found in chloroplasts and MnSODs only exist in the inner mitochondrial space. Regardless to the incorporated metal center, all types of SODs show a metal-centered redox potential of ~ +0.3 V, at which the oxidative (E = -0.16 V [9]) and the reductive (E = +0.89 V [9]) half-reaction of superoxide dismutation are thermodynamically roughly equally favored.[9]

Manganese containing SODs (MnSODs) are found in dimers and tetramers. The active site of a MnSOD subunit consists of a mononuclear manganese(III) center (in the oxidized form), which is coordinated by three histidines, one aspartic acid residue and a water molecule in a trigonal-bipyramidal coordination geometry.[11, 13-15] The oxidative (1) and the reductive (2) half-reaction of the catalytic $O_2^{\cdot-}$ dispropotionation are given by

(1) $Mn^{III}SOD(OH^-) + O_2^{\cdot-} + H^+ \rightarrow Mn^{II}SOD(OH_2) + O_2$ (E = -0.16 V [9])

(2) $Mn^{II}SOD(OH_2) + O_2^{\cdot-} + H^+ \rightarrow Mn^{III}SOD(OH^-) + H_2O_2$ (E = +0.89 V [9])

In contrast to all other SODs, a “dead-end” species is formed in the case of the MnSODs at high $[O_2^-]$:[MnSOD] ratios. Based on optical absorption spectra, structural and mechanistic considerations, at high $O_2^-$ concentrations manganese(III) side-on peroxo complexes are formed, which are inactive and thus lead to a reduced SOD activity.[12, 16]

$$Mn^{II}SOD + O_2^- \rightarrow Mn^{III}\text{-}(\eta^2\text{-}O_2^{2-})\text{-}SOD$$

Potential SOD mimics are explored as synthetic antioxidants for medical applications, i.e. the suppression of oxidative stress injuries. The most important requirements for such model

systems generally are (i) an appropriate redox potential, which should be similar to that of the natural enzymes (~ +0.3 V), (ii) redox stability and (ii) no toxic side-effects *in vivo*.

An overview of MnSOD mimics is given in a very detailed review by Batinić-Haberle *et al.*,[9] where structure-reactivity relationships as well as the results of *in vitro* and *in vivo* studies concerning SOD activities and $O_2^-$ dismutation rates are summarized. Among the metal containing MnSOD mimics, manganese containing porphyrins and porphyrin related compounds like phthalocyanins and biliverdins are most favorable. They are easily accessible, very stable and open up a large number of possibilities to adjust the corresponding redox potentials and pharmaceutical distribution by chemical modifications of the porphyrin ligand core. They are the most active MnSOD mimics and can reach $O_2^{\cdot-}$ dismutation rates similar to that of the natural enzymes. Additionally, manganese *salen* (*salen* = *N,N'*-bis(salicylidene)ethylenediamine) and cyclic polyamine complexes also have been studied as MnSOD mimics.[9, 10, 17, 18] Also fullarenes and nitroxides were studied with respect to SOD activity, but in general non-metallic SOD mimics are far less efficient than metal containing ones and even less efficient than aquated $Mn^{2+}$ ions ($Mn_{aq}$), which are also able to catalytically decompose superoxide radicals.[9, 10]

The SOD activity of potential new SOD model compounds can be routinely studied in a qualitative colorimetric experiment using an NBT/xanthine oxidase (XAO) assay (NBT = nitro blue tetrazolium chloride).[19, 20] Superoxide radicals are generated as side-products of the enzymatic oxidation of hypoxanthine by XAO. $O_2^{\cdot-}$ then reduces nitro blue tetrazolium chloride, which changes its color from yellow to blue resulting in an absorption maximum at $\lambda_{max}$ = 540 nm in the UV/Vis spectrum. In the presence of an SOD-active compound, the reduction of the NBT dye is significantly decreased due to the lower $O_2^{\cdot-}$ concentrations. This can be followed by the decrease of the absorption maximum in the corresponding UV/Vis spectrum.

*Manganese Containing Catalase (MnCat)*

During cellular oxygen metabolism an estimated 10 percent of $O_2$ is incompletely reduced to form hydrogen peroxide[21] which has to be constantly removed to prevent cells from oxidative damage. $H_2O_2$ is decomposed by the enzyme catalase which catalyzes the disproportionation of $H_2O_2$ into water and dioxygen.

$$2\ H_2O_2 \rightarrow 2\ H_2O + O_2$$

Beside iron heme catalases (type I), which are most prevalent, also manganese containing catalases (MnCat, type II) are found in heme deficient and thermophilic bacteria.[21] Structural data have mainly been obtained from single crystal X-ray diffraction[22, 23] and X-ray absorption spectroscopy, especially EXAFS, and are completed by magnetic measurements, EPR and UV/Vis spectroscopic studies on the natural enzymes as well as on different model complexes.[24, 25]

MnCat consists of hexamers that are formed by six equivalent, trigonally arranged subunits. The active site of each monomer contains a dinuclear manganese center (Figure 1.1). The manganese ions are coordinated to histidine and glutamate residues and a terminal water molecule. Additionally, they are bridged by an oxido ligand and a solvent molecule (hydroxide or water) in the case of the oxidized form (Scheme 1.1, C). For the reduced form a μ-hydroxido-μ-aqua bridging is suggested (Scheme 1.1, A).[22, 23] The resulting $Mn_2O_2$ core is non-planar and has to provide a high degree of structural flexibility, as Mn-Mn distances and Mn-O-Mn bond angles vary upon oxidation and reduction during the catalytic cycle. The first coordination sphere is completed by an additional bridging glutamate which connects the two manganese ions in a 1,3-μ-carboxylato geometry.[22, 23] A non-coordinating glutamate is additionally made out close to the $Mn_2O_2$ core which may serve as internal base during catalytic turnover. [23-25]

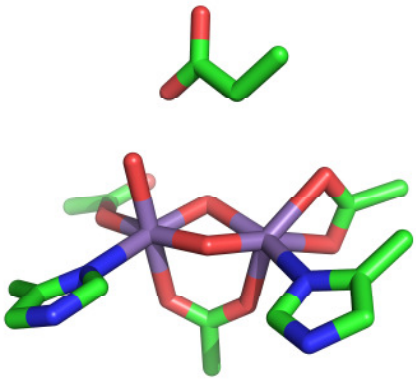

**Figure 1.1.** Active site of MnCat (*Lactobacillus plantarum*) in the $Mn_2$(III,III) state. The structure is based on the single crystal X-ray structure of Barynin *et al*.[23] The figure was provided by Hans-Martin Berends.[26]

During catalytic turnover, the two manganese ions switch between the $Mn_2$(II,II) and the $Mn_2$(III,III) oxidation states[27], so only concerted two-electron transfer steps are involved. One-electron oxidation or reduction are suppressed and the mixed-valence $Mn_2$(II,III) intermediate is not observed within the catalytic cycle of the natural enzyme. However, it can be formed from the $Mn_2$(III,III) state by one-electron reductants like hydroxylamine.[21] In the presence of $H_2O_2$ the $Mn_2$(II,III) state is then quantitatively oxidized to the catalytically inactive bis-μ-oxido bridged $Mn_2$(III,IV) state ("super-oxidized" catalase).[21]

**Scheme 1.1.** Proposed mechanism for the disproportionation of hydrogen peroxide into $O_2$ and $H_2O$, adapted from ref.[24] Only two-electron transfer steps are involved for both the oxidative and reductive half-reactions. Alternatively a terminal coordination of $HOO^-$ to the $Mn_2$(II,II) state (A → B) is also discussed in the literature.[25]

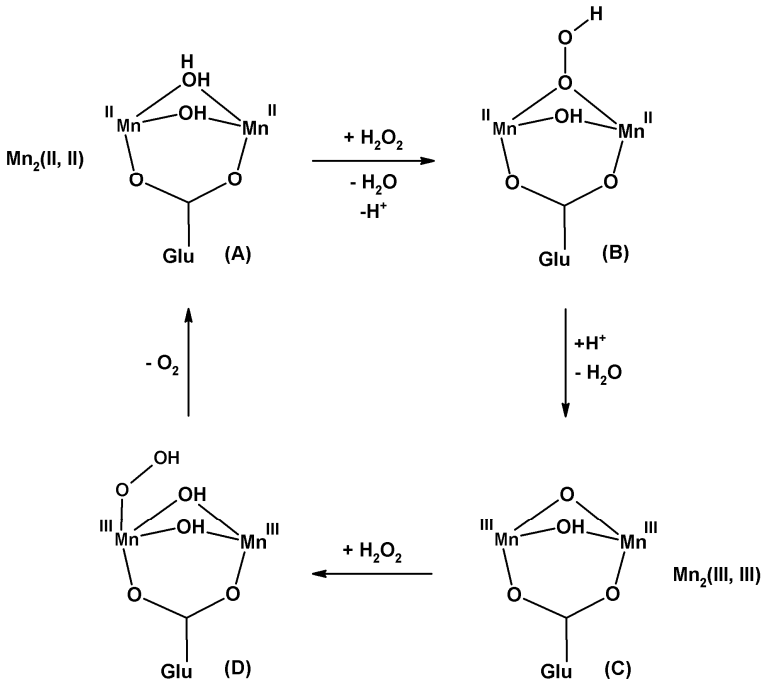


Various mechanisms have been proposed for the catalytic cycle of hydrogen peroxide dispropotionation, although some critical steps and exact mechanistic details especially considering the actual electron transfer still seem to be unclear. However, two facts are unquestioned,

(i) only two-electron steps are involved in $H_2O_2$ disproportionation and

(ii) the associated proton transfer is mediated by an adjacent glutamate residue as an internal base.[23-25]

One proposed mechanism of $H_2O_2$ disproportionation by MnCat is depicted in Scheme 1.1. Starting from the reduced hydroxido-aqua bridged Mn(II,II) state (A) one $H_2O_2$ molecule is deprotonated by an internal base (Glu) and replaces the bridging aqua ligand, so that a μ-1,1-hydroperoxido Mn(II,II) intermediate (B) is formed. From that a water molecule is released after two-electron reduction and heterolytic O-O bond cleavage.[24] Another possibility considers a terminal bonding of $H_2O_2$ for the reductive half-reaction.[25] In both cases, however, the oxido-hydroxido bridged Mn(III,III) state (C) is formed which terminally binds a second $H_2O_2$ molecule to one of the manganese(III) ions to reach a bis-μ-hydroxido hydroperoxido $Mn_2$(III,III) state (D). The $O_2$ molecule is formed after two-electron oxidation and released to regenerate the original Mn(II,II) state (A).[24, 25, 28]

The elucidation of mechanistic details is quite difficult as it is impossible to isolate and characterize any of the reactive intermediates (B, D) of the catalytic cycle due to the very fast reaction rates. The actual mechanism was therefore studied on anion-inhibited forms (X = $N_3$, $Cl^-$, $F^-$, $SCN^-$, $CN^-$)[25, 27, 29, 30] of the enzyme than on the natural catalase itself. Another possibility to get an idea of the catalytic cycle of $H_2O_2$ disproportionation is to study synthetic dinuclear manganese complexes.[25] First reactivity models of MnCat have been prepared in the form of Mn(III,III) diporphyrinato complexes.[25, 31, 32] Other dinuclear manganese complexes also serve as structural and spectroscopic model systems of the natural enzyme. They predominantly bear nitrogen and oxygen donor ligands to mimic the coordinating environment in the MnCat active site as closely as possible and are classified according to the number of bridging oxo/hydroxo and carboxylato ligands.[25, 28]

One of the most efficient catalase model system is the 1,3-bis-μ-actetato bridged Mn(II,II) complex $[Mn_2(OAc)_2bpia_2]^{2-}$ (*bpia* = bis(picolyl)(*N*-methylimidazol-2-yl)amine), that reaches catalytic rates of $k_{cat} = 1.07 \cdot 10^{-3}\ s^{-1}$ in *N*-methylformamide.[33] However, whether the corresponding Mn(III,III) complex is part of the catalytic cycle for the oxidative half-reaction has not been confirmed in this case.[25] For synthetic model systems, the catalytic cycle is indeed not necessarily limited to the (II,II) and (III,III) oxidation states. It has been shown by a systematic kinetic study on dinuclear manganese complexes bearing mixed pyridine/carboxylate ligands that also the Mn(III,IV) compounds show catalase activity.[34] On successive replacement of the pyridine arms of a *tpa* ligand (*tpa* = trispyridylamine) by one to three carboxylates, the catalytic $H_2O_2$ disproportionation rates of the corresponding

Mn(III,III) and Mn(III,IV) complexes are significantly increased. This might not only be due to the lowered redox potentials but also to the fact that covalently bound carboxylates which might de-coordinate during catalytic turnover may serve as internal bases in a similar way as it is proposed for the glutamate residue which mediates proton transfer within the active site of the natural enzyme.[34]

MnSOD mimics like manganese *salen* or polyamine complexes which are applied as physiological antioxidants *in vivo* often also show catalase activity,[10] but this is not additionally considered here.

### 1.1.2 Photosynthetic Water Oxidation by the *Oxygen-Evolving Complex* of Photosystem II

Oxygenic photosynthesis is the essential energy conversion process to enable life on earth.

$$6\ CO_2 + 12\ H_2O + h\upsilon \rightarrow C_6H_{12}O_6 + 6\ O_2 + 6\ H_2O$$

Solar energy is converted into physiologically accessible and storable chemical energy in the form of carbohydrates associated with the oxidation of water to dioxygen by autotrophic organisms which are capable of oxygenic photosynthesis (plants, algae, cyanobacteria). This has been the precondition for the evolution of heterotrophic organisms which are only able to gain their energy from the reverse process, respiration.

The photo-induced water-splitting (primary process, light reaction) takes place in the thylakoid membrane of phototrophic organisms and provides the electrons (in form of NADPH) and the energy (ATP) for the reduction of carbon dioxide in the Calvin cycle (secondary process, dark reaction). Dioxygen is generated as a waste-product of water oxidation. The protons are released into the luminal bulk phase inside the thylakoid membrane where they lead to a transmembrane proton gradient used by the ATP synthase to generate ATP.

$$2\ H_2O \rightarrow O_2 + 4\ H^+ + 4\ e^-$$

Photosynthetic water oxidation is catalyzed by the *oxygen-evolving complex* (OEC) which is identical for all phototrophic organisms and is located at the luminal side of photosystem II (PS II) in the thylakoid membrane of plants, algae and cyanobacteria. The protein structure of photosystem II including the arrangement of the various co-factors (e.g. chlorophylls, carotinoids, lipids, anions, plastochinons etc.) and, in particular, the structure of the *oxygen-evolving complex* have been elucidated by single crystal X-ray diffraction[35-38] and X-ray absorption spectroscopy.[39-41] The active site of the OEC consists of a $Mn_4CaO_5$ cluster (Figure 1.2).[36, 38] While the arrangement of the metal ions has already been more or less determined during the last years, [36, 37, 40, 42] the positions of the bridging oxido ligands as well as the exact metal-metal and metal-ligand distances could be extracted for the first time from the latest X-ray structure of PS II, which now provides an improved resolution of 1.9 Å.[38]

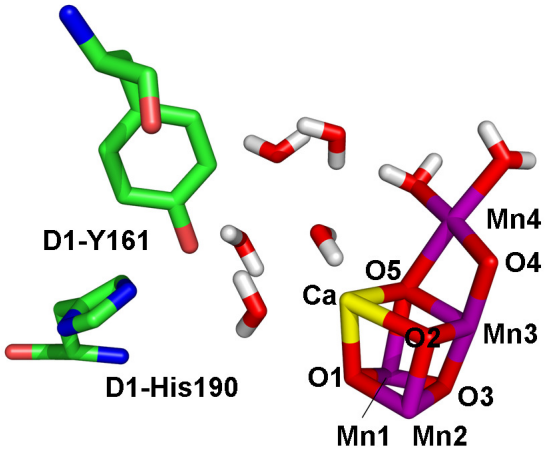


**Figure 1.2.** Arrangement of the $Mn_4CaO_5$ cluster located in the active site of the *oxygen-evolving complex* at the luminal site of photosystem II based on the 1.9 Å resolution single crystal X-ray structure by Umena *et al.* [38]. The figure was provided by Hans-Martin Berends.[26]

Three manganese ions, Mn1 – Mn3, and the calcium ion are arranged in a distorted cubane-like structure being connected by four di-μ-oxido ligands. The fourth manganese ion is not part of this cubane cluster, but connected to the Mn1 and Mn3 atoms by O5, which belongs to the $Mn_3CaO_4$ cluster, and additionally to the Mn3 atom by an external μ-oxido bridge (O4).[38] In contrast to the oxido ligands O1 – O4, O5 is linked to four metal centers, so that the Mn-O5 distances are significantly longer (2.4 – 2.6 Å) compared to the other Mn-O bond distances (1.8 Å - 2.1 Å).[38] Hence it is suggested, that the Mn-O5 bonds are weak and O5 could be one of the oxygen atoms which forms the dioxygen molecule during catalytic turnover. The Ca-O distances vary between 2.4 Å and 2.7 Å. All metal centers are coordinated

by redox stable aspartate, glutamate, alanine and histidine residues of the D1 and CP43 protein subunits.[36-39] Additionally, several water molecules have been identified close to the OEC, which are partly coordinated to the external manganese ion Mn4 and to the calcium ion and may serve as substrates for catalytic water-splitting as well as part of the proton exit channel.

The oxidation of water to dioxygen is a four-electron process, which is catalyzed by the OEC in four successive one-electron steps. Thus, the $Mn_4O_5Ca$ cluster cycles through five distinct oxidation states ($S_i$, $i = 0 – 4$) during catalytic turnover (Kok cycle).[43, 44] The accumulation of four positive charges, that theoretically would occur at the same time, is avoided by *proton-coupled electron transfer* (PCET), i.e. the release of a proton from a water or a hydroxido ligand after each oxidation step.[45] Electron transfer between the OEC and the actual reaction center of photosystem II ($P_{680}$) is mediated by a redox active tyrosine residue ($Y_Z$ = D1-Y161) which may also be part of the proton exit channel to the luminal bulk phase.[38] The individual oxidation steps ($S_0 \rightarrow S_1 \rightarrow S_2 \rightarrow S_3$) are predominantly manganese-centered ($Mn^{III} \rightarrow Mn^{IV}$). Only the last oxidation ($S_3 \rightarrow S_4$) might be oxygen-centered generating a reactive $Mn^{IV}$-oxyl ($Mn\text{-}O^{\cdot-}$) intermediate, which would show the unusual reactivity of an electrophile being capable of O-O bond formation by a nucleophilic attack of a bulk water molecule or a coordinated aquo/hydroxido ligand.[44, 46, 47]

### 1.1.3 Catalytic Water-Splitting and Solar Fuel Generation by Artificial Photosynthesis

Mechanistic details of the photosynthetic water oxidation, especially the actual formation of the dioxygen molecule, are generally rather studied on molecular model systems than on the natural enzyme. Three possible mechanisms are discussed for the O-O bond formation:[44, 46]

(i) a radical mechanism,

(ii) a nucleophilic attack of a bulk water or a coordinated aquo/hydroxide ligand to a $Mn^{IV}$-oxyl species (*vide supra*) or

(iii) the direct coupling of two proximate water molecules after deprotonation.

Potential catalytic model systems require polynuclear oxido-bridged manganese centers in oxidation stable, but flexible ligand environments with potential coordination sites for substrate water molecules.[7] The aim to fully mimic the active site of the *oxygen-evolving complex*, i.e. the pentanuclear $Mn_4CaO_5$ cluster including its ligand environment, is very ambitious. However, in theory two manganese centers are also sufficient to catalyze the four-electron water oxidation, so dinuclear manganese complexes are often studied as simplified model compounds with respect to their spectroscopic properties, redox potentials and potential catalytic activities.[48-50] They often contain a $Mn_2(\mu\text{-}O)_x$ (x = 1 - 3) motif with the two manganese centers being in the +II, +III or +IV oxidatition states.

One of the most prominent and most intensively studied model systems is the bis-μ-oxido bridged manganese(III,IV) complex $[Mn_2(O)_2(H_2O)_2terpy_2]$ (*terpy* = 2,2';6',2"-terpyridine).[51, 52] Like most dinuclear manganese complexes, it is able to generate $O_2$ in the presence of $H_2O_2$, $HSO_5^-$, $^t$BuOOH or other oxygen-containing oxidants and thus turned out to be an excellent catalase mimic (*vide supra*). However, if one-electron oxidants like Ce(IV) are used, only very, very poor water-oxidation activities are observed in the most cases - if any at all, so none of the exisiting dinuclear manganese complexes can be considered as a real water-oxidation catalyst so far.[7, 26]

Another very important aspect of developing functional water oxidation catalysts is the envisioned concept of solar fuel generation by artificial photosynthesis.[53] Solar energy is to be used to catalytically oxidize water to generate electrons which are directly transferred to an associated electron acceptor unit to be used for the catalytic reduction of $H^+$.[54, 55] In this way, the generation of $H_2$ by solar energy conversion eventually could replace the energy-intensive processes of $H_2$ production like fossil fuel reforming and electrolytic water splitting to some extent. It is obvious that very efficient, cheap and robust catalysts will be needed for industrial applications. For that reason, molecular catalysts like di- and - even to a lesser extent - polynuclear manganese complexes will most likely not be considered to be appropriate large-scale water oxidation catalysts.

However, if dinuclear manganese complexes are adsorbed on clay minerals like kaolinite or montmorillonite “true” – heterogeneous – water oxidation catalysts are formed on the clay surfaces[56-59] which do not only show dioxygen evolution in the presence of oxygen-

containing oxidants as most dinuclear manganese complexes in solution (*vide supra*), but also with the one-electron oxidant Ce(IV).[59] UV/Vis and EPR spectroscopic measurements reveal that the electronic structures of the considered complexes completely change upon the adsorption on the clay surfaces. Additionally, they indicate that the actual catalytically active species might even be a polynuclear manganese unit which may be formed on the surface by the dimerization of two dinuclear manganese complexes, for example.[7, 26, 59]

Another approach completely gives up the concept of molecular water oxidation catalysts and deals with the catalytic activity of manganese and mixed manganese-calcium oxides. These are obtained from solvothermal syntheses and turned out to be very efficient water oxidation catalysts also with the one-electron oxidant Ce(IV).[7, 60] As most of these oxides are amorphous powders structural information is mostly gained from X-ray absorption spectroscopy. Some important structural analogies to the $MnCaO_x$ arrangement of the natural OEC have been discovered within these oxides.[61] Corresponding to the active site of photosystem II and to simple dinuclear model complexes they also contain Mn(III) and Mn(IV) centers which are linked by μ-oxido bridges.[61] This confirms that these might indeed be the crucial requirements for catalytic water oxidation. The Mn-Ca oxides might therefore probably be considered as the first and only true biomimetic water oxidation catalysts. At the same time they represent a very promising route to large scale applications as they are robust, cheap and very easily accessible.

## 1.2 Molybdenum Containing Metalloenzymes

### 1.2.1 Industrial $N_2$ Fixation

The physiological availability of nitrogen is the limiting factor in plant growth, as nitrogen mainly exists as non-reactive dinitrogen molecules in the atmosphere with the triple bonds of $N_2$ being very stable ($E = 942\ kJmol^{-1}$) and the dissociation energy of the first π-bond being very high.[62, 63] However, to make nitrogen accessible for biosynthesis $N_2$ has to be oxidized to nitrogen oxides or reduced to ammonia. Millions of tons of $NH_3$ are therefore produced as a feedstock of fertilizers every year. In the Haber-Bosch process $NH_3$ is obtained directly from the elements $N_2$ and $H_2$ in the presence of a promoted iron catalyst ($Fe_3O_4$). As high pressure and high temperatures are required to directly hydrogenate $N_2$, the Haber-Bosch process is one of most energy demanding industrial processes of all, not to mention the energy which is additionally needed for the production of $H_2$. Considering the catalytic mechanism, $N_2$ and $H_2$ dissociate after the adsorption on the catalyst surface before $NH_3$ is formed. The rate-limiting step is the chemisorption of the dinitrogen molecules and the dissociation of their first π-bond. The exploration of this and other mechanistic details led to the Nobel Prize in Chemistry in 2007 to Gerhard Ertl.[64, 65]

### 1.2.2 Enzymatic $N_2$ Fixation

Diazotrophic bacteria containing the enzyme nitrogenase like *azotobacter vinelandii*, *clostridrium pasteurianum* or the endosymbiotic *rhizobia* are also capable of nitrogen fixation. In contrast to the Haber-Bosch process the enzymatic fixation of $N_2$ occurs under physiological conditions, i.e. room temperature and atmospheric pressure. The overall enzymatic reaction is:

$$N_2 + 8\ H^+ + 8\ e^- + 16\ MgATP \rightarrow 2\ NH_3 + H_2 + 16\ MgADP + 16\ P^i$$

This implies that the reductive fixation of $N_2$ is also associated with the formation of $H_2$.

Molybdenum containing nitrogenase consists of an iron protein (Fe protein) and an iron-molybdenum protein (MoFe protein). The iron protein is a dimer of two identical subunits linked by a [4Fe-4S] cluster, acting an electron transfer protein which is responsible for the

delivery of the energy for the actual catalytic reactions by the splitting of ATP. The MoFe protein consists of two heterodimers ($\alpha_2\beta_2$). Each heterodimer contains a so-called P-cluster consisting of a $Fe_8S_7$ unit and the iron-molybdenum co-factor (FeMoCo).The P-cluster mediates the electron transfer between the iron protein and the iron-molybdenum co-factor, which is the active site of the enzyme where dinitrogen is bound and reduced to ammonia. The FeMoCo consists of a six-coordinate molybdenum center and seven four-coordinate iron atoms which are all bridged by sulfur ligands. The arrangement and the individual bridgings of the different metal centers has been elucidated by single crystal X-ray diffraction[66, 67] with the only exception of one central bridging atom which is assumed to be a carbon atom based on recent X-ray emission spectroscopy (XES) measurements.[68] The isolated FeMoCo is not capable of $N_2$ reduction to form ammonia but is still able to reduce protons to dihydrogen.[69, 70]

The proposed catalytic mechanism of the biological nitrogen fixation incorporates an Fe protein cycle[71] and a MoFe protein cycle.[72-75] In contrast to the Haber-Bosch process the enzymatic reduction of $N_2$ to $NH_3$ occurs in alternating reduction and protonation steps. However, certain mechanistic details of the enzymatic nitrogen fixation, for example the role of the unknown atom in the center of the FeMoCo, as well as the geometries of some of the reactive intermediates are still unclear. Although there is evidence that $N_2$ binds to one of the iron centers of the FeMoCo[76-78] and not to the molybdenum atom, as it has been discussed for a long time, the exact position and the way of binding (end-on versus side-on) is also still not known. For the actual reduction and protonation reactions of $N_2$ a “D” (distal) and an “A” (alternate) mechanism are discussed in the literature.[79]

### 1.2.3 Synthetic $N_2$ Fixation: Chatt Cycle

Designed after the example of the natural enzyme which is capable of $N_2$ fixation under ambient conditions different molecular model systems have been developed, mainly to get insight into mechanistic details of catalytic nitrogen reduction. A general requirement for potential catalytic model systems is good reduction stability, as very low potentials ($\leq$ -2 V) are required for the reduction of $N_2$. Additionally, the coordinated $N_2$ ligand must be

sufficiently activated for protonation and reduction reactions. On the other hand the activation should not be too high to be able to study the various intermediates during catalytic turnover.

The most important model systems have been inspired by the former idea that the molybdenum atom might be the actual catalytically active center of the FeMoCo and thus are based on molybdenum (and tungsten) transition metal complexes. However, the only model system that forms ammonia by the *catalytic* reduction of dinitrogen is the [Mo(*hiptN$_3$N*)N$_2$] complex (*hiptN$_3$N* = hexaisopropyl terphenyl triamidoamine) developed by Schrock *et al.* One $N_2$ molecule binds to a molybdenum(III) center and is stepwise reduced to $NH_3$.[80-83] Compared to the enzymatic $N_2$ fixation by nitrogenase the proposed catalytic mechanism of the so-called Schrock cycle also involves alternating protonation and reduction steps.[82-84] With decamethylchromocene and lutidiniumtetrakis(3,5-bis-trifluoro-methylphenyl) being used as reducing agent and proton source, respectively, an average of four catalytic cycles is achieved with the Schrock system. Many of the proposed intermediates have already been isolated and characterized.

Another important model system had already been developed before the Schrock system by Chatt *et al.* to study mechanistic details of reductive nitrogen fixation and the individual intermediates of the catalytic cycle. It is based on molybdenum and tungsten complexes with bidentate phosphine ligands. Here, $N_2$ binds to a molybdenum/tungsten(0) center. As can be deduced from the lowered vibrational frequency of the N-N stretch and the elongated N-N bond distance compared to free $N_2$ molecules, the $N_2$ ligands of these Chatt type complexes are moderately activated for protonation and reduction reactions.[85-88]

According to the proposed catalytic mechanism of the so-called Chatt cycle (Scheme 1.2) the molybdenum/tungsten(0) bis-dinitrogen complex (**C1**) is first protonated in two steps. The coordinated $N_2$ ligand is then reduced in a two-electron reduction to form a molybdenum/ tungsten(II) hydrazido complex (**C4**). Another protonation of this intermediate leads to the splitting of the N-N bond and the release of one equivalent $NH_3$. The resulting molybdenum/ tungsten(IV) nitrido species (**C5**) is protonated forming the molybdenum/tungsten(IV) imido intermediate **C6**. This is followed by another two-electron reduction and two protonation steps to form the molybdenum/tungsten(II) amine species (**C9**). After a final two-electron reduction the second equivalent of ammonia is released and, upon the binding of two $N_2$

molecules, the catalytic cycle is closed and could start again with the protonation of the molybdenum/tungsten(0) bis-dinitrogen complex **C1**. Compared to the natural enzyme and to the Schrock system the electrons and protons are not transferred in strictly alternating one-electron and one-proton steps during the Chatt cycle. Starting from the molybdenum/tungsten(0) bis-dinitrogen complex **C1** two protons are transferred before a two-electron reduction which is again followed by the transfer of another two protons and so on. In consequence, the metal center only changes between the oxidation states +II and +IV in the case of the Chatt system while the Schrock cycle involves the oxidation states Mo(III), Mo(IV) and Mo(V).

**Scheme 1.2.** Synthetic nitrogen fixation: proposed catalytic mechanism of the Chatt cycle: **C1**: bisdinitrogen-Mo/W(0), **C2**: diazenido-Mo/W(II), **C3**: hydrazido-Mo/W(IV), **C4**: hydrazido-Mo/W(II), **C5**: nitrido-Mo/W(IV), **C6**: imido-Mo/W(IV), **C7**: imido-Mo/W(II), **C8**: amido-Mo/W(II), **C9**: amine-Mo/W(II).[88] The figure was provided by Ameli Dreher.[89]

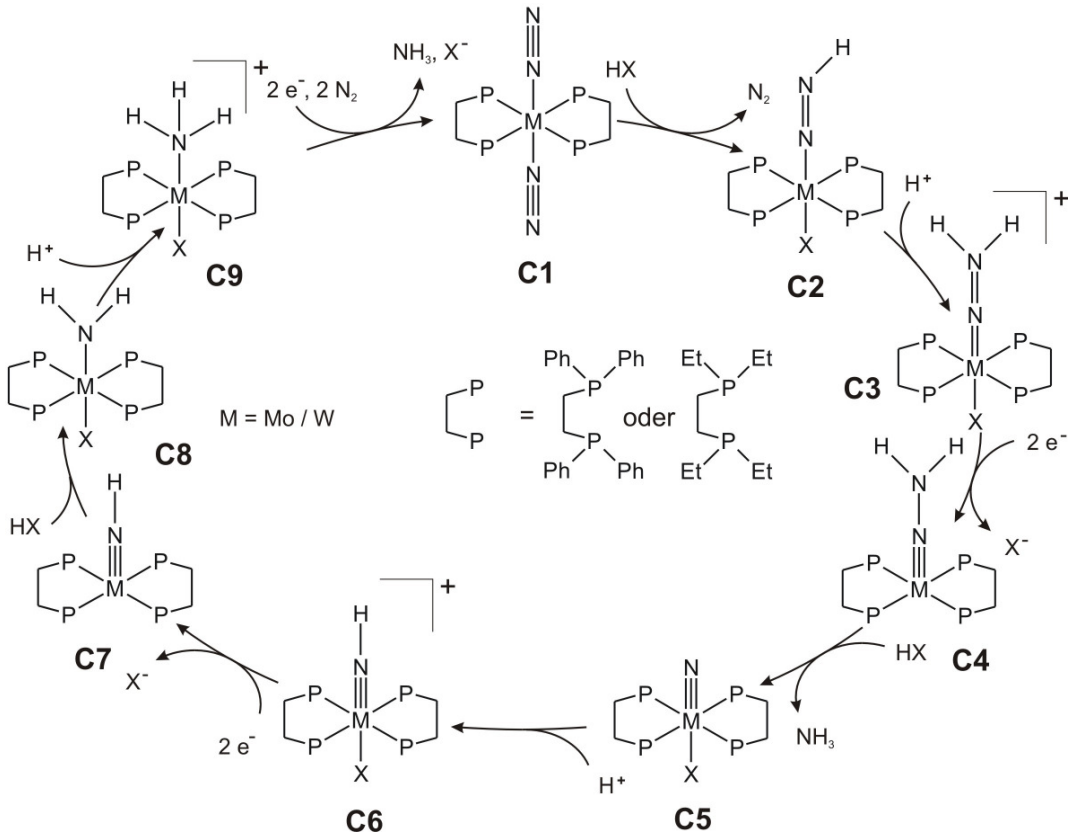


Although $NH_3$ has been obtained from the hydrazido complex $[W(OTf)(NNH_2)(dppe)_2](OTf)$ (*dppe* = 1,2-bis(diphenylphosphino)ethane) electrochemically in the presence of trifluoro-methanesulfonic acid with the bisdinitrogen complex $[W(N_2)_2(dppe)_2]$ being formed at the

same time,[90] a true catalytic formation of ammonia with Chatt type complexes has not been realized yet. One reason for that are side reactions which gradually inactivate the catalyst after passing through the catalytic cycle. If the coordinated counter anion $X^-$ of the applied acid does not de-coordinate upon $N_2$ binding at the last step of the catalytic cycle (**C9** → **C1**, Scheme 1.2) a molybdenum(I) species, $[M(X)(N_2)(dppe)_2]$, is formed which is susceptible to disproportionation reactions (Scheme 1.3). While the resulting molybdenum(0) complex, $[M(N_2)_2(dppe)_2]$, is part if the catalytic cycle (**C1**), the resulting molybdenum(II) dihalogenido species $[M(X)_2(dppe)_2]$ cannot be converted into a catalytically active intermediate again. In this way, up to 50 percent of the catalyst might get lost for the catalytic cycle during each turnover.

**Scheme 1.3.** Mo(I) complexes which can be formed after passing through the Chatt cycle disproportionate into Mo(0) and Mo(II) complexes. While the Mo(0) species is part of the catalytic cycle (**C1**) the Mo(II) dihalogenido complex cannot be converted into a catalytically active species again. The figure was provided by Ameli Dreher.[89]

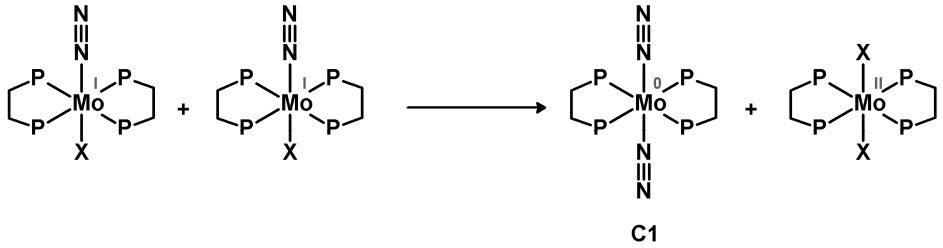


This side reaction can be avoided by the synthesis of Chatt type complexes with tripodal or pentapodal phosphine and heterophosphine ligands in which the position *trans* to the $N_2$ ligand is no longer accessible to ligand exchange (*vide infra*, chaper 5).[6]

# 2 Electronic Properties of Mononuclear Manganese and Molybdenum Complexes – Methods of Characterization

To spectroscopically characterize the electronic structure of transition metal complexes, UV/Vis absorption spectroscopy is commonly used to gain information about oxidation states and the ligand environment. However, electron paramagnetic resonance (EPR) and magnetic circular dichroism (MCD) spectroscopy often provide further information with respect to the electronic properties. Both, EPR and MCD spectroscopy were to be (re)established in the Tuczek/Kurz groups for the characterization of mononuclear molybdenum and manganese complexes during this work

The basic principles of EPR and MCD spectroscopy as well as UV/Vis absorption spectroscopy are therefore shortly introduced and partly laid out on very general examples considering mononuclear manganese and molybdenum complexes without the intention of giving a complete review of this topic. Additionally, a short introduction to the basic principles of ligand field and (TD)DFT calculations is given.

However, analytical methods that were not intensively used during this work like (spectro-) electrochemistry and magnetic methods are not considered here. Needless to say, that in other contexts they might be very helpful as complementary techniques to characterize the electronic and redox properties of transition metal complexes and therefore, in general, should of course not be neglected.

For the basic principles of coordination chemistry the reader is referred to the basic literature.[91-94]

## 2.1 Spectroscopic Methods

### 2.1.1 UV/Vis Absorption Spectroscopy (UV/Vis)

The absorption of electromagnetic radiation may cause a change in the electronic state of a molecule, as electrons can be promoted from bonding and non-bonding molecular orbitals into antibonding MOs by the absorption of ultraviolet and visible light (200 – 1 000 nm).

In solution the absorbance of a sample depends on the concentration $c$, the path length $d$ and the molar extinction coefficient $\varepsilon$ according to the Lambert-Beer law:

$$E = -\lg\frac{I}{I_0} = \varepsilon \cdot c \cdot d \qquad \text{with} \qquad \frac{I}{I_0} = T \qquad \text{(transmission)}$$

Considering transition metal complexes three types of electronic transitions can be observed in the UV/Vis absorption spectra:

(i) metal-centered d → d ligand field transitions

(ii) ligand-to-metal and metal-to-ligand charge transfer (LMCT, MLCT) and

(iii) inner-ligand transitions.

The ligand field and charge transfer transitions provide information about the metal ion(s), like oxidation states, spin states, coordination geometries, ligand arrangements and ligand field strengths (*vide infra*). Additionally the magnitude of the interelectronic repulsion within the metal d-orbitals, which is described by the Racah-parameters B and C and provides information about the covalence of metal-ligand bonds, can be extracted from UV/Vis absorption spectra.

The relevant selection rules for electronic transitions in transition metal complexes are $\Delta S = 0$ (spin rule) and $\Delta L = \pm 1$ (orbital (Laporte) rule). The spin rule is self-explanatory and says that transitions between electronic states of different multiplicity are spin-forbidden. However, if electronic states with different multiplicities are mixed via spin-orbit coupling,

very weak intercombination bands ($\varepsilon = 10^{-3}$ - 1 $Lmol^{-1}cm^{-1}$) might be observed in the UV/Vis spectra (at very high concentrations). The Laporte rule says that electronic transitions between orbitals which do *not* change their symmetry with respect to the inversion center (g, u) are Laporte-forbidden. In consequence, the metal-centered d → d ligand field transitions (g → g) are generally not allowed. However, relaxation of this rule may occur through vibronic coupling. It refers to the coupling of the "gerade" electronic states (g) with "ungerade" vibrations, i.e. vibrations which are antisymmetric (u) with respect to the molecular inversion center. The mixing of "ungerade" symmetry to a formerly "gerade" state leads to weak absorption intensities of these transitions ($\varepsilon = 1$ - 10 $Lmol^{-1}cm^{-1}$). As a general rule, a lower overall symmetry of a complex results in more intensity of the d → d ligand field transitions. The same is true for tetrahedral complexes and other coordination geometries which do not have a molecular center of symmetry at all ($\varepsilon > 100$ $Lmol^{-1}cm^{-1}$).

Due to the Laporte-rule, metal-centered ligand field transitions are often superimposed by charge transfer transitions. The latter are not affected by this rule and therefore show significantly higher intensities ($\varepsilon > 1\,000$ $Lmol^{-1}cm^{-1}$), so that they usually dominate the UV/Vis absorption spectra. The number of expected ligand field transitions for a particular transition metal complex, can be described using ligand field theory considerations. For the analysis of charge-transfer transitions, however, molecular orbital theory must be considered (*vide infra*).

#### 2.1.1.1 UV/Vis Absorption Spectra of Mononuclear Manganese Complexes

*Manganese(II)*

As mononuclear manganese(II) complexes usually are high-spin systems (S = 5/2, $^6S$ ground term), metal-centered d → d transitions are spin-forbidden. These compounds are therefore only weakly colored or, in solution, even colorless, if low-energy charge transfer transitions in the spectral region of visible light (400 – 800 nm) are absent. However, at very high concentrations very weak intercombination bands, i.e. spin-forbidden transitions into excited quartet states, originating from the ligand field splitting of the $^4G$, $^4D$ and $^4P$ excited terms of the free manganese(II) ion, may be observed. The most prominent example is the UV/Vis

absorption spectrum of the manganese(II) hexaaquo complex.[95] The pale pink color of $[Mn(H_2O)_6]^{2+}$ is only observed at very high concentrations due to the very low intensities ($\varepsilon \leq 0.05$ Lmol$^{-1}$cm$^{-1}$) of several spin-forbidden transitions. They are made out as five distinct absorption bands in the UV/Vis spectrum between 18 000 cm$^{-1}$ and 30 000 cm$^{-1}$.[92, 95, 96]

*Manganese(III)*

Manganese(III) complexes are integer spin systems (S = 2, $^5$D ground term). The number and the energies of the observed d → d ligand field transitions strongly depend on the coordination geometries and the actual symmetries of the considered complexes. In theory only one spin-allowed ligand field transition, $^4E_g \rightarrow {}^4T_{2g}$, is expected for an ideal octahedral manganese(III) high-spin complex. However, as a result of the Jahn-Teller effect[97] manganese(III) complexes nearly always adopt tetragonally elongated or tetragonally compressed coordination geometries of $D_{4h}$ (or lower) symmetry. In consequence, up to four spin-allowed ligand field transitions might be observed in the corresponding UV/Vis absorption spectra.[98] The ligand field diagram of a d$^4$ high-spin system like manganese(III) is given in Scheme 2.1. Note that the symmetry of the individual electronic states is given by the symmetry of the unoccupied metal d-orbital.

**Scheme 2.1.** Ligand field diagram of a d$^4$ high-spin system. The $^5$D ground term splits into the $^5E_g$ ground state and the $^5T_{2g}$ excited state in octahedral symmetry ($O_h$). Jahn-Teller distortion leads to a further splitting of the d-orbitals with a $^5B_{1g}$ ground state in the case of axial elongation along the molecular $z$ axis ($D_{4h}$). If the overall complex symmetry is further reduced ($C_{2v}$, $C_S$), up to four d → d transitions might be observed in the UV/Vis absorption spectra. Note that the symmetry of the individual electronic states is given by the symmetry of the unoccupied orbital which is given in parenthesis.

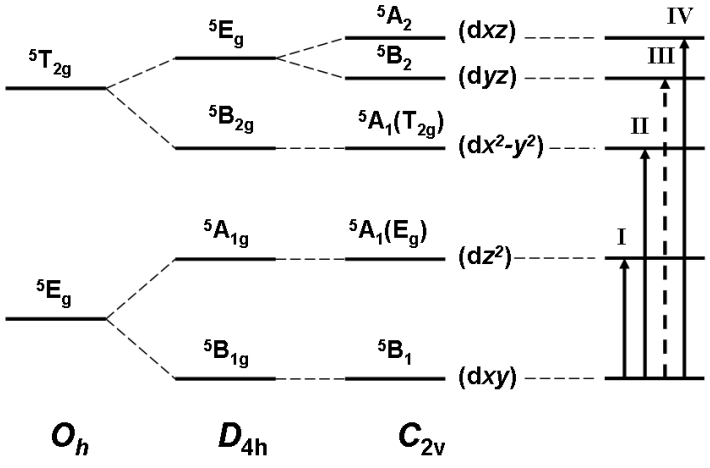

In general, UV/Vis absorption spectra of manganese(III) complexes are somewhat underrepresented in the literature. Some specific examples, however, are discussed in the following.

In the UV/Vis absorption spectrum of the $[Mn^{III}(py_2(NMe)_2)F_2]$ ($py_2(NMe)_2$ = *N,N'*-dimethyl-2,11-diaza-[3,3](2,6)pyridinophane) the $^5B_1 \rightarrow {}^5A_1$ transition ($dz^2 \rightarrow dxy$, band I) is observed at 850 nm, while the transitions into the excited states arising from the former $^5T_{2g}$ state are observed at 400 – 500 nm.[98] According to the single crystal X-ray structure the complex symmetry is $C_{2v}$. However, also the $^5B_1 \rightarrow {}^5B_2$ ($dyz \rightarrow dxy$, band III) transition, which is actually forbidden in $C_{2v}$ symmetry, is observed as a sharp distinct absorption feature at 465 nm. This indicates that the actual complex symmetry in solution is further reduced to $C_2$ or $C_S$ symmetry.[98]

In case of the square-pyramidal complex $[MnCl_5]^{2-}$ ($C_{4v}$) the unoccupied manganese d-orbital is $dx^2\text{-}y^2$. The $^5B_1 \rightarrow {}^5B_2$ transition ($dxy \rightarrow dx^2\text{-}y^2$, band II) is forbidden due to the rotational symmetry. In the single crystal polarized UV/Vis absorption spectra the observed d → d transitions at 11 500 $cm^{-1}$ and 16 000 $cm^{-1}$ are therefore assigned to the $^5B_1 \rightarrow {}^5A_1$ ($dz^2 \rightarrow dx^2\text{-}y^2$, band I) and the $^5B_1 \rightarrow {}^5E$ ($dxz$, $dyz \rightarrow dx^2\text{-}y^2$) transitions.[99]

For the square-pyramidal complexes [Mn(*salen*)X] (*salen* = salicylaldehydeethylenediimine, X = $F^-$, $Cl^-$, $Br^-$, $I^-$, $N_3^-$, $SCN^-$) three ligand field transitions are expected to appear in the UV/Vis spectrum. They are assigned to weak absorption shoulders at 12 000 $cm^{-1}$ ($dz^2 \rightarrow dx^2\text{-}y^2$), 15 000 $cm^{-1}$ ($dxy \rightarrow dx^2\text{-}y^2$) and 20 000 $cm^{-1}$ ($dxz$, $dyz \rightarrow dx^2\text{-}y^2$).[100]

The UV/Vis absorption spectra of the mononuclear manganese(III) complexes containing the bisphenoidal coordinating mixed picolyl/imidazole ligands *bpia* (bis(picolyl)(*N*-methylimidazole-2-yl)amine) and *bipa* (bis(*N*-methylimidazole-2-yl)picolyl-amine) show two ligand field transitions at ~ 450 nm and 700 - 800 nm if they are measured in MeOH. Measured in MeCN, however, only one d → d band is observed at 500 – 550 nm.[33, 101]

*Manganese(IV)*

Manganese(IV) complexes are $d^3$ high-spin systems (S = 3/2, $^4F$ ground term). Considering octahedral coordination geometries the $^4F$ ground term splits into the $^4A_{2g}$ ground state and two excited states, $^4T_{2g}$ and $^4T_{1g}$. Additionally considering the $^4T_{1g}(^4P)$ excited state three spin-allowed ligand field transitions (band I - III) are expected in the UV/Vis absorption spectrum according to the ligand field diagram (Scheme 2.2) which has been derived from the corresponding Tanabe-Sugano diagram.[102]

**Scheme 2.2.** Ligand field diagram of a $d^3$ high-spin system derived from the corresponding Tanabe-Sugano diagram[102] The ground state is represented by a $^4F$ term.

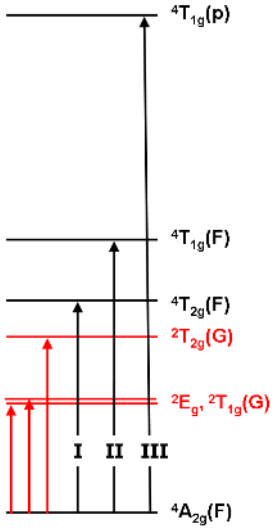


While band I and II are made out in the visible region of the optical absorption spectra band III is often superimposed by more intense charge transfer transitions. According to the ligand field diagram low-lying doublet states originate from the ligand field splitting of the $^2G$ excited state of the free metal ion. In consequence, two (three) spin-forbidden transitions would be additionally expected to appear in the near-infrared (NIR) region, but are usually not observed in the UV/Vis spectra of manganese(IV) and other $d^3$ complexes of the first transition metal row.

In the UV/Vis absorption spectrum of the facially coordinated manganese(IV) complex $[Mn(OMe)_3Me_3tacn]PF_6$ (*$Me_3$tacn* = *N,N',N"*-trimethyl-1,4,7-triazacyclyononan) the ligand field transition bands I and II are made out at 18 500 $cm^{-1}$ and 21 500 $cm^{-1}$ (Figure 2.1) while

band III is hidden beneath three prominent charge-transfer transitions which have already been mentioned in the literature.[103]

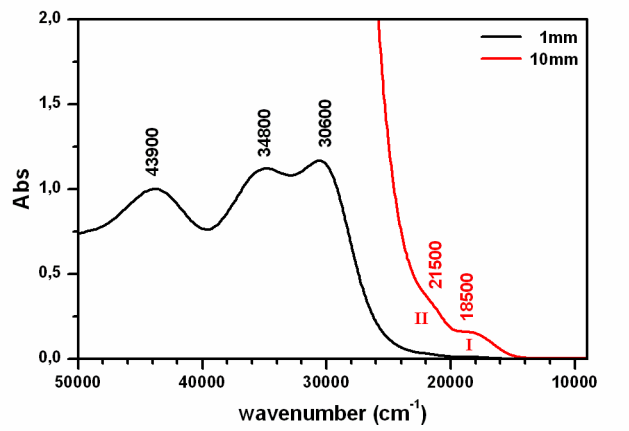


**Figure 2.1:** UV/Vis absorption spectrum of $[Mn^{IV}(OMe)_3Me_3tacn]PF_6$, 1mM in MeCN (d = 1/10 mm).[104]

### 2.1.1.2 UV/Vis Spectra of Molybdenum(III) and -(V) Complexes

*Molybdenum(III)*

Molybdenum(III) complexes can either be high-spin (S = 3/2) or low-spin (S = 1/2) complexes. In case of a high-spin configuration the same ligand field transitions are expected as for manganese(IV) (*vide supra*). However, in contrast to mangasese(IV) and other $d^3$ first row transition metal complexes, also the spin-forbidden doublet transitions might be observed in the UV/Vis absorption spectra at higher concentrations due to the increased spin-orbit coupling going to the second transition metal period (for comparison: $\zeta_{Mn(IV)} = 420\ cm^{-1}$, $\zeta_{Mo(III)} = 820\ cm^{-1}$).[105] As in the case of the first row $d^3$ complexes the $^4A_{2g} \rightarrow {}^4T_{1g}(P)$ transition (band III) is not observed in the UV/Vis absorption spectra as it is usually masked by more intense charge-transfer transitions.

In the UV/Vis absorption spectra of $[MoX_6]^{3-}$, $[MoX_3py_3]$ and $[MoX_3(4\text{-}pic)_3]$ (X = $Cl^-$, $Br^-$) the spin-forbidden $^4A_{2g} \rightarrow {}^2E_g$, $^2T_{1g}$ and $^4A_{2g} \rightarrow {}^2T_{2g}$ transitions are observed at 8 800 $cm^{-1}$ - 9 500 $cm^{-1}$ and 14 500 - 14 800 $cm^{-1}$. Compared to these doublet transitions the spin-allowed quartet transitions are more sensitive to the variation of the ligand field strength. In the case of the pure halogenido complexes $[MoX_6]^{3-}$ the $^4A_{2g} \rightarrow {}^4T_{2g}$ transition (band I) is observed

below 20 000 $cm^{-1}$, while it appears at 27 000 – 27 600 $cm^{-1}$ for the mixed halogenido-pyridine and -picoline complexes $[MoX_3py_3]$ and $[MoX_3(4\text{-}pic)_3]$ (X = $Cl^-$, $Br^-$). For the latter complexes the $^4A_{2g} \rightarrow {}^4T_{1g}$ transition (band II) is not observed as it is hidden beneath charge transfer and inner-ligand transitions. In contrast it is observed at 24 200 $cm^{-1}$ and 23 200 $cm^{-1}$ in the UV/Vis spectra of $[MoCl_6]^{3-}$ and $[MoBr_6]^{3-}$.[106-109]

*Molybdenum(V)*

Molybdenum(V) complexes only have a single unpaired electron (S = 1/2, $^2P$ ground term) Jahn-Teller distortion often leads to a tetragonally compressed octahedral coordination geometry of $D_{4h}$ (or lower) symmetry. According to the corresponding ligand field splitting diagram of a $d^1$ complex three ligand field transitions are expected in the UV/Vis absorption spectrum (Scheme 2.3). However, not all of them may actually be observed.

**Scheme 2.3.** Ligand field splitting of the metal d-orbitals $d^1$ complex in the usual tetragonally compressed, octahedral coordination geometry ($D_{4h}$).

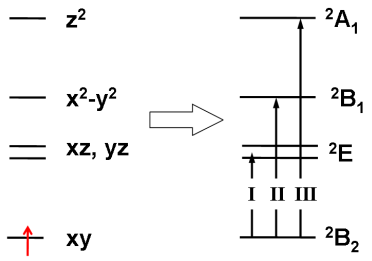


In general, UV/Vis spectroscopy often leaves many question unanswered, especially with respect to the metal centered ligand field transitions. Magnetic circular dichroism (MCD) spectroscopy may therefore be used as a complementary technique to analyze the electronic transitions of paramagnetic transition metal complexes. The basic principles of MCD spectroscopy are shortly introduced in the following.

### 2.1.2 Magnetic Circular Dichroism Spectroscopy (MCD)

Magnetic circular dichroism (MCD) spectroscopy is a very powerful tool to gain insight into the electronic structure of transition metal complexes. By means of this technique the differential absorption $\Delta\varepsilon$ between left (lcp) and right (rcp) circular polarized light of a sample is measured in the presence of a longitudinal magnetic field. As $\Delta\varepsilon$ can be positive or negative, the observed MCD transitions exhibit positive or negative signs. This property renders MCD complementary (and potentially superior) to ordinary electronic absorption spectroscopy where only (intrinsically positive) absorption intensities are measured. This is shown in Figure 2.2 for the dinuclear manganese(III,IV) complex $[Mn_2(O)_2(OAc)tpen]^{2+}$ (*tpen* = *N,N,N′,N′*-tetrakis(2-pyridylmethyl) ethylene diamine).[110, 111]

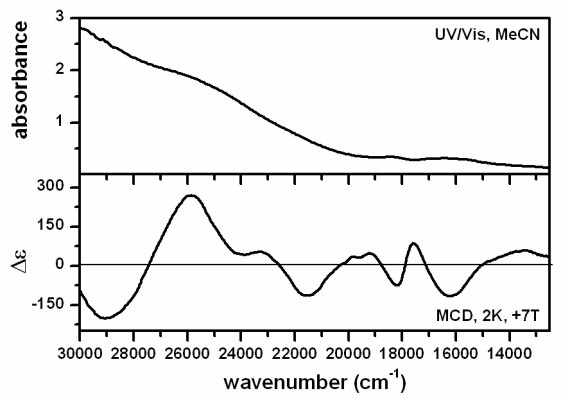


**Figure 2.2.** UV/Vis and MCD spectrum of the dinuclear manganese(III,IV) complex $[Mn_2(O)_2(OAc)tpen]^{2+}$ (*tpen* = *N,N,N′,N′*-tetrakis(2-pyridylmethyl) ethylene diamine). The UV/Vis spectrum (MeCN) has already been reported.[110] The MCD spectrum was recorded in a frozen complex solution (1 mM in PrCN/BuCN) at T = 2 K and B = +7 T. The MCD transitions have already been analyzed by Gamelin *et al.*[111]

Three different mechanisms contribute to the intensity of an MCD signal, designated as *A*-, *B*- and *C*-terms.[112-115]

$$I \sim \left[ A_1 \left( \frac{-\partial f(E)}{\partial E} \right) + \left( B_0 + \frac{C_0}{kT} \right) f(E) \right]$$

While the *A*-term intensity arises from the splitting of a degenerate excited state in the presence of an external magnetic field and shows a derivative band shape, the *C*-term intensity is observed as a consequence of the splitting of a degenerate ground state. Additionally a third contribution, the *B*-term intensity, arises from the coupling of two

formerly independent excited states in the presence of an external magnetic field. Like the MCD *C*-term transitions it shows a usual absorption band shape. In contrast to the *A*- and *B*-term intensities the MCD *C*-term intensity is temperature dependent. It increases with 1/T and thus dominates the MCD spectrum at low temperatures.[116]

MCD *C*-term transitions into two final states of different symmetry arising from a formerly degenerate E state may show opposite signs and (if the excited-state splitting is comparable to the band width) appear as one derivative-shaped band, which then is called a *pseudo-A*-term. If the starting orbitals of two *pseudo-A*-terms correspond to the symmetric and antisymmetric linear combination of atomic orbitals with respect to the mirror plane of a complex, two corresponding *pseudo-A*-terms are observed in the MCD spectrum, leading to a "double *pseudo-A*-term". This feature consists of four transitions of equal intensity which are arranged in a +/-/-/+ or a -/+/+/- fashion.

Considering the excited states, three types of electronic transitions are generally observed in open-shell paramagnetic transition metal complexes (Scheme 2.4):

(i) transitions from doubly occupied molecular orbitals into singly occupied MOs (type I),

(ii) transitions from singly occupied MOs into unoccupied MOs (type II) and

(iii) transitions from doubly occupied MOs into unoccupied MOs (type III).

**Scheme 2.4.** Type I, type II and type III electronic transitions.

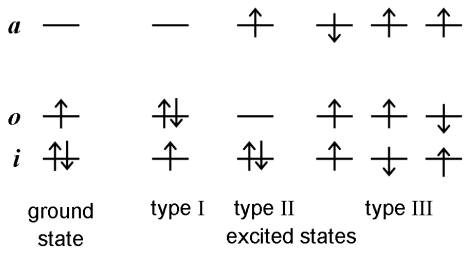


While the excited states of type I and type II electronic transitions can be represented by single determinants, multi-determinant expressions are needed to correctly describe the excited states of type III electronic transitions (*vide infra*, chapter 3).[117]

From variable temperature - variable field (VTVH) measurements of the MCD *C*--term intensity characteristic ground state properties including *g*-values, zero-field splitting parameters, coupling constants and the polarization of the individual transitions can be obtained.[8] However, in many cases MCD spectroscopy has only been used to gain ground state information and the individual transitions have been assigned without accounting for the positive and negative signs of the MCD (*C*-term) intensities.[111, 118-127] The determination of the MCD signs is in fact not trivial, but being neglected leads to an incomplete utilization of the potential of this method, a loss of spectral information with respect to the manifold of excited states and to the possibility of erroneous band assignments.

In the context of this thesis, magnetic circular dichroism spectra of manganese containing SOD, catalase and some mono- and dinuclear manganese complexes have already been reported in the literature.[111, 125, 127-131] The assignments of the observed transitions are mainly based on geometry considerations, resonance Raman investigations and (time dependent) density functional theory calculations throughout these studies.[111, 125, 127, 131] In addition, the analysis of the MCD spectra of different dinuclear cobalt complexes has shown that ligand field calculations are also a very useful tool for the assignment of MCD bands.[132-134] However, in most cases no explanations of the particular signs have been given.

Theoretical tools to calculate MCD transitions, including their signs are still fragmentarily developed. This is indeed the intrinsic problem of analyzing MCD spectra and only some very few examples have been reported, that are concerning the direct calculation of MCD transitions.[135-142] So far, they often do not show a satisfying agreement between the experimental and the calculated spectra. Of course, the calculation of molecular orbitals is possible using density functional theory (DFT) methods and also electronic transitions, i.e. UV/Vis spectra, can be computed by the use of time-dependent DFT (TDDFT). However, UV/Vis and MCD intensities arise from completely different mechanisms. They are based on completely different selection rules and cannot be compared. Therefore, it must be concluded that a complete and comprehensive understanding of MCD spectra is lacking at the present state of knowledge and that new, effective methods to analyze MCD spectra still have to be developed.

As they only have one single unpaired electron (S = 1/2) molybdenum(V) complexes seemed to be appropriate systems to develop new, general approaches and spectroscopic methods for basic studies on the electronic properties of transition metal complexes. The low-temperature MCD spectra of several mononuclear molybdenum(V) complexes have already been reported.[142-146] In the work of Ziegler and co-workers the assignment of the MCD *C*-term transitions including their signs is based on TDDFT calculations[142] employing the approach of magnetic perturbation theory.[141]

### 2.1.2.1 Setup of a Low-Temperature MCD Spectrometer

MCD spectroscopy measures the differential absorption $\Delta\varepsilon$ between left (lcp) and right (rcp) circular polarized light of a sample in the presence of a *longitudinal* magnetic field. The low-temperature MCD spectrometer used during the work of this thesis consists of a JASCO J-810 CD spectropolarimeter with an air cooled 150 W xenon lamp used as light source, an OXFORD Spectromag$^{4000}$ cryostat containing a superconducting magnet and a detector (Scheme 2.5).[147] The latter must be placed in a certain distance to the cryostat not to be affected by the magnetic field. Using two interchangeable photomultiplier tubes, a combined wavelength range of 170 – 1100 nm can be detected.

**Scheme 2.5.** Setup of a low-temperature MCD spectrometer

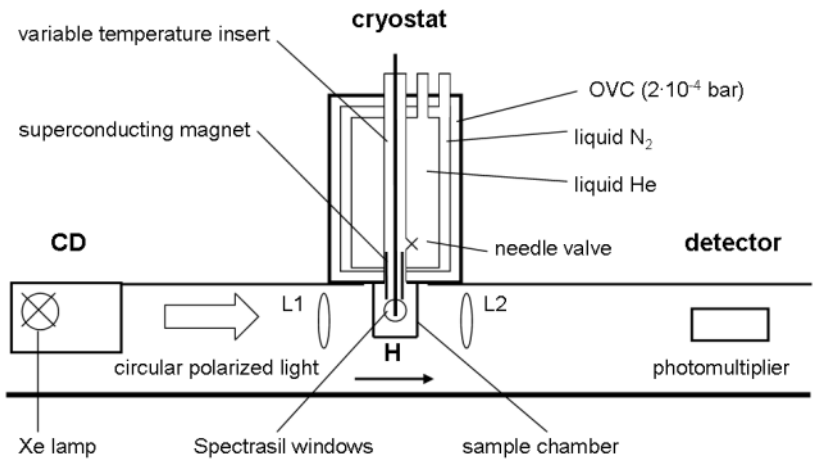


The cryostat comprises the coils of the superconducting magnet which are cooled by liquid helium. Magnetic field strengths up to ± 7 T can be achieved. The liquid helium reservoir is

surrounded by a liquid nitrogen bath and an outer vacuum chamber (OVC, $2 \cdot 10^{-4}$ bar). Samples are placed into the sample chamber via the variable temperature insert (VTI) which is connected to the liquid helium bath by a needle valve, so that the sample can directly be cooled down to 2 K by a helium stream. Via heating operating temperatures up to 25 K can also be achieved. Four Spectrasil windows allow access the sample at the bottom of the VTI for the circular polarized light being focused and defocused by two lenses, L 1 and L 2.

MCD samples usually are prepared as polystyrene films, frozen solutions (glasses) or mulls.

### 2.1.3 Electron Paramagnetic Resonance (EPR)[94, 148-150]

Electron paramagnetic resonance (EPR) spectroscopy is a very sensitive and well-established technique to characterize electronic ground states and also the higher spin states of paramagnetic systems. In the context of this thesis it is used to analyze both the active sites of natural enzymes and bioinorganic model complexes as well as to detect and characterize reactive intermediates during redox reactions, for example. From the EPR spectra different oxidation and spin states of individual metal centers can be distinguished and characteristic parameters like *g*-values, zero-field splitting parameters and coupling constants can be obtained.

Due to their unpaired electrons, paramagnetic compounds always have a non-zero magnetic moment which can interact with the external magnetic field. Electron paramagnetic resonance is based on the electron Zeeman effect which describes the linear splitting of the electronic spin states in the presence of an external magnetic field. The Zeeman interaction between the magnetic field and the magnetic moment of an unpaired electron is given by

$$H = \mu_B \vec{B} \cdot g_e \cdot \vec{S}$$

with $\mu_B$ being the Bohr magneton ($\mu_B = 9.27401 \cdot 10^{-24}$ JT$^{-1}$), $\vec{B}$ the magnetic field vector and $g_e$ the electronic *g* factor which is always about 2.00 with the exact value being dependent on the actual electronic environment.

As a parallel orientation of the electronic spin to the applied (static) magnetic field $B_0$ is preferred compared to the antiparallel orientation, the degeneracy of the electronic spin states ($m_S = \pm 1/2$) is removed in the presence of an external magnetic field. If an oscillating magnetic field $B_1$ in form of electromagnetic radiation with the energy $h\upsilon_1$ is applied perpendicular to the static magnetic field $B_0$, transitions between the two electronic spin states can be induced. Resonance is given by

$$\Delta E = h\upsilon_1 = \mu_B g_e B_0 \quad \text{with} \quad \Delta m_S = \pm 1 \quad \text{(selection rule)}$$

At this the excitation energy $E = h\upsilon_1$ of an electronic spin transition is in the energy region of microwaves (X-band EPR 9 – 10 GHz).

For a complete description of the electronic spin states in the presence of an external magnetic field further interactions have to be considered. In many cases the hyperfine interaction between the electronic spin and the nuclear spin(s) $\boldsymbol{I}$ in the vicinity has to be included which leads to the splitting of each EPR signal into a $2\boldsymbol{I} + 1$ manifold. Regarding nuclear hyperfine coupling, the selection rules for electronic spin transitions are $\Delta M_S = \pm 1$ and $\Delta M_I = \pm 0$. Additionally, the axial and rhombic zero-field splitting (zfs) has to be considered. It is a consequence of spin-orbit coupling and leads to the splitting of the different $M_S$ levels of the electronic ground state even at $B_0 = 0$ in the case of $S > 1/2$.

Including all these different terms and taking into account that the individual interactions might be anisotropic, the spin Hamiltonian to describe the electronic spin states is given by

$$\hat{H} = \mu_B \vec{B}_0 \cdot \tilde{g}_e \cdot \hat{S} + \hat{I} \cdot \tilde{A} \cdot \hat{S} + D[\hat{S}_z{}^2 - 1/3(S+1)] + E(\hat{S}_x{}^2 - \hat{S}_y{}^2)$$

with $\tilde{g}_e$ the electron $g$ tensor, $\tilde{A}$ the nuclear hyperfine tensor and $\hat{I}$ the nuclear spin operator. $D$ and $E$ are the axial and rhombic zero-field splitting parameters which can adopt positive or negative values. The theoretical calculation of the spin Hamiltonian is already established.

### 2.1.3.1 Setup of a cw X-band EPR Spectrometer

The cw X-band EPR spectrometer used for recording the EPR spectra during the work of this thesis is a reflection spectrometer. It consists of a microwave source, a microwave bridge with the interchangeable cavity (resonator) placed between the coils of the magnet and a phase sensitive detector (PSD) (Figure 2.3, Scheme 2.6).

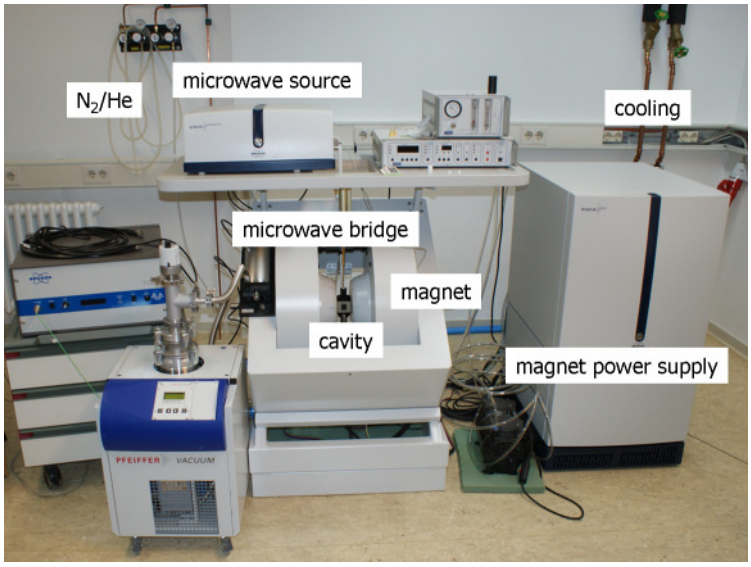


**Figure 2.3:** cw X-band EPR spectrometer

**Scheme 2.6.** Setup of a reflection cw X-band EPR spectrometer. The figure was provided by Hans-Martin Berends.[26]

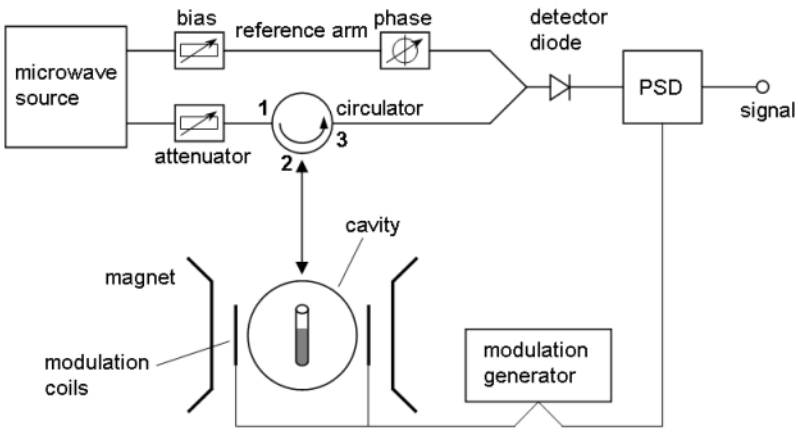


The microwave energy is generated by a Gunn diode and adjusted to the resonator by the variation of the frequency between 9 and 10 GHz. The microwave power is individually adjusted to each measurement by an attenuator. The detector diode only detects microwaves

which are reflected from the cavity and converts them into an electric current. It is sensitive to noise, interference and perturbation, so an additional modulation of the magnetic field is usually applied. This leads to an increase of the sensitivity as now the first derivative of the signal is detected. Via a bias the reference arm ensures that the detector always operates with an optimum current throughout the measurements.

Due to the very fast spin-lattice relaxation of the induced spin-transitions, the EPR spectra of manganese complexes always have to be measured at low temperatures, which make liquid helium cooling compulsory. However, molybdenum complexes also show clear hyperfine-resolved EPR signals at room temperature. However, the low-temperature spectra should additionally be measured in the case of molybdenum compounds to eventually distinguish the different oxidation states and to determine the zero-field splitting parameters $D$ and $E$.

As the zero-field splitting of the individual $M_S$ spin states is usually larger than the X-band microwave frequency of ~ 9 GHz ($\triangleq$ ~ 0.3 $cm^{-1}$) transition metal complexes with an even number of unpaired d-electrons, so-called non-Kramers systems, do not show signals in the "normal" perpendicular X-band EPR spectra, although they are, of course, still paramagnetic. However, certain spin transitions within these systems can be induced, if the oscillating magnetic field $B_1$ is not applied perpendicular but *parallel* to the static magnetic field $B_0$ ($B_1 \| B_0$, parallel mode EPR).

### 2.1.3.2 EPR Spectra of Mononuclear Manganese Complexes

EPR spectroscopy is essential and has often been used to characterize the active sites of MnSOD, MnCat and photosystem II.[21, 30, 151-158] In consequence, this technique is also already well-established for the characterization of mono-, di-, and polynuclear manganese model complexes.[153, 159-162] Due to the hyperfine interaction between the electronic spin and the nuclear spin of $\boldsymbol{I} = 5/2$ of $^{55}$Mn (natural abundance 100 %) the EPR signals of mononuclear manganese compounds split into sextets.

*Manganese(II)*

Manganese(II) complexes have five d-electrons and always occur in the high-spin configuration (S = 5/2). Axial zero-field splitting (zfs) leads to the splitting of the $M_S$ spin states as it is depicted in Scheme 2.7. Five spin transitions are allowed in general ($\Delta m_S = \pm 1$, $\Delta m_I = 0$). However, only the $|-1/2\rangle \rightarrow |+1/2\rangle$ transition is observed in the X-band EPR spectrum. Due to hyperfine coupling with the nuclear spin the signal is split into a sextet. Beside these "central" transitions ($\Delta M_S = \pm 1$, $\Delta M_I = \pm 0$), formally forbidden transitions ($\Delta M_S = \pm 1$, $\Delta M_I = \pm 1$) are also observed in between as sets of doublets. They arise from the mixing of different $M_I$ states in consequence of zfs interaction. Additionally, "outer" transitions might be observed at the edges of the original signal as well arising from the $|\pm 1/2\rangle \rightarrow |\pm 3/2\rangle$ and $|\pm 3/2\rangle \rightarrow |\pm 5/2\rangle$ transitions.[163]

**Scheme 2.7.** Splitting of the $M_S$ spin states of an S = 5/2 ($d^5$ high-spin) system with positive axial zero-field splitting. $D$ is large compared to the X-band microwave frequency, the rhombic zero field splitting $E$ is not considered. Only the $|-1/2\rangle \rightarrow |+1/2\rangle$ transition is observed in the X-band EPR spectrum. Adapted from ref[163].

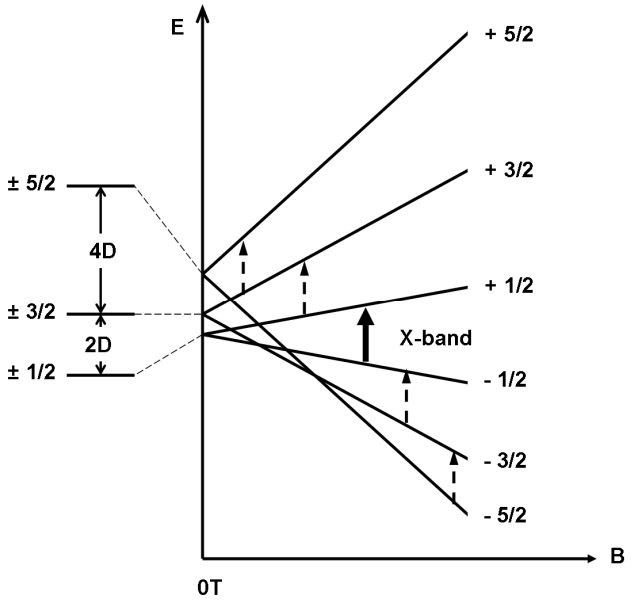


EPR is very sensitive to manganese(II), so even small amounts and impurities are detected. An example is the EPR spectrum of manganese(III) acetate which is known to be a strong oxidant. $Mn(OAc)_3$ is not soluble in methanol itself and does not show any parallel mode EPR spectrum (*vide infra*) because of its trimer structure[62] but shows the characteristic EPR spectrum of a manganese(II) compound due to small amounts of Mn(II). Both the hyperfine

split "central" $\left|-1/2\right\rangle \rightarrow \left|+1/2\right\rangle$ transition (*) and the forbidden transitions (°) are made out in the low-temperature EPR spectrum while no "outer" transitions are observed in this case (Figure 2.4)

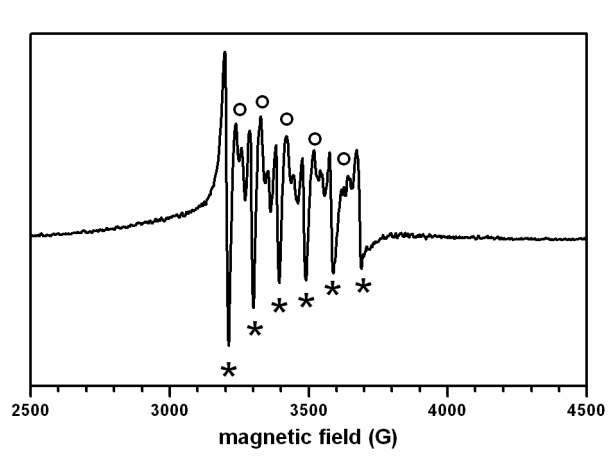


**Figure 2.4.** Low-temperature cw X-band EPR spectrum of $Mn^{2+}$ in MeOH, T = 4 K, microwave frequency: 9.643 GHz, microwave power 2 mW, modulation amplitude 10G, modulation frequency 100 kHz.

*Manganese(III)*

Manganese(III) is a non-Kramers ion as it has an even number of d-electrons ($d^4$). Solving the spin Hamiltonian (*vide supra*) for a $d^4$ high-spin system (S = 2) with a positive axial zero-field splitting $D$ the energies of the $M_S$ spin state levels are obtained according to Scheme 2.8.[159] Depending on whether $D$ is positive or negative the non-degenerate $M_S = 0$ level or the $M_S = \pm 2$ non-Kramers doublet is the lowest in energy. In consequence of $D$ being large compared to the X-band microwave frequency, the $\Delta M_S = \pm 1$ transitions, which would be detected in the "normal" perpendicular detection mode, are not accessible for these systems. However, if the oscillating magnetic field $B_1$ is applied *parallel* to the static magnetic field $B_0$ (parallel detection mode) spin transitions between the closely spaced $M_S = \pm 2$ levels can be induced.[151, 159]

Due to hyperfine interaction with the nuclear spin of $^{55}Mn$ ($I$ = 5/2) the EPR signal splits into a sextet as is shown in Figure 2.5 for the six coordinate manganese(III) complex *trans*-[Mn(*cyclam*)$Cl_2$]Cl (*cyclam*: 1,4,8,11-tetraazacyclotetradecane).

**Scheme 2.8.** Schematic splitting of the $M_S$ spin states of an S = 2 ($d^4$ high-spin) system with a positive axial zero-field splitting. $D$ is large compared to the X-band microwave frequency. The $|-2\rangle \rightarrow |+2\rangle$ transition can be induced if $B_1$ is applied parallel to $B_0$ (parallel mode EPR). Adapted from ref.[159].

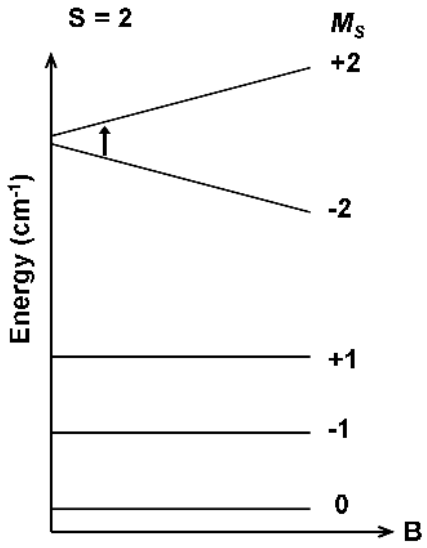


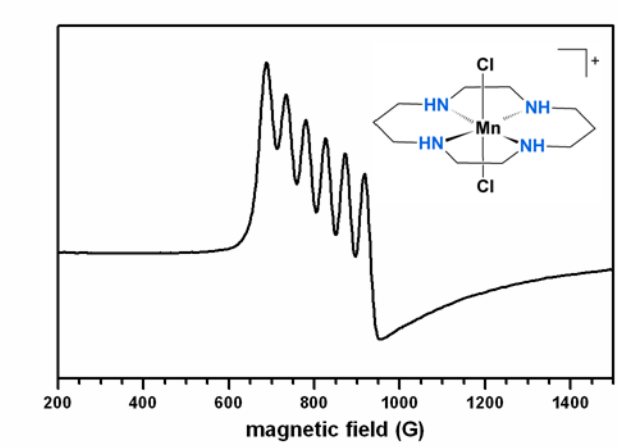


**Figure 2.5.** Low-temperature parallel mode cw X-band EPR spectrum of *trans*-[Mn(*cyclam*)$Cl_2$]Cl (*cyclam* = 1,4,8,11-tetraaza-cyclotetradecane) measured in a frozen MeOH solution (1 mM) at T = 4 K; microwave frequency 9.391 GHz, microwave power 2 mW, modulation amplitude 10G, modulation frequency 100 kHz.

*Manganese(IV)*

Mangnese(IV) complexes have three unpaired d-electrons (S = 3/2). In consequence of axial zero-field splitting two Kramers doublets, $M_S = \pm 1/2$ and $M_S = \pm 3/2$, are obtained (Scheme 2.9). Two characteristic signals are observed in the low-temperature cw X-band EPR spectra

of manganese(IV) complexes. They are ascribed to the $|-3/2\rangle \rightarrow |+3/2\rangle$ (signal I) and $|-1/2\rangle \rightarrow |+1/2\rangle$ transitions (signal II) at the $B_0 \parallel z$ orientation of the applied magnetic field. If the axial zero-field splitting $|D|$ is larger than 0.3 $cm^{-1}$ ($\triangleq$ ~ 9 GHz, X-band microwave frequency) spin transitions *between* the two Kramers doublets are not possible.[164] An additional signal would be expected arising from the $|-1/2\rangle \rightarrow |+1/2\rangle$ transition in the $B_0 \parallel x$ orientation of the magnetic field,[164] which is often not resolved but hidden beneath the asymmetric tail of signal I. A non-zero rhombic zero-field splitting parameter ($E \neq 0$) results in a slight splitting signal II.[164]

**Scheme 2.9.** Splitting of the $M_S$ spin states of an S = 3/2 ($d^3$ high-spin) system with a negative axial zero-field splitting, rhombic zero field splitting is not considered. $|D|$ is large compared to the X-band microwave frequency, so spin transitions *between* the two Kramers doublets are no possible. Adapted from ref.[164].

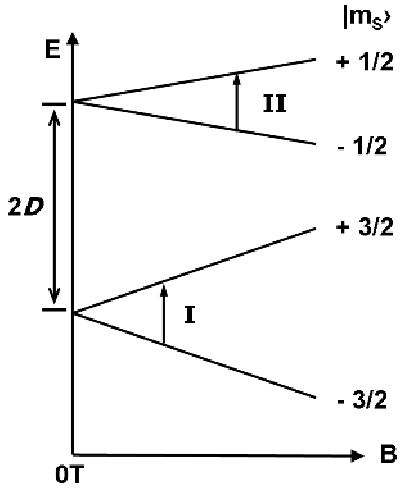


In the low-temperature cw X-band EPR spectrum of $[Mn^{IV}(OMe)_3Me_3tacn]PF_6$ (*tacn* = 1,4,7-Triazacyclononane) both signals, signal I and signal II are observed. Signal II shows the same hyperfine coupling pattern which already has been described for manganese(II) compounds (*vide supra*, Figure 2.4): the allowed spin transitions ($\Delta M_S = \pm 1$, $\Delta M_I = 0$) between the $M_S = \pm 1/2$ states result in a well-resolved sextet (*). Additionally, formally forbidden transitions ($\Delta M_S = \pm 1$, $\Delta M_I = \pm 1$) occur as doublets (°) between the "central" transitions due to the mixing of the individual $M_I$ states.

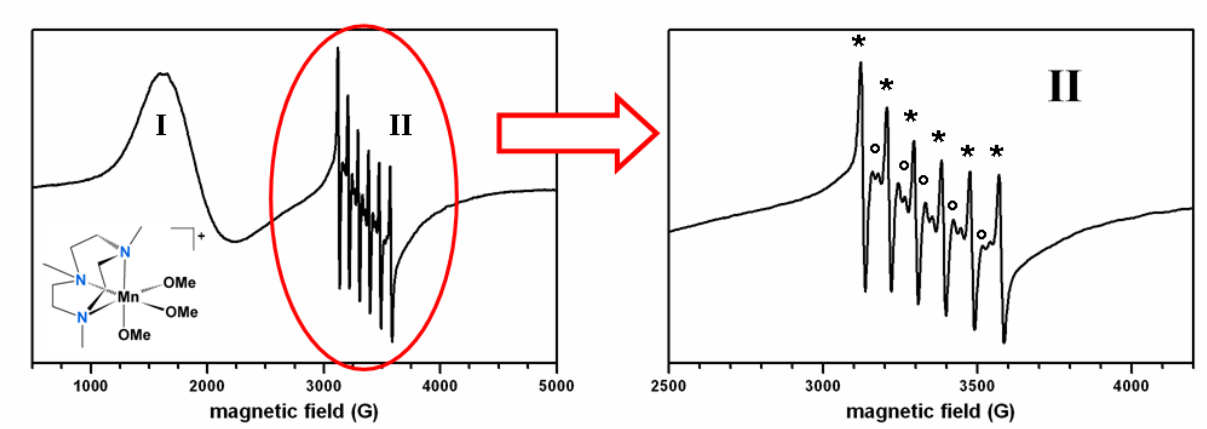


**Figure 2.6.** Low-temperature X-band EPR spectrum of $[Mn(OMe)_3Me_3tacn]PF_6$ (*tacn* = 1,4,7-Triazacyclononane) measured in a frozen MeCN solution (1 mM) at T = 4 K, microwave frequency 9.388 GHz; microwave power 2 mW, modulation amplitude 10 G, modulation frequency 100 kHz.[104]

### 2.1.3.3 EPR Spectra of Paramagnetic Molybdenum Complexes

In contrast to mononuclear manganese complexes, only very few EPR spectra of paramagnetic molybdenum complexes are already reported in the literature. Due to the hyperfine interaction of the electronic spin with the nuclear spin of the molybdenum isotopes $^{95}$Mo and $^{97}$Mo isotopes ($\boldsymbol{I}$ = 5/2) the EPR spectra of mononuclear molybdenum compounds exhibit additional signals at the flanks of the actual signal. As the total natural abundance of $^{97}$Mo and $^{95}$Mo is only 25 % ($^{95}$Mo 15.9 %; $^{97}$Mo 9.6 %) the so-called molybdenum satellites always show significantly lower intensities than the central signal.

*Molybdenum(III)*

Molybdenum(III) complexes can either be high-spin (S = 3/2) or low-spin (S = 1/2) complexes which cannot be distinguished by the means of their room-temperature EPR spectra as in both cases only *one* EPR signal is expected which arises from the $|-1/2\rangle \rightarrow |+1/2\rangle$ transition. However, at low temperatures a molybdenum(III) high-spin complex shows an additional signal arising from $|-3/2\rangle \rightarrow |+3/2\rangle$ transition corresponding to

manganese(IV) complexes (*vide supra*, Scheme 2.9) which is not observed in the low-temperature EPR spectrum of molybdenum(III) low-spin complexes, of course.[165]

*Molybdenum(V)*

As molybdenum(V) complexes have only one single unpaired d-electron only one spin transition can be induced. One EPR signal is therefore observed both at room temperature and at low temperatures.[166, 167]

## 2.2 Theoretical Methods

### 2.2.1 Ligand Field Calculations - *Angular Overlap Model* (AOM)

*Ligand field theory*

In ligand field theory the ligands of a transition metal complex are considered as idealized negative point charges which are arranged around the central metal ion in a defined way. Due to electrostatic interactions between these negative point charges and the metal d-electrons, the metal d-orbitals are lifted in energy. Because of this interaction and depending on the individual coordination geometry of the considered complex, the orbital degeneracy is removed leading to a splitting within the manifold of the metal d-orbitals with the metal-ligand bonds being considered to be purely ionic bonds.

In octahedral coordination geometries six ligands are arranged on the molecular *x*, *y* and *z* axes. The d$x^2$-$y^2$ and d$z^2$ metal d-orbitals point along these axes so they do interact with the ligands respective negative point charges and thus are lifted in energy. At the same time the d*xz*, d*yz* and d*xy* orbitals that point right between the axes and do not interact with the ligands are stabilized by the same energy. In consequence, two sublevels are obtained, $e_g$ and $t_{2g}$, which are separated by a distinct energy $\Delta_{oct}$ = 10 Dq depending on the ligand field strength of the individual ligands. By tetragonal elongation or compression along the molecular *z* axis in consequence of Jahn-Teller distortion, the degeneracy of the metal d-orbitals is further removed (Scheme 2.10).[97]

**Scheme 2.10.** Ligand field splitting of the metal d-orbitals of octahedral transition metal complexes

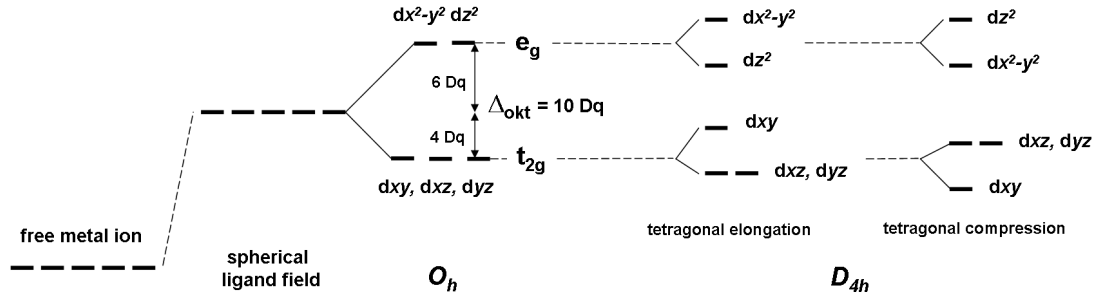


Going back to the ideal octahedral coordination geometry, electrons are filled into the $t_{2g}$ and $e_g$ orbitals according to Hund's first rule, i.e. the rule of maximum spin multiplicity. For $d^4$ - $d^7$ transition metal ions having four to seven d-electrons to place, high-spin or low-spin

configurations can be obtained depending on whether the ligand field splitting $\Delta_{oct}$ is smaller or greater than the electron-pairing energy (Scheme 2.11).

**Scheme 2.11.** High-spin and low-spin configuration of a $d^5$ transition metal ion ($Fe^{3+}$, $Mn^{2+}$)

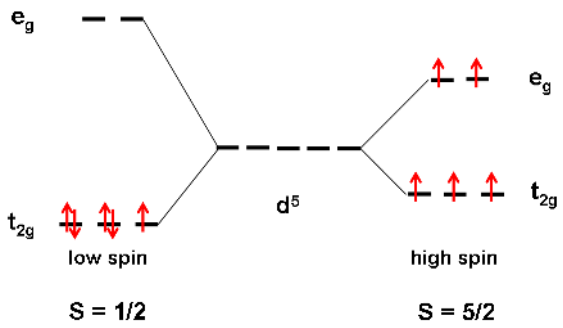


Sorting the ligands in the order of increasing ligand field strengths, the spectrochemical series of ligands is obtained:[92]

$$I^- < Br^- < S^{2-} < SCN^- < Cl^- < N_3^- < F^- < OH^- < O^{2-} < H_2O < NCS^- < NH_3, py < en < CN^- < CO$$

σ-donors/π-acceptors like aqua ligands lead to moderate ligand field splittings. π-donors like the halogenido ligands are weak ligands leading to small ligand field splittings. In consequence, halogenido complexes are mainly high-spin complexes. π-acceptors like CO or cyanide are very strong ligands leading to very high ligand field splittings and thus to the formation of low-spin complexes. Additionally, complexes of the second-row transition metals show significantly larger ligand field splittings compared to first-row transition metal complexes and are therefore mostly low-spin complexes.

*Angular Overlap Model*[93, 94]

The angular overlap model (AOM) describes the energies of the metal d-orbitals in consequence of metal-ligand interaction in terms of σ- and π-antibonding parameters leading to the relation of

$$\Delta_{oct} = 10\ Dq = 3e_\sigma - 4e_\pi$$

in case of an octahedral complex. At this $e_\sigma$ and $e_\pi$ only depend on the overlap between the individual metal and ligand orbitals, i.e. they only depend on the given bond angles, while

bond distances are not considered. Note that the π-bonding parameter $e_\pi$ can either be positive or negative depending on whether the considered ligand is a π-donor or a π-acceptor. $\Delta_{oct}$ is the ligand field splitting between the $t_{2g}$ and $e_g$ orbitals and can be determined experimentally from the UV/is absorption spectra (*vide supra*). However, being related to two unknown variables, the absolute values of $e_\sigma$ and $e_\pi$ cannot be obtained. This might be the reason why the angular overlap approach was not able to supplant the ligand field theory as the standard model for the description of transition metal complexes.[168] To solve this problem the $e_\pi$ parameter of amine ligands, which are known to be not able to form π-bonds, has been set to zero to define some kind of an "internal reference" for the determination of AOM parameters. Although the absolute values of these parameters cannot be obtained, they reflect the σ- and π-bonding properties of different ligands to some extent and may thus probably be considered as the origin of a "two-dimensional spectrochemical series".[94]

The AOMX program developed by H. Adamsky is based on the angular overlap model and can be used to calculate the energies of electronic d → d transitions by fitting the σ- and π-bonding parameters as well as the Racah parameters B and C of a given transition metal complex to the experimental energies of known ligand field transitions which are already identified in the optical absorption spectra. Additionally, by including spin-orbit coupling into these calculations, the values of the axial and rhombic zero-field splitting, *D* and *E*, can be obtained.[169, 170]

*Molecular Orbital Theory*

Ligand field theory only deals with the metal d-electrons and does not consider the electronic properties of the involved ligand. However, the nephaulexetic effect, which describes the decrease in the interelectronic repulsion (Racah) parameters B and C of a coordinated transition metal ion compared to the free, uncoordinated metal ion, already indicated that the metal-ligand bonds of transition metal complexes cannot be considered as pure ionic bonds. To a certain extent they also show a covalent character which can be described with the help of molecular orbital (MO) theory.

Assuming that the valence electrons are shared between the metal ion and the coordinating ligands, metal and ligand orbitals have to be combined into the symmetric and antisymmetric

linear combinations of the former two to properly describe the electronic properties of the considered complex. As the resulting molecular orbitals now have a larger extension compared to the individual metal and ligand orbitals, the repulsive electron-electron interaction is thus reduced leading to the aforementioned decrease in the interelectronic repulsion parameters B and C.

Additionally, the σ- and π-donor/acceptor properties, which are the reason for the sequence of the individual ligands within the spectrochemical series (*vide supra*), finally can only be explained with the molecular orbital theory.[92]

Considering the potential overlap between metal and ligand orbitals, only orbitals which have the same symmetry can be combined to obtain the molecular orbitals of a considered complex. At this an intermediate approach is to first build symmetry-adapted ligand group orbitals (LGO) by specific linear combinations of ligand orbitals. These LGOs are then combined with the corresponding metal d-orbitals of appropriate symmetry.

### 2.2.2 Quantum Chemical Methods

*Hartree-Fock Theory*[171]

If molecular properties are calculated by quantum chemical computations, the correct description of the electron-electron interaction always determines the performance of a considered method. Hartree-Fock is an SCF (self-consistent field) method which uses a Slater determinant to approximate the over-all wave function Ψ of an *N*-electron system. The energy of a Slater determinant is given by

$$E = 2\sum_{i}^{N/2} h_{ii} + \sum_{i}^{N/2}\sum_{j}^{N/2}\{2J_{ij} - K_{ij}\} \quad \text{with} \quad 2\sum_{i}^{N/2} h_{ii} \text{ being the one-electron energy.}$$

Note that antiparallel electrons are uncorrelated in a Slater determinant as the exchange integral

$$K_{ij} = \left\langle \psi_i(1)\psi_j(2) \left| \frac{1}{r_{12}} \right| \psi_j(1)\psi_i(2) \right\rangle = (ij|ji)$$

only considers the correlation of parallel electrons (Fermi hole). The Coulomb integral

$$J_{ij} = \left\langle \psi_i(1)\psi_j(2) \left| \frac{1}{r_{12}} \right| \psi_i(1)\psi_j(2) \right\rangle = (ii|jj) = \iint |\psi_i|^2 \frac{1}{r_{12}} |\psi_j|^2 dr_1 dr_2$$

is independent of the electron spin and can be interpreted as the classical interaction of the two charge densities $|\psi_i|^2$ and $|\psi_j|^2$.

The orbitals $\psi_i$ could be obtained from $\hat{h}\psi_i = \varepsilon_i\psi_i$ but are rather determined through variational optimization by the minimization of $E = \langle \Psi | \hat{H}_{el} | \Psi \rangle$. This leads to coupled one-electron equations which have to be solved iteratively. The electronic Hamilton operator $\hat{H}_{el}$ is exactly known. In consequence, $\left( \frac{\partial E}{\partial \Psi} \right) = 0$ must be fulfilled to deliver the correct overall wave function $\Psi$.

Solving the Hartree-Fock equations

$$\hat{f}|\psi_i\rangle = \varepsilon_i|\psi_i\rangle$$

with $\hat{f}$ being the one-electron Fock operator

$$\hat{f}(1) = \hat{h}(1) + \sum_j \{2\hat{j}_j(1) - k_j(1)\}$$

the orbitals $\psi_i$ can be obtained as eigenfunctions of $\hat{f}$ with the orbital energies given by

$$\varepsilon_i = \langle \psi_i | \hat{f} | \psi_i \rangle .$$

The orbitals $\psi_i$ are usually expressed by linear combinations of basis functions:

$$|\psi_i\rangle = \sum_{\nu=1}^{K} C_{\nu i} |\phi_\nu\rangle$$

To solve $\sum_\nu C_{\nu i} \langle \phi_\mu | \hat{f} | \phi_\nu \rangle = \varepsilon_i \sum_\nu C_{\nu i} \langle \phi_\mu | \phi_\nu \rangle$, which can also be written as $\hat{F}\hat{C} = \hat{S}\hat{C}\hat{\varepsilon}$ in the matrix notation (Roothaan-Hall equation) and represents a general eigenvalue problem, now only the coefficients $C_{\nu i}$ are varied to minimize the energy while the Fock matrix element $\langle \phi_\mu | \hat{f} | \phi_\nu \rangle$ and the overlap matrix element $\langle \phi_\mu | \phi_\nu \rangle = S_{\mu\nu}$ are invariant during the calculation. As the basis functions are usually not orthogonal, $\hat{F}\hat{C} = \hat{S}\hat{C}\hat{\varepsilon}$ first has to be transformed to an orthogonal basis by $\hat{X}^\dagger \hat{F}\hat{X}\hat{C}' = \hat{X}^\dagger \hat{S}\hat{X}\hat{C}'\hat{\varepsilon}$ with the unitary transformation matrix $\hat{X}$. Note that the diagonalization of $\hat{F}' = \hat{X}^\dagger \hat{F}\hat{X}$ is the rate limiting step of a Hartree-Fock calculation (scaling by $N^3$).

After a given input geometry has been optimized by the minimization of the overall energy $E = \langle \Psi | \hat{H}_{el} | \Psi \rangle$ the first, second and third derivatives of $E$ deliver electric dipole moments, force constants, the energies and intensities of IR and Raman transitions and other specific ground state properties of the considered molecule.

Paramagnetic systems are calculated spin-unrestriced, i.e. the *alpha* and *beta* spin electrons are treated separately.

Potential shortcomings of the Hartree-Fock (HF) method are due to the incomplete description of the electron-electron correlation (*vide supra*). It can be further improved by configuration interaction (CI) and coupled cluster (CC) methods which use linear combinations of Slater determinants instead of only *one* single determinant to express the overall wave function Ψ. Multi-configuration SCF methods like CASSCF combine HF and CI by simultaneously optimizing MO and CI coefficients. Perturbation theory methods (MP2, MP3, MP4, …) use another approach by introducing perturbation operators to describe the electron-electron correlation.

*(Time-dependent) Density Functional Theory - (TD)DFT*[171]

So far, it has been assumed that ground state properties like the electron density $\rho$(r) can be calculated from the energy of a considered molecule after the Schrödinger equation $\hat{H}\Psi = E\Psi$ has been solved by the variational optimization of Ψ. At this, the Hamilton operator

$$\hat{H} = -\frac{1}{2}\sum_{i=1}^{N}\nabla_i^2 - \sum_{k,i}\frac{Z_k}{R_{ki}} + \sum_{i<j}\frac{1}{r_{ij}}$$

and thus all molecular properties are determined by the number of electrons *N* and the atomic coordinates, i.e. the external potential $V(r) = -\sum_{k,i}\frac{Z_k}{R_{ki}}$. According to the first theorem of Hohenberg and Kohn *V(r)* is determined by the electron density $\rho$(r). The number of electrons is then given by $N = \int \rho(r)dr$. In consequence, the ground state energy *E* of an *N* electron system can be also expressed as an exact functional of $\rho$(r):

$$E[\rho] = V_{ne}[\rho] + T[\rho] + V_{ee}[\rho]$$

$V_{ee}[\rho]$ contains the Coulomb functional $J[r]$ and non-classical terms to describe the electronic exchange and Coulomb correlation. According to the second theorem of Hohenberg and Kohn the energy can now be minimized by the variation of $\rho$(r). By defining a non-interacting reference system which can be expressed by a Slater determinant and has the same electron density as an interacting system (theorem of Kohn and Sham), an exchange-correlation functional $E_{xc}[\rho]$ is introduced. Nowadays, hybrid functionals are used for $E_{xc}[\rho]$ containing exchange correlation functionals $E_x$ and Coulomb correlation functionals $E_c$ which are specified by the local density or the generalized gradient approximation (LDA, GGA) of the electron density.

One of the most common hybrid functionals is B3LYP.[172-174] It has also been used for all quantum chemical DFT calculations within this thesis except for the calculation of the molecular orbitals. The B3LYP exchange-correlation functional $E_{xc}[\rho]^{B3LYP}$ is given by

$$E_{xc}^{B3LYP} = (1-a)E_x^{LDA} + aE_x^{HF} + bE_x^B + cE_c^{LYP} + (1-c)E_c^{LDA}$$

Additionally to Becke's exchange functional $E_x^B$ [175] and the exchange functional $E_c^{LYP}$ of Lee, Yang and Parr[173, 174] also Hartree-Fock exchange $E_x^{HF}$ is included. From this expression it also becomes clear, that denstity functional theory (DFT) is not an *ab initio* method like Hartree-Fock as it contains three empirical parameters *a*, *b* and *c*.

Considering molecular orbital (MO) computations, the Hartree-Fock exchange contribution $E_x^{HF}$ eventually leads to wrong results with respect to the relative energies of *alpha* and *beta* spin orbitals. In consequence, the BP86 functional, which only contains Becke's exchange functional (B)[175] and Perdew's gradient corrected (GGA) correlation functional (P86),[176, 177] was used for the calculations of molecular orbitals.

Time-dependent DFT (TDDFT) methods are based on the so-called response theory which considers the (linear) response of a system to a time-dependent perturbation. At this, the propagation of a wavefunction over time is assumed to be expressed by the superposition of stationary states containing time-dependent coefficients. From TDDFT calculations information with respect to excited states can be gained and the excitation energies of electronic transitions, i.e. UV/visible absorption spectra, can be calculated.

Within this thesis the LANL2DZ basis set was used in all calculations for all types of atoms. It contains the Dunning/Huzinaga basis functions (D95) for the first transition metal row[178] and effective core potentials (Los Alamos) plus double zeta (DZ) basis functions for all other types of atoms. [179-181]

*Quantum chemical calculation of MCD spectra*

For the quantum chemical calculation of MCD *A*-, *B*- and *C*-term intensities Ziegler and co-workers have developed TDDFT methods which are based on the linear response theory.[137, 138, 141, 182-184] A corresponding routine for the calculation of MCD spectra is already implemented in the ADF program package.[185] Based on that the MCD spectra of several molybdenum(V) complexes have been calculated including their signs to assign the observed positive and negative bands to the individual MCD *C*-term transitions.[142] They have also

been tested on the calculation of the MCD spectra of several organic and (bio)inorganic compounds.[137, 141, 182, 183]

In contrast, Neese and co-workers use the approach of calculating MCD spectra with highly correlated multi-reference configuration interaction (MRCI) *ab initio* methods.[135] These have already been tested on the MCD spectra of some tetrahedral cobalt(II) complexes.[136]

# 3 MCD Spectrum of the Mo(V) Complex [Mo(O)Cl$_3$*dppe*]: *C*-Term Signs and Intensities for Multi-Determinant Excited Doublet States

Previous studies on the low-temperature MCD spectra of mononuclear molybdenum(V) complexes[142-146] already suggest that molybdenum(V) with its $d^1$ electron configuration is an excellent system to establish new procedures of spectra analysis and the quantum chemical calculation of electronic transitions and MCD signs. The MCD spectra of Mo(V)-oxido complexes are often dominated by a "double *pseudo-A*-term" feature.[142, 144, 145]

In this work, the low-temperature MCD spectrum of [Mo(O)Cl$_3$*dppe*] (*dppe*: 1,2-bis(diphenylphosphino)ethane) was analyzed. The assignment of the "double *pseudo-A*-term" was used to develop a general treatment of the MCD *C*-term intensity of type III electronic transitions. It is presented in the following manuscript which is to be submitted for publication soon.

[Mo(O)Cl$_3$*dppe*] is an oxido-halogenido molybdenum(V) complex studied in the Tuczek group as a precursor for the synthesis of Chatt type $Mo^0(N_2)$ complexes. One envisioned synthetic route would involve substitution of the chlorido ligands by an anionic silyl phosphine ligand followed by electrochemical reduction of the Mo-oxido moiety under $N_2$ atmosphere to give a Mo(0)-dinitrogen complex. A synthetic route for Mo(0)-bis-dinitrogen complexes starting from the oxido-halogenido [Mo(O)Cl$_2$(PMe)$_3$] precursor has already been established.[2]

[Mo(O)Cl$_3$*dppe*] has been synthesized by Henning Broda[186] and was thoroughly characterized by vibrational spectroscopy within this work. The molecular orbitals and electronic transitions were calculated with (TD)DFT. A "double *pseudo-A*-term" is identified to be the most prominent spectral feature of the low-temperature MCD spectrum. It was assigned to ligand-to-metal charge transfer from the $p_\pi$ orbitals of the equatorial chlorido ligands into the molybdenum d*xz* and d*yz* orbitals. Describing the MCD *C*-term intensity of these transitions the multi-determinant character of the excited states was explicitly considered.[8, 117, 187] At this, only configuration interaction between the sing-doublet and the trip-doublet excited states provides a mechanism for non-zero MCD *C*-term intensities. In this way, a general treatment for the MCD *C*-term intensity of type III electronic transitions has

been developed. The derived equations are based on the description of the MCD *C*-term intensity by Neese and Solomon.[8] The particular signs of the individual transitions were directly determined from the corresponding transition densities based on the calculated molecular orbitals.

# MCD Spectrum of the Mo(V) Complex [Mo(O)$Cl_3$*dppe*]: *C*-Term Signs and Intensities for Multi-Determinant Excited Doublet States

*Anne Westphal*[†], *Henning Broda*[†], *Philipp Kurz*[†], *Frank Neese*[‡] *and Felix Tuczek*[†]*

[†] Institut für Anorganische Chemie, Christian-Albrechts-Universität zu Kiel, D-24118 Kiel, Germany

[‡] Max-Planck-Institut für Bioanorganische Chemie, D - 45470 Mülheim an der Ruhr, Germany

**RECEIVED DATE …**

CORRESPONDING AUTHOR: E-mail: ftuczek@ac.uni-kiel.de, phone +49 431 880-1410, fax +49 431 880-1520

**ABSTRACT** The molybdenum(V) complex [Mo(O)$Cl_3$*dppe*] (*dppe*: 1,2-bis(diphenylphosphino)-ethane) is considered as an appropriate system for a combined study on the electronic structure using UV/Vis absorption and MCD (*magnetic circular dichroism*) spectroscopy, including the determination of the MCD *C*-term signs of the individual electronic transitions. In the MCD spectrum of [Mo(O)$Cl_3$*dppe*] the most intense band at 20 000 $cm^{-1}$ corresponds to a very intense UV/Vis absorption band and is assigned to the d$x^2$-

$y^2 \rightarrow$ d*xy* ligand field transition as supported by resonance Raman spectroscopy. The most prominent feature of the MCD spectrum is a "double *pseudo-A*-term" which consists of two corresponding *pseudo-A*-terms centered at 27 000 $cm^{-1}$ and 32 500 $cm^{-1}$. These are 70assigned to the ligand-to-metal charge transfer transitions from the $p_\pi$ orbitals of the equatorial chlorido ligands into the d*yz* and d*xz* molybdenum d-orbitals. Based on the theoretical expressions developed by Neese and Solomon[1] we present a general treatment of the MCD *C*-term intensity of these transitions which explicitly considers the multi-determinant character of the excited states. The individual MCD signs are determined from the corresponding transitions densities based on the calculated molecular orbitals of the title complex (BP86/LANL2DZ).

**Introduction**

Magnetic circular dichroism (MCD) spectroscopy is a powerful tool to gain insight into the electronic structure of transition metal complexes. In MCD spectroscopy, the differential absorption $\Delta\varepsilon$ between left (lcp) and right circular polarized light (rcp) of a sample is measured in the presence of a longitudinal magnetic field.[2-14] As $\Delta\varepsilon$ can be positive or negative, the observed MCD transitions exhibit positive or negative signs. This property renders MCD complementary (and potentially superior) to ordinary electronic absorption spectroscopy where only (intrinsically positive) absorption intensities are measured.

Three different mechanisms contribute to the intensity of an MCD signal, designated as *A*-, *B*- and *C*-terms.[15, 16] While the *A*-term intensity arises from the splitting of a degenerate excited state in the presence of an external magnetic field and shows a derivative band shape, the *C*-term intensity is observed as a consequence of the splitting of a degenerate ground state. A third contribution, the *B*-term intensity, arises from the coupling of two formerly independent excited states in the presence of an external magnetic field. Like the MCD *C*-term mechanism it gives rise to a usual absorption band shape. In contrast to the *A*- and *B*-term intensities the

MCD *C*-term intensity is temperature dependent (~ 1/T) and thus dominates the MCD spectrum at very low temperatures. *C*-term transitions into two final states of different symmetry arising from a formerly degenerate E state may show opposite signs and, if the excited-state splitting is comparable to the bandwidth, appear as one derivative-shaped band, which then is called *pseudo-A*-term.

From variable temperature - variable field (VTVH) measurements of the *C*-term intensity characteristic ground state properties including *g*-values, zero-field splitting parameters, coupling constants and the polarization of the individual transitions can be obtained.[1] In many cases MCD spectroscopy is only used to gain ground state information, and the individual transitions are assigned without accounting for the positive and negative signs of the MCD (*C*-term) intensities.[3-8, 10-14] The determination of the MCD signs is in fact not trivial, but being neglected leads to an incomplete utilization of the potential of this method, a loss of spectral information with respect to the manifold of excited states and to the possibility of erroneous band assignments.

A general quantum-mechanical method to calculate the signs and intensities of MCD *C*-term transitions for spins $\geq$ ½ has been described by Neese and Solomon.[1] This treatment, however, only considers cases where the electronic ground state and the excited states are represented by single-determinant wave functions. This in particular applies for two types of electronic transitions; i.e., (i) transitions from doubly occupied molecular orbitals into singly occupied MOs (type I) and (ii) transitions from singly occupied MOs into unoccupied MOs (type II). To the best of our knowledge, no theoretical treatment of *C*-term transitions exists so far for the case of (iii) transitions from doubly occupied MOs into unoccupied MOs (type III). In this case multi-determinant wave functions are needed to correctly describe the excited states.[17] It is the purpose of the present paper to consider this case on the basis of the

most simple example, a transition-metal $d^1$ system. Obviously this system gives rise to type I, type II and type III electronic transitions (**Scheme 12**). While the S=1/2 ground state and the S=1/2 excited states involved in the type I and type II transitions can be represented single determinants, the doublet excited states for type III transitions split into sing-doublet and trip-doublet states. It will be described how this situation can be treated theoretically to derive the signs and intensities of the corresponding *C*-term transitions.

**Scheme 12.** Type I, type II and type III electronic transitions.

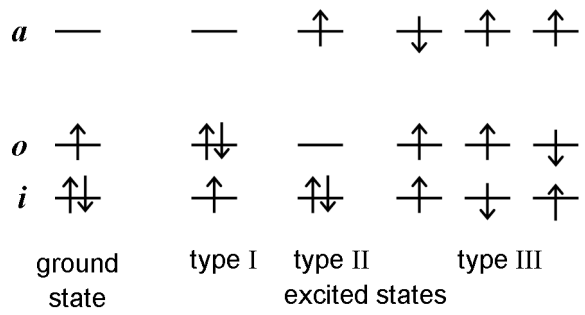


In the present study we focus on the molybdenum(V) ($d^1$) complex [Mo(O)$Cl_3$*dppe*] (*dppe*: 1,2-bis(diphenylphosphino)ethane). The MCD spectra of the pseudo-$C_S$ symmetric [Mo(O)$X_2$L] complexes (L = hydrotris(3,5-dimethyl-1-pyrazolyl)borate, X = O (diol, chatecholato), Cl, S (dithiolato)) have been investigated before. [2] The observed bands were assigned according to a rule which states that transitions between two electronic states with different symmetries (a' → a'') result in positive signed MCD bands, while negative signs are obtained, if no change of symmetry is involved (a' → a', a'' → a''). In the present paper, we will develop a more general treatment which does not rely on the symmetry properties of the complex under investigation and, in addition, allows to calculate the intensities of the MCD *C*-term transitions on the basis of the theoretical expressions presented by Neese and Solomon.[1] The signs of the *C*-term transitions will be directly derived from the MO scheme obtained by DFT. Ziegler and co-workers have assigned the MCD spectra of several molybdenum(V) complexes based on TDDFT calculations of the MCD *C*-term intensities and

signs,[18] employing the approach of magnetic perturbation theory.[19] However, this study has also not explicitly considered the multi-determinant structure of the excited doublet states, which is the subject of the present paper.

To exemplify the application of the described protocol, UV/Vis and low-temperature MCD spectra of the complex [Mo(O)$Cl_3$*dppe*] are measured in $CH_2Cl_2$ solution and $CH_2Cl_2$/polystyrene films, respectively. Electronic transitions are assigned on the basis of DFT and TDDFT calculations. Then, theoretical expressions for the MCD *C*-term intensities of type III electronic transitions are developed which allow to calculate the intensities of the observed spectroscopic features. The corresponding MCD signs are determined from the calculated MO scheme and the derived transition densities. Complementary information is derived from infrared and Raman spectroscopy, leading to a much advanced understanding of the electronic and vibrational structure of the title complex.

## Experimental Section

[Mo(O)$Cl_3$*dppe*] was synthesized using common Schlenk techniques ($N_2$). Sample preparation was always carried out under dinitrogen atmosphere.

**Synthesis.** [Mo(O)$Cl_3$*dppe*] (*dppe*: 1,2-bis(diphenylphosphino)ethane) was synthesized according to a previously reported literature procedure[20] and obtained as a red crystalline powder in a yield of 43 %. The purity of the obtained product was confirmed by elemental analysis (found (calc.): **C** 51.5 (51.6), **H** 3.4 (3.9), **Cl** 15.9 (17.3) %).

**Vibrational spectra.** The MIR infrared spectrum was obtained from KBr pellets by using a Bruker IFS v66/S FT-IR spectrometer. The FT-Raman spectra of the solid sample were recorded with a Bruker IFS 666/CS NIR FT-Raman spectrometer. A Nd:YAG laser with an excitation wavelength of 1064 nm was used as a light source.

**UV/Vis absorption spectra.** The UV/Vis absorption spectra of 1 mM and 0.1 mM solutions of the title complex in $CH_2Cl_2$ were recorded with a Cary 5000 NIR spectrometer using quartz cuvettes (path length d = 10 mm)

**Magnetic Circular Dichroism (MCD) Spectra.** Low-temperature MCD data were recorded at T = 2 K using a JASCO J810 CD spectropolarimeter associated with an OXFORD SM 4 000-9 magnetocryostat, as previously described.[10] Magnetic field strengths were varied between 0 T and ±3 T. Thin polystyrene film samples were prepared by the evaporation of a 1 mM dichloromethane complex solution containing a sufficient amount of polystyrene. After the subtraction of the B = 0 T reference spectrum the resulting MCD spectra were deconvoluted by Gaussian curve fits to resolve the individual transitions.

**Computational details.** Spin-unrestricted DFT calculations were performed using Gaussian03.[21] The B3LYP hybrid functional[22-24] was employed for the geometry optimization of the complex structure, the calculation of the vibrational spectra and for the time-dependent DFT calculations of the electronic transitions, while the calculation of the molecular orbitals was done using the BP86 functional. [25-27] The LANL2DZ basis set was always used for all types of atoms. [28] [29-31] The molecular orbitals were plotted with Gabedit.[32]

## Results and Discussion

**Complex structure and vibrational spectra.** The optimized structure of [Mo(O)$Cl_3$*dppe*] shows a slightly distorted octahedral complex geometry of pseudo-$C_S$ symmetry (**Figure 7**, **Table 1**). The *dppe* ligand and two chlorine atoms are equatorially coordinated. The third chlorido ligand is found *trans* to the oxido group with a Mo-$Cl_{ax}$ metal-ligand bond length being elongated by 0.12 Å compared to the two Mo-$Cl_{eq}$ distances. Due to the short ethylene bridge of the *dppe* ligand the P-Mo-P angle is only 81°, resulting in a $Cl_{eq}$-Mo-$Cl_{eq}$ angle which is significantly larger than 90°. The axial chlorido ligand and the oxido group are

significantly bent from the molecular *z* axis towards the *dppe* ligand with a $Cl_{ax}$-Mo-O angle of only 158°.

**Table 1.** Metal-ligand bond distances and bond angles of [Mo(O)$Cl_3$*dppe*] obtained from a quantum chemical geometry optimization (B3LYP/LANL2DZ)

| **bond distances (Å)** | | | **bond angles** | |
|---|---|---|---|---|
| Mo-P | 2.70/2.69 | | P-Mo-P | 81° |
| Mo-$Cl_{eq}$ | 2.41/2.41 | | $Cl_{eq}$-Mo-$Cl_{eq}$ | 97° |
| Mo-$Cl_{ax}$ | 2.53 | | P-Mo-$Cl_{eq}$ | 90°/91° |
| Mo-O | 1.73 | | O-Mo-$Cl_{ax}$ | 158° |
| | | | $Cl_{eq}$-P-P-$Cl_{eq}$ | -3.4° |

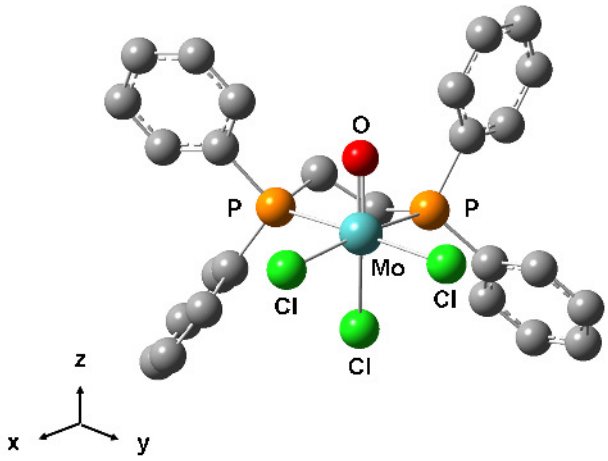


**Figure 7.** Optimized complex structure of [Mo(O)$Cl_3$*dppe*] obtained from a DFT geometry optimization (B3LYP/LANL2DZ). Hydrogen atoms are omitted for clarity.

The vibrational spectra (MIR, FT-Raman) of [Mo(O)$Cl_3$*dppe*] (**Figure 8**) are dominated by the various phenyl C=C and C-H stretching and bending vibrations of the *dppe* ligand. However, the most characteristic vibrations are the metal-ligand stretches which can be assigned with the help of DFT calculations. The Mo-oxido stretching vibration (IR: 941 $cm^{-1}$, Raman: 943 $cm^{-1}$) and the Mo-P stretch (IR: 520 $cm^{-1}$) show very high intensities, especially

in the IR spectra. The Mo-Cl stretching vibrations are observed in the Raman spectrum at 332 $cm^{-1}$ (Mo-$Cl_{eq}$, symm.) and 234 $cm^{-1}$ (Mo-$Cl_{ax}$). An overview of the most intense vibrations is given in **Table 2**. The very good match between the experimental and the calculated IR and Raman spectra assures the reliability of the optimized complex structure for its further use in the quantum chemical calculations of molecular orbitals and electronic transitions.

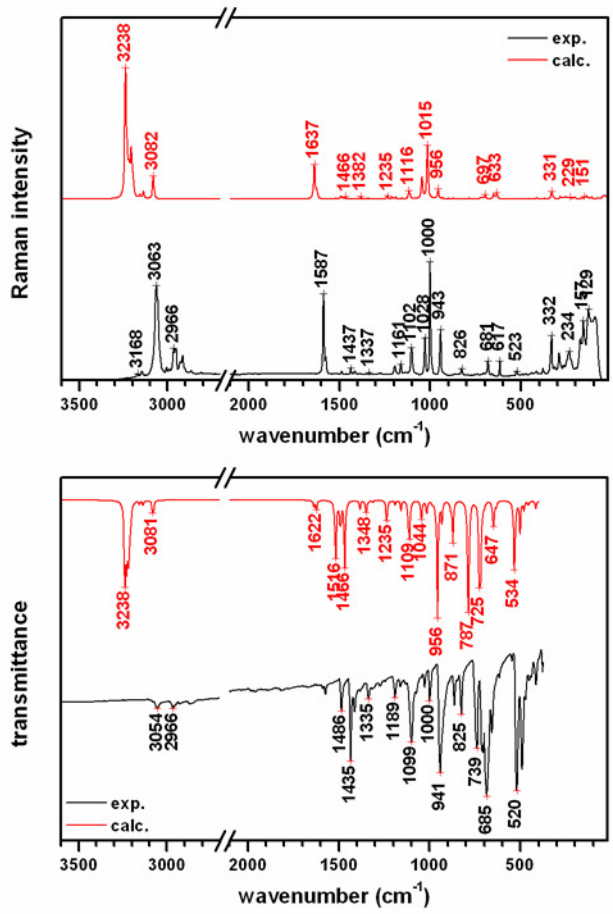


**Figure 8.** Experimental and calculated MIR and Raman spectra of [Mo(O)$Cl_3$*dppe*]. Theoretical spectra were computed by DFT calculations (B3LYP/LANL2DZ).

**Table 2.** Overview of the most characteristic vibrations of [Mo(O)$Cl_3$*dppe*]. Experimental and calculated IR and Raman frequencies are given for comparison.

| IR ($cm^{-1}$) | | Raman ($cm^{-1}$) | | vibration |
|---|---|---|---|---|
| exp. | calc. | exp. | calc. | |
| -- | 228 | 234 | 228 | Mo-$Cl_{ax}$ stretch |
| -- | 331 | 332 | 331 | Mo-$Cl_{eq}$ stretch (symmetric) |
| 491 | 502 | -- | -- | C-P bending vibrations |
| 520 | 534 | -- | -- | Mo-P stretch |
| 656 | 647 | 617 | (630) | combined P-$C_{en}$ stretch (symm. + antisymm.) |
| 685-740 | 725, 787 | 681 | -- | C(-H)$_{phenyl}$, out-of-plane bending |
| 941 | 956 | 943 | 956 | Mo=O stretch |
| -- | -- | 1000 | 1015 | (C=C)$_{phenyl}$, symmetric in-plane bending (ring |
| 1028, 1099 | 1044, 1109 | 1028, 1102 | 1045, 1116 | P-$C_{Ph}$ stretch |
| 1435, 1486 | 1466, 1516 | 1486 | 1493 | C=C stretch (antisymmetric) |
| 1572 | 1622 | 1587 | 1637 | C=C stretch (symmetric) |
| 3054 | 3238 | 3063 | 3238 | C-H stretch (phenyl) |

**UV/Vis absorption spectra.** For a $d^1$ transition metal complex in a quadratic-bipyramidal geometry like [Mo(O)$Cl_3$*dppe*] the d*xy* orbital is expected to be the lowest in energy. It is singly occupied leading to a $^2B_2$ ground state and three excited states, if the degeneracy of the d*xz* and d*yz* orbitals is assumed to be maintained (**Scheme 13**).

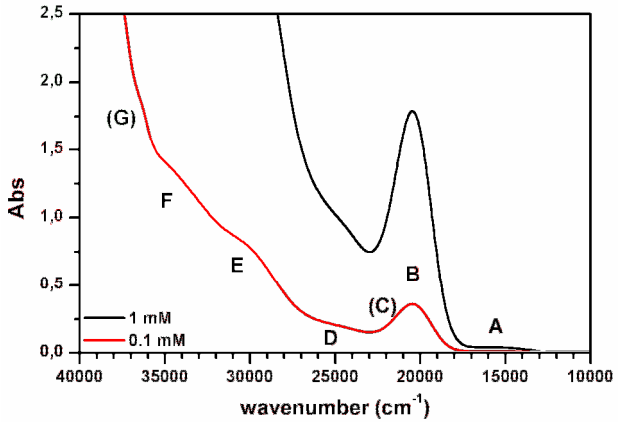


**Figure 9.** UV/Vis absorption spectra of [Mo(O)$Cl_3$*dppe*] in $CH_2Cl_2$ (1/0.1 mM d = 10 mm).

**Scheme 13.** Ligand field splitting of the metal d-orbitals for a distorted octahedral $d^1$ system. It is characteristic for the tetragonally compressed complex geometry of [Mo(O)$Cl_3$*dppe*].

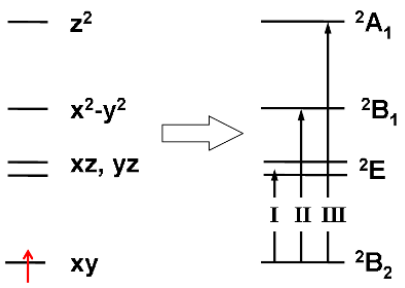


The most prominent feature of the UV/Vis spectrum of [Mo(O)$Cl_3$*dppe*] is a distinct absorption band centered at 20 500 $cm^{-1}$ ($\varepsilon$ = 3 600 $Lmol^{-1}cm^{-1}$, **Figure 9**, band B). This band has already been reported for [Mo(O)$Cl_3$*dppe*] and [Mo(O)$Cl_3$*dppen*] (*dppen* = 1,2-bis(diphenylphosphino)ethene)[33] and was already assigned to the $^2B_2 \rightarrow {}^2B_1$ ($dxy \rightarrow dx^2\text{-}y^2$) ligand field transition.[33, 34] Note that this transition shows an unusually high absorption intensity compared to the broad absorption band A at 15 500 $cm^{-1}$ which is assigned to the $^2B_2 \rightarrow {}^2E$ ($dxy \rightarrow dxz$, $dyz$) ligand field transition, in accordance with the literature.[2, 35, 36] However, also in the UV/Vis spectrum of the octahedral Mo(V) complex [Mo(O)$Cl_2$L] (L = hydrotris(3,5-dimethyl-1-pyrazolyl)borate) an absorption shoulder of moderate intensity ($\varepsilon \sim 500$ $Lmol^{-1}cm^{-1}$) at 23 000 $cm^{-1}$ has been assigned to the $dxy \rightarrow dx^2\text{-}y^2$ ligand field transition based on the corresponding MCD spectrum.[2] However, an explanation for the very high intensity in the case of [Mo(O)$Cl_3$*dppe*] is still lacking (see below).

The third ligand field transition, $^2B_2 \rightarrow {}^2A_1$ ($dxy \rightarrow dz^2$), is expected at energies greater than 35 000 $cm^{-1}$ [34] and thus is not observed in the UV/Vis spectrum of [Mo(O)$Cl_3$*dppe*], as it is hidden beneath more intense charge transfer transitions.

Additionally, four shoulders can be identified at 25 000 $cm^{-1}$ (band D), 30 000 $cm^{-1}$ (band E), 34 000 $cm^{-1}$ (band F) and 36 000 $cm^{-1}$ (and G) in the tail of a rising absorbance (**Figure 9**).

They might arise from various charge transfer transitions from the different chlorido p-orbitals into molybdenum d-orbitals (LMCT). In addition, the possible presence of Mo → P metal-to-ligand charge transfer (MLCT) as well as oxido → Mo ligand-to-metal charge transfer (LMCT) transitions has to be taken into account. In general, the UV/Vis spectrum leaves many questions. Thus, low-temperature MCD spectra were recorded which provide further information with respect to the LF- and CT-excited states of the title complex.

**Low Temperature MCD Spectra.** In the low temperature MCD spectrum of [Mo(O)$Cl_3$*dppe*] four distinct absorption features are observed between 20 000 $cm^{-1}$ and 37 000 $cm^{-1}$ with two points of zero-crossing at 27 000 $cm^{-1}$ and 32 000 $cm^{-1}$ (**Figure 10**) which is different from the band pattern observed in the MCD spectra of any of the $C_S$ symmetric oxido-molybdenum(V) [Mo(O)$X_2$L] complexes (L = hydrotris(3,5-dimethyl-1-pyrazolyl)borate, X = O (diol, chatecholato), Cl or S (dithiolato)), that have already been reported.[2, 9, 18]

The features of the MCD spectrum could be successfully modeled by six Gaussian curves (**Figure 10**, right). At positive magnetic field strengths three positive bands (band 1 - 3) are observed between 20 000 $cm^{-1}$ and 25 000 $cm^{-1}$. They are followed by two transitions with negative MCD intensities around 30 000 $cm^{-1}$ (band 4 and 5) and another positive band centered at 34 100 $cm^{-1}$ (band 6).

There is a good correlation of the most intense MCD transition (band 1) with the very intense UV/Vis absorption band at 20 500 $cm^{-1}$ (band B). This band has been assigned to the d$xy$ → d$x^2$-$y^2$ ligand field transition (*vide supra*). The positions of MCD bands 3, 4/5 and 6 correspond to the observed shoulders in the UV/Vis spectrum at 25 000 $cm^{-1}$, 30 000 $cm^{-1}$ and 34 000 $cm^{-1}$ (band D - F).

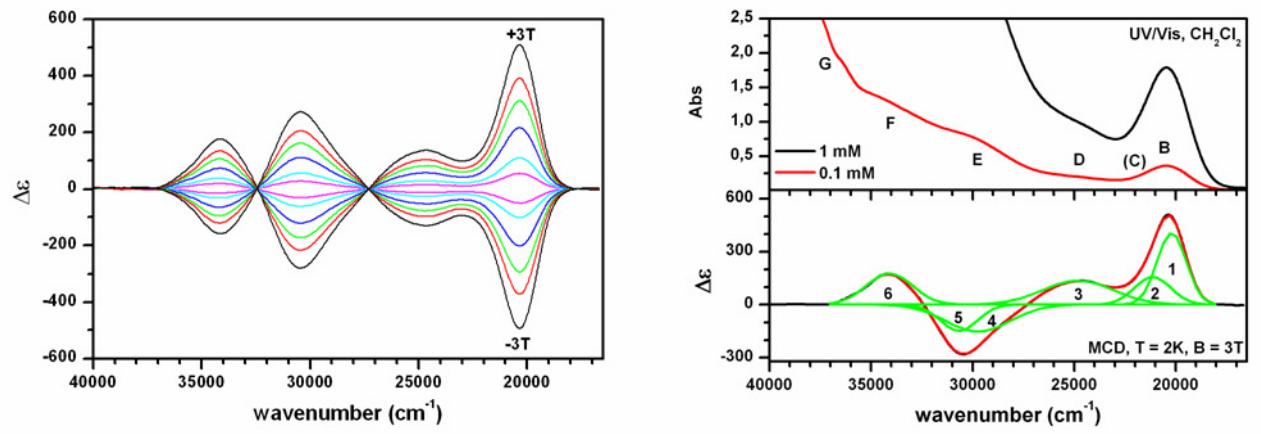


**Figure 10**. **left:** Low temperature MCD spectra of [Mo(O)$Cl_3$*dppe*], measured in polystyrene/$CH_2Cl_2$ at T = 2 K. The sample was prepared from a 1 mM solution of the title complex. The magnetic field strength was varied from B = -3 T to +3 T. **right**: Gaussian curve fit of the low temperature MCD spectrum obtained at T = 2 K and B = +3 T between 20 000 $cm^{-1}$ and 37 000 $cm^{-1}$ and UV/Vis absorption spectrum for comparison.

The MCD bands 3 - 6 all show the same intensity in a positive-negative-negative-positive pattern and should therefore be considered as two corresponding *pseudo-A*-terms, a negative *pseudo-A*-term centered at 27 000 $cm^{-1}$ (band 3 + 4,) and a positive *pseudo-A*-term centered at 32 500 $cm^{-1}$ (band 5 + 6), giving rise to a "double *pseudo-A*-term" (*vide supra*). This implies that both the ground states and the excited states derive from two nearly or formerly degenerate E states and the transition-dipole moments of the individual transitions between these states each have opposite signs (see below). A "double *pseudo-A*-term" has also been identified as the dominating spectral feature in the MCD spectra of several molybdenum(V) oxido-dithiolato complexes and was assigned to S → Mo ligand-to-metal charge transfer.[2, 9, 18] A more detailed assignment of the observed UV/Vis and MCD transitions is only possible based on the time-dependent DFT calculation of the electronic transitions, as well as

molecular orbital and symmetry considerations which will also give an explanation for the positive and negative signs of the individual MCD bands.

**DFT evaluation of the MO scheme.** The molecular orbitals of [Mo(O)$Cl_3$*dppe*] obtained from an unrestricted DFT calculation do not show a large extent of spin polarization, with the only exception of the singly occupied molecular orbital (SOMO, 117). *Alpha* and *beta* spin orbitals thus coincide in orbital numbers and orbital types, so **Figure 11** only shows the relevant *alpha* spin orbitals, which are also listed and described in **Table 3**. Compared to the ligand field diagram shown in **Scheme 13** the expected energy sequence of the molybdenum d-orbitals is confirmed by DFT.

For a $C_S$ symmetrical complex, the mirror plane (*xz*) defines the molecular axes, so that the d*xy* orbital, which is the highest (- singly!) occupied molecular orbital (117, SOMO), has to be relabelled into d$x^2$-$y^2$ (and *vice versa*). Note that this changed notation will be used from now on, so that the starting orbital of potential ligand field and metal-to-ligand charge transfer transitions will now denoted as d$x^2$-$y^2$ in the following. The four unoccupied metal d-orbitals are d*yz* and d*xz* (118, 119), d*xy* (120, formerly d$x^2$-$y^2$) and d$z^2$ (129).

The energetically highest ligand orbitals are the $p_y$ and $p_x$ orbitals of the axial chlorido ligand (116, 115). To describe the p-orbitals of the equatorial chlorido ligands four possible linear combinations have to be considered as both the in-plane and the out-of-plane orbitals can be combined symmetrically (s) or antisymmetrically (a) with respect to the molecular mirror plane *xz*. Additionally the bonding and antibonding interactions with the corresponding molybdenum d-orbitals and the p-orbitals of the axial ligands have to be taken into account. The symmetric combination of the in-plane chlorido p-orbitals is stabilized by the metal d$x^2$-$y^2$ orbital, resulting in a bonding and an antibonding combination (100, 117). In contrast, the antisymmetric linear combination of the in-plane chlorido p-orbitals cannot be stabilized by

any of the molybdenum d-orbitals, but instead shows a large contribution of phosphorus $sp^3$ orbitals (114).

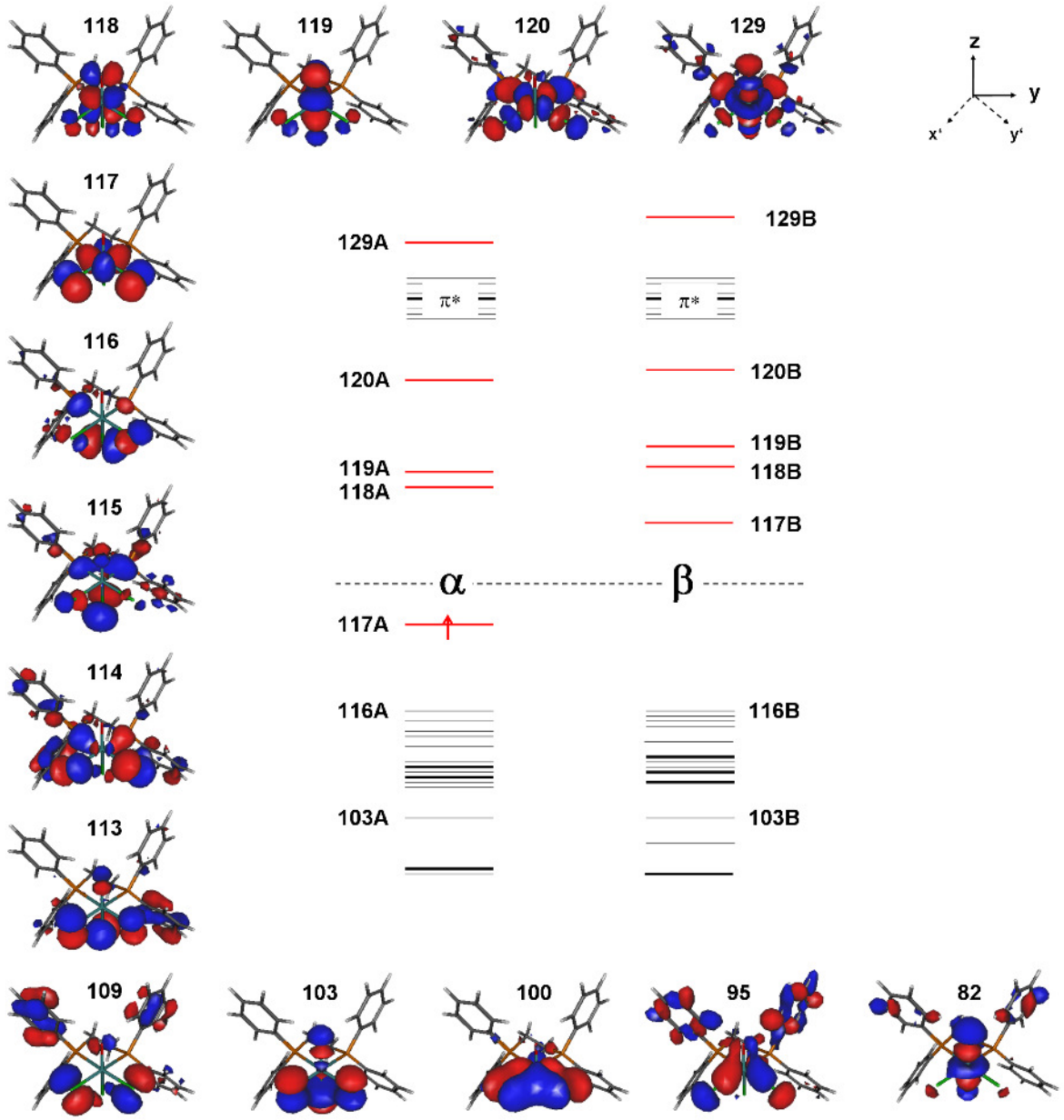


**Figure 11.** Molecular orbitals (*alpha* spin orbitals) of [Mo(O)$Cl_3$*dppe*] as obtained from the DFT calculation (BP86/LANL2DZ).

**Table 3** Molecular orbitals of [Mo(O)$Cl_3$*dppe*] obtained from the DFT calculation (BP86/LANL2DZ).

| | | sym [a] | Mo | $Cl_{eq}$ | $Cl_{ax}$ | O | description |
|---|---|---|---|---|---|---|---|
| 129 | $z^2$ | **a'** | d$z^2$ | $\sigma_{svm}(Cl_{eq}+P)$ | $p_z$ | $p_z$ | σ–antibonding, unoccupied metal d orbital phenyl π* orbitals |
| 120 | ***xy*** | **a"** | d*xy* | $\sigma_2(Cl_{eq}+P)$ | -- | -- | σ–antibonding, unoccupied metal d orbital |
| 119 | ***xz*** | **a'** | d*xz* | $p_{out\text{-}of\text{-}plane}$ (s) | $p_x$ | $p_x$ | π–antibonding, unoccupied metal d orbital |
| 118 | ***yz*** | **a"** | d*yz* | $p_{out\text{-}of\text{-}plane}$ (a) | $p_y$ | $p_y$ | π–antibonding, unoccupied metal d orbital |
| 117 | $x^2$-$y^2$ | **a'** | d$x^2$-$y^2$ | $p_{in\text{-}plane}$ (s) | -- | -- | d$x^2$-$y^2$/$p_{in\text{-}plane}$, π–antibonding, singly |
| 116 | **$p_y$ ($Cl_{ax}$)** | **a"** | -- | "e" ($Cl_{eq}$+ P) | $p_y$ | ($p_y$) | axial chlorido p orbital ($Cl_{ax}$) |
| 115 | **$p_x$ ($Cl_{ax}$)** | **a'** | -- | "e" ($Cl_{eq}$+ P) | $p_x$ | ($p_x$) | axial chlorido p orbital ($Cl_{ax}$) |
| 114 | **$p_{in\text{-}plane}$(a)** | **a"** | -- | $p_{in\text{-}plane}$ (a) | ($p_y$) | -- | in-plane ligand p orbital ($Cl_{eq}$) |
| 113 | **$p_{out\text{-}of\text{-}plane}$(s)** | **a'** | -- | $p_{out\text{-}of\text{-}plane}$ (s) | $p_x$ | $p_x$ | out-of-plane chlorido $p_\pi$ orbital, $p_x$ phenyl π orbitals |
| 109 | **$p_{out\text{-}of\text{-}}$** | **a"** | -- | $p_{out\text{-}of\text{-}plane}$ (a) | $p_y$ | ($p_y$) | out-of-plane chorido $p_\pi$ orbital ($Cl_{eq}$) phenyl π orbitals |
| 103 | **$p_{out\text{-}of\text{-}plane}$(s)** | **a'** | -- | $p_{out\text{-}of\text{-}plane}$ (s) | $p_x$ | $p_x$ | out-of-plane chlorido $p_\pi$ orbital ($Cl_{eq}$), $p_x$ p ($Cl_{eq}$) + $sp^3$ (P) |
| 100 | $x^2$-$y^2$ | **a'** | d$x^2$-$y^2$ | $p_{in\text{-}plane}$ (s) | -- | -- | d$x^2$-$y^2$/$p_{in\text{-}plane}$, π-binding analogue of MO |
| 95 | ***xy*** | **a"** | d*xy* | $\sigma_2(Cl_{eq}+P)$ | -- | -- | d*xy*/$\sigma_2$, σ-binding analogue of MO 120 |
| 82 | $z^2$ | **a'** | d$z^2$ | $\sigma_{svm}(Cl_{eq}+P)$ | $p_z$ | $p_z$ | d$z^2$/$\sigma_{sym.}$, σ-binding analogue of MO 129 |

[a] $C_S$ symmetry (mirror plane *xz*)

The symmetric linear combination of the out-of-plane $p_\pi$ orbitals interacts with the $p_x$ orbital of the axial chlorido ligand, again resulting in a bonding and an antibonding linear combination (103, 113). It also interacts with the d*xz* orbital: MO 119 exhibits an antibonding interaction, whereas the bonding analogue is not observed among the highest twenty occupied orbitals. The antisymmetric linear combination of the out-of-plane $p_\pi$ orbitals shows a large percentage of phenyl π-character (109). It can also interact with the d*yz* orbital: MO 118 exhibits an antibonding interaction, whereas the bonding analogue is again not observed among the highest twenty occupied orbitals. The σ-bonding counterparts of the unoccupied

d*xy* and d$z^2$ metal d-orbitals, in contrast, can be clearly identified in the manifold of the higher lying occupied MOs (MO 95 and 82). Due to the molecular symmetry, all molecular orbitals are either symmetric (a') or antisymmetric (a'') with respect to the mirror plane *xz*. Molecular orbitals, that are not displayed in **Figure 11** are mainly π- and π*-orbitals of the *dppe* phenyl groups. Some of them show significant contributions of the different chlorido p-orbitals, the occupied *dppe* π-orbitals are often mixed with the chlorido $p_{out\text{-}of\text{-}plane}$(a) orbital (MO 105, 107 and 111). There are no *alpha* or *beta* spin orbitals among the highest twenty occupied molecular orbitals which exhibit pure phosphorus or oxido p-character.

The same types of molecular orbitals have also been described for the oxido-chlorido molybdenum(V) complex [Mo(O)$Cl_2$L] (L = hydrotris(3,5-dimethyl-1-pyrazolyl)borate),[2] with exception of the axial chlorido p-orbitals, of course, as no axial chlorido ligand was present in this complex. Due to this difference in coordination, the symmetric and the antisymmetric equatorial out-of-plane chlorido $p_\pi$ orbitals and the d*xz* and d*yz* orbitals are inverted in energy in the case of [Mo(O)$Cl_3$*dppe*] compared to [Mo(O)$Cl_2$L] (L = hydrotris(3,5-dimethyl-1-pyrazolyl)borate).[2] The same also applies for the corresponding Mo(V)=O dithiolate complexes [Mo(O)$S_2$L]. [2, 9, 18]

**TDDFT calculation of the electronic transitions and assignment of the UV/Vis spectrum.**

The electronic transitions of [Mo(O)$Cl_3$*dppe*] were calculated by TDDFT. The results are shown in **Figure 12** and **Table 4**, respectively. The most intense electronic transitions in the calculated UV/Vis spectrum are various LMCT transitions from different chlorido p-orbitals into the d*xy* orbital at energies around 35 000 $cm^{-1}$, probably corresponding to the weak shoulder at 36 000 $cm^{-1}$ (band G) in the experimental UV/Vis spectrum. An additional shoulder is calculated at 26 000 $cm^{-1}$ which might correspond to the observed shoulder at 25 000 $cm^{-1}$ (band D) in the experimental UV/Vis spectrum.

The energies of the d$xy$ → d$xz$, d$yz$ ligand field transitions, which are observed at 15 500 $cm^{-1}$ in the experimental UV/Vis absorption spectrum, appear too low in the calculated spectrum (11 900 $cm^{-1}$, 13 600 $cm^{-1}$). In contrast, the calculated d$x^2$-$y^2$ → d$xy$ transition is found at 21 100 $cm^{-1}$, in very good agreement with the assignment of the experimentally observed UV/Vis absorption band B at 20 500 $cm^{-1}$.[34] However, there is no satisfactory correlation between the measured and calculated absorption intensities for this band. The most intense transition in the spectral region around 20 000 $cm^{-1}$ of the calculated spectrum is the $p_{in\text{-}plane}$(a) → d$x^2$-$y^2$ LMCT transition at 19 500 $cm^{-1}$. The calculated energy of d$x^2$-$y^2$ → d$z^2$ ligand field transition is 33 600 $cm^{-1}$. This is in good accordance with the predicted energy of ~ 35 000 $cm^{-1}$ for the experimental energy (*vide supra*).[34]

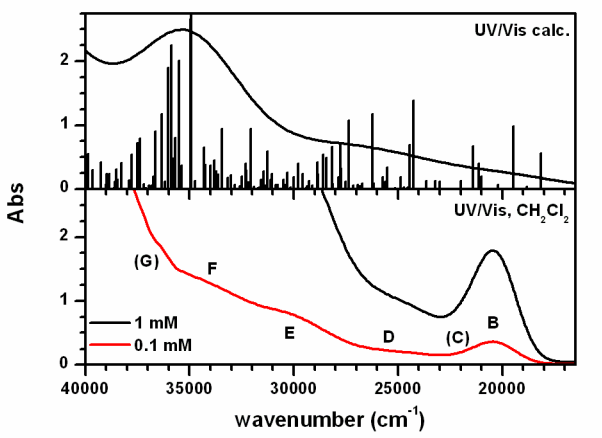


**Figure 12.** Experimental and calculated UV/Vis spectrum of [Mo(O)$Cl_3$*dppe*] for comparison. The experimental UV/Vis spectrum was measured in $CH_2Cl_2$ (1/0.1 mM d = 10 mm). The calculated UV/Vis spectrum was computed by time-dependent DFT (B3LYP/LANL2DZ).

The TDDFT calculations also provide information with respect to ligand-to-metal charge transfer (LMCT) transitions into the unoccupied molybdenum d-orbitals. Theoretically such

transitions can either occur within the *alpha* or the *beta* spin orbitals, but as no spin polarization between these two sides has been observed in the calculation of the molecular orbitals (*vide supra*), no splitting is expected between corresponding LMCT transitions in the manifolds of spin-up and spin-down orbitals.

The LMCT transitions from the p-orbitals of the axial chlorido ligand into the d*yz* and d*xz* orbitals are predicted between 21 000 $cm^{-1}$ and 28 000 $cm^{-1}$. The most intense of these transitions in the calculated UV/Vis spectrum, $p_x \rightarrow dyz$, is found at 24 300 $cm^{-1}$ which might correspond to the experimentally observed absorption feature at 25 000 $cm^{-1}$ (band D) and thus to band 3 in the MCD spectrum.

**Table 4.** Electronic transitions of [Mo(O)$Cl_3$*dppe*] calculated by TDDFT (B3LYP/LANL2DZ). Only d → d ligand field transitions and CT transitions with oscillator strengths > 0.0020 are listed.

| energy | oscillator strength | description | | |
|---|---|---|---|---|
| 11 900 | 0.0007 | $x^2$-$y^2$ → yz | d → d | 117A → 118A |
| 13 600 | 0.0003 | $x^2$-$y^2$ → xz | d → d | 117A → 119A |
| **18 200** | 0.0056 | $p_y$ → $x^2$-$y^2$ | $L_{ax}$MCT | 116B → 117B |
| **19 500** | 0.0098 | $p_{in\text{-}plane}$(a) → $x^2$-$y^2$ | $L_{eq}$MCT | 114B → 117B |
| **21 100** | 0.0020 | $p_y$ → yz | $L_{ax}$MCT | 116B → 118B |
| **21 100** | 0.0040 | $x^2$-$y^2$ → xy | d → d | 117A → 120A |
| **21 400** | 0.0067 | $p_x$ → yz | $L_{ax}$MCT | 115A → 118A |
| **24 300** | 0.0139 | $p_x$ → yz | $L_{ax}$MCT | 115A → 118A |
| **24 500** | 0.0069 | $p_x$/$p_y$ → yz | $L_{ax}$MCT | 115/116B → 118B |
| **26 200** | 0.0118 | $p_{out\text{-}of\text{-}plane}$(s) → yz | $L_{eq}$MCT | 113B → 118B |
| **27 400** | 0.0107 | $p_x$ → xz | $L_{ax}$MCT | 115B → 119B |
| **27 700** | 0.0032 | $p_{out\text{-}of\text{-}plane}$(s,a) → xy, yz | $L_{eq}$MCT | 103/105 → 117/118 |
| **28 200** | 0.0066 | phenyl π → xz | LMCT | 104A → 119A |
| **28 400** | 0.0049 | phenyl π ( $p_{out\text{-}of\text{-}plane}$(a)) → yz | $L_{eq}$MCT | 106/112A → 118A |
| **28 600** | 0.0054 | $p_{out\text{-}of\text{-}plane}$(s) → xz | $L_{eq}$MCT | 113B → 119B |
| **28 800** | 0.0023 | $p_{out\text{-}of\text{-}plane}$(a), phenyl π → yz | $L_{eq}$MCT | 110A → 118A |
| **28 900** | 0.0042 | phenyl π ( $p_{in\text{-}plane}$(a)) → xz | $L_{eq}$MCT | 112A → 119A |

| | | | | |
|---|---|---|---|---|
| **29 600** | 0.0024 | phenyl π ( $p_{out\text{-}of\text{-}plane}$(a)) → xz | $L_{eq}$MCT | 105B → 119B |
| **30 300** | 0.0024 | $p_{out\text{-}of\text{-}plane}$(a) (phenyl π) → yz | LMCT | 109/110B → 118B |
| **31 100** | 0.0024 | $p_{out\text{-}of\text{-}plane}$(a) (phenyl π) → xz | LMCT | 109/110 → 118/119 |
| **31 300** | 0.0059 | $p_{in\text{-}plane}$(s)→ $x^2$-$y^2$ | $L_{eq}$MCT | 100B → 117B |
| **31 500** | 0.0028 | $p_{out\text{-}of\text{-}plane}$(a) → yz | $L_{eq}$MCT | 107B → 118B |
| **32 100** | 0.0094 | $p_x$ → xy | $L_{ax}$MCT | 115A → 120A |
| **32 300** | 0.0029 | $p_{out\text{-}of\text{-}plane}$(s, a) → yz, xz | $L_{eq}$MCT | 103/107 → 118/119 |
| **32 300** | 0.0040 | $p_{out\text{-}of\text{-}plane}$(a), phenyl π → xz | LMCT | 109/110B → 119B |
| **32 500** | 0.0020 | $p_{out\text{-}of\text{-}plane}$(a) → yz, xz | $L_{eq}$MCT | 107/111B → 118/119B |
| **33 000** | 0.0022 | $p_{in\text{-}plane}$(a), $p_y$ → xy | $L_{eq}$/$L_{ax}$MC | 114/116A → 120A |
| **33 400** | 0.0094 | phenyl π ( $p_{out\text{-}of\text{-}plane}$(s)) → xz | $L_{eq}$MCT | 108B → 119B |
| **33 400** | 0.0034 | $p_{in\text{-}plane}$(s), $p_{out\text{-}of\text{-}plane}$(s) → yz | $L_{eq}$MCT | 102/103B → 119B |
| **33 600** | 0.0023 | phenyl π ( $p_{out\text{-}of\text{-}plane}$(a)) → xz | $L_{eq}$MCT | 108B → 119B |
| | | $x^2$-$y^2$ → $z^2$ | d → d | 117A → 129A |
| **33 700** | 0.0028 | $p_{in\text{-}plane}$(s)/$x^2$-$y^2$ → yz | $L_{eq}$MCT | 102B → 118B |
| **33 800** | 0.0045 | phenyl π→xz, $p_{out\text{-}of\text{-}plane}$(s) → | $L_{eq}$MCT | 106B → 119B, 113A → 120A |
| **34 000** | 0.0038 | $p_{out\text{-}of\text{-}plane}$(s) → xy | $L_{eq}$MCT | 113A → 120A |
| **34 300** | 0.0065 | $p_{in\text{-}plane}$(a), $p_y$ → xy | $L_{eq}$/$L_{ax}$MC | 114/116A → 120A |
| **34 900** | 0.1067 | $p_x$ → xy | $L_{ax}$MCT | 115A → 120A |
| **35 000** | 0.0267 | $p_{in\text{-}plane}$(a) → xy | $L_{eq}$MCT | 114A → 120A |
| **35 400** | 0.0029 | $p_{in\text{-}plane}$(s), $p_{out\text{-}of\text{-}plane}$(s) → xz | $L_{eq}$MCT | 102/103 → 119 |
| **35 500,** | 0.0201, 0.0080 | ligand σ → $x^2$-$y^2$ | -- | 96/97B → 117B |
| **35 800** | 0.0048 | $p_{in\text{-}plane}$(s), $p_{out\text{-}of\text{-}plane}$(s) → xy | $L_{eq}$MCT | 102/103 → 120 |
| **35 900** | 0.0225 | $p_{out\text{-}of\text{-}plane}$(s) → xy | $L_{eq}$MCT | 113A → 120A |

Further LMCT transitions originating from the symmetric combination of the out-of-plane $p_\pi$ orbitals of the equatorial chlorido ligands (MO 113) are found at 26 200 $cm^{-1}$ and 28 600 $cm^{-1}$, $p_{out\text{-}of\text{-}plane}$(s) → d*yz*, d*xz* and might correspond to the observed shoulders at 25 000 $cm^{-1}$ (band D) and 30 000 $cm^{-1}$ (band E) in the experimental UV/Vis spectrum und thus to band 3 and 4, i.e. the negative *pseudo-A-term*, in the MCD spectrum. The corresponding $p_{out\text{-}of\text{-}plane}$(a) → d*yz*, d*xz* transitions, in contrast, only appear with very low intensities in the calculated UV/Vis spectrum.

A possible assignment of the observed shoulder at 36 000 $cm^{-1}$ (band G) in the experimental UV/Vis absorption spectrum might be the $p_{in\text{-}plane}(a) \rightarrow d_{xy}$ transition (MO 114 → 120) which shows a very high intensity in the calculated UV/Vis spectrum at 35 000 $cm^{-1}$.

Considering the overall spectral shape, a clear-cut correlation between the experimental and the theoretical spectrum is not possible. Although some trends considering the type of electronic transitions (d → d, LMCT) can be obtained for particular spectral regions, a definite assignment of the observed UV/Vis transitions (which can also be transferred to the assignment of the MCD spectrum) is not possible based on the TDDFT calculation alone. Additionally, this type of calculation gives no explanation of the positive and negative signs of the individual MCD transitions. Therefore an assignment of the electronic transitions on the basis of molecular orbital considerations is presented in the following section.

**Assignment of the Electronic Transitions Based on the MO Scheme and Symmetry Considerations.** The MO scheme of [Mo(O)$Cl_3$*dppe*] (**Figure 11**) suggests that the $^2B_2 \rightarrow {}^2B_1$ ($d_{x^2-y^2} \rightarrow d_{xy}$) ligand field transition and metal-to-ligand-charge transfer transitions from chlorido p-orbitals into the singly occupied $d_{x^2-y^2}$ orbital are the lowest energy transitions and should appear in the spectral region between 20 000 $cm^{-1}$ and 25 000 $cm^{-1}$ in accordance with the literature.[2] The assignment of the positive MCD bands 1 and 2 is possible based on resonance Raman measurements (**Figure 13**).

The resonance Raman spectrum obtained at the excitation energy of 19 500 $cm^{-1}$ reveals that the symmetric Mo-$Cl_{eq}$ stretching vibration at 332 $cm^{-1}$ and the Mo-P stretch at 523 $cm^{-1}$ are very strongly enhanced. They receive 150 % respectively 60 % of the intensity of the symmetric *dppe* phenyl C=C ring breathing vibration at 1 000 $cm^{-1}$, which is the most intense vibration in the "off-resonance" FT-Raman spectrum. The relative intensities in the "off-resonance" FT-Raman spectrum are 0.4, 0.4 and 0.04 of the intensity of the $(C{=}C)_{phenyl}$ ring

breathing vibration for the Mo-O stretch, the symmetric Mo-$Cl_{eq}$ stretch and the Mo-P stretch, respectively (*vide supra*, **Figure 8**).

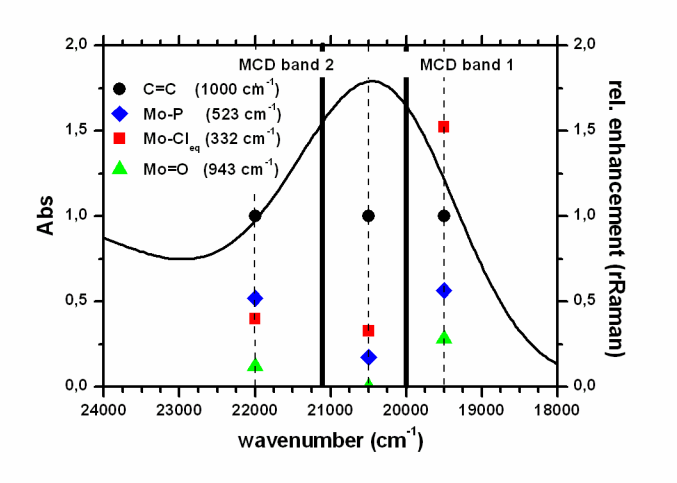


**Figure 13.** UV/Vis absorption spectrum ($CH_2Cl_2$, 1 mM, d = 1 mm) and resonance Raman excitation profile of the characteristic metal-ligand vibrations of [Mo(O)$Cl_3$*dppe*]. The bold lines are the positions of the MCD bands 1 and 2. The dashed lines represent the excitation energies of the resonance Raman spectra.

As only Mo-$Cl_{eq}$ and Mo-P vibrations in the equatorial plane (*xy*) are enhanced in the resonance Raman spectrum at the excitation energy of 19 500 $cm^{-1}$, the *xy* orbital which is antibonding to the equatorial $\sigma_{Cl}$- and $\sigma_P$-orbitals ($\sigma_2$, *vide supra*, **Figure 11**) must be involved in an electronic transition at this energy. The MCD band 1 at 20 000 $cm^{-1}$ can therefore with a great probability be assigned to the d$x^2$-$y^2$ → d*xy* ligand field transition. This also matches a previous report for the assignment of the UV/Vis absorption band B at 20 500 $cm^{-1}$.[34] The explanation for the remarkably high intensity of this d → d ligand field transition might be that it gets its intensity from the d*xy*/$\sigma_2$ bonding → antibonding transition (MO 95 → MO 120), as in $C_S$ symmetry the "starting orbitals" d$x^2$-$y^2$ and d*xy* are coupled through spin-orbit coupling via $L_Z$.

Band 2 at 21 100 $cm^{-1}$ then may arise from an LMCT transition into the singly occupied $dx^2$-$y^2$ orbital. With an excitation energy of 22 000 $cm^{-1}$ a strong enhancement of Mo-P stretch is observed in the resonance Raman spectrum, which implies that an equatorial molecular orbital must also be involved in the electronic transition at this energy. As already mentioned the antisymmetric in-plane p-orbital of the equatorial chlorido ligands ($p_{in\text{-}plane}$(a), 114) shows large contributions of phosphorus p-orbitals (*vide supra*). Band 2 is therefore assigned to the $p_{in\text{-}plane}(a) \rightarrow dx^2\text{-}y^2$ ligand-to-metal charge transfer transition, in accordance to the TDDFT calculations (*vide supra*).

An additional argument in favor of the specified assignments of the MCD bands 1 and 2 to the $dx^2\text{-}y^2 \rightarrow dxy$ and $p_{in\text{-}plane}(a) \rightarrow dx^2\text{-}y^2$ transitions is that the Mo-O stretch at 943 $cm^{-1}$ is not enhanced in the resonance Raman spectra using excitation energies between 19 500 $cm^{-1}$ and 22 000 $cm^{-1}$. Its relative intensity is even reduced compared to the "off-resonance" FT-Raman spectrum. This clearly indicates that only in-plane metal and ligand orbitals are involved in the electronic transition within this spectral region.

The MCD bands 3 - 6 all exhibit the same intensities in a positive-negative-negative-positive pattern of two corresponding *pseudo-A-term*s. This implies that two nearly or formerly degenerate E states must be involved in these transitions and that the individual transitions must be polarized in different directions resulting in transition densities of opposite signs. Three pairs of nearly or formerly degenerate orbitals with different symmetries can be identified in the molecular orbital scheme (**Figure 11**) which are

(i) the $p_y$ and $p_x$ orbitals of the axial chlorido ligand *trans* to the oxido group,

(ii) the symmetric and antisymmetric out-of-plane $p_\pi$ orbitals of the equatorial chlorido ligands $p_{out\text{-}of\text{-}plane}$(s, a) and

(iii) the $dyz$ and $dxz$ molybdenum d-orbitals.

Although the $p_x \rightarrow dyz, dxz$ transitions are indeed predicted by TDDFT as possible assignments for the MCD bands 3 and 4 from their calculated energies, this possibility is not considered for the following reason: The $p_x \rightarrow dxz$ and the $p_y \rightarrow dyz$ transitions are both *z*-polarized, while the transition densities of the $p_x \rightarrow dyz$ and the $p_y \rightarrow dxz$ transitions are zero. The $p_x, p_y \rightarrow dyz, dxz$ transitions are thus expected to result only in two equally signed MCD bands, but could by no means give rise to a "double *pseudo-A*-term" and can therefore definitely be ruled out for the assignment of the MCD bands 3 – 6.

The only possibility therefore is the assignment of the "double *pseudo-A*-term" to the ligand-to-metal charge transfer from the equatorial out-of-plane chlorido $p_\pi$ orbitals, $p_{out\text{-}of\text{-}plane}(s, a)$, into the d*yz* and d*xz* orbitals. The $p_{out\text{-}of\text{-}plane}(s) \rightarrow dyz, dxz$ transition was already predicted by the TDDFT calculation as another possibility for the assignment of the MCD bands 3 + 4 (negative *pseudo-A*-term), while the $p_{out\text{-}of\text{-}plane}(a) \rightarrow dyz, dxz$ transitions were only found with relatively low intensities in the calculated UV/Vis spectrum. According to the molecular orbital scheme (**Figure 11**), however, they should appear at higher energies than band 3 and 4 and might therefore be assigned to the positive *pseudo-A*-term at 32 500 $cm^{-1}$ (band 5 + 6).

As already mentioned the UV/Vis absorption band G might be assigned to the $p_{in\text{-}plane}(a) \rightarrow dxy$ transition. From the molecular orbital scheme and the computation of the electronic transitions by time-dependent DFT no evidence is given for Mo → P metal-to-ligand charge transfer (MLCT) or oxido → Mo ligand-to-metal charge transfer (LMCT) transitions.

The complete assignment of the individual electronic transitions is summarized in **Table 5**.

**Table 5.** Assignment of the electronic transitions of [Mo(O)$Cl_3$*dppe*]. UV/Vis and MCD transitions are given in $cm^1$

| UV/Vis | | MCD | | assignment/description | |
|---|---|---|---|---|---|
| (A) | 15 500 | | -- | $x^2$-$y^2$ →-*yz*, *xz* | d → d |
| (B) | 20 500 | (1) | 20 000 (+) | $x^2$-$y^2$ → xy | d → d |
| ((C)) | | (2) | 21 100 (+) | $p_{in\text{-}plane}$(a) → $x^2$-$y^2$ | $L_{eq}$MCT |
| (D) | 25 000 | (3) | 24 800 (+) | $p_{out\text{-}of\text{-}plane}$(s) → yz | $L_{eq}$MCT |
| (E) | 30 000 | (4) | 29 600 (-) | $p_{out\text{-}of\text{-}plane}$(s) → xz | $L_{eq}$MCT |
| -- | | (5) | 30 600 (-) | $p_{out\text{-}of\text{-}plane}$(a) → yz | $L_{eq}$MCT |
| (F) | 34 000 | (6) | 34 100 (+) | $p_{out\text{-}of\text{-}plane}$(a) → yz | $L_{eq}$MCT |
| ((G) | 36 000) | | -- | $p_{in\text{-}plane}$(a) → xy | $L_{eq}$MCT |

**Theory of MCD *C*-term intensities for multi-determinant excited doublet states.** To particularly verify the assignment of the observed "double *pseudo-A*-term" to the $p_{out\text{-}of\text{-}plane}$(s, a) → d*yz*, d*xz* transitions a general procedure for the determination of MCD *C*-term intensities is applied, which has been presented by Neese and Solomon.[1] To account for the intensities, however, it will be necessary to explicitly consider the multi-determinant character of the excited states. The signs of the MCD bands are then determined from the transition densities of the individual transitions considering the overlap of the involved starting and target molecular orbitals.

In the limit of a pure *C*-term mechanism, the MCD intensity is given by

$$\frac{\Delta\varepsilon}{E} = \frac{\varepsilon_{lcp} - \varepsilon_{rcp}}{E} = \frac{\gamma\,\beta_B\,B}{k\,T}\,\overline{C_0}\;f(E)$$

where $\gamma$ is a collection of constants, $\beta_B$ is the Bohr magneton, $k$ is the Boltzmann constant, T is the absolute temperature, B is the magnetic flux density and *f(E)* is a line shape function. Here, it is sufficient to consider *f(E)* as a $\delta$-function and $E$ as the transition energy. After orientational averaging the $C_0$ parameter results as

$$\overline{C}_0 = -\tfrac{1}{6}\left(M_{yz}^{eff}\ g_x + M_{xz}^{eff}\ g_y + M_{xy}^{eff}\ g_z\right)$$

where $g_u$ are the components of the ground-state g-tensor (u = x, y and z and the $M_{uv}^{eff}$ are effective transition dipole moments (uv = *xy*, *xz* and *yz*). For *xy* polarized transitions only $M_{xy}^{eff}$ has to be considered, which is given by

$$M_{xy}^{eff} = \sum_{K\neq A,J}\left(\vec{D}_x^{AK}\ \vec{D}_y^{AJ} - \vec{D}_y^{AK}\ \vec{D}_x^{AJ}\right)\frac{\overline{L}_z^{KJ}}{\Delta_{KJ}} + \left(\vec{D}_x^{AJ}\ \vec{D}_y^{JK} - \vec{D}_y^{AJ}\ \vec{D}_x^{JK}\right)\frac{\overline{L}_z^{KA}}{\Delta_{KA}}$$

The states A and B are given as eigenfunctions of S and $M_S$; i.e., A = $\left|ASM_S\right\rangle$ and B = $\left|BSM_S\right\rangle$. The transition dipole matrix elements $D_u^{AB}$ are defined as

$$\vec{D}_u^{AB} = \left\langle ASM_S\left|\mu_u\right|BSM_S\right\rangle$$

and the generalized spin-orbit coupling matrix elements $\overline{L}_u^{AB}$ are defined as

$$\overline{L}_u^{AB} = \mathrm{Im}\left\langle ASS\left|\sum_i h_u(i)\ s_0(i)\right|BSS\right\rangle_0$$

where the sum runs over all electrons i. In this expression, the operator $h_u(i)$ is given by

$$h_u(i) = \sum_N \xi(r_{iN}) l_{N,u}(i)$$

where N denotes the atom (i.e. Mo or one of the donor atoms) and $\xi$ is the spin-orbit coupling constant. For systems with an S = 1/2 ground state and if only transitions within $\alpha$-orbitals are considered, the $s_0(i)$ operator in $\overline{L}_u^{AB}$ can be replaced by a constant factor of 1/2. Furthermore, spin-orbit coupling is usually only considered within the metal atom (here N = Mo).

The above equations indicate that MCD *C*-term intensity may arise through spin-orbit coupling between the excited states *J* and *K* (*A* → *J*, *A* → *K, J* and *K* being coupled through spin-orbit coupling; "*J-K* coupling") or between the ground state *A* and an excited state *K* (*A* → *J*, *K* → *J, A* and *K* being coupled through spin-orbit coupling; "*A-K* coupling").[1]

Considering ligand-to-metal charge transfer from the symmetric and antisymmetric out-of-plane chlorido $p_\pi$ orbitals into the d*xz* and d*yz* molybdenum d-orbitals, one has to take a closer look at the excited states of the individual transitions to describe the MCD *C*-term intensities correctly. The $p_\pi$(s, a) → d*xz*, d*yz* transitions are transitions from doubly occupied molecular orbitals (*i*) into unoccupied molecular orbitals (*a, b*) and thus clearly correspond to type III transitions (*vide supra*).[17] In this case the multi-determinant character of the excited states has to be taken into account.[17] Specifically, in the case of spin-allowed type III electronic transitions from the S = 1/2 ground state, all excited doublet states split into sing-doublet and trip-doublet states. In the case of an $i \rightarrow a$ transition, the sing-doublet $M_S$ = +1/2 and -1/2 states correspond to

$$\left|C_i^a +1/2\right\rangle = \frac{1}{\sqrt{2}}\left(\left|\psi_1^+\psi_1^-...\psi_i^+\psi_a^-...\psi_n^+\psi_n^-\psi_o^+\right| + \left|\psi_1^+\psi_1^-...\psi_a^+\psi_i^-...\psi_n^+\psi_n^-\psi_o^+\right|\right)$$

and

$$\left|C_i^a -1/2\right\rangle = \frac{1}{\sqrt{2}}\left(\left|\psi_1^+\psi_1^-...\psi_i^+\psi_a^-...\psi_n^+\psi_n^-\psi_o^-\right| + \left|\psi_1^+\psi_1^-...\psi_a^+\psi_i^-...\psi_n^+\psi_n^-\psi_o^-\right|\right)$$

whereas the trip-doublet $M_S$ = +1/2 and -1/2 excited doublet states correspond to

$$\left|D_i^a +1/2\right\rangle = \frac{1}{\sqrt{6}}\left(\left|\psi_1^+\psi_1^-...\psi_i^+\psi_a^-...\psi_n^+\psi_n^-\psi_o^+\right| - \left|\psi_1^+\psi_1^-...\psi_a^+\psi_i^-...\psi_n^+\psi_n^-\psi_o^+\right| + 2\left|\psi_1^+\psi_1^-...\psi_i^+\psi_o^-...\psi_n^+\psi_n^-\psi_a^+\right|\right)$$

and

$$\left|D_i^a -1/2\right\rangle = \frac{1}{\sqrt{6}}\left(\left|\psi_1^+\psi_1^-...\psi_a^+\psi_i^-...\psi_n^+\psi_n^-\psi_o^-\right| - \left|\psi_1^+\psi_1^-...\psi_i^+\psi_a^-...\psi_n^+\psi_n^-\psi_o^-\right| + 2\left|\psi_1^+\psi_1^-...\psi_o^+\psi_i^-...\psi_n^+\psi_n^-\psi_a^-\right|\right)$$

In analogy to the "luminescent states" of copper, cobalt and vanadyl porphyrin complexes considered by Gouterman and co-worker we also assume that the sing-doublet excited states are higher in energy than the trip-doublet excited states, i.e. $E(C_i^a) > E(D_i^a)$.[37]

The transition from the electronic ground state into a sing-doublet excited state has electric dipole intensity. Assuming the ground state configuration to be $\left|\psi_i^+\psi_i^-\psi_o^+\right\rangle$ the transition dipole moment of a sing-doublet excitation is given by

$$\left\langle \psi_i^+\psi_i^-\psi_o^+ \left|\underline{\mu}\right| C_i^a +1/2\right\rangle = \frac{1}{\sqrt{2}}\left\{\left\langle \psi_i^+\psi_i^-\psi_o^+ \left|\underline{\mu}\right| \psi_i^+\psi_a^-\psi_o^+\right\rangle + \left\langle \psi_i^+\psi_i^-\psi_o^+ \left|\underline{\mu}\right| \psi_a^+\psi_i^-\psi_o^+\right\rangle\right\}$$

$$= \frac{1}{\sqrt{2}}\left\{\left\langle \psi_i^- \left|\underline{\mu}\right| \psi_a^-\right\rangle + \left\langle \psi_i^+ \left|\underline{\mu}\right| \psi_a^+\right\rangle\right\} = \sqrt{2}\left\langle \psi_i \left|\underline{\mu}\right| \psi_a\right\rangle \neq 0 .$$

However, due to the form of the generalized spin-orbit coupling operator $L_z$ two sing-doublet excited states $i \rightarrow a$ and $i \rightarrow b$ do not interact via spin-orbit coupling, even if the $l_z$ matrix element between $\psi_a$ and $\psi_b$ is non-zero:

$$\left\langle C_i^a +1/2\left|\sum_i l_z(i)s_z(i)\right| C_i^b +1/2\right\rangle = \frac{1}{2}\left\{\left\langle \psi_a^- \left| l_z s_z \right| \psi_b^-\right\rangle + \left\langle \psi_a^+ \left| l_z s_z \right| \psi_b^+\right\rangle\right\} = \frac{1}{2}\left\{-\frac{1}{2}\mathrm{Im}\left(\left\langle \psi_a \left| l_z \right| \psi_b\right\rangle\right) + \frac{1}{2}\mathrm{Im}\left(\left\langle \psi_a \left| l_z \right| \psi_b\right\rangle\right)\right\} = 0$$

,

These transitions therefore do <u>not</u> contribute to the MCD *C*-term intensity.

The trip-doublet excited states $i \rightarrow a$ and $i \rightarrow b$, in contrast, <u>do</u> interact via spin-orbit coupling,

$$\left\langle D_i^a +1/2\left|\sum_i l_z(i)s_z(i)\right| D_i^b +1/2\right\rangle = \frac{1}{6}\cdot 4\cdot \mathrm{Im}\left(\left\langle \psi_a \left| l_z \right| \psi_b\right\rangle\right) \neq 0 ,$$

and thus theoretically give rise to MCD *C*-term intensity. However, the corresponding transition dipole moments $\left\langle \psi_i^+\psi_i^-\psi_o^+ \left|\underline{\mu}\right| D_i^a +1/2\right\rangle$ are zero, so that the trip-doublet excited states are in fact not accessible from the ground state by electronic dipole transitions.

The following mixed sing-doublet/trip-doublet spin-orbit coupling terms are also non-zero:

$$\left\langle D_i^a +1/2\left|\sum_i l_z(i)s_z(i)\right| C_i^b +1/2\right\rangle = \left\langle C_i^a +1/2\left|\sum_i l_z(i)s_z(i)\right| D_i^b +1/2\right\rangle = -\frac{1}{\sqrt{12}}\cdot \mathrm{Im}\left(\left\langle \psi_a \left| l_z \right| \psi_b\right\rangle\right) \neq 0$$

Configuration interaction (CI) between the sing-doublet and trip-doublet excited states provides a mechanism which gives rise to the non-zero MCD *C*-term intensity of type III electronic transitions. To this end new states are formed:

(1) $A_+ = \sin\theta \cdot C_i^a + \cos\theta \cdot D_i^a$

(2) $A_- = \cos\theta \cdot C_i^a - \sin\theta \cdot D_i^a$

(3) $B_+ = \sin\theta \cdot C_i^b + \cos\theta \cdot D_i^b$

and (4) $B_- = \cos\theta \cdot C_i^b - \sin\theta \cdot D_i^b$

Note that $\theta$ is small, if the sing-doublet excited states are much higher in energy than the trip-doublet states, i.e. $E(C_i^{a,b}) >> E(D_i^{a,b})$ and the CI matrix element is small (see below).[37] In this case the main contribution to the $A_+$ and $B_+$ excited states are the trip-doublet states while the $A_-$ and $B_-$ excited states are dominated by the sing-doublet contributions. $\sin\theta$ is given by

$$\sin\theta = \frac{\left\langle C_i^a \left| \frac{e^2}{r_{12}} \right| D_i^a \right\rangle}{\Delta E(C_i^a - D_i^a)} \qquad \text{with} \qquad \left\langle C_i^a \left| \frac{e^2}{r_{12}} \right| D_i^a \right\rangle = \frac{\sqrt{3}}{2}(K_{ao} - K_{io})$$ [37]

which is positive if $K_{ao} > K_{io}$ ($K_{ao}$, $K_{io}$: exchange integrals).

All of these states (1) - (4) interact through spin-orbit coupling:

(i) $$\left\langle A^+ \left| \sum_i l_z(i)s_z(i) \right| B^+ \right\rangle = \sin\theta\cos\theta \left\langle C_i^a \left| \sum_i l_z(i)s_z(i) \right| D_i^b \right\rangle + \cos\theta\sin\theta \left\langle D_i^a \left| \sum_i l_z(i)s_z(i) \right| C_i^b \right\rangle$$

$$+ \cos^2\theta \left\langle D_i^a \left| \sum_i l_z(i)s_z(i) \right| D_i^b \right\rangle$$

$$= 2\sin\theta\cos\theta \cdot \left( -\frac{1}{\sqrt{12}} \right) \langle \psi_a | l_z | \psi_b \rangle + \cos^2\theta \cdot \left( \frac{2}{3} \right) \langle \psi_a | l_z | \psi_b \rangle$$

$$= \left( -\frac{1}{\sqrt{3}} \right) \langle \psi_a | l_z | \psi_b \rangle \sin\theta\cos\theta + \left( \frac{2}{3} \right) \langle \psi_a | l_z | \psi_b \rangle \cos^2\theta$$

$$= \left( -\frac{1}{\sqrt{3}} \sin\theta\cos\theta + \frac{2}{3}\cos^2\theta \right) \langle \psi_a | l_z | \psi_b \rangle$$

(ii) $$\left\langle A^+ \left| \sum_i l_z(i) s_z(i) \right| B^- \right\rangle = -\sin^2\theta \left\langle C_i^a \left| \sum_i l_z(i) s_z(i) \right| D_i^b \right\rangle + \cos^2\theta \left\langle D_i^a \left| \sum_i l_z(i) s_z(i) \right| C_i^b \right\rangle$$

$$- \cos\theta\sin\theta \left\langle D_i^a \left| \sum_i l_z(i) s_z(i) \right| D_i^b \right\rangle$$

$$= \left(\cos^2\theta - \sin^2\theta\right) \cdot \left( -\frac{1}{\sqrt{12}} \right) \langle \psi_a | l_z | \psi_b \rangle - \sin\theta\cos\theta \cdot \left( \frac{2}{3} \right) \langle \psi_a | l_z | \psi_b \rangle$$

$$= \left( -\frac{1}{\sqrt{12}} \left(\cos^2\theta - \sin^2\theta\right) - \frac{2}{3} \sin\theta\cos\theta \right) \langle \psi_a | l_z | \psi_b \rangle$$

(iii) $$\left\langle A^- \left| \sum_i l_z(i) s_z(i) \right| B^+ \right\rangle = \cos^2\theta \left\langle C_i^a \left| \sum_i l_z(i) s_z(i) \right| D_i^b \right\rangle - \sin\theta\cos\theta \left\langle D_i^a \left| \sum_i l_z(i) s_z(i) \right| D_i^b \right\rangle$$

$$- \sin^2\theta \left\langle D_i^a \left| \sum_i l_z(i) s_z(i) \right| C_i^b \right\rangle$$

$$= \left(\cos^2\theta - \sin^2\theta\right) \cdot \left( -\frac{1}{\sqrt{12}} \right) \langle \psi_a | l_z | \psi_b \rangle - \sin\theta\cos\theta \cdot \left( \frac{2}{3} \right) \langle \psi_a | l_z | \psi_b \rangle$$

$$= \left( -\frac{1}{\sqrt{12}} \left(\cos^2\theta - \sin^2\theta\right) - \frac{2}{3} \sin\theta\cos\theta \right) \langle \psi_a | l_z | \psi_b \rangle$$

and

(iv) $$\left\langle A^- \left| \sum_i l_z(i) s_z(i) \right| B^- \right\rangle = -\sin\theta\cos\theta \left\langle C_i^a \left| \sum_i l_z(i) s_z(i) \right| D_i^b \right\rangle - \cos\theta\sin\theta \left\langle D_i^a \left| \sum_i l_z(i) s_z(i) \right| C_i^b \right\rangle$$

$$+ \sin^2\theta \left\langle D_i^a \left| \sum_i l_z(i) s_z(i) \right| D_i^b \right\rangle$$

$$= -2\sin\theta\cos\theta \cdot \left( -\frac{1}{\sqrt{12}} \right) \langle \psi_a | l_z | \psi_b \rangle + \sin^2\theta \cdot \left( \frac{2}{3} \right) \langle \psi_a | l_z | \psi_b \rangle$$

$$= \left( \frac{1}{\sqrt{3}} \right) \langle \psi_a | l_z | \psi_b \rangle \sin\theta\cos\theta + \left( \frac{2}{3} \right) \langle \psi_a | l_z | \psi_b \rangle \sin^2\theta$$

$$= \left( \frac{1}{\sqrt{3}} \sin\theta\cos\theta + \frac{2}{3} \sin^2\theta \right) \langle \psi_a | l_z | \psi_b \rangle$$

Furthermore, the individual transition dipole matrix elements are given by

$$\left\langle A\left|\mu\right|A^{+}\right\rangle = \sin\theta\left\langle A\left|\mu\right|C_a^i\right\rangle + \cos\theta\left\langle A\left|\mu\right|D_a^i\right\rangle = \sin\theta\left\langle A\left|\mu\right|C_a^i\right\rangle = \sqrt{2}\cdot\sin\theta\left\langle\psi_i\left|\mu\right|\psi_a\right\rangle$$

$$\left\langle A\left|\mu\right|A^{-}\right\rangle = \cos\theta\left\langle A\left|\mu\right|C_a^i\right\rangle - \sin\theta\left\langle A\left|\mu\right|D_a^i\right\rangle = \cos\theta\left\langle A\left|\mu\right|C_a^i\right\rangle = \sqrt{2}\cdot\cos\theta\left\langle\psi_i\left|\mu\right|\psi_a\right\rangle$$

$$\left\langle A\left|\mu\right|B^{+}\right\rangle = \sin\theta\left\langle A\left|\mu\right|C_b^i\right\rangle + \cos\theta\left\langle A\left|\mu\right|D_b^i\right\rangle = \sin\theta\left\langle A\left|\mu\right|C_b^i\right\rangle = \sqrt{2}\cdot\sin\theta\left\langle\psi_i\left|\mu\right|\psi_b\right\rangle$$

and $\left\langle A\left|\mu\right|B^{-}\right\rangle = \cos\theta\left\langle A\left|\mu\right|C_b^i\right\rangle - \sin\theta\left\langle A\left|\mu\right|D_b^i\right\rangle = \cos\theta\left\langle A\left|\mu\right|C_b^i\right\rangle = \sqrt{2}\cdot\cos\theta\left\langle\psi_i\left|\mu\right|\psi_b\right\rangle$

The MCD *C*-term intensity of an *xy* polarized transition $A \rightarrow J,\ K$ ( *J*-*K* coupling) is given by

$$\frac{\Delta\varepsilon}{E} \sim -\sum_{K\neq A,J}\frac{\overline{L}_z^{KJ}}{\Delta_{KJ}}\left(\vec{D}_x^{AK}\ \vec{D}_y^{AJ} - \vec{D}_y^{AK}\ \vec{D}_x^{AJ}\right) = -\sum_{K\neq A,J}\frac{\left\langle K\left|\overline{L}_z\right|J\right\rangle}{\Delta_{KJ}}\left\{\left\langle A\left|\mu_x\right|K\right\rangle\left\langle A\left|\mu_y\right|J\right\rangle - \left\langle A\left|\mu_y\right|K\right\rangle\left\langle A\left|\mu_x\right|J\right\rangle\right\}$$

For the individual electronic transitions, the two different paths arising from the two possible couplings have to be summed up. Contributions containing $\sin\theta$ to the power of two and three are neglected ($\theta \approx 0$). The results for the four transitions are then

(1) $A \rightarrow J = A^{+};\ K = B^{+},\ B^{-}$

$$\frac{\Delta\varepsilon}{E} \sim -\sum_{K\neq A,J}\frac{\overline{L}_z^{KJ}}{\Delta_{KJ}}\left(\vec{D}_x^{AK}\ \vec{D}_y^{AJ} - \vec{D}_y^{AK}\ \vec{D}_x^{AJ}\right)$$

$$= -\frac{\overline{L}_z^{B_+A_+}}{\Delta_{B_+A_+}}\left(\vec{D}_x^{AB_+}\ \vec{D}_y^{AA_+} - \vec{D}_y^{AB_+}\ \vec{D}_x^{AA_+}\right) - \frac{\overline{L}_z^{B_-A_+}}{\Delta_{B_-A_+}}\left(\vec{D}_x^{AB_-}\ \vec{D}_y^{AA_+} - \vec{D}_y^{AB_-}\ \vec{D}_x^{AA_+}\right)$$

$$\frac{\Delta\varepsilon}{E} \sim -\frac{1}{\Delta_{B_+A_+}}\cdot\left(-\frac{1}{\sqrt{3}}\sin\theta\cos\theta + \frac{2}{3}\cos^2\theta\right)\cdot\mathrm{Im}\left(\left\langle\psi_b\left|l_z\right|\psi_a\right\rangle\right)$$

$$\cdot\sin^2\theta\left\{\left\langle\psi_i\left|\mu_x\right|\psi_b\right\rangle\left\langle\psi_i\left|\mu_y\right|\psi_a\right\rangle - \left\langle\psi_i\left|\mu_y\right|\psi_b\right\rangle\left\langle\psi_i\left|\mu_x\right|\psi_a\right\rangle\right\}$$

$$-\frac{1}{\Delta_{B_-A_+}}\cdot\left(-\frac{1}{\sqrt{12}}\left(\cos^2\theta - \sin^2\theta\right) - \frac{2}{3}\sin\theta\cos\theta\right)\cdot\mathrm{Im}\left(\left\langle\psi_b\left|l_z\right|\psi_a\right\rangle\right)$$

$$\cdot\sin\theta\cos\theta\left\{\left\langle\psi_i\left|\mu_x\right|\psi_b\right\rangle\left\langle\psi_i\left|\mu_y\right|\psi_a\right\rangle - \left\langle\psi_i\left|\mu_y\right|\psi_b\right\rangle\left\langle\psi_i\left|\mu_x\right|\psi_a\right\rangle\right\}$$

$$\cong 0 + \frac{1}{\Delta_{B\_A_+}} \cdot \frac{1}{\sqrt{12}} \sin\theta \cdot \mathrm{Im}\left(\langle \psi_b | l_z | \psi_a \rangle\right) \cdot \left\{ \langle \psi_i | \mu_x | \psi_b \rangle \langle \psi_i | \mu_y | \psi_a \rangle - \langle \psi_i | \mu_y | \psi_b \rangle \langle \psi_i | \mu_x | \psi_a \rangle \right\}$$

with $\sin\theta = \lambda = \dfrac{\left\langle C_i^a \left| \dfrac{e^2}{r_{12}} \right| D_i^a \right\rangle}{\Delta E(C_i^a - D_i^a)}$ (*vide supra*) and $\cos\theta = \sqrt{1-\lambda^2} \cong 1$ for $\theta \approx 0$.[37] As the first contribution is zero and assuming that $\Delta_{B\_A_+} = E_{B\_} - E_{A_+}$ is comparatively large (**Figure 8**), electronic transitions into the $A_+$ state only get very weak MCD *C*-term intensity. This, of course, would have been expected as the $A_+$ excited state mainly contains the $D_i^a$ trip-doublet state which is not accessible by electronic dipole transitions (*vide supra*).

(2) $A \rightarrow J = A^-, K = B^+, B^-$

$$\frac{\Delta\varepsilon}{E} \sim -\sum_{K \neq A,J} \frac{\overline{L}_z^{KJ}}{\Delta_{KJ}} \left( \vec{D}_x^{AK} \, \vec{D}_y^{AJ} - \vec{D}_y^{AK} \, \vec{D}_x^{AJ} \right)$$

$$= -\frac{\overline{L}_z^{B_+A_-}}{\Delta_{B_+A_-}} \left( \vec{D}_x^{AB_+} \, \vec{D}_y^{AA_-} - \vec{D}_y^{AB_+} \, \vec{D}_x^{AA_-} \right) - \frac{\overline{L}_z^{B_-A_-}}{\Delta_{B_-A_-}} \left( \vec{D}_x^{AB_-} \, \vec{D}_y^{AA_-} - \vec{D}_y^{AB_-} \, \vec{D}_x^{AA_-} \right)$$

$$\frac{\Delta\varepsilon}{E} \sim -\frac{1}{\Delta_{B_+A_-}} \cdot \left( -\frac{1}{\sqrt{12}} \left( \cos^2\theta - \sin^2\theta \right) - \frac{2}{3} \sin\theta\cos\theta \right) \cdot \mathrm{Im}\left(\langle \psi_b | l_z | \psi_a \rangle\right)$$

$$\cdot \cos\theta \sin\theta \left\{ \langle \psi_i | \mu_x | \psi_b \rangle \langle \psi_i | \mu_y | \psi_a \rangle - \langle \psi_i | \mu_y | \psi_b \rangle \langle \psi_i | \mu_x | \psi_a \rangle \right\}$$

$$-\frac{1}{\Delta_{B_-A_-}} \cdot \left( \frac{1}{\sqrt{3}} \sin\theta\cos\theta + \frac{2}{3} \sin^2\theta \right) \cdot \mathrm{Im}\left(\langle \psi_b | l_z | \psi_a \rangle\right)$$

$$\cdot \cos^2\theta \left\{ \langle \psi_i | \mu_x | \psi_b \rangle \langle \psi_i | \mu_y | \psi_a \rangle - \langle \psi_i | \mu_y | \psi_b \rangle \langle \psi_i | \mu_x | \psi_a \rangle \right\}$$

$$\cong -\frac{1}{\sqrt{12}} \left( 2 \cdot \frac{1}{\Delta_{B\_A_-}} - \frac{1}{\Delta_{B_+A_-}} \right) \cdot \sin\theta \cdot \mathrm{Im}\left(\langle \psi_b | l_z | \psi_a \rangle\right) \cdot \left\{ \langle \psi_i | \mu_x | \psi_b \rangle \langle \psi_i | \mu_y | \psi_a \rangle - \langle \psi_i | \mu_y | \psi_b \rangle \langle \psi_i | \mu_x | \psi_a \rangle \right\}$$

$\Delta_{B\_A\_} = E_{B\_} - E_{A\_}$ is small compared to $\Delta_{B\_A_+} = E_{B\_} - E_{A_+}$ (**Figure 8**). In consequence, the MCD *C*-term intensity of electronic transitions into the $A_-$ state is much higher than that of the $A \rightarrow A_+$ transitions. As the main contribution to the $A_-$ state is the $C_i^a$ sing-doublet excited state being accessible by electronic dipole transitions, this would also have been expected intuitively. Considering the absolute values, $\Delta_{B\_A\_}$ is also small compared to $\left|\Delta_{B_+A\_}\right|$. In consequence, the MCD *C*-term intensity of the $A \rightarrow A_-$ transitions is dominated by spin-orbit coupling between the $A_-$ and $B_-$ states.

(3) $A \rightarrow J = B^+, K = A^+, A^-$

$$\frac{\Delta\varepsilon}{E} \sim -\sum_{K\neq A,J} \frac{\overline{L}_z^{KJ}}{\Delta_{KJ}} \left(\vec{D}_x^{AK}\ \vec{D}_y^{AJ} - \vec{D}_y^{AK}\ \vec{D}_x^{AJ}\right)$$

$$= -\frac{\overline{L}_z^{A_+B_+}}{\Delta_{A_+B_+}} \left(\vec{D}_x^{AA_+}\ \vec{D}_y^{AB_+} - \vec{D}_y^{AA_+}\ \vec{D}_x^{AB_+}\right) - \frac{\overline{L}_z^{A\_B_+}}{\Delta_{A\_B_+}} \left(\vec{D}_x^{AA\_}\ \vec{D}_y^{AB_+} - \vec{D}_y^{AA\_}\ \vec{D}_x^{AB_+}\right)$$

$$\frac{\Delta\varepsilon}{E} \sim -\frac{1}{\Delta_{A_+B_+}} \cdot \left(-\frac{1}{\sqrt{3}}\sin\theta\cos\theta + \frac{2}{3}\cos^2\theta\right) \cdot \mathrm{Im}\left(\langle\psi_a|l_z|\psi_b\rangle\right)$$

$$\cdot \sin^2\theta \left\{\langle\psi_i|\mu_x|\psi_a\rangle\langle\psi_i|\mu_y|\psi_b\rangle - \langle\psi_i|\mu_y|\psi_a\rangle\langle\psi_i|\mu_x|\psi_b\rangle\right\}$$

$$-\frac{1}{\Delta_{A\_B_+}} \cdot \left(-\frac{1}{\sqrt{12}}\left(\cos^2\theta - \sin^2\theta\right) - \frac{2}{3}\sin\theta\cos\theta\right) \cdot \mathrm{Im}\left(\langle\psi_a|l_z|\psi_b\rangle\right)$$

$$\cdot \sin\theta\cos\theta \left\{\langle\psi_i|\mu_x|\psi_a\rangle\langle\psi_i|\mu_y|\psi_b\rangle - \langle\psi_i|\mu_y|\psi_a\rangle\langle\psi_i|\mu_x|\psi_b\rangle\right\}$$

$$\cong 0 + \frac{1}{\Delta_{A\_B_+}} \cdot \frac{1}{\sqrt{12}}\sin\theta \cdot \mathrm{Im}\left(\langle\psi_a|l_z|\psi_b\rangle\right) \cdot \left\{\langle\psi_i|\mu_x|\psi_a\rangle\langle\psi_i|\mu_y|\psi_b\rangle - \langle\psi_i|\mu_y|\psi_a\rangle\langle\psi_i|\mu_x|\psi_b\rangle\right\}$$

Corresponding to $A \rightarrow A_+$ transition, the MCD *C*-term intensity of this transition is very weak as well, as the first contribution is zero and $\Delta_{A\_B_+}$ is comparatively large (**Figure 8**).

(4) $A \rightarrow J = B^-, K = A^+, A^-$

$$\frac{\Delta\varepsilon}{E} \sim -\sum_{K\neq A,J} \frac{\overline{L}_z^{KJ}}{\Delta_{KJ}} \left(\vec{D}_x^{AK}\ \vec{D}_y^{AJ} - \vec{D}_y^{AK}\ \vec{D}_x^{AJ}\right)$$

$$= -\frac{\overline{L}_z^{A_+B_-}}{\Delta_{A_+B_-}}\left(\vec{D}_x^{AA_+}\ \vec{D}_y^{AB_-} - \vec{D}_y^{AA_+}\ \vec{D}_x^{AB_-}\right) - \frac{\overline{L}_z^{A_-B_-}}{\Delta_{A_-B_-}}\left(\vec{D}_x^{AA_-}\ \vec{D}_y^{AB_-} - \vec{D}_y^{AA_-}\ \vec{D}_x^{AB_-}\right)$$

$$\frac{\Delta\varepsilon}{E} \sim -\frac{1}{\Delta_{A_+B_-}}\cdot\left(-\frac{1}{\sqrt{12}}\left(\cos^2\theta - \sin^2\theta\right) - \frac{2}{3}\sin\theta\cos\theta\right)\cdot \mathrm{Im}\left(\langle\psi_a|l_z|\psi_b\rangle\right)$$

$$\cdot \sin\theta\cos\theta\left\{\langle\psi_i|\mu_x|\psi_a\rangle\langle\psi_i|\mu_y|\psi_b\rangle - \langle\psi_i|\mu_y|\psi_a\rangle\langle\psi_i|\mu_x|\psi_b\rangle\right\}$$

$$-\frac{1}{\Delta_{A_-B_-}}\cdot\left(\frac{1}{\sqrt{3}}\sin\theta\cos\theta + \frac{2}{3}\sin^2\theta\right)\cdot \mathrm{Im}\left(\langle\psi_a|l_z|\psi_b\rangle\right)$$

$$\cdot \cos^2\theta\left\{\langle\psi_i|\mu_x|\psi_b\rangle\langle\psi_i|\mu_y|\psi_a\rangle - \langle\psi_i|\mu_y|\psi_b\rangle\langle\psi_i|\mu_x|\psi_a\rangle\right\}$$

$$\cong -\frac{1}{\sqrt{12}}\left(2\cdot\frac{1}{\Delta_{A_-B_-}} - \frac{1}{\Delta_{A_+B_-}}\right)\cdot\sin\theta\cdot\mathrm{Im}\left(\langle\psi_a|l_z|\psi_b\rangle\right)\cdot\left\{\langle\psi_i|\mu_x|\psi_a\rangle\langle\psi_i|\mu_y|\psi_b\rangle - \langle\psi_i|\mu_y|\psi_a\rangle\langle\psi_i|\mu_x|\psi_b\rangle\right\}$$

Corresponding to the transition into the $A_-$ state, the MCD *C*-term intensity of the $A \rightarrow B_-$ transition is also much higher than that of the $A \rightarrow B_+$ transition. As expected, it is also dominated by spin-orbit coupling between the $A_-$ and $B_-$ states, as $\left|\Delta E_{(A_- - B_-)}\right| << \left|\Delta E_{(A_+ - B_-)}\right|$, considering the absolute values (**Figure 8**).

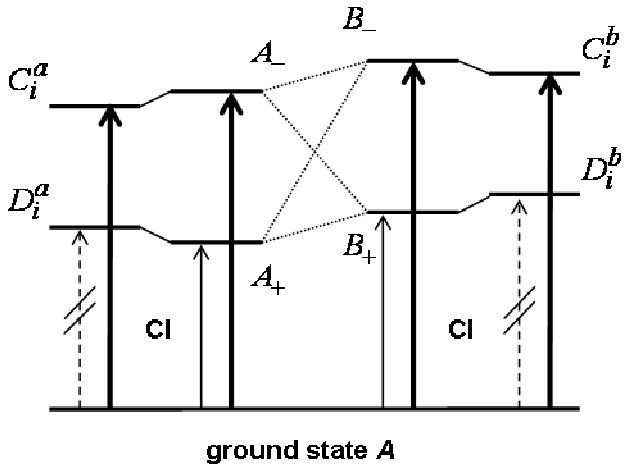


**Figure 14.** Considering type III electronic transitions, configuration interaction (CI) between the sing-doublet and the trip-doublet excited states provides a mechanism which gives rise to

non-zero MCD *C*-term intensity. The prevailing contributions are the $A \rightarrow A_-$ and $A \rightarrow B_-$ transitions. Dotted lines denote spin-orbit coupling.

Summing up, it has to be concluded that in the case of type III electronic transitions, only configuration interaction between the sing-doublet and the trip-doublet excited states provides a mechanism which gives rise to a non-zero MCD *C*-term intensity. Multi-determinant expressions therefore have to be used to correctly describe the excited states. At this the $A \rightarrow A_-$ and $A \rightarrow B_-$ transitions have been identified as the prevailing contributions as they are dependent on $\frac{1}{\Delta_{B\_A\_}}$ respectively $\frac{1}{\Delta_{A\_B\_}}$ with $\Delta_{B\_A\_}$ and $\left|\Delta_{A\_B\_}\right|$ being comparatively small. In consequence, the MCD *C*-term intensity is determined by the spin-orbit coupling between the $A_-$ and $B_-$ states. Assuming that the energy difference between the sing-doublet and trip-doublet excited states is large, i.e. in the range of several thousand wavenumbers, the $A \rightarrow A_+$ and $A \rightarrow B_+$ transitions would be expected in the NIR (near IR) region of the MCD spectra. However, as has been demonstrated on the derivation of the corresponding MCD *C*-term intensities, they would show significantly lower intensities compared to the $A \rightarrow A_-$ and $A \rightarrow B_-$ transitions. Note that, of course, the same MCD signs are expected for the $A \rightarrow A_+$ ($A \rightarrow B_+$) and $A \rightarrow A_-$ ($A \rightarrow B_-$) transitions.

For further interpretation, it might be resumed that the contributions of the second, less important excitation paths arising from the second possibility of coupling ($A_- \leftrightarrow B_+$, $A_+ \leftrightarrow B_-$) is a weakening contribution to the actual *C*-term intensity of a type III electronic transition, depending on the energy difference between the $A_+/B_+$ and $A_-/B_-$ states. Note that $\left|\Delta_{A\_B_+} = E_{A_-} - E_{B_+}\right|$ and $\Delta_{B\_A_+} = E_{B_-} - E_{A_+}$ are slightly different. Different intensities are therefore expected for the $A \rightarrow A_-$ ($A_+$) and the $A \rightarrow B_-$ ($B_+$) transitions.

**Assignment of the "double *pseudo-A*-term"**. Considering the "double *pseudo-A*-term" feature in the MCD spectra of [Mo(O)$Cl_3$*dppe*], the assignment to $p_{out\text{-}of\text{-}plane}$(a, s) → d*yz*, d*xz* ligand-to-metal charge transfer has already been suggested. This assignment is now confirmed based on the derived equations of the MCD *C*-term intensity by determining the MCD signs of the individual transitions from the corresponding transition densities. Based on the calculated MO scheme (**Figure 11**), MO 109/113 and MO 118/119 are the molecular orbitals under consideration.

As the starting orbitals (*i*) are ligand orbitals and the target orbitals (*a*) are molybdenum d-orbitals as well as the singly occupied d*xy* orbital (*o*) the one-center exchange integral $K_{ao}$ is larger than the two-center exchange integral $K_{io}$:

$$K_{ao} > K_{io}$$

$\mathrm{Sin}\,\theta$ therefore is positive throughout the following expressions (*vide supra*).

For the $p_{out\text{-}of\text{-}plane}$(s) → d*yz*, d*xz* transitions (*i* → *a, b*) the transition densities are determined as follows:

i. $p_{out\text{-}of\text{-}plane}$(s) → d*yz* (*i* → *a*, MO 113 → MO 118):

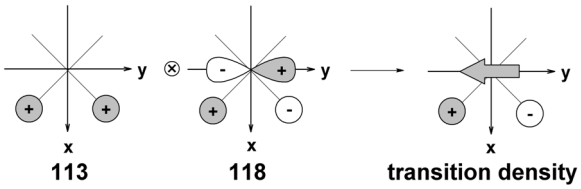


→ *y-polarized* (negative direction)

ii. $p_{out\text{-}of\text{-}plane}$(s) → d*xz* (*i* → *b,* MO 113 → MO 119):

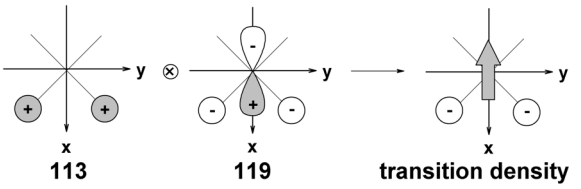


→ *x-polarized* (negative direction)

Note that the transition densities along *x* and *y* have a fixed phase relationship (either + or -) with the corresponding transition dipole moments. As the product of two transition dipole moments enters the formula for the MCD intensity, however, we do not have to deal with this issue.

The MCD *C*-term intensity of the $p_{\text{out-of-plane}}(s) \rightarrow dyz$ ($A \rightarrow A_-$) transition is positive:

$$\frac{\Delta\varepsilon}{E} \sim -\frac{1}{\sqrt{12}}\left(2\cdot\frac{1}{\Delta_{B_-A_-}}-\frac{1}{\Delta_{B_+A_-}}\right)\cdot\sin\theta\cdot\mathrm{Im}\left(\langle\psi_b|l_z|\psi_a\rangle\right)\cdot\left\{\langle\psi_i|\mu_x|\psi_b\rangle\langle\psi_i|\mu_y|\psi_a\rangle-\langle\psi_i|\mu_y|\psi_b\rangle\langle\psi_i|\mu_x|\psi_a\rangle\right\}$$

$$=-\frac{1}{\sqrt{12}}\left(2\cdot\frac{1}{\Delta_{B_-A_-}}-\frac{1}{\Delta_{B_+A_-}}\right)\cdot\sin\theta\cdot\mathrm{Im}\left(\langle xz|l_z|yz\rangle\right)\cdot\left\{\langle p_\pi(s)|\mu_x|xz\rangle\langle p_\pi(s)|\mu_y|yz\rangle-\langle p_\pi(s)|\mu_y|xz\rangle\langle p_\pi(s)|\mu_x|\psi_a\rangle\right.$$

$$=-\frac{1}{\sqrt{12}}\left(2\cdot\frac{1}{\Delta_{B_-A_-}}-\frac{1}{\Delta_{B_+A_-}}\right)\cdot\sin\theta\cdot(-1)\cdot\mathrm{Im}\left(\langle xz|l_z|yz\rangle\right)\cdot\left\{(-1)\left|\langle p_\pi(s)|\mu_x|xz\rangle\right|\cdot(-1)\left|\langle p_\pi(s)|\mu_y|yz\rangle\right|-0\right\}>0$$

as $\Delta_{B_-A_-}=E_{B_-}-E_{A_-}=E_{xz}-E_{yz}>0$ and $\Delta_{B_+A_-}$ is comparatively large.

The MCD *C*-term intensity of the $p_{\text{out-of-plane}}(s) \rightarrow dxz$ ($A \rightarrow B_-$) transition, in contrast, has a negative sign:

$$\frac{\Delta\varepsilon}{E} \sim -\frac{1}{\sqrt{12}}\left(2\cdot\frac{1}{\Delta_{A_-B_-}}-\frac{1}{\Delta_{A_+B_-}}\right)\cdot\sin\theta\cdot\mathrm{Im}\left(\langle\psi_a|l_z|\psi_b\rangle\right)\cdot\left\{\langle\psi_i|\mu_x|\psi_a\rangle\langle\psi_i|\mu_y|\psi_b\rangle-\langle\psi_i|\mu_y|\psi_a\rangle\langle\psi_i|\mu_x|\psi_b\rangle\right\}$$

$$=-\frac{1}{\sqrt{12}}\left(2\cdot\frac{1}{\Delta_{A_-B_-}}-\frac{1}{\Delta_{A_+B_-}}\right)\cdot\sin\theta\cdot\mathrm{Im}\left(\langle yz|l_z|xz\rangle\right)\cdot\left\{\langle p_\pi(s)|\mu_x|yz\rangle\langle p_\pi(s)|\mu_y|xz\rangle-\langle p_\pi(s)|\mu_y|yz\rangle\langle p_\pi(s)|\mu_x|xz\rangle\right.$$

$$= -\frac{1}{\sqrt{12}}\left(2\cdot\frac{1}{\Delta_{A\_B\_}}-\frac{1}{\Delta_{A_+B\_}}\right)\cdot\sin\theta\cdot(+1)\cdot\mathrm{Im}\left(\langle yz|l_z|xz\rangle\right)\cdot\left\{0-(-1)\left|\langle p_\pi(s)|\mu_y|yz\rangle\right|\cdot(-1)\left|\langle p_\pi(s)|\mu_x|xz\rangle\right|\right\}<0$$

with $\Delta_{A\_B\_} = E_{A\_} - E_{B\_} = E_{yz} - E_{xz} < 0$ and $\left|\Delta_{A_+B\_}\right|$ being comparatively small.

The $p_{\text{out-of-plane}}(s) \rightarrow d_{yz}, d_{xz}$ transitions thus result in a negative *pseudo-A*-term and are now definitely assigned to the MCD bands 3 and 4 at 24 800 $cm^{-1}$ and 29 600 $cm^{-1}$. They correspond to the observed shoulder at 25 000 $cm^{-1}$ (band D) and 30 000 $cm^{-1}$ (band E) in the UV/Vis spectrum.

The transition densities of the $p_{\text{out-of-plane}}(a) \rightarrow d_{yz}, d_{xz}$ ($i \rightarrow a, b$) transitions are:

i. $p_{\text{out-of-plane}}(a) \rightarrow d_{yz}$ ($i \rightarrow a$, MO 109 → MO 118)

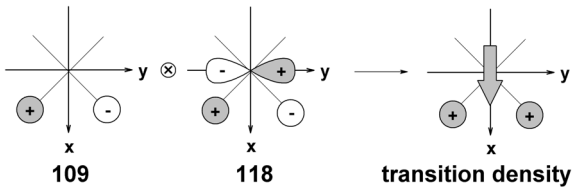


→ *x-polarized* (positive direction)

ii. $p_{\text{out-of-plane}}(a) \rightarrow d_{xz}$ ($i \rightarrow b$, MO 109 → MO 119)

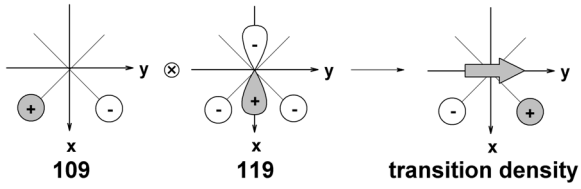


→ *y-polarized* (positive direction)

The MCD *C*-term intensity of the $p_{\text{out-of-plane}}(a) \rightarrow d_{yz}$ ($A \rightarrow A\_$) transition is negative:

$$\frac{\Delta\varepsilon}{E} \sim -\frac{1}{\sqrt{12}}\left(2\cdot\frac{1}{\Delta_{B\_A\_}}-\frac{1}{\Delta_{B_+A\_}}\right)\cdot\sin\theta\cdot\mathrm{Im}\left(\langle\psi_b|l_z|\psi_a\rangle\right)\cdot\left\{\langle\psi_i|\mu_x|\psi_b\rangle\langle\psi_i|\mu_y|\psi_a\rangle-\langle\psi_i|\mu_y|\psi_b\rangle\langle\psi_i|\mu_x|\psi_a\rangle\right\}$$

$$= -\frac{1}{\sqrt{12}}\left(2\cdot\frac{1}{\Delta_{B\_A\_}}-\frac{1}{\Delta_{B+A\_}}\right)\cdot\sin\theta\cdot\mathrm{Im}\left(\langle xz|l_z|yz\rangle\right)\cdot\left\{\langle p_\pi(a)|\mu_x|xz\rangle\langle p_\pi(a)|\mu_y|yz\rangle-\langle p_\pi(a)|\mu_y|xz\rangle\langle p_\pi(a)|\mu_x|\psi_a\rangle\right\}$$

$$= -\frac{1}{\sqrt{12}}\left(2\cdot\frac{1}{\Delta_{B\_A\_}}-\frac{1}{\Delta_{B+A\_}}\right)\cdot\sin\theta\cdot(-1)\cdot\mathrm{Im}\left(\langle xz|l_z|yz\rangle\right)\cdot\left\{0-(+1)\left|\langle p_\pi(a)|\mu_y|xz\rangle\right|\cdot(+1)\left|\langle p_\pi(a)|\mu_x|\psi_a\rangle\right|\right\}<0$$

while the MCD *C*-term intensity of the $p_{\text{out-of-plane}}(a) \rightarrow dxz$ ($A \rightarrow B_-$) transition is positive:

$$\frac{\Delta\varepsilon}{E}\sim -\frac{1}{\sqrt{12}}\left(2\cdot\frac{1}{\Delta_{A\_B\_}}-\frac{1}{\Delta_{A+B\_}}\right)\cdot\sin\theta\cdot\mathrm{Im}\left(\langle\psi_a|l_z|\psi_b\rangle\right)\cdot\left\{\langle\psi_i|\mu_x|\psi_a\rangle\langle\psi_i|\mu_y|\psi_b\rangle-\langle\psi_i|\mu_y|\psi_a\rangle\langle\psi_i|\mu_x|\psi_b\rangle\right\}$$

$$= -\frac{1}{\sqrt{12}}\left(2\cdot\frac{1}{\Delta_{A\_B\_}}-\frac{1}{\Delta_{A+B\_}}\right)\cdot\sin\theta\cdot\mathrm{Im}\left(\langle yz|l_z|xz\rangle\right)\cdot\left\{\langle p_\pi(a)|\mu_x|yz\rangle\langle p_\pi(a)|\mu_y|xz\rangle-\langle p_\pi(a)|\mu_y|yz\rangle\langle p_\pi(a)|\mu_x|xz\right.$$

$$= -\frac{1}{\sqrt{12}}\left(2\cdot\frac{1}{\Delta_{A\_B\_}}-\frac{1}{\Delta_{A+B\_}}\right)\cdot\sin\theta\cdot(+1)\cdot\mathrm{Im}\left(\langle yz|l_z|xz\rangle\right)\cdot\left\{(+1)\left|\langle p_\pi(a)|\mu_x|yz\rangle\right|\cdot(+1)\left|\langle p_\pi(a)|\mu_y|xz\rangle\right|-0\right\}>0$$

Taken together, the $p_{\text{out-of-plane}}(a) \rightarrow dyz$, $dxz$ transitions lead to a positive *pseudo-A*-term and are therefore definitely assigned to the MCD bands 5 and 6 at 30 600 $cm^{-1}$ and 34 100 $cm^{-1}$ which correspond to the absorption shoulders at 30 000 $cm^{-1}$ (band E, together with the MCD band 4) and 34 000 $cm^{-1}$ (band F) in the UV/Vis spectrum.

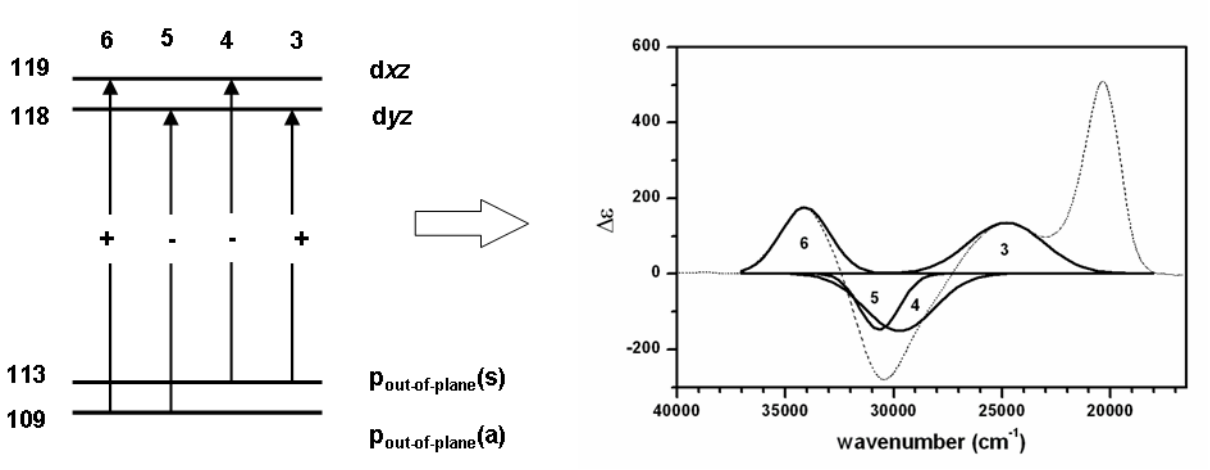


**Figure 15.** Analysis of the "double *pseudo-A*-term" feature in the low temperature MCD spectrum of [Mo(O)$Cl_3$*dppe*] from molecular orbital considerations.

The assignment of the "double *pseudo-A*-term" feature in the MCD spectrum of [Mo(O)$Cl_3$*dppe*] to the $p_{out\text{-}of\text{-}plane}$(s, a) → d*yz*, d*xz* ligand-to-metal charge transfer transitions is depicted in **Figure 15**.

Note that it is in agreement with the literature. In the MCD spectrum of various [Mo(O)L(1,2-dithiolate)] (L = hydrotris(3,5-dimethyl-1-pyrazolyl)borate) a negative-positive-positive-negative pattern of MCD bands between 20 000 $cm^{-1}$ and 30 000 $cm^{-1}$ had already been interpreted as ligand-to-metal charge transfers from the symmetric and antisymmetric out-of-plane sulfur $p_\pi$ orbitals into the d*xz* and d*yz* molybdenum d-orbitals.[2, 9] The symmetric and antisymmetric sulfur $p_\pi$ orbitals and also the d*xz* and d*yz* orbitals are inverted in energy in the case of the [Mo(O)L(1,2-dithiolate)] complexes compared to [Mo(O)$Cl_3$*dppe*]. This leads to the observed inversion of signs within the "double *pseudo-A*-term" feature which are determined by the symmetry of the starting orbitals.[1]

In the case of the title complex [Mo(O)$Cl_3$*dppe*], LMCT transitions from the bonding equivalent of the $p_{out\text{-}of\text{-}plane}$(s) orbital (MO 103) into the d*yz* and d*xz* orbitals should result in another negative *pseudo-A*-term at significantly higher energies (> 35 000 $cm^{-1}$) which was

out of range in the MCD measurements. Theoretically, a "double *pseudo-A*-term" of very, very weak intensity would also be expected in the NIR region of the MCD spectrum which arises from the corresponding $A \rightarrow A_+$ and $A \rightarrow B_+$ transitions.

## Conclusions

In the preceding sections the molybdenum(V) complex [Mo(O)$Cl_3$*dppe*] has been investigated with respect to its electronic structure and its spectroscopic properties. As this complex only has a single electron and exhibits clear $C_S$ symmetry it turned out to be an excellent system for a combined study on the electronic structure using UV/Vis and MCD spectroscopy, including the determination of the *C*-term signs of the individual electronic transitions. From the DFT calculation of the molecular orbitals, the metal and ligand character of the individual molecular orbitals could clearly be determined and, based on that, some trends considering the types and energies of the electronic transitions could be derived from the TDDFT calculations.

The very intense UV/Vis absorption band at 20 500 $cm^{-1}$ (band B) has been assigned to the $dx^2\text{-}y^2 \rightarrow dxy$ ligand field transition. This assignment was supported by resonance Raman measurements and the calculated UV/Vis spectrum (TDDFT). The most prominent feature of the MCD spectra are two corresponding *pseudo-A*-terms between 22 000 $cm^{-1}$ and 35 000 $cm^{-1}$, giving rise to a "double *pseudo-A*-term". From molecular orbital considerations the two individual *pseudo-A*-terms were assigned to the $p_{out\text{-}of\text{-}plane}$(s, a) $\rightarrow$ d*yz*, d*xz* ligand-to-metal charge transfer transitions. Describing the MCD *C*-term intensity of these transitions, the multi-determinant character of the excited states was explicitly considered.[1, 17, 37] In this way a general treatment for the MCD *C*-term intensity of type III electronic transitions has been developed. At this, configuration interaction between the sing-doublet and the trip-doublet excited states has been identified to provide the only mechanism to give rise to non-

zero MCD *C*-term intensities. The derived equations are based on the description of the MCD *C*-term intensity by Neese and Solomon.[1] The particular signs of the individual transitions were directly determined from the corresponding transition densities based on the calculated molecular orbitals and do not rely on the symmetry properties of the title complex.

**Acknowledgement**

**Supporting Information**

**References**

1. Neese, F.; Solomon, E. I., *Inorg. Chem.* **1999,** *38*, 1847-1865.
2. Carducci, M. D.; Brown, C.; Solomon, E. I.; Enemark, J. H., *J. Am. Chem. Soc.* **1994,** *116*, 11856-11868.
3. Gamelin, D. R.; Kirk, M. L.; Stemmler, T. L.; Pal, S.; Armstrong, W. H.; Pennerhahn, J. E.; Solomon, E. I., *J. Am. Chem. Soc.* **1994,** *116*, 2392-2399.
4. Solomon, E. I.; Pavel, E. G.; Loeb, K. E.; Campochiaro, C., *Coord. Chem. Rev.* **1995,** *144*, 369-460.
5. Farrar, J. A.; Neese, F.; Lappalainen, P.; Kroneck, P. M. H.; Saraste, M.; Zumft, W. G.; Thomson, A. J., *J. Am. Chem. Soc.* **1996,** *118*, 11501-11514.
6. Neese, F.; Solomon, E. I., *J. Am. Chem. Soc.* **1998,** *120*, 12829-12848.
7. Gamelin, D. R.; Randall, D. W.; Hay, M. T.; Houser, R. P.; Mulder, T. C.; Canters, G. W.; de Vries, S.; Tolman, W. B.; Lu, Y.; Solomon, E. I., *J. Am. Chem. Soc.* **1998,** *120*, 5246-5263.
8. Brunold, T. C.; Gamelin, D. R.; Stemmler, T. L.; Mandal, S. K.; Armstrong, W. H.; Penner-Hahn, J. E.; Solomon, E. I., *J. Am. Chem. Soc.* **1998,** *120*, 8724-8738.
9. Inscore, F. E.; McNaughton, R.; Westcott, B. L.; Helton, M. E.; Jones, R.; Dhawan, I. K.; Enemark, J. H.; Kirk, M. L., *Inorg. Chem.* **1999,** *38*, 1401-1410.
10. Paulat, F.; Lehnert, N., *Inorg. Chem.* **2008,** *47*, 4963-76.
11. Johansson, F. B.; Bond, A. D.; Nielsen, U. G.; Moubaraki, B.; Murray, K. S.; Berry, K. J.; Larrabee, J. A.; McKenzie, C. J., *Inorg. Chem.* **2008,** *47*, 5079-5092.
12. Larrabee, J. A.; Johnson, W. R.; Volwiler, A. S., *Inorg. Chem.* **2009,** *48*, 8822-8829.
13. Geiger, R. A.; Chattopadhyay, S.; Day, V. W.; Jackson, T. A., *J. Am. Chem. Soc.* **2010,** *132*, 2821-2831.
14. Chattopadhyay, S.; Geiger, R. A.; Yin, G. C.; Busch, D. H.; Jackson, T. A., *Inorg. Chem.* **2010,** *49*, 7530-7535.
15. Stephens, P. J., *J. Chem. Phys.* **1970,** *52*, 3489-3516.
16. Stephens, P. J., *Annu. Rev. Chem. Phys.* **1974,** *25*, 201-232.

17. Neese, F. PhD thesis, Universität Konstanz, 1997.
18. Hernandez-Marin, E.; Seth, M.; Ziegler, T., *Inorg. Chem.* **2010,** *49*, 1566-1576.
19. Seth, M.; Ziegler, T.; Autschbach, J., *J. Chem. Phys.* **2008,** *129*, 104105.
20. Butcher, A. V.; Chatt, J., *J. Chem. Soc. (A)* **1971**, 2356-2358.
21. Frisch, M. J.; Trucks, G. W.; Schlegel, H. B. S., G. E.; Robb, M. A.; Cheeseman, J. R.; Montgomery, Jr., J. A.; Vreven, T.; Kudin, K. N.; Burant, J. C.; Millam, J. M.; Iyengar, S. S.; Tomasi, J.; Barone, V.; Mennucci, B.; Cossi, M.; Scalmani, G.; Rega, N.; Petersson, G. A.; Nakatsuji, H.; Hada, M.; Ehara, M.; Toyota, K.; Fukuda, R.; Hasegawa, J.; Ishida, M.; Nakajima, T.; Honda, Y.; Kitao, O.; Nakai, H.; Klene, M.; Li, X.; Knox, J. E.; Hratchian, H. P.; Cross, J. B.; Bakken, V.; Adamo, C.; Jaramillo, J.; Gomperts, R.; Stratmann, R. E.; Yazyev, O.; Austin, A. J.; Cammi, R.; Pomelli, C.; Ochterski, J. W.; Ayala, P. Y.; Morokuma, K.; Voth, G. A.; Salvador, P.; Dannenberg, J. J.; Zakrzewski, V. G.; Dapprich, S.; Daniels, A. D.; Strain, M. C.; Farkas, O.; Malick, D. K.; Rabuck, A. D.; Raghavachari, K.; Foresman, J. B.; Ortiz, J. V.; Cui, Q.; Baboul, A. G.; Clifford, S.; Cioslowski, J.; Stefanov, B. B.; Liu, G.; Liashenko, A.; Piskorz, P.; Komaromi, I.; Martin, R. L.; Fox, D. J.; Keith, T.; Al-Laham, M. A.; Peng, C. Y.; Nanayakkara, A.; Challacombe, M.; Gill, P. M. W.; Johnson, B.; Chen, W.; Wong, M. W.; Gonzalez, C.; Pople, J. A., *Gaussian 03, Revision C.02*. Gaussian, Inc., Wallingford CT, 2004.
22. Becke, A. D., *J. Chem. Phys.* **1993,** *98*, 5648-5652.
23. Lee, C. T.; Yang, W. T.; Parr, R. G., *Phys Rev B* **1988,** *37*, 785-789.
24. Miehlich, B.; Savin, A.; Stoll, H.; Preuss, H., *Chem. Phys. Lett.* **1989,** *157*, 200-206.
25. Becke, A. D., *Phys. Rev. A* **1988,** *38*, 3098-3100.
26. Perdew, J. P., *Phys Rev B* **1986,** *33*, 8822-8824.
27. Perdew, J. P., *Phys Rev B* **1986,** *34*, 7406-7406.
28. Dunning, T. H., Jr.; Hay, P. J., *Modern Theoretical Chemistry*. Ed. H. F. Schaefer III (Plenum): New York, 1976.
29. Hay, P. J.; Wadt, W. R., *J. Chem. Phys.* **1985,** *82*, 270-283.
30. Hay, P. J.; Wadt, W. R., *J. Chem. Phys.* **1985,** *82*, 299-310.
31. Wadt, W. R.; Hay, P. J., *J. Chem. Phys.* **1985,** *82*, 284-298.
32. Allouche, A. R., *J Comput Chem* **2011,** *32*, 174-82.
33. Levason, W.; McAuliffe, C. A.; Sayle, B. J., *J. Chem. Soc. Dalton Trans.* **1976**, 1177-1181.
34. Lever, A. B. P., *Inorganic Electronic Spectroscopy*. Elsevier: Amsterdam, 1986.
35. Collison, D., *J. Chem. Soc. Dalton Trans.* **1990**, 2999-3006.
36. Pence, H. E.; Selbin, J., *Inorganic Chemistry* **1969,** *8*, 353-&.
37. Ake, R. L.; Gouterman, M., *Theor. Chim. Acta* **1969,** *15*, 20-42.

# 4 Electronic Structure and Spectroscopic Properties of Mononuclear Manganese(III) Schiff Base Complexes: A Systematic Study on [Mn(*acen*)X] Complexes by UV/Vis, MCD and EPR Spectroscopy

Having worked out in detail on the example of the mononuclear molybdenum(V) complex [Mo(O)$Cl_3$*dppe*] (dppe = 1,2-bis(diphenylphosphino)ethane, chapter 3), how the MCD *C*-term intensity of electronic transitions within a $C_S$ symmetric $d^1$ transition metal complex is calculated, this procedure was next transferred to a multi-electron system. For this purpose a series of five-coordinate manganese(III) $d^4$ high spin complexes was chosen which contain the aliphatic Schiff base ligand $acen^{2-}$ ($H_2acen$ = *N,N'*-ethylenebis(acetyl-acetone)imine) plus an anionic co-ligand X in a square-pyramidal coordination geometry and thus exhibit (pseudo-)$C_S$ symmetry as well (Figure 4.1).[188] Upon the exchange of the apical ligand X ($X = I^-, Br^-, Cl^-, NCS^-$) small changes of the ligand field were induced, so that the influence of a varying ligand field strength ($I^- < Br^- < Cl^- < NCS^-$) within a distinct coordination geometry on the UV/Vis, MCD and EPR spectra could be studied. In general, all three types of electronic transitions (type I, type II, type III, *vide supra*, chapter 2 and 3) may be observed within the [Mn(*acen*)X] complexes.

## 4.1 Synthesis

The $H_2acen$ ligand was prepared by the condensation reaction of ethylene diamine and two equivalents of acetyl acetonate and recrystallized from water.[189] The synthesis of the [Mn(*acen*)X] complexes was done according to literature procedures[188] achieving good yields and high purities which were checked by elemental analysis and atomic absorption spectroscopy (Table 4.1).

**Table 4.1.** Elemental analysis (CHNS, $Hal^-$) and atomic absorption spectroscopy (Mn) of [Mn(*acen*)X]

| | N (%) | C (%) | H (%) | S (%) | Mn (%)[a] | Hal (%)[b] |
|---|---|---|---|---|---|---|
| **[Mn(*acen*)I]** | 6.3 (6.9) | 33.5 (35.7) | 4.4 (4.5) | -- | 11.2 (13.6) | -- (31.4) |
| **[Mn(*acen*)Br]** | 7.8 (7.8) | 40.3 (40.4) | 5.1 (5.1) | -- | 14.8 (15.4) | 28.5 (22.4) |
| **[Mn(*acen*)Cl]** | 8.9 (9.0) | 46.0 (46.1) | 6.0 (5.8) | -- | 15.6 (17.6) | 10.8 (11.3) |
| **[Mn(*acen*)NCS]** | 12.0 (12.5) | 46.6 (46.6) | 5.5 (5.4) | 9.2 (9.6) | 15.21 (16.38) | -- |

[a] AAS
[b] potentiometric titration

## 4.2 Optimized complex structures and vibrational spectra

Comparing the calculated structures of the [Mn(*acen*)X] complexes which were obtained from quantum chemical DFT geometry optimizations the Mn-O and Mn-N metal-ligand bond distances, as expected, do not differ within the series (Table 4.2).The increasing ligand field strength of the axial ligand X going from $I^-$ to $NCS^-$ is very well reproduced by decreasing Mn-X metal-ligand bond lengths going from 2.85 Å for [Mn(*acen*)I] to 2.04 Å for [Mn(*acen*)NCS]. The manganese(III) ion is displaced from the equatorial (*xy*) plane in positive *z* direction towards the apical ligand. The axial displacement is increased with the increasing ligand field strength of the axial ligand from 0.19 Å for [Mn(*acen*)I] to 0.24 Å for [Mn(*acen*)NCS].

Containing an aliphatic ethylene diamine bridge, the $acen^{2-}$ Schiff base ligand is non-planar, so that the [Mn(*acen*)X] complexes only exhibit pseudo-$C_S$ symmetry (Figure 4.1). By bisecting the $acen^{2-}$ ligand between the ethylene diamine $CH_2$ groups, two planar ligand fragments ($acen^{\#}$) are obtained. These contain six delocalized π-electrons each and are twisted by about 9° versus each other. In consequence, the coordinating *acen* N and O atoms are not co-planar.

In the case of the chlorido complex [Mn(*acen*)Cl], the calculated complex structure can be compared to the structural data which has been obtained from single crystal X-ray analysis.[188] The calculated Mn-O/N distances perfectly fit the averaged Mn-O (1.901 Å) and Mn-N (1.969 Å) bond lengths from the crystal structure. In contrast the calculated Mn-Cl distance of 2.43 Å is somewhat longer than compared to the crystal structure (2.381 Å), while the axial displacement of the manganese ion of 0.22 Å is significantly smaller in the calculated structure. In the single crystal X-ray structure, the four coordinating *acen* N and O atoms are nearly co-planar and the acetyl acetone imine backbones of the two $acen^{\#}$ branches are folded towards the unoccupied coordination side of the manganese ion by 14.9° and 18.6°.[188] These are the most remarkable differences compared to the geometry optimized complex structure, where the four coordinating N and O atoms are not co-planar and the $acen^{2-}$ ligand is twisted along the (virtual) N-N axis. The same conformation is also observed throughout the other calculated [Mn(*acen*)X] complex structures (X = $I^-$, $Br^-$, $NCS^-$).

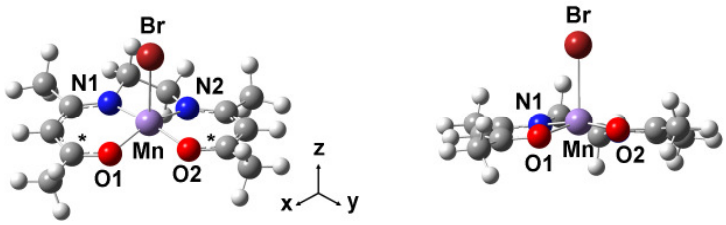


**Figure 4.1.** DFT geometry optimized complex structure of [Mn(*acen*)Br] (B3LYP/LANL2DZ). The coordinating *acen* N and O atoms are not coplanar (**right**)

**Table 4.2.** Overview of the most important structural parameters of the [Mn(*acen*)X] complexes extracted from quantum chemically optimized complex geometries (B3LYP/LANL2DZ)

| | Mn-X [Å] | Mn-N1/N2 [Å] | Mn-O1/O2 [Å] | N1-O2-Mn | Mn displacement [a] | X-Mn-O1 | *acen* twist |
|---|---|---|---|---|---|---|---|
| **[Mn(*acen*)I]** | 2.85 | 1.97/2.00 | 1.91/1.89 | 5.9° | 0.19 Å | 104.4° | -9.2° |
| **[Mn(*acen*)Br]** | 2.62 | 1.97/2.00 | 1.91/1.89 | 6.5° | 0.21 Å | 105.5° | -8.8° |
| **[Mn(*acen*)Cl]** (X-ray | 2.43 (2.38) | 1.97/2.01 (1.97) | 1.92/1.90 (1.90) | 6.7° | 0.22 Å (0.344 Å) | 107.2° | -9.5° |
| **[Mn(*acen*)NCS]** | 2.04 | 1.98/2.01 | 1.93/1.90 | 7.3° | 0.24 Å | 106.2° | -8.5° |

[a] The axial displacement b of the manganese ion is determined by b = sin(N1-O2-Mn angle)·Mn-O2 distance.

Comparing the vibrational spectra of the [Mn(*acen*)X] complexes only small shifts of the vibrational frequencies are observed throughout the series considering both the experimental and the calculated infrared (IR) and Raman spectra. In consequence, the analysis of the vibrational energies is presented in detail only using the example of the bromido complex [Mn(*acen*)Br]. A very good correlation of the experimental and calculated IR and Raman spectra is obtained with respect to the number and the intensity ratios of the individual vibrational transitions allowing an unambiguous assignment of the molecular vibrations (Figure 4.2, Table 4.3).

Experimental and calculated IR spectra match very well within the far infrared energy region (FIR; Figure 4.2, top), where important metal-ligand stretching and bending vibrations are observed (100 - 500 $cm^{-1}$). The Mn-X metal-ligand stretch is observed at 280 $cm^{-1}$ for the chlorido complex and shifts on the exchange of the axial ligand by $Br^-$, $I^-$ and $NCS^-$ to 233 $cm^{-1}$ (Mn-Br), 223 $cm^{-1}$(Mn-I) and 269 $cm^{-1}$ (Mn-*N*-CS). The metal-ligand vibrations of the quasi-planar Mn-N/O-*acen* core are derived from the normal modes of a square-planar complex ($D_{4h}$ symmetry) and labeled using the common group theory notation given in parentheses in Table 4.3.

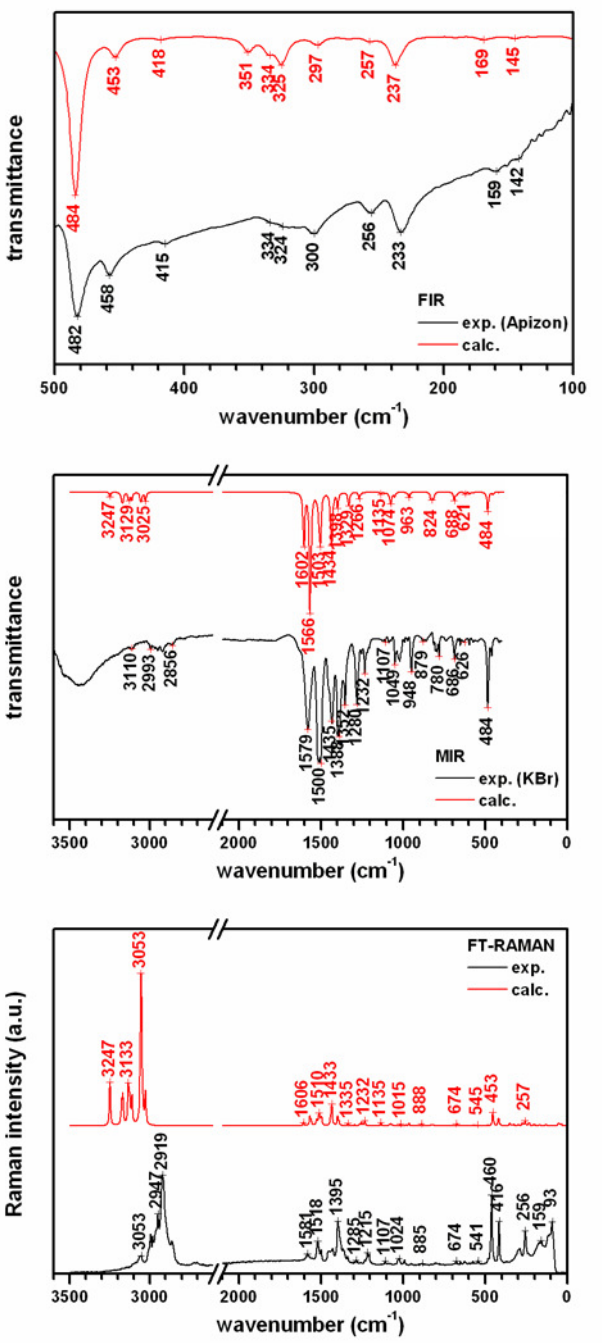


**Figure 4.2.** Experimental and calculated FIR (**top**), MIR (**middle**) and FT-Raman (**bottom**) spectra of [Mn(*acen*)Br]; a very good correlation is achieved especially within the FIR region.

**Table 4.3.** Vibrational energies (in $cm^{-1}$) for [Mn(*acen*)Br]. The assignment of the observed transitions is based on DFT calculations of the molecular vibrations. The calculated frequencies are given in parenthesis. Additionally, the characteristic Mn-X metal-ligand stretching frequencies of the other three [Mn(*acen*)X] complexes ($X = I^-$, $Cl^-$, $NCS^-$) are also listed.

| IR ($cm^{-1}$) | Raman ($cm^{-1}$) | vibrational mode |
|---|---|---|
| -- | 93 (93) | $CH_2 + CH_3$ tilting vibration, out-of-plane |
| 142 (145) | -- | Mn-O bending out-of-plane, *acen* twist (out-of-plane) |
| 159 (169) | -- | Mn-N bending out-of-plane, *acen* twist (out-of-plane) |
| 223 (230) | **--** | **metal-ligand stretch, Mn-I, [Mn(*acen*)I]** |
| 233 (237) | **--** | **metal-ligand stretch, Mn-Br, [Mn(*acen*)Br]** |
| 280 (279) | **--** | **metal-ligand stretch, Mn-Cl, [Mn(*acen*)Cl]** |
| 269 (267) | **--** | **metal-ligand stretch, Mn-*N*-CS, [Mn(*acen*)NCS]** |
| 256 (257) | 256 (257) | symmetric Mn-*acen* breathing vibration, Mn-N/O bending, in-plane („$B_{2g}$“) |
| 300 (297) | 290 | symmetric/antisymmetric *acen*-$CH_3$ bending, in-plane |
| 324, 334 (325, 334) | -- | N(2) out-of-plane , Mn in-plane |
| -- (351) | -- | N(1) out-of-plane |
| 415, 458 (418, 453) | 416, 460 (418, 453) | Mn-N/O bending in-plane („$E_{u,\ bend}$“), symmetric *acen* bending |
| 482 (484) | -- | antisymmetric Mn-*acen* breathing vibration |
| -- | 541 (544) | $CH_3$/C=C tilting vibration, out-of-plane |
| 595 (592) | -- | antisymmetric *acen* rocking vibration, in-plane |
| 621 (621) | 625 | symmetric Mn-N/O stretch („$E_{u,\ stretch}$(a)“) |
| -- | 674 (674) | symmetric Mn-N/O stretch („$A_{1g}$“), backbone rocking |
| 686 (688) | -- | antisymmetric Mn-N/O stretch, („$E_{u,\ stretch}$(b)“) |
| 780 (813) | -- | antisymmetric Mn-N stretch + C-H twist ($CH_2$) |
| ~ 800 (824, 830) | -- | C-H bending, out-of-plane (CH) |
| 879 | 885 (888) | symmetric Mn-N stretch + C-H bending ($CH_2$) |
| 948 (961) | -- (965) | C=O/C-$CH_3$/C-CH stretch, symmetric combination |
| -- | 991 (1015) | C-C stretch ($CH_2$) + $CH_3$ tilting (in-plane) |
| 1 018, 1 049 (1 051, 1 074) | 1 024 (1 074) | $CH_3$ tilting, in-plane |
| 1 107 (1 135) | 1 107 (1 135) | C=C bending, C-C /N-C stretch ($CH_2$-$CH_2$/N-$CH_2$) |
| 1 232 (1 266) | 1 215 (1 232) | C-C twist ($CH_2$-$CH_2$) + C-H in-plane bending (CH) |
| 1 280 (1 329) | 1 285 (1 335) | HC=C bending/C-C $H_3$ stretch (*acen* backbone bending) |
| 1 352 (1 398) | 1 364 (1 397) | C-H bending ($CH_2$) |
| 1 388 (1 434-1 442) | 1 395 (1 434) | C-H bending ($CH_3$, “umbrella vibrations”) |
| 1 435-1 452 (1 503-1 510) | 1 452, 1 428 (1 510) | C-H bending ($CH_2$,$CH_3$) |
| 1 500-1 513 (1 559-1 566) | 1 518, 1 499 (1 566) | C=C stretches, *acen* backbone vibrations |
| 1 579 (1 602) | 1 581 (1 606) | C=O/C=N stretch |
| 2 860-3 050 (3 025-3 250) | 2 860-3 050 (3 025-3 250) | C-H stretches (CH, $CH_2$, $CH_3$) |
| 2 919 (3 053) | 2 919 (3 054) | C-H stretch ($CH_3$) |
| -- (3 246/47) | 3 053 (3 246/47) | C-H stretch (CH) |

The most intense bands of the MIR spectrum (Figure 4.2, middle) arise from the C=C (1 500 $cm^{-1}$) and C=N/C=O (1 580 $cm^{-1}$) double bond stretches as well as from various C-H bending vibrations (1 350 - 1 450 $cm^{-1}$). Different *acen* backbone bending vibrations are observed around 1 280 $cm^{-1}$, while the twisting vibrations of the ethylene diamine $CH_2$ groups appear around 1 220 - 1 230 $cm^{-1}$. Transitions observed around 1 000 -1 050 $cm^{-1}$ derive from the in-plane tilting vibrations of the $CH_3$ groups.

Within the MIR fingerprint region (1 000 - 500 $cm^{-1}$) different Mn-O/N stretches are observed combined with C-H bending and/or additional *acen* backbone vibrations. The most intense band here is assigned to the simultaneous stretch of the C=O, C-$CH_3$ and C-CH bonds at two of the quaternary C atoms (C*, Figure 4.1) of the *acen* backbone (950 $cm^{-1}$).

The most intense transition observed in the Raman spectrum (Figure 4.2, bottom) is assigned to a symmetric C-H stretch (2 920 $cm^{-1}$, $CH_3$). In addition also the C-H bending vibrations of the $CH_3$ groups ("umbrella vibrations") at 1 395 $cm^{-1}$ and the Mn-O/N in-plane bending vibrations at 460 $cm^{-1}$, 416 $cm^{-1}$ and 256 $cm^{-1}$, that are hardly observed in the infrared spectra, show relatively high Raman intensities.

The very good match between the experimental and the calculated IR and Raman spectra assures the reliability of the optimized complex structures for their further use in the quantum chemical calculations of molecular orbitals and electronic transitions for all [Mn(*acen*)X] complexes.

## 4.3 [Mn(*acen*)X] Complexes as SOD Models? - Check of the Catalytic Activity with Respect to the Dismutation of Superoxide

Manganese(III) complexes containing the common Schiff base ligand *salen* (*salen* = *N,N'*-bis(salicylidene)ethylenediamine) are known to be efficient SOD mimics.[9] So obviously also the [Mn(*acen*)X] complexes were to be tested for their catalytic activity with respect to the dismutation of superoxide ($4\,O^{\cdot-} + 4\,H^+ \rightarrow H_2O_2 + O_2$) as well. However, using the NBT/xanthine oxidase (XAO) assay mentioned above (NBT = nitro blue tetrazolium chloride, chapter 2),[19, 20] no SOD-like activity could be observed in the presence of any of the

[Mn(*acen*)X] complexes.[a] This can be explained by the low redox potentials of the Mn(III) → Mn(II) reduction which are significantly lower than that of the natural enzyme (-0.16 V).[9] Measured vs. $Fc/Fc^+$ in $CH_2Cl_2$ (0.1 mM, containing 0.1 M *tert*-butylammonium hexafluorophosphate, $TBAPF_6$) they vary from -0.97 V for [Mn(*acen*)I] to -1.36 V for [Mn(*acen*)NCS] (cyclovoltammograms not shown). Besides, it must be assumed from the EPR and UV/Vis spectra (*vide infra*) that water binds to the free coordination site of the [Mn(*acen*)X] complexes which then is not accessible to the coordination of superoxide radical anions any more.

## 4.4 Electron Paramagnetic Resonance

To make sure that the [Mn(*acen*)X] are present in solutions as mononuclear manganese(III) species, low-temperature EPR spectra were recorded. As $Mn^{3+}$ is an integer spin system (S = 2), EPR spectra have to be measured in the parallel detection mode (*vide supra*, chapter 2.1.3). One signal is detected around B = 850 G in the low-temperature parallel mode cw X-band EPR spectra of the [Mn(*acen*)X] series (Figure 4.3) which is assigned to the $|-2\rangle \rightarrow |+2\rangle$ transition of an S = 2 system with a large axial zero-field splitting value *D* ($|D| > 0.3$ cm$^{-1}$).[151, 190]

A hyperfine splitting of approximately 42 G is observed for all [Mn(*acen*)X] complexes. It arises from the coupling of the $M_S$ sublevels with the nuclear spin *I* of 5/2 for $^{55}$Mn which leads to the observed sextet based on the selection rule of $\Delta I = 0$. Note that hyperfine coupling with the halogenido ligands ($I_{Cl, Br} = 3/2$, $I_I = 5/2$) or the N atom (I = 1, $^{14}$N) of the isothiocyanato and $acen^{2-}$ ligands is not resolved due to the very small A-values.

[a] NBT, hypoxanthine and xanthin oxidase (XO) were solved in 0.1 M phosphate buffer (pH 7.4). The [Mn(*acen*)X] complexes were solved in $H_2O$. 100 µL of a 1.5 mM hypoxanthine solution were added to a mixture of 200 µL of a 2.5 mM NBT solution, 100 µL of a xanthine oxidase solution (1 mg XO in 0.5 mL of phosphate buffer), 0 – 300 µL of a 0.3 mM complex solution and 600-300 µL of phosphate buffer to give a total sample volume: of 1 mL. UV/Vis spectra of this solution were recorded for 10 min at 15 s intervals between 800 and 400 nm in PMMA one-way cuvettes. The decrease of the NBT absorption maximum at 540 nm plotted against time.

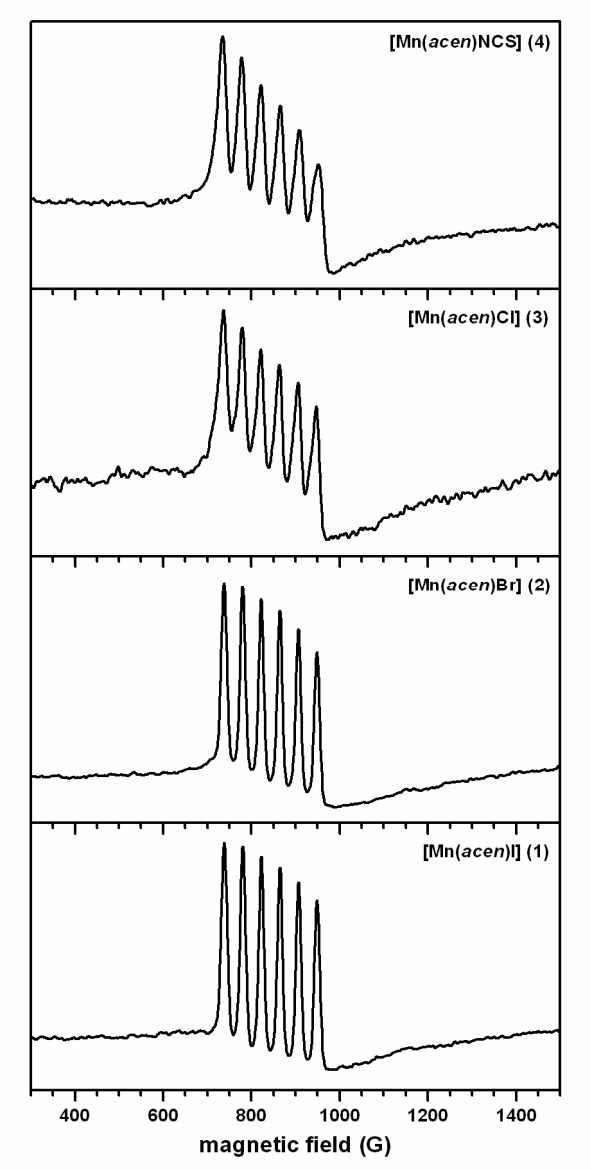


**Figure 4.3.** Low-temperature parallel mode cw X-band EPR spectra of [Mn(*acen*)X] measured in frozen $CH_2Cl_2$/toluene solutions (7:3, 2 mM), T = 5 K, microwave power 2 mW, modulation frequency 100 kHz, modulation amplitude 10 G.

Unlike to a previous study on the parallel mode EPR spectra of Jacobsen's epoxidation catalyst [Mn(*salen**)Cl] (*salen** = (*R,R*)-(-)-*N, N'*-bis(3,5-di-*tert*-butylsalicylidene)-1,2-cyclohexane-imine)[159] no additives are needed to detect the well-resolved sextets, which are characteristic for mononuclear manganese(III) species in well-defined molecular geometries. The presence of dimers, chains or aggregates can therefore be ruled out at the used concentrations of 2 mM. However, at higher concentrations (> 5 mM) the parallel mode EPR spectra of the [Mn(*acen*)X] complexes show additional lines (Figure 4.4) which are similar to the EPR spectra of [Mn(*salen**)Cl] *without* additives[159] suggesting the formation of di- or polynuclear species like $\mu$-carboxido- or μ-halogenido-bridged dimers,[191, 192] $[Mn(acen)X]_x$

clusters or chains which could also possibly be formed in solution by polymerisation via the axial ligands. [193]

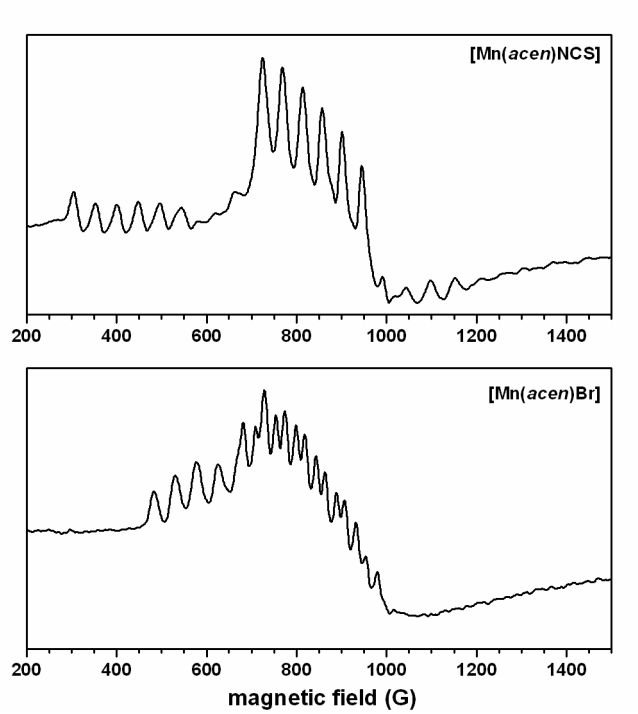


**Figure 4.4.** Low-temperature parallel mode cw X-band EPR spectra of [Mn(*acen*)Br] and [Mn(*acen*)NCS] measured in frozen $CH_2Cl_2$ solutions at high concentrations (10 mM), T = 4 K, microwave power 2 mW, modulation frequency 100 kHz, modulation amplitude 10 G.

From spectral simulations using the XSophe software suite,[1] the parallel hyperfine tensor and *g*-tensor values ($A_{||}$, $g_{||}$) as well as the axial and rhombic zero-field splitting parameters (*D* and *E*) are obtained. As expected, they do not differ much throughout the [Mn(*acen*)X] series. As $A\perp$ and $g\perp$ cannot be obtained from the parallel mode EPR measurements, spectral simulations are not sensitive to these values and typical values for manganese(III) ions in axially elongated coordination geometries had to be chosen from the literature.[159] The sign of the zero-field splitting parameters cannot be obtained directly from the spectral simulations. However, from the results of the AOMX calculations (*vide infra*, chapter 4.7) *D* is assumed to be negative for [Mn(*acen*)X].[159, 194] The parallel mode EPR spectrum of [Mn(*acen*)Cl] has been fitted with $A\perp = 69.2 \cdot 10^{-4}$ cm$^{-11}$, $A_{||} = 39.2 \cdot 10^{-4}$ cm$^{-1}$, $g\perp = 2.00$, $g_{||} = 1.98$, $D = -2.5$ cm$^{-1}$ and $|E| = 0.18$ cm$^{-1}$. All parameters are within the typical ranges for mononuclear manganese(III) compounds.[151, 159] It should be noted that two different line widths are observed within the different [Mn(*acen*)X] spectra (Figure 4.5), as the hyperfine lines of [Mn(*acen*)I] and [Mn(*acen*)Br] are much sharper (line width 31 G) than those of

[Mn(*acen*)Cl] and [Mn(*acen*)NCS] (line width 56 G). This could probably be explained by small monomer - dimer equilibria which can be neglected for the iodido and bromido complex, but lead to the presence of very small amounts of dimers and/or polymers in the case of the chlorido and *N*CS complex.

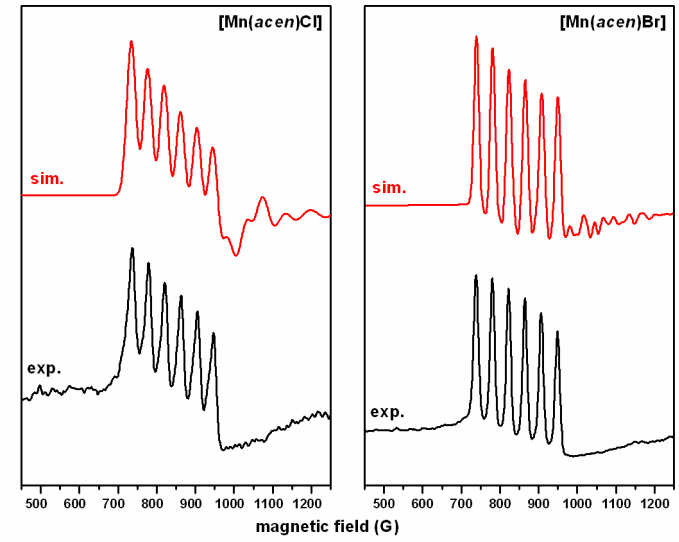


**Figure 4.5.** Parallel mode cw X-band EPR spectra of [Mn(*acen*)Cl] (**left**) and [Mn(*acen*)Br] (**right**), measured in frozen $CH_2Cl_2$/toluene solutions (7:3, 2 mM) at T = 5.4 K (microwave power 2 mW, modulation frequency 100 kHz, modulation amplitude 10 G) and spectral simulations - [Mn(*acen*)Cl]: $A_\perp = 69.2 \cdot 10^{-4}$ cm$^{-1}$, $A_{||} = 39.2 \cdot 10^{-4}$ cm$^{-1}$, $g_\perp = 2.00$, $g_{||} = 1.98$, $D = -2.5$ cm$^{-1}$ and $|E| = 0.18$ cm$^{-1}$, line width: 56 G; [Mn(*acen*)Br]: $A_\perp = 70.2 \cdot 10^{-4}$ cm$^{-1}$, $A_{||} = 38.9 \cdot 10^{-4}$ cm$^{-1}$, $g_\perp = 2.00$, $g_{||} = 1.98$, $D = -2.5$ cm$^{-1}$ and $|E| = 0.056$ cm$^{-1}$, line width: 31 G.

Another argument in favor of this explanation is, that in coordinating solvents like MeOH the same narrow line widths of approximately 30 G (Figure 4.6) are detected for all [Mn(*acen*)X] complexes, indicating that the solvent molecules coordinate to the unoccupied axial positions of the metal ions and only discrete mononuclear species are present then.

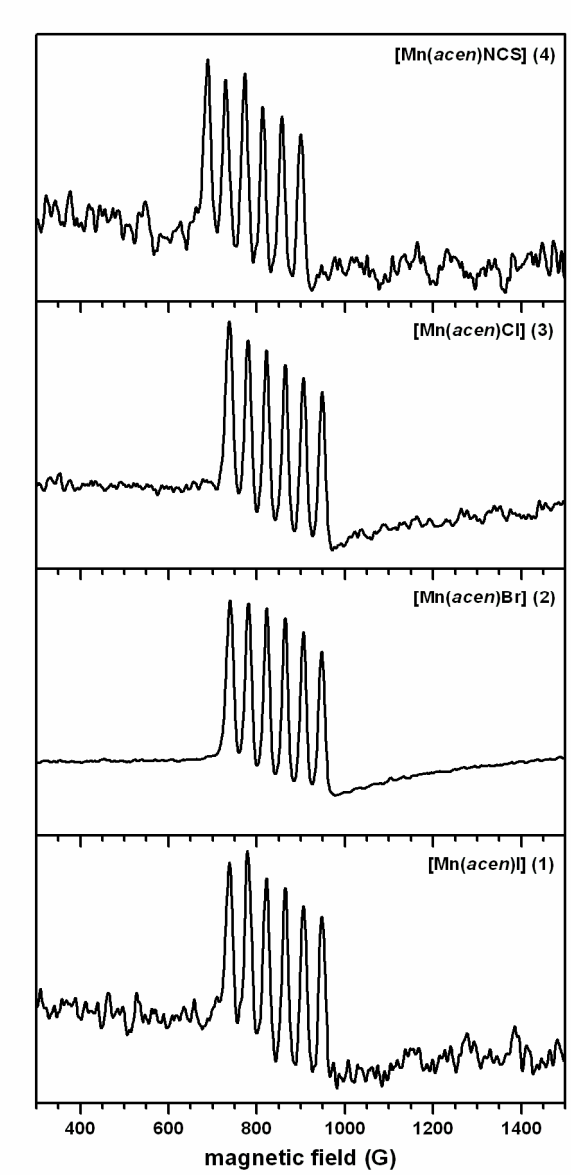


**Figure 4.6.** Low-temperature parallel mode cw X-band EPR spectra of [Mn(*acen*)X] measured in frozen MeOH solutions (2 mM) at T = 4 K, microwave power 2 mW, modulation frequency 100 kHz, modulation amplitude 10 G.

A power study had to be done before temperature-dependent EPR measurements could be performed. Plotting the relative signal height against $P^{1/2}$ a linear relationship is obtained as it is shown for the EPR signal of [Mn(*acen*)Cl] at T = 4.0 K (Figure 4.7, inset). This clearly illustrates, that the EPR signal is not saturated within this power range between 0.005 mW and 20 mW at this temperature. A microwave power of 2 mW was then used for the temperature dependent measurements with the temperature being varied between 4.0 K and 25 K. The temperature dependence of the parallel mode EPR signals follows Curie's law, resulting in a straight line (signal height versus $T^{-1}$, Figure 4.7) with the same slope of 12.5 K

for all [Mn(*acen*)X] complexes which confirms, that the observed spin transitions all arise from the same $M_S$ = -2 spin state.

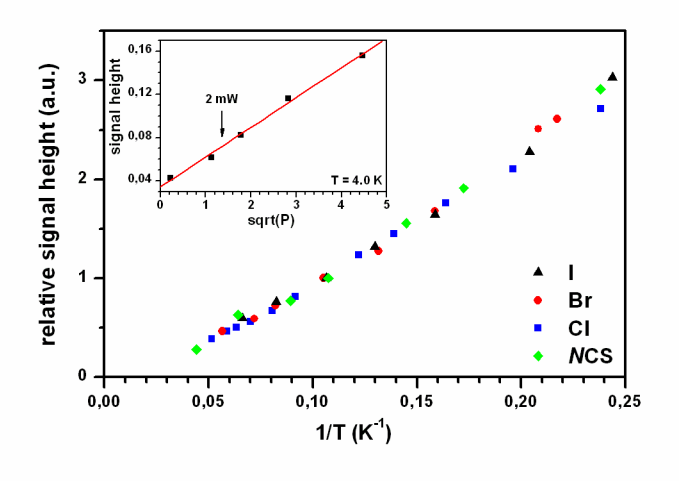


**Figure 4.7.** Temperature dependence of the parallel mode cw X-band EPR signals of the [Mn(*acen*)X] compounds measured in frozen $CH_2Cl_2$/toluene solutions (7:3, 2 mM) at temperatures between 4.0 K and 25 K; **inset**: Power dependence of the parallel mode EPR spectrum of [Mn(*acen*)Cl] at T = 4.0 K. The microwave power was varied from 0.005 to 20 mW. The arrow denotes the non-saturating microwave power of 2 mW used for the temperature dependent measurements.

## 4.5 UV/Visible Absorption Spectra

No significant differences are observed within the UV/visible absorption spectra of the different [Mn(*acen*)X] complexes with respect to the energies and the extinction coefficients of the observed transitions (Figure 4.8).

Considering the metal-centered ligand field transitions, three d → d bands are generally expected in the UV/Vis absorption spectrum (bands I - III) according to the ligand field splitting diagram (Scheme 4.1), as the d-orbitals of a five-coordinate manganese(III) ion in an idealized square-pyramidal coordination geometry split into one degenerate and three non-degenerate sublevels. Within the $d^4$ high spin configuration of manganese(III) the $dx^2$-$y^2$ orbital is left unoccupied which leads to a $^5B_1$ ground state and three excited states with the symmetry of these states being determined by the symmetry of the vacant orbital. In a distorted square-pyramidal complex geometry the d → d band III ($^5B_1 \rightarrow {}^5E$) may split into two transitions, if the degeneracy of the d*xz* and d*yz* orbitals is removed.

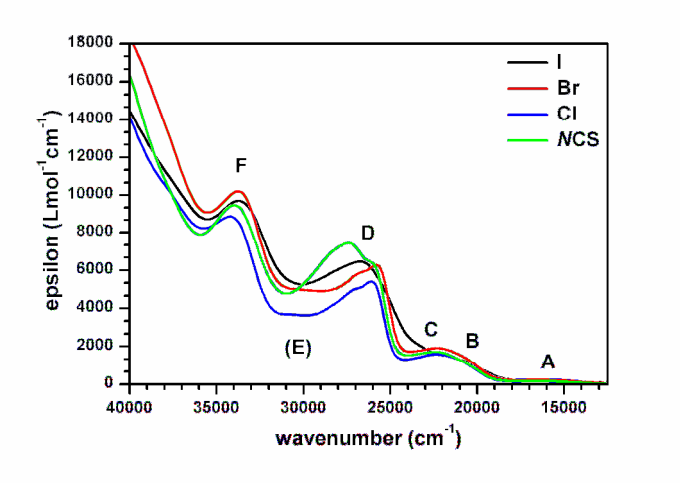


**Figure 4.8.** UV/Vis absorption spectra of [Mn(acen)X] complexes, measured in $CH_2Cl_2$.

**Scheme 4.1.** [Mn(*acen*)X]: schematic ligand field splitting of the manganese d-orbitals and term diagram for the square-pyramidal $d^4$ high-spin complex deduced from UV/Vis absorption measurements.[188]

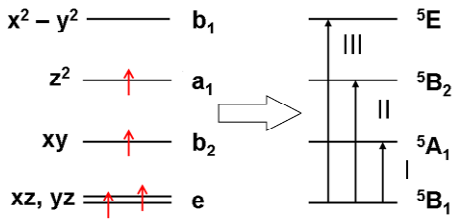


Considering the overlap between metal and ligand orbitals, ligand-to-metal charge transfer (LMCT) transitions between the p-orbitals of the axial ligand and the manganese d-orbitals and metal-to-ligand charge transfer (MLCT) into the π* orbitals of the $acen^{2-}$ ligand might be observed additionally.

An assignment of the individual electronic transitions of the [Mn(*acen*)X] complexes has already been reported by *Boucher et al.*. According to this work the first ligand field transition (band I) is expected at very low energies (< 8 000 $cm^{-1}$)[188] and has never been observed so far for any [Mn(*acen*)X] compound. In perfect agreement with the reported spectra the broad, low-intensity band at 16 400 $cm^{-1}$ ($\varepsilon$ = 200 $mol^{-1}cm^{-1}$, band A) is assigned to the second d → d transition, $^5B_1 \rightarrow {}^5B_2$ (band II).[188] Band III is expected to be observed around 20 500 $cm^{-1}$,[188] but is hidden beneath a charge transfer transition centered at 22 300 $cm^{-1}$ ($\varepsilon$ = 1 600 - 1 900 $cm^{-1}$). This band has already been assigned to the d*xy* → π* transition as no energetic shift of this band was observed throughout the [Mn(*acen*)X] series.[188] From the UV/Vis spectrum of the iodido complex it can be assumed that this band actually consists of

(at least) two transitions (band B, C). Another charge transfer transition is observed at 25 000 - 27 000 $cm^{-1}$ ($\varepsilon$ = 5 500 – 7 500 $cm^{-1}$ band D) being assigned to the d*xz*, d*yz* → π* transition.[188] The splitting of this band has been explained by the splitting of the $^5E$ state in a distorted square-pyramidal coordination geometry (*vide supra*). The ligand-centered π → π* transition of the *acen*$^{2-}$ ligand is detected around 33 500 $cm^{-1}$ ($\varepsilon$ = 8 800 – 10 200 $cm^{-1}$, band F).[188]

Going into further detail, some slight differences are observed for the different [Mn(*acen*)X] compounds. In the UV/Vis absorption spectra of [Mn(*acen*)Br] and [Mn(*acen*)Cl], a large "plateau" is observed at around 30 500 $cm^{-1}$, indicating the presence of an additional absorption band (E) which has not been described in the literature so far and is not as clearly identified in the UV/Vis spectra of [Mn(*acen*)I] and [Mn(*acen*)NCS]. It is confirmed by the low-temperature UV/Vis spectrum of [Mn(*acen*)Cl] in which band E is centered at 30 800 $cm^{-1}$ (Figure 4.9).

As already mentioned, the splitting of the first charge transfer band into more than one transition, centered at 21 200 $cm^{-1}$ (band B) and 23 500 $cm^{-1}$ (band C), is clearly resolved in the UV/Vis spectrum of [Mn(*acen*)I]. In contrast, the splitting of band D at around 26 000 $cm^{-1}$ is not well resolved in the case of the iodido complex as well as a probable absorption band E around 30 000 $cm^{-1}$. For [Mn(*acen*)NCS] the splitting of band D is clearly resolved but shows a different intensity ratio compared to the halogenido complexes. However, an additional shoulder is also observed at 28 500 $cm^{-1}$ in the UV/Vis spectrum of the *N*CS complex.

To make sure that the [Mn(*acen*)X] complexes are also present as molecular species in the polystyrene film samples as they are prepared for the MCD measurements, the UV/Vis absorption spectra of these films were measured for comparison. No additional absorption features are made out within the film spectra of any of the [Mn(*acen*)X] complexes. It is therefore assumed that mononuclear, non-aggregated species are present in these polystyrene films and that the formation of dimers, chains or aggregates on the evaporation of the solvent can be ruled out. Taking a closer look at the film UV/Vis spectrum of [Mn(*acen*)Cl] (Figure

4.10) it is confirmed that the first charge transfer band around 22 000 $cm^{-1}$ indeed consists of (at least) two transitions (band B, C).

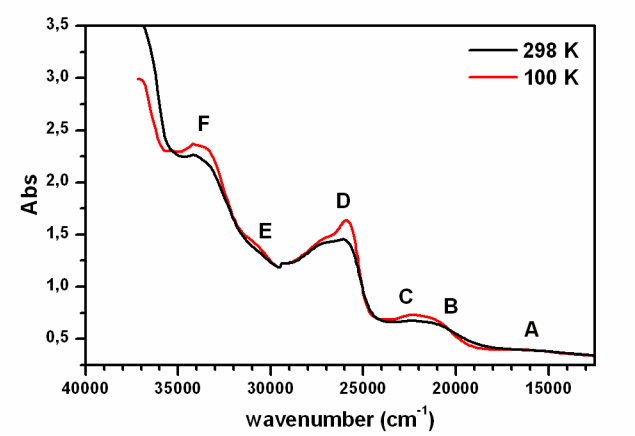


**Figure 4.9.** UV/Vis absorption spectra of [Mn(*acen*)Cl], measured in a polystyrene film at room temperature and at T = 100 K. The film was prepared by the evaporation of 200 µL of a 1 mM complex solution in dichloromethane containing dissolved polystyrene.

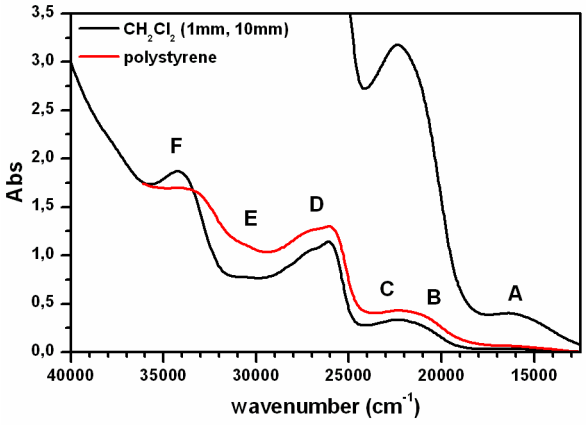


**Figure 4.10.** UV/Vis absorption spectra of [Mn(*acen*)Cl] - solution and polystyrene film spectra are shown for comparison. Solution spectra: 2 mM complex in $CH_2Cl_2$ for 1 mm and 10 mm path length.

The resonance Raman spectra recorded with an excitation energy of 22 000 $cm^{-1}$ also reveal that (at least) two electronic transitions originating from different types of orbitals are observed within this energy region, as two different types of vibrations are enhanced. The resonance Raman spectrum of [Mn(*acen*)Br] is shown in Figure 4.11. Beside the very strong enhancement of the symmetric *in-plane* Mn-N/O vibrations at 418 $cm^{-1}$ and 651 $cm^{-1}$, the Mn-X metal-ligand vibration *perpendicular* to the equatorial plane at 236 $cm^{-1}$ is also strongly enhanced.

If the UV/Vis spectra are measured in coordinating solvents like methanol, ethanol or water/glycerol, a blue shift especially of the absorption band D of ca. 2 000 $cm^{-1}$ is observed as it is shown in Figure 4.12 for [Mn(*acen*)Br]. It is also associated with a slightly increased absorbance. This indicates that the starting orbitals of this transition might indeed be d*xz* and d*yz*, as these two orbitals are affected upon the bonding of solvent molecules to the free coordination site. In propionitrile and butyronitrile no blue shift of band D is observed in the UV/Vis spectrum, which implies, that these two solvents do not coordinate to [Mn(*acen*)X] and thus would also have been appropriate solvents for the MCD measurements instead of $CH_2Cl_2$.

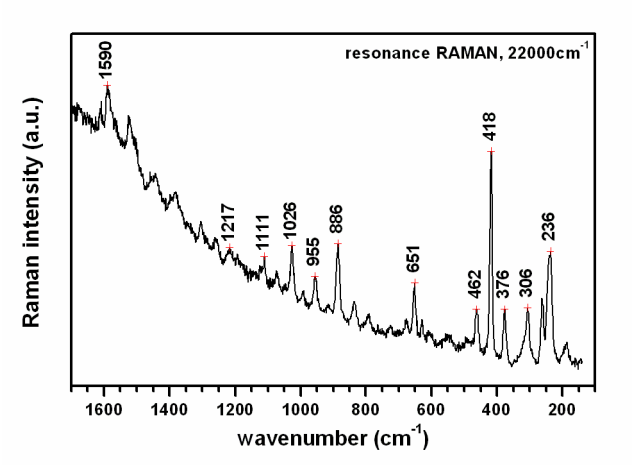


**Figure 4.11.** Resonance Raman spectrum of [Mn(*acen*)Br] between 100 $cm^{-1}$ and 1 700 $cm^{-1}$ measured with an excitation energy of 22 000 $cm^{-1}$ which corresponds to the first UV/Vis charge transfer band centered at 22 300 $cm^{-1}$.

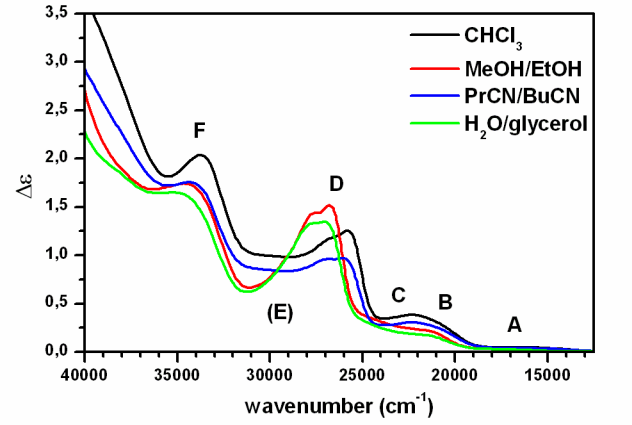


**Figure 4.12.** Comparison of the UV/Vis absorption spectra of [Mn(*acen*)Br] measured in different solvents (2 mM, d = 1 mm), the second MLCT charge transfer band (xz, yz → π*, band D) significantly shifts to higher energies in coordinating solvents

## 4.6 Magnetic Circular Dichroism Spectra

In the low-temperature MCD spectra of the [Mn(*acen*)X] complexes, three to four broad absorption features with a distinct number of zero-crossings are observed between 20 000 $cm^{-1}$ and 38 000 $cm^{-1}$ (Figure 4.13). They can be modeled with 14 to 16 of Gaussian curves (Figure 4.14, Table 4.4). As could be seen in the previous section small changes of the ligand field due to the variation of the apical ligand X almost do not affect the UV/Vis absorption spectra of the [Mn(*acen*)X] complexes. In contrast, but they cause dramatic changes in the corresponding MCD spectra (Figure 4.13).

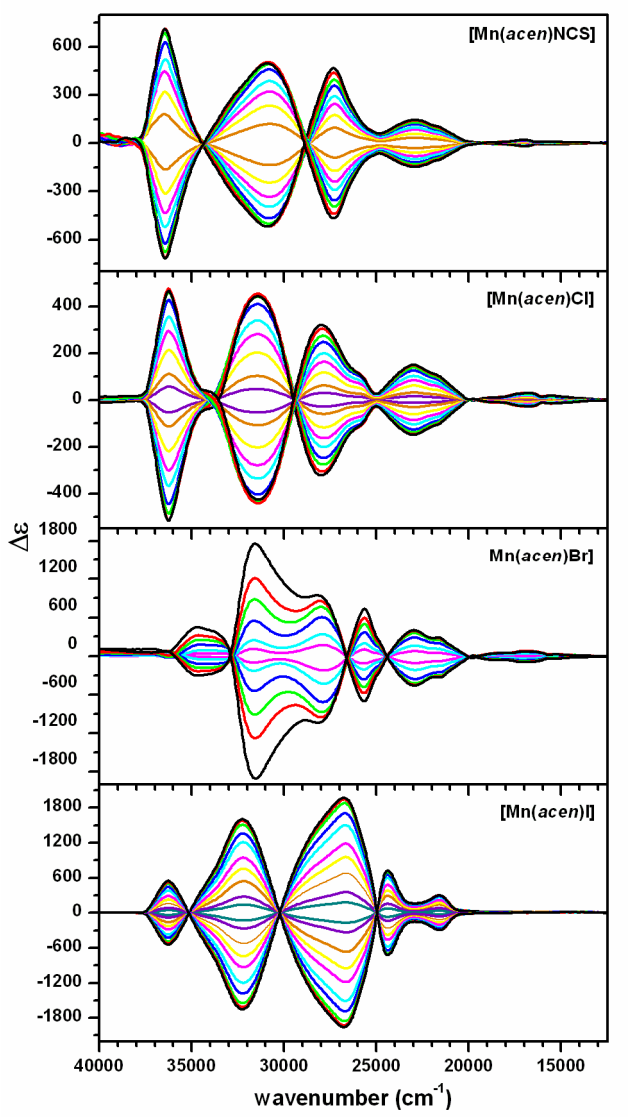


**Figure 4.13.** Low-temperature MCD spectra of the [Mn(*acen*)X] complexes measured in $CH_2Cl_2$/polystyrene (T = 2 K). Film samples were prepared from 1 mM complex solutions.

Virtually no differences are observed when the MCD spectra of [Mn(*acen*)Cl] and [Mn(*acen*)NCS] are compared with respect to the number, the energies and the relative intensities of the observed transitions. At positive magnetic field strengths, four positive signed MCD transitions are observed between 21 000 $cm^{-1}$ and 28 000 $cm^{-1}$ (band 8 - 11) followed by two negative signed bands between 30 000 $cm^{-1}$ and 33 000 $cm^{-1}$ (band 12, 13) and another two positive transitions around 36 000 $cm^{-1}$ (band 14, 15). Especially the spectrum of [Mn(*acen*)NCS] shows similar intensities for the MCD bands 11 – 14 in a positive-negative-negative-positive pattern. They should therefore be considered as a double feature with a negative *pseudo-A*-term centered at 29 000 $cm^{-1}$ (band 11 + 12) followed by a positive *pseudo-A*-term centered at 34 000 $cm^{-1}$ (band 13 + 14). This implies that both the ground states and the excited states derive from two nearly or formerly degenerate E states showing different symmetries with respect to the mirror plane *xz* and that the transition-dipole moments of the individual transitions between these states each have opposite signs.

Compared to the MCD spectra of the chlorido and the *N*CS complex, two positive signed bands are also found at 21 400 $cm^{-1}$ and 23 300 $cm^{-1}$ in the MCD spectrum of [Mn(*acen*)Br] (band 8, 9). However, in contrast to the former two complexes, an additional change of sign is observed in the MCD spectrum of the bromido complex around 25 000 $cm^{-1}$. The MCD bands 11 +12 and the bands 13 + 15 might also be considered as a double *pseudo-A*-term feature. Compared to [Mn(*acen*)Cl] and [Mn(*acen*)NCS], however, it shows inverted signs (negative-positive-positive-negative), i.e. a positive *pseudo-A*-term is centered at 26 700 $cm^{-1}$ (band 11 + 12) followed by a negative *pseudo-A*-term around 31 000 – 32 000 $cm^{-1}$ (band 13 + 15) in the MCD spectrum of [Mn(*acen*)Br]. Another positive *pseudo-A*-term may be centered at 35 500 $cm^{-1}$ (band 16 + 17).

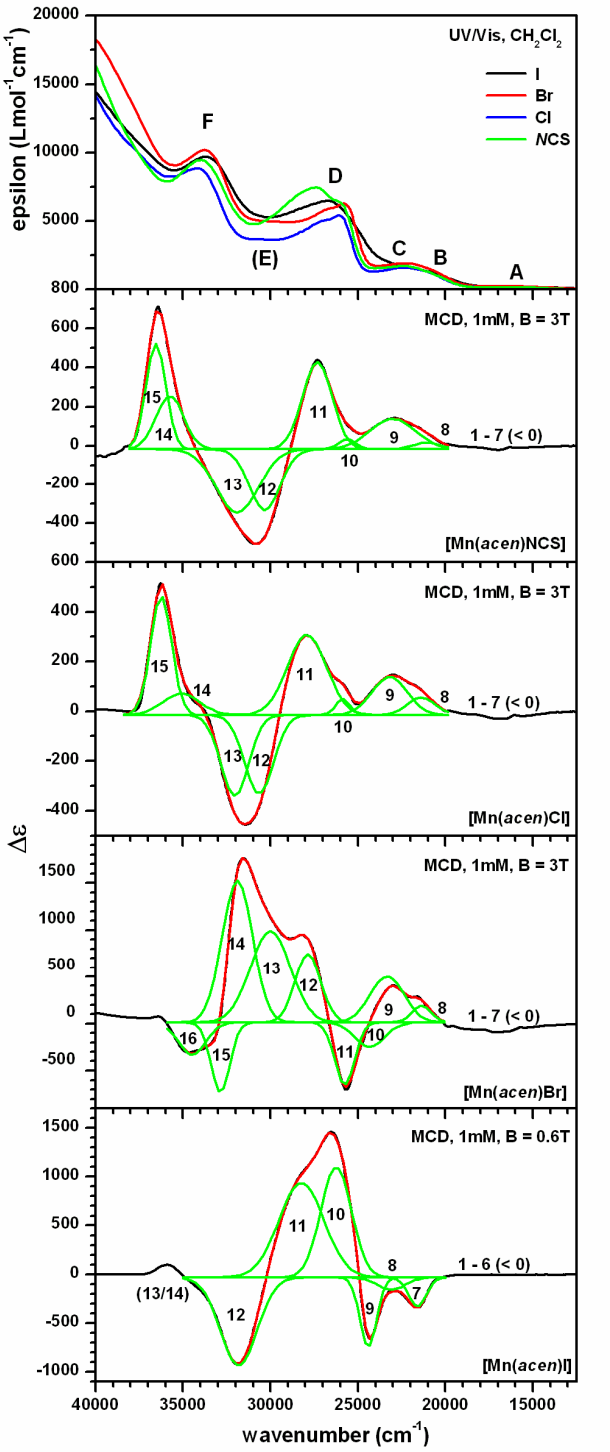


**Figure 4.14.** Low-temperature MCD spectra of the [Mn(*acen*)X] complexes measured in $CH_2Cl_2$/polystyrene (T = 2 K). Film samples were prepared from 1 mM complex solutions. Spectral deconvolution: Gaussian curve fits; (**top**) UV/Vis absorption spectra measured in $CH_2Cl_2$ for comparison.

Band 14 in the MCD spectrum might correspond to band 15 in the MCD spectra of [Mn(*acen*)Cl] and [Mn(*acen*)NCS] which may be shifted to lower energies in the case of [Mn(*acen*)Br]. There are two possible explanations for the occurrence of the unique negative band 10 in the MCD spectrum of the bromido complex: (i) band 10 actually is a small

positive band corresponding to band 10 in the MCD spectra of [Mn(*acen*)Cl] and [Mn(*acen*)NCS], which hardly visible next to the large negative band 11 or (ii) it could in fact be a negative band which probably corresponds to band 7 in the MCD spectrum of [Mn(*acen*)I] and is blue-shifted on the increase of the ligand field strength. In this case it would not be resolved beneath the intense negative bands 12 and 13 in the MCD spectra of the chlorido and the *N*CS complex. A small positive band corresponding to band 10 in the MCD spectra of the latter two complexes might then also not be resolved in the MCD spectrum of [Mn(*acen*)Br].

Compared to the UV/Vis absorption spectra the MCD bands 8 and 9 certainly correspond to the UV/Vis transitions B and C, while the double *pseudo-A*-term features match the energies of the UV/Vis absorption bands D + E and F. The MCD band 10 might also be linked to the UV/Vis absorption band D. Correlations between the UV/Vis and MCD bands are listed in Table 4.4.

**Table 4.4.** UV/Vis and MCD transitions of the [Mn(*acen*)X] complexes in $cm^{-1}$ and MCD signs at positive magnetic field strength

| UV/Vis | [Mn(*acen*)I] | [Mn(*acen*)Br] | [Mn(*acen*)Cl] | [Mn(*acen*)NCS] |
|---|---|---|---|---|
| | -- | (1) 14 800 (-) | (1) 14 900 (-) | (1) 14 800 (-) |
| | -- | (2) 15 200 (-) | (2) 15 400 (-) | (2) 15 500 (-) |
| | (1) 15 600 (-) | (3) 15 500 (-) | (3) 15 700 (-) | (3) 16 100 (-) |
| (A) 16 400 | (2) 16 400 (-) | (4) 16 400 (-) | (4) 16 500 (-) | (4) 16 900 (-) |
| | (3) 16 900 (-) | (5) 17 200 (-) | (5) 17 200 (-) | (5) 17 300 (-) |
| | (4) 18 200 (-) | (6) 18 200 (-) | (6) 17 600 (-) | (6) 17 900 (-) |
| | (5) 18 800 (-) | (7) 18 900 (-) | (7) | (7) 18 700 (-) |
| | (6) 19 700 (-) | -- | -- | -- |
| (B, C) 22 300 | (7) 21 600 (-) | (8) 21 400 (+) | (8) 21 400 (+) | (8) 21 400 (+) |
| | (8) 23 300 (-) | (9) 23 300 (+) | (9) 23 200 (+) | (9) 23 200 (+) |
| | (9) 24 400 (-) | (10) 24 300 (-) | -- | -- |
| (D) 25 000-27 000 | (10) 26 200 (+) | (11) 25 800 (-) | (10) 25 900 (+) | (10) 25 300 (+) |
| | (11) 28 400 (+) | (12) 27 900 (+) | (11) 27 900 (+) | (11) 27 500 (+) |
| ((E) 30 500 [a]) | -- | (13) 30 000 (+) | (12) 30 700 (-) | (12) 30 700 (-) |
| | (12) 31 800 (-) | (14) 31 900 (+) | (13) 32 100 (-) | (13) 32 800 (-) |
| (F) 33 500 | -- | (15) 32 900 (-) | -- | -- |
| | (13) | (16) 34 500 (-) | -- | -- |
| | (14) | -- | (14) 35 100 (+) | (14) 35 800 (+) |
| | -- | -- | (15) 36 300 (+) | (15) 36 400 (+) |

[a] [Mn(*acen*)Br] and [Mn(*acen*)Cl]

For [Mn(*acen*)I] the MCD transitions between 20 000 $cm^{-1}$ and 25 000 $cm^{-1}$ (band 7 - 9) show negative signs at positive magnetic field strengths. This is completely different from the MCD spectra of the other three complexes. However, it cannot be ruled out that the MCD band 8 actually is a positive band centered between the two negatively signed bands 7 and 9 and corresponds to band 9 in the MCD spectra of the other three complexes. The negative band 7 in the MCD spectrum of the iodido complex might correspond to the negative band 10 in the MCD spectrum of [Mn(*acen*)Br], if the latter is in fact considered to be a negatively signed transition being blue-shifted compared to [Mn(*acen*)I]. Small positive bands corresponding to the MCD bands 8 and 10 in the MCD spectra of the chlorido and *N*CS complexes are not resolved in the MCD spectrum of [Mn(*acen*)I]. In contrast, two very intense positive transitions are observed for the iodido complex at 26 200 $cm^{-1}$ and 28 400 $cm^{-1}$ (band 10, 11) followed by another negative transition at 31 800 $cm^{-1}$ (band 12). Band 9 - 12 show the same negative-positive-positive-negative pattern of MCD intensities already found band 11 + 12 and 13 + 15 in the MCD spectrum of the bromido complex. They should therefore also be considered as a double *pseudo-A*-term corresponding to the MCD spectra of the other three complexes. An additional positive *pseudo-A*-term can probably be made out around 35 000 $cm^{-1}$ (band 13, 14).

As shown in Figure 4.15 broad, low-intensity absorption features without zero-crossings are additionally observed between 14 000 $cm^{-1}$ and 19 000 $cm^{-1}$ for all [Mn(*acen*)X] complexes corresponding to the broad UV/Vis absorption band A. They can be modeled by six to seven Gaussian curves which all show positive signs at negative magnetic field strengths.

Within this spectral region, no significant differences are observed between the MCD spectra of the bromido, chlorido and *N*CS complexes. Three bands of comparatively low intensities are made out between 14 000 $cm^{-1}$ and 16 000 $cm^{-1}$ (band 1 - 3). They might be assigned to spin-forbidden ligand field transitions arising from low-lying triplet states, as no spin-allowed $d \rightarrow d$ transitions are expected at these energies. They are followed by three bands of higher intensities between 16 000 $cm^{-1}$ and 18 500 $cm^{-1}$ (band 4 - 6) of which the MCD band 4 (16 400 - 16 900 $cm^{-1}$) is assigned to the second spin-allowed ligand field transition ($^5B_1 \rightarrow {}^5B_2$, band II) in accordance with the maximum of the absorption band A (*vide supra*, chapter 4.5). One additional low-intensity band can clearly be made out at around 19 000 $cm^{-1}$

(band 7) for [Mn(*acen*)Br] and [Mn(*acen*)NCS], which might probably be assigned to another spin-forbidden ligand field transition. No transitions are observed below 14 000 $cm^{-1}$. Again, the first spin-allowed d → d ligand field transition ($^5B_1 \rightarrow {}^5A_1$, band I) is supposed to be observed below 8 000 $cm^{-1}$ according to the literature,[188] so its energy has been out of range in our measurements.

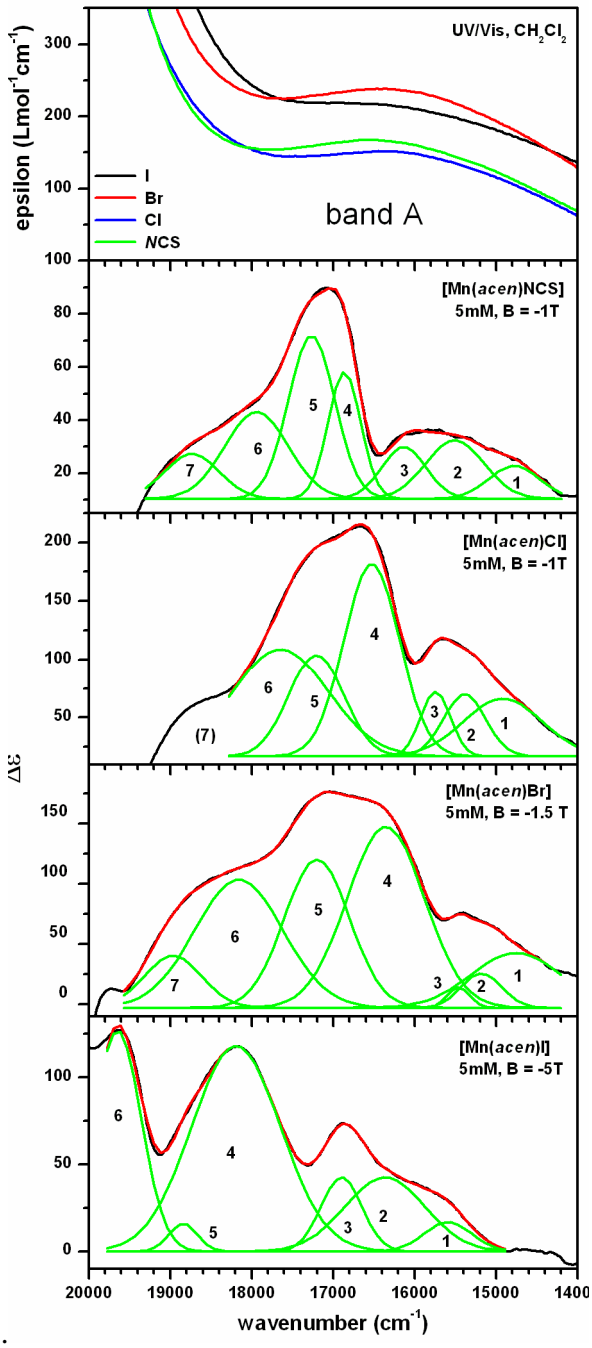


**Figure 4.15.** Low-temperature MCD spectra of [Mn(*acen*)X] measured in $CH_2Cl_2$/polystyrene films between 14 000 $cm^{-1}$ and 20 000 $cm^{-1}$ (T = 2 K). Film samples were prepared from 5 mM complex solutions. (**top**) UV/Vis absorption spectra ($CH_2Cl_2$) for comparison.

For [Mn(*acen*)I] only very small intensities were obtained for all MCD transitions below 20 000 $cm^{-1}$. The most intense transition is band 4, but its energy of 18 200 $cm^{-1}$ is too high to be assigned to the second spin-allowed ligand field transition (band II) compared to the other three complexes. Considering their energies, band 2 or 3 could be assigned to the ligand field transition band II, while band 4 and 6 rather should be assigned to low-energy charge transfer transitions. Band 6 at 19 700 $cm^{-1}$, which is only resolved at high magnetic field strengths of $|B| > 3$ T, shows the same intensity as band 4. Band 1 and 5 then could be assigned to spin-forbidden triplet transitions due to their comparatively low intensities.

So far, all band assignments are based on the previous study of the UV/Vis spectra by Boucher *et. al.*[188] which do explain the huge differences observed in the MCD spectra of the [Mn(*acen*)X] complexes. In the following, thus a detailed analysis of the observed MCD bands based on time-dependent DFT calculations of the electronic transitions as well as on molecular orbital and symmetry considerations was carried out. The latter will also give an explanation of the positive and negative signs of the individual MCD transitions and especially explain the change of sign of the double *pseudo-A*-terms which is observed within the [Mn(*acen*)X] series.

## 4.7 Ligand Field Calculations (AOMX[169])

Input coordinates of the coordinating ligand atoms (bond distances and bond angles) were taken from the DFT optimized complex structures. The AOMX calculations were carried out without an effective symmetry assignment. The parameters $e_\sigma$ and $e_\pi$, which can be interpreted as a measure of the donor and acceptor properties of the corresponding ligands, were fitted to two experimental energies taken from Gaussian curve fits of the MCD spectra. Starting parameters were taken from a previously published data.[168] An averaged parameter set was chosen to describe the coordinating properties of the $acen^{2-}$ ligand (keto/amine) without the additional consideration of the conjugated double bonds. Another $e_\sigma/e_\pi$ parameter set was used for the apical ligand X.

Eight excited ligand field states are obtained from the AOM calculation for all [Mn(*acen*)X] complexes between 10 000 $cm^{-1}$ and ~ 20 000 $cm^{-1}$ (Table 4.5). As these calculations are

carried out without effective symmetry assignments only the spin multiplicity of the resulting states is obtained. However, assigning the MCD transition at 16 400 – 16 900 $cm^{-1}$ to the second spin-allowed d → d ligand field transition ($^5B_1 \rightarrow {}^5B_2$, band II) corresponding to the UV/Vis absorption maximum of band A at 16 400 $cm^{-1}$, three low-lying triplet states are obtained between 14 000 $cm^{-1}$ and 16 000 $cm^{-1}$ from the AOM ligand field calculations. They arise from the ligand field splitting of the $^3H$ excited state. The MCD bands 1 – 3 of the bromido, the chlorido and the *N*CS complex as well as the MCD band 1 of the iodido complex all show very low intensities and are therefore assigned to spin-forbidden triplet transitions (Table 4.5).

**Table 4.5.** Overview of the experimental (UV/Vis and MCD) and calculated (AOM) ligand field states of the [$Mn^{III}$(*acen*)X] complexes. All energies are given in $cm^{-1}$.

| | | $^5B_1$ | $^5A_1$ | triplet ($^3H$) | | | $^5B_2$ | $^5E$ | | triplet ($^3H$) |
|---|---|---|---|---|---|---|---|---|---|---|
| **ref.**[188] | **UV/Vis** | 0 | (<8 000) | -- | -- | -- | 16 400 | (~ 22 000) | | -- |
| **$I^-$** | **UV/Vis** | -- | -- | -- | -- | -- | 16 400 | -- | -- | -- |
| | **MCD** | -- | -- | -- | -- | 15 600 [a] | 16 400 [a] | 16 900 | -- | 18 800 |
| | **calc.** | 0 | 10 700 | 14 400 | 15 200 | 15 600 | 16 400 | 17 000 | 18 000 | 19 800 |
| **$Br^-$** | **UV/Vis** | -- | -- | -- | -- | -- | 16 400 | -- | -- | -- |
| | **MCD** | -- | -- | 14 600 | 15 200 [a] | 15 500 | 16 400 [a] | 17 200 | 18 200 | 18 900 |
| | **calc.** | 0 | 10 400 | 14 400 | 15 200 | 15 600 | 16 400 | 17 000 | 18 000 | 20 000 |
| **$Cl^-$** | **UV/Vis** | -- | -- | -- | -- | -- | 16 400 | -- | -- | -- |
| | **MCD** | -- | -- | 14 900 | 15 400 [a] | 15 700 | 16 500 [a] | 17 200 | 17 700 | -- |
| | **calc.** | 0 | 10 400 | 14 600 | 15 400 | 15 800 | 16 500 | 17 000 | 18 000 | 20 300 |
| ***N*CS$^-$** | **UV/Vis** | -- | -- | -- | -- | -- | 16 400 | -- | -- | -- |
| | **MCD** | -- | -- | 14 800 | 15 500 [a] | 16 100 | 16 900 [a] | 17 300 | 18 000 | 18 700 |
| | **calc.** | 0 | 10 200 | 14 600 | 15 500 | 16 100 | 16 900 | 17 700 | 18 700 | 21 000 |

[a] energies used for the fit of the AOM parameters)

According to the results of the AOMX calculations, the first spin-allowed d → d ligand field transition (band I) is expected between 10 000 $cm^{-1}$ and 11 000 $cm^{-1}$ for all [Mn(*acen*)X] complexes. This is noticeably higher in energy than previously assumed (< 8 000 $cm^{-1}$, *vide supra*, chapter 4.5).[188] Two quintet transitions occur between 17 000 - 18 700 $cm^{-1}$. They result from the splitting of the third ligand field transition due to the splitting of the $^5E$ state into two separate quintet states. Their energy is significantly lower than it was previously assumed for band III (~ 20 500 $cm^{-1}$, *vide supra*, chapter 4.5).[188] However, the MCD bands 5

and 6 in the case of the bromido, the chlorido and the *N*CS complex and the MCD band 3 of the iodido complex could indeed this third ligand field transition (band III), as the bands show equal intensities compared to the MCD bands 4, or 2, respectively. The MCD band 7 in the spectra of the former three complexes and the MCD band 5 in the case of the iodido complex could then arise from another spin-forbidden triplet transition.

The differences which are obtained for the ligand field states of the [Mn(*acen*)X] complexes from the AOMX calculations are, of course, reflected in the ligand field bonding parameters $e_\sigma$ and $e_\pi$. In each case, they were fitted to the energies of two different transitions taken from the Gaussian curve fits of the considered MCD spectra (denoted with an [a] in Table 4.5). The large deviation of $e_\sigma$(*acen*) and $e_\pi$(*acen*) from their starting values indicates, that the nature of the conjugated π bonds of the $H_2$*acen* ligand should be described as an enol/imine system rather than keto/amine. Note that this is also confirmed by the DFT geometry optimization of the uncoordinated $acen^{2-}$ ligand (not shown). All σ- and π-bonding parameters are increased with the increasing ligand field strength of the axial ligand going from [Mn(*acen*)I] to [Mn(*acen*)NCS]. The values of the Racah interelectronic repulsion parameters B follow the expected trend within the nephelauxetic series resulting in higher B values for the "harder" ligands $NCS^-$ (875 $cm^{-1}$) and $Cl^-$ (848 $cm^{-1}$) compared to lower values for the more polarizable ligands $Br^-$ (831 $cm^{-1}$) and $I^-$ (817 $cm^{-1}$).

**Table 4.6.** AOM parameters of the [Mn(*acen*)X] complexes in $cm^{-1}$.

| | **[Mn(*acen*)I]** | | **[Mn(*acen*Br]** | | **[Mn(*acen*)Cl]** | | **[Mn(*acen*)NCS]** | |
|---|---|---|---|---|---|---|---|---|
| | input | fit | input | fit | input | fit | input | fit |
| $\mathbf{e_\sigma(}$***acen***$\mathbf{)}$ | 6 800 | 7 700 | 6 800 | 7 700 | 6 800 | 7 900 | 6 800 | 8 000 |
| $\mathbf{e_\pi(}$***acen***$\mathbf{)}$ | 1 400 | 1 400 | 1 440 | 1 460 | 1 440 | 1 490 | 1 400 | 1 500 |
| $\mathbf{e_\sigma(X)}$ | 4 140 | 4 390 | 5 050 | 4 820 | 5 610 | 5 020 | 6 240 | 5 400 |
| $\mathbf{e_\pi(X)}$ | 670 | 720 | 690 | 685 | 910 | 870 | 380 | 370 |
| **B** [a] | 820 | 817 | 830 | 831 | 840 | 848 | 870 | 875 |
| **C** [b] | 3 800 | 3 800 | 3 800 | 3 800 | 3 900 | 3 900 | 4 000 | 4 000 |
| ***D*** | -- | 4.0 | -- | 3.9 | -- | 3.8 | -- | 3.8 |
| **\|*E*\|** | -- | 0.098 | -- | 0.095 | -- | 0.094 | -- | 0.097 |

[a] free ion value Mn(III): B = 1142 $cm^{-1}$ [195]
[b] C = 4.6·B

By including spin orbit coupling into the AOM calculations which is $\zeta = 352\ cm^{-1}$ for a manganese(III) ion[105, 195] the zero-field splitting parameters *D* and *E* can be obtained. *D* is

negative for all [Mn(*acen*)X] complexes. However, the computed absolute *D* values are too high throughout the series compared to the *D* values obtained from the simulations of the EPR spectra (*vide infra,* chapter 4.4) as the negative spin-orbit coupling of the axial ligands ($\zeta_{Hal} < 0$) is not considered.

## 4.8 DFT Computations of the Molecular Orbitals

*Ligand*

To illustrate how the molecular orbitals of the uncoordinated ligand the $acen^{2-}$ molecule look like, the ligand molecule is - theoretically - cut between the $CH_2$ groups of the ethylene diamine bridge. Each of the two resulting $acen^{\#}$ moieties contains two delocalized double bonds and six delocalized π-electrons, so that five $acen^{\#}$ π-orbitals are obtained: two bonding ($\pi_1$, $\pi_2$) and one non-bonding π-orbital ($\pi^{n.b.}$) and two antibonding π*-orbitals ($\pi_1$*, $\pi_2$*). The molecular orbitals of the original $acen^{2-}$ ligand are nom derived from the symmetric (s) and antisymmetric (a) linear combinations of each one of these $acen^{\#}$ π-orbitals with the corresponding – laterally reversed – counterparts which leads to a total number of ten ligand π-orbitals (Figure 4.16, left). In total twelve π-electrons have to be placed into these MOs, so that the two bonding and the non-bonding *acen* π-orbitals are doubly occupied while the symmetric and antisymmetric π*-orbitals, $\pi_1$*(s, a) and $\pi_2$*(s, a), are left unoccupied in the electronic ground state. Additionally, the in-plane p-orbitals of the *acen* heteroatoms are symmetrically (s) and antisymmetrically (a) recombined to form two types of ligand σ-orbitals, $p_\sigma(O,N)_{s,a}$ and $p_\sigma(O/N)_{s,a}$ (Figure 4.16, left). Note that the overlap of the *acen* N and O $p_\sigma$ orbitals within the $p_\sigma(O,N)_s$ and $p_\sigma(O,N)_a$ orbitals is an artifact of the way the *acen* ligand is shown here, as, for a better comparison with the molecular orbitals of the corresponding manganese(III) complexes, it is depicted in the metal-depleted form and not in the linear conformation that would actually be obtained from the DFT geometry optimization, for example.

*[Mn(acen)X] complexes*

The molecular orbitals of the [Mn(*acen*)X] complexes are generated by the linear combination of the $acen^{2-}$ ligand orbitals, the manganese d-orbitals and the p-orbitals of the apical ligand X. Due to the high covalence of the metal-ligand bonds the description of the molecular orbitals is rather difficult. A clear distinction between metal centered d-orbitals and ligand orbitals is no longer possible, but it is obvious that only certain linear combinations can occur considering the potential overlaps between metal and ligand orbitals. Each manganese d-orbital is theoretically expected to be observed in both symmetric and antisymmetric linear combinations with appropriate *acen* ligand orbitals, which, of course, leads to additional splittings of the molecular orbitals. In every calculation four singly occupied *alpha* spin orbitals are obtained - as expected for the considered $d^4$ high spin configuration of the [Mn(*acen*)X] complexes. A large extent of spin polarization is observed between *alpha* and *beta* spin orbitals. In consequence, the numbers and orbital types do not always coincide on the *alpha* and *beta* side of the molecular orbital schemes.

To illustrate systematically how the molecular orbitals of the [Mn(*acen*)X] complexes are constructed they first have been calculated for symmetrical [Mn($acen^{\#}$)X] complexes which exhibit true $C_S$ symmetry in ideal square-pyramidal coordination geometries. For this purpose the ethylene diamine bridge of the $acen^{2-}$ ligand has been abbreviated by hydrogen atoms. The resulting two planar $acen^{\#}$ ligand moieties have been symmetrically arranged and the manganese(III) ion was <u>not</u> allowed to leave the equatorial plane formed by the N and O donor atoms. The results of these supporting calculations are presented in detail in the following, using the example of the symmetrized bromido complex [Mn($acen^{\#}$)Br] (Figure 4.16 (right), Table 4.7).

In general, the mirror plane *xz* defines the molecular axes of a $C_S$ symmetric molecule. In consequence, the former d*xy* orbital has to be relabelled into $dx^2\text{-}y^2$ and *vice versa*. The molecular orbitals are either symmetric (a') or antisymmetric (a'') with respect to the mirror plane *xz*.

Which linear combinations of metal and ligand orbitals are allowed in general can be described by a few simple rules arising from symmetry considerations. Obviously, the d*xz*, d*yz* and $dz^2$ manganese d-orbitals can only be combined with the *acen* $p_\pi$ orbitals, while d*xy* and $dx^2\text{-}y^2$ can only interact with the $p_\sigma$ orbitals of the coordinating N and O *acen* ligand

atoms. Due to their particular symmetries d$xz$, d$x^2$-$y^2$ (formerly d$xy$) and d$z^2$ are only found in linear combinations with symmetric (s) ligand σ- and π-orbitals, while d$yz$ and d$xy$ (formerly d$x^2$-$y^2$) are only combined with antisymmetric (a) ligand orbitals. Due to their symmetries, the all-symmetric $\pi_1$(s) and the $p_\sigma(O,N)_s$ orbitals do not interact with any of the metal d-orbitals and therefore do not appear within the molecular orbitals of the [Mn(*acen*)X] complexes.

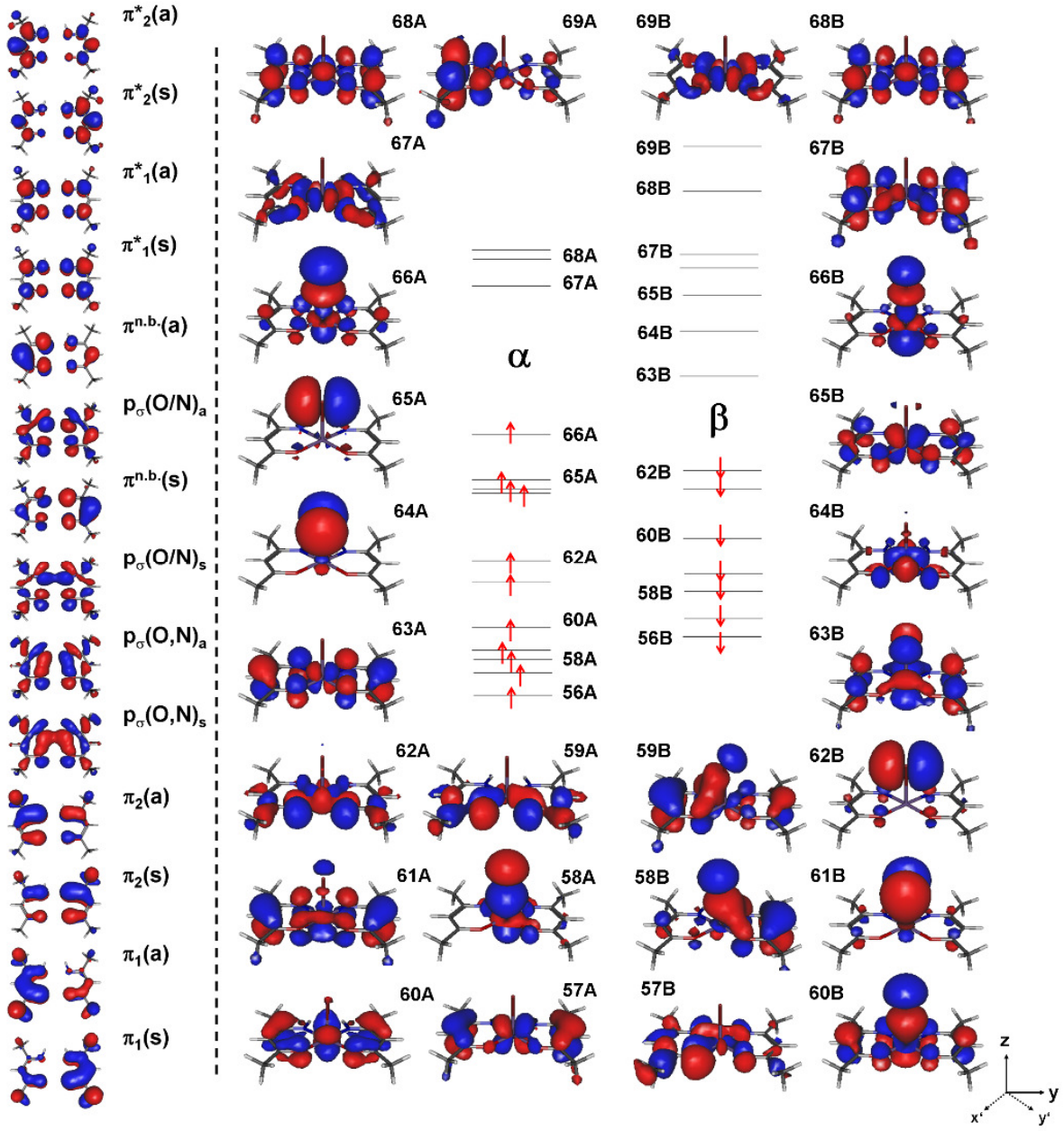


**Figure 4.16. left**: Molecular orbitals of the symmetrized *acen*$^{\#}$ ligand with the ethylene diamine bridge of the *acen*$^{2-}$ molecule substituted by two hydrogen atoms. **right**: molecular orbitals of the symmetrized bromido complex [Mn(*acen*$^{\#}$)Br] in an idealized square-planar coordination geometry (BP86/LANL2DZ).

**Table 4.7.** Molecular orbitals of the symmetrized complex [Mn(*acen*$^{\#}$)Br] ($C_S$ symmetry, BP86/LANL2DZ). Only atomic orbital contributions greater than 10 % are listed.

| **α spin** | | **sym. ($C_S$)** | **$Mn^{3+}$** | | ***acen*$^{2-}$** | **axial ligand ($Br^-$)** | | **description** |
|---|---|---|---|---|---|---|---|---|
| 74A [a] | **$\pi_2$*** | a'' | yz | 11.1 % | $\pi_2$*(a) | -- | -- | *acen* π*-orbital, $\pi_2$*(a) |
| 73A [a] | **$\pi_2$*** | a' | -- | -- | $\pi_2$*(s) | -- | -- | *acen* π*-orbital, $\pi_2$*(s) |
| 71A | **$\pi_1$*** | a' | $z^2$ | 12.4 % | $\pi_2$*(s) | -- | -- | *acen* π*-orbital, $\pi_2$*(s) |
| 69A | **$\pi_1$*** | a' | xz | 20.1 % | $\pi_1$*(s) | -- | -- | *acen* π*-orbital, $\pi_1$*(a) |
| | | | xy | 11.3 % | | | | |
| 68A | **$\pi_1$*** | a'' | xy | 26.7 % | $\pi_1$*(a) | -- | -- | *acen* π*-orbital, $\pi_1$*(a) |
| | | | xz | 11.6 % | | | | |
| 67A | **xy/$p_\sigma$** | a' | xy | 71.9 % | $p_\sigma(O/N)_a$ | -- | -- | metal d-orbital (d*xy*), antibonding, LUMO |
| 66A | **$z^2$/$p_z$** | | $z^2$ | 51.0 % | ($\pi^{n.b.}$(s)) | $p_z$ | 41.0 % | metal d-orbital ($dz^2$), antibonding, HOMO |
| 65A | **$p_y$** | a'' | (yz) | (9.0 %) | ($\pi^{n.b.}$(a)) | $p_y$ | 52.0 % | ligand p-orbital ($p_y$) |
| 64A | **$p_x$** | a' | xz | 18.0 % | __ | $p_x$ | 51.9 % | ligand p-orbital ($p_x$) |
| 63A | **yz/π** | a'' | yz | 52.9 % | $\pi^{n.b.}$(a) | -- | -- | metal d-orbital (d*yz*), antibonding |
| 62A | **$x^2$-$y^2$/$p_\sigma$** | a' | $x^2$-$y^2$ | 50.3 % | $p_\sigma(O/N)_s$ | -- | -- | metal d-orbital ($dx^2$-$y^2$), antibonding |
| 61A | **$\pi^{n.b.}$** | a' | xz | 23.3 % | $\pi^{n.b.}$(s) | ($p_z$) | (9.3 %) | $\pi^{n.b.}$(s), *acen* π-orbital |
| | | | $z^2$ | 18.3 % | | -- | -- | |
| 60A | **xz/π** | a' | xz | 70.6 % | $\pi_2$(s) | -- | -- | metal d-orbital (d*xz*), antibonding |
| 59A | **xy/$p_\sigma$** | a'' | xy | 26.2 % | $p_\sigma(O/N)_a$ | -- | -- | bonding analogue of MO 67A |
| 58A | **$z^2$/$p_z$** | a' | $z^2$ | 56.7 % | ($p_\sigma(O/N)_s$ | $p_z$ | 29.6 % | bonding analogue of MO 66A |
| 57A | **yz/π** | a'' | yz | 64.0 % | $\pi^{n.b.}$(a) | -- | -- | bonding analogue of MO 63A |
| 56A [a] | **$x^2$-$y^2$/$p_\sigma$** | a' | $x^2$-$y^2$ | 61.5 % | $p_\sigma(O/N)_s$ | -- | -- | bonding analogue of MO62A |
| 55A [a] | **$\pi_2$** | a'' | (yz) | (9.0 %) | $\pi_2$(a) | -- | -- | $\pi_2$(a), *acen* π-orbital |
| 54A [a] | **xz/π** | a' | xz | 38.9 % | $\pi_2$(s) | -- | -- | bonding analogue of MO 60A |
| **β spin** | | | | | | | | |
| 74B [a] | **$\pi_2$*** | a'' | yz | 21.5 % | $\pi_2$*(a) | -- | -- | *acen* π*-orbital, $\pi_2$*(a) |
| 73B [a] | **$\pi_2$*** | a' | -- | -- | $\pi_2$*(s) | -- | -- | *acen* π*-orbital, $\pi_2$*(s) |
| 72B | **$\pi_2$*** | a' | $z^2$ | 17.8 % | $\pi_2$*(s) | -- | -- | *acen* π*-orbital, $\pi_2$*(s) |
| 69B | **xy** | a'' | xy | 81.7 % | $p_\sigma(O/N)_a$ | -- | -- | metal d-orbital (d*xy*), antibonding |
| 68B | **xz/π*** | a' | xz | 54.7 % | $\pi_1$*(s) | -- | -- | metal d-orbital (d*xz*), antibonding |
| 67B | **yz/π*** | a'' | yz | 26.7 % | $\pi_1$*(a) | -- | -- | metal d-orbital (d*yz*), antibonding |
| 66B | **$z^2$/$p_z$** | a' | $z^2$ | 66.1 % | ($\pi^{n.b.}$(s)) | $p_z$ | 24.2 % | metal d-orbital ($dz^2$), antibonding |
| 65B | **yz/π** | a'' | yz | 73.9 % | $\pi^{n.b.}$(a) | -- | -- | metal d-orbital (d*yz*), antibonding |
| 64B | **$x^2$-$y^2$** | a' | $x^2$-$y^2$ | 76.4 % | $p_\sigma(O/N)_s$ | -- | -- | metal d-orbital ($dx^2$-$y^2$), antibonding |
| 63B | **xz/π*** | a' | xz | 61.9 % | $\pi_1$*(s) | $p_x$ | 18.3 % | metal d-orbital (d*xz*), bonding, $p_x$ antibonding |
| 62B | **$p_y$** | a'' | -- | -- | $\pi^{n.b.}$(a) | $p_y$ | 50.6 % | ligand p-orbital ($p_y$) |
| 61B | **$p_x$** | a' | xz | 17.8 % | $\pi_2$(s) | $p_x$ | 48.6 % | ligand p-orbital ($p_x$) |
| 60B | **$z^2$/$p_z$** | a' | $z^2$ | 30.7 % | $\pi^{n.b.}$(s) | $p_z$ | 33.7 % | ligand p-orbital ($p_z$), bonding analogue of MO 66B |

| | | | | | | | | |
|---|---|---|---|---|---|---|---|---|
| 59B | **$\pi$/yz** | a'' | yz | 23.7 % | $\pi^{n.b.}$(a) | $p_z$ | 13.2 % | *acen* $\pi$-orbital, $\pi^{n.b.}$(a), bonding analogue of MO 65B |
| | | | | | | $p_y$ | 10.0 % | |
| 58B | **$\pi/z^2$** | a' | $z^2$ | 13.0 % | $\pi^{n.b.}$(s) | $p_z$ | 26.2 % | *acen* $\pi$-orbital, $\pi^{n.b.}$(s), bonding analogue of MO 66B |
| | | | (yz) | (9.8 %) | | | | |
| 57B | **$p_\sigma(x^2-y^2)$** | a' | $x^2-y^2$ | 16.5 % | $p_\sigma(O/N)_s$ | -- | -- | bonding analogue of MO 64B |
| 56B [a] | **$p_\sigma$(xy)** | a'' | xy | 20.8 % | $p_\sigma(O/N)_a$ | -- | -- | bonding analogue of MO 69B |
| 55B [a] | **$\pi_2$** | a'' | -- | -- | $\pi_2$(a) | -- | -- | *acen* $\pi$-orbital |
| 54B [a] | **$\pi_2$** | a' | xz | 14.6 % | $\pi_2$(s) | -- | -- | bonding interaction |

[a] not shown in Figure 4.16

Considering the *alpha* spin orbitals, the four highest occupied molecular orbitals of the [Mn(*acen*$^{\#}$)Br] complex, 66A – 63A, are singly occupied. In accordance with the ligand field diagram (Scheme 4.1) the lowest unoccuppied molecular orbital is d*xy* (formerly d$x^2$-$y^2$, 67A). The highest occupied molecular orbital is the d$z^2$ manganese d-orbital ($z^2/p_z$, 66A). The lowest lying manganese d-orbital is d*xz* which is stabilized by the symmetric $\pi_2$ ligand orbital (xz/$\pi_2$(s), antibonding: 60A, bonding: 54A). In contrast to the conventional ligand field splitting diagram (Scheme 4.1) the d*yz* orbital is found higher in energy than d$x^2$-$y^2$ ($x^2$-$y^2/p_\sigma$, formerly d*xy*, antibonding: 62A, bonding: 56A). It interacts with the non-bonding $\pi^{n.b.}$(a) ligand orbital (yz/$\pi^{n.b.}$(a), antibonding: 63A, bonding: 57A). The $p_y$ and $p_x$ orbitals of the axial bromido ligand are found among the singly occupied *alpha* spin orbitals, antibonding to d*yz* and d*xz* (65A, 64A). The *alpha* spin orbital 55A is a pure *acen* $\pi$-orbital, $\pi_2$(a), with only a very small contribution of d*yz* and also the *alpha* spin orbital 61A can be considered as a pure non-bonding *acen* $\pi$-orbital, $\pi^{n.b.}$(s). Lower lying *alpha* spin orbitals (< 54A) predominantly exhibit *acen* ligand character. The unoccupied $\pi$*-orbitals (68A/69A, 71A - 74A) are also pure $\pi$* ligand orbitals ($\pi_1$* and $\pi_2$*) with only very small contributions of manganese d-orbitals.

The highest occupied *beta* spin orbitals are the non-bonding *acen* $\pi$-orbitals ($z^2/\pi^{n.b.}$, yz/$\pi^{n.b.}$(a), 58B, 59B), followed by the bromido p-orbitals, $p_z$, $p_y$ and $p_x$ (60B - 62B), in the bonding linear combinations with the corresponding metal d-orbitals. The *beta* spin orbital 60B on the one hand is the antibonding analogue of the $z^2/\pi^{n.b.}$ orbital (58B), on the other hand - and to a larger extent - it is a bonding $p_z/z^2$ metal-ligand hybrid orbital, i.e. the bonding analogue of MO 66B ($z^2/p_z$). As expected, the lowest unoccupied *beta* spin orbitals are the five manganese d-orbitals (63B – 69B). Compared to the *alpha* spin orbitals, of course, the same sequence of the manganese d-orbitals is also obtained among the unoccupied *beta* spin

orbitals. However, both the bonding and the antibonding linear combinations of d*xz* (65B, 67B) and d*yz* (63B, 68B) with the antisymmetric and symmetric $\pi_1$* *acen* orbitals are observed among the unoccupied *beta* spin orbitals, while the bonding equivalents of the MOs 69B (xy), 66B ($z^2/p_z$) and 64B ($x^2$-$y^2$) are found among the occupied *beta* spin orbitals.

In general, nearly no mixing of different metal or ligand orbitals occurs within the same molecular orbitals of the symmetrized complexes.

Considering the symmetry of the non-bonding *acen* π-orbitals, the antisymmetric $\pi^{n.b.}$(a) ligand orbital interacts with the d*yz* orbital (63/57A, 65/59B), while the symmetric $\pi^{n.b.}$(s) ligand orbital is combined with d$z^2$ (66/58A, 66/58B). In consequence, d*yz* ($\pi^{n.b.}$(a)) and d$z^2$ ($\pi^{n.b.}$(s)) are related manganese d-orbitals within the molecular orbitals of the [Mn(*acen*$^{(\#)}$)X] complexes.

If all these metal-ligand overlap considerations are finally transferred to the original, unsymmetrized [Mn(*acen*)X] complexes, the metal/ligand character of the individual *alpha* and *beta* spin orbitals is mainly reproduced. However, an increased mixing of different metal and/or ligand orbitals within the individual molecular orbitals is observed as the molecular symmetry is reduced from an idealized to a non-symmetrical complex. Nevertheless, the resulting molecular orbitals can still be correlated with the *alpha* and *beta* spin orbitals of the symmetrized complexes in most parts. They are described in detail again using the example of the bromido complex, [Mn(*acen*)Br] (Figure 4.17, Table 4.8). In general, formerly symmetric MOs (a') might now become antisymmetric (a'') by being intermixed with antisymmetric metal and/or ligand orbitals. This is observed for d$z^2$ (a'), which is partly mixed with d*xy* and d*yz* (a'') and combined with antisymmetric π* orbitals in the case of MO 73/74B (a'') of the unsymmetrized complex. It is also the case for the bonding d*xz*/$\pi_2$(s) orbital (a'), which is combined with the antisymmetric d*yz*/$\pi^{n.b.}$(a) orbital (a'') to result in two d*xz*/d*yz*(π) hybrid orbitals (66/67A, a'') in the case [Mn(*acen*)X]. The antibonding d*yz*/$\pi^{n.b.}$(a) *alpha* spin orbital shows more *acen* π-character than d*yz* metal d-character (70A) when compared to the idealized complex. However, the bonding analogue of the d*xy*/$p_\sigma$(O/N)$_a$ *alpha* spin orbital (74A, LUMO) shows a significant contribution of d*yz* (64A). Compared to the symmetrized complex no splitting of the d*yz*/$\pi^{n.b.}$(a) orbital is observed within the unoccupied *beta* spin

orbitals, as the corresponding antibonding equivalent of MO 72B rather exhibits $dz^2$/d*xy* character than d*yz* character (74B).

As already mentioned, d*yz* ($\pi^{n.b.}$(a)) and $dz^2$ ($\pi^{n.b.}$(s)) are related manganese d-orbitals. In the case of the unsymmetrized complexes they become a pair of nearly degenerate orbitals within the *beta* spin orbitals (72/73B, 66/67B) instead of d*yz* and d*xz* which are degenerate manganese d-orbitals in the conventional ligand field splitting diagram (Scheme 4.1).

Compared to the bromido complex a further increased mixing of metal and ligand orbitals is generally observed within the individual molecular orbitals of the other three complexes, especially for [Mn(*acen*)I] (Figure 4.18, Table 4.9) and [Mn(*acen*)Cl] (Figure 4.19, Table 4.10). The contributions of the various manganese d-orbitals differ on the exchange of the axial ligand X, but nevertheless the molecular orbitals of the iodido, chlorido and *N*CS complexes can still be identified. They are correlated with the molecular orbitals of [Mn(*acen*)Br] in Table 4.12 and the relative MO energies of the individual [Mn(*acen*)X] complexes are depicted in Figure 4.21.

Among the *alpha* spin orbitals of [Mn(*acen*)Cl] the p-orbitals of the axial chlorido ligand are mixed to give two $p_x/p_y$ hybrid orbitals (70/71A) which, in contrast to the iodido and the bromido complex, appear lower in energy than the antibonding d*yz*/$\pi^{n.b.}$(a) orbital 72A (Figure 4.19). Note that the axial displacement of the manganese ion might generally be too low throughout the calculated complex structures (*vide supra*, chapter 4.2), so that the p-orbitals of the axial ligands in fact might be even lower in energy and, as can be guessed from the corresponding *beta* spin orbitals, should with a very high probability not be expected among the singly occupied *alpha* orbitals at all. This, of course, applies to all of the three halogenido complexes. Additionally, the d*yz*/d*xy*/$p_\sigma$ (65A) and the bonding $z^2/p_z$ orbitals (64A) are also calculated to be inverted in energy in the case of [Mn(*acen*)Cl] (Figure 4.19).

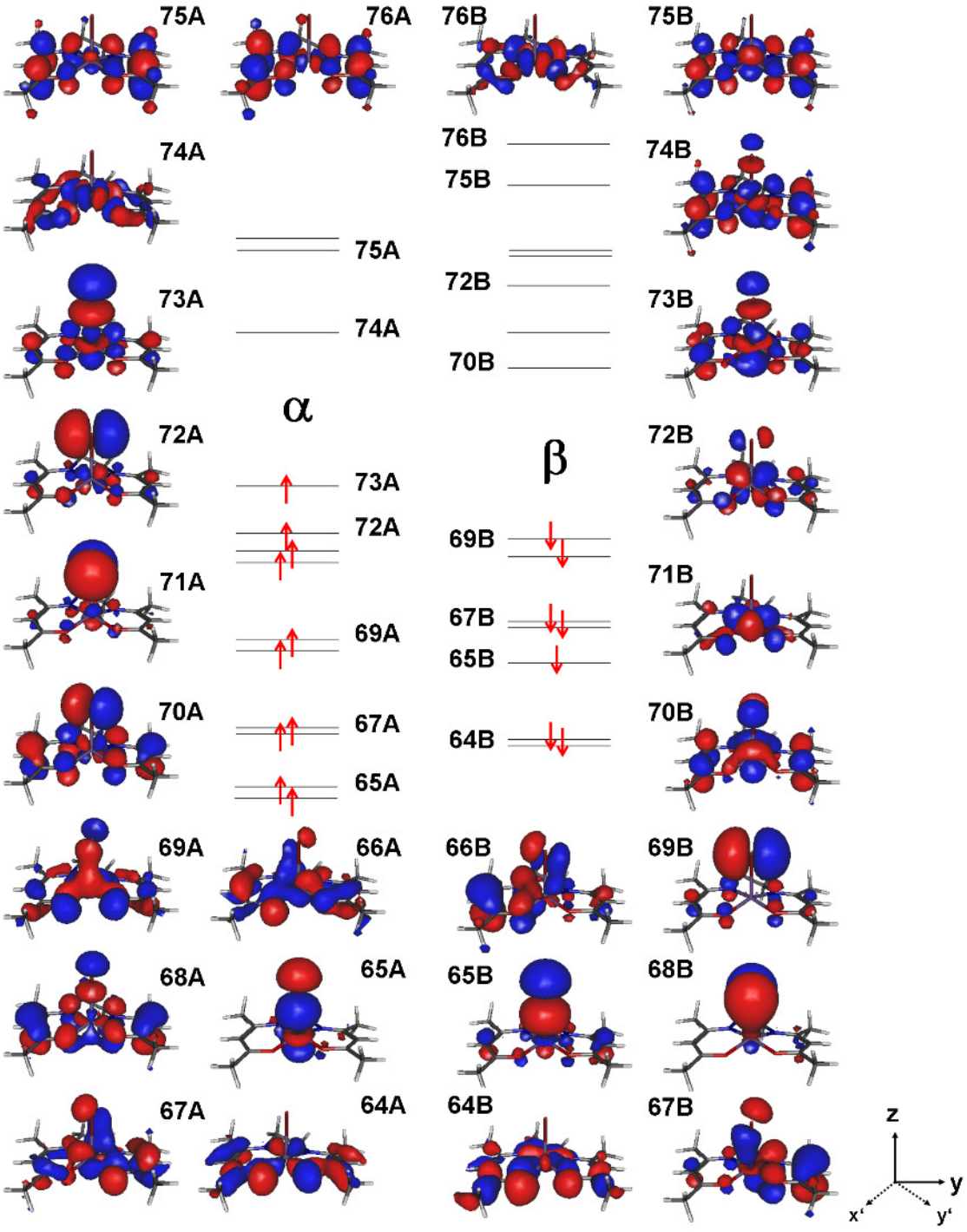


**Figure 4.17.** Molecular orbitals of [Mn(*acen*)Br] (BP86/LANL2DZ).

**Table 4.8.** Molecular orbitals of [Mn(*acen*)Br] (BP86/LANL2DZ). Only atomic orbital contributions greater than 10 % are listed.

| **α spin** | | **sym. ($C_S$)** | **$Mn^{3+}$** | | ***acen*$^{2-}$** | **axial ligand ($Br^-$)** | | **description** |
|---|---|---|---|---|---|---|---|---|
| 81A [a] | **$\pi_2$*** | a'' | -- | -- | $\pi_2$*(a) | -- | -- | *acen* π*-orbital, $\pi_2$*(a) |
| 80A [a] | **$\pi_2$*** | a' | -- | -- | $\pi_2$*(s) | -- | -- | *acen* π*-orbital, $\pi_2$*(s) |
| 79A | **$\pi_1$*** | a' | ($z^2$) | (9.1 %) | $\pi_2$*(s) | -- | -- | *acen* π*-orbital, $\pi_2$*(s) |
| 76A | **$\pi_1$*** | a'' | xy | 27.8 % | $\pi_1$*(a) | -- | -- | *acen* π*-orbital, $\pi_1$*(a) |
| 75A | **$\pi_1$*** | a' | xz | 19.8 % | $\pi_1$*(s) | -- | -- | *acen* π*-orbital, $\pi_1$*(s) |
| 74A | **xy** | a'' | xy | 70.0 % | $p_\sigma(O/N)_a$ | -- | -- | metal d-orbital (d*xy*), antibonding, LUMO |
| 73A | **$z^2/p_z$** | a' | $z^2$ | 56.6 % | -- | $p_z$ | 37.4 % | metal d-orbital (d$z^2$), antibonding, HOMO |
| 72A | **$p_y$** | a'' | yz | 37.3 % | $\pi^{n.b.}$(a) | $p_y$ | 44.7 % | ligand p-orbital ($p_y$) |
| 71A | **$p_x$** | a' | xz | 24.1 % | $\pi^{n.b.}$(s) | $p_x$ | 49.0 % | ligand p-orbital ($p_x$) |
| 70A | **yz/π** | a'' | yz | 26.4 % | $\pi^{n.b.}$(a) | $p_y$ | 25,5 % | metal d-orbital (d*yz*), antibonding |
| 69A | **$x^2$-$y^2$/$p_\sigma$** | a' | $x^2$-$y^2$ | 43.0 % | $p_\sigma(O/N)_s$ | $p_x$ | 11,00% | metal d-orbital (d$x^2$-$y^2$), antibonding |
| | | | xz | 26.2 % | | -- | -- | |
| 68A | **$\pi^{n.b.}$** | a' | $z^2$ | 13.8 % | $\pi^{n.b.}$(s) | $p_z$ | 16.4 % | non-bonding *acen* π-orbital, $\pi^{n.b.}$(s) |
| | | | $x^2$-$y^2$ | 13.6 % | | | | |
| 67A | **xz/yz(π)** | a'' | xz | 47.6 % | $\pi_2$(s) | -- | -- | xz/yz, mixed metal d-orbital |
| | | | yz | 33.3 % | $p_\sigma(O, N)_a$ | -- | -- | |
| 66A | **xz/yz(π)** | a'' | xz | 44.8 % | $\pi_2$(s) | -- | -- | xz/yz, mixed metal d-orbital |
| | | | yz | 36.5 % | $p_\sigma(O, N)_a$ | -- | -- | |
| 65A | **$z^2/p_z$** | a' | $z^2$ | 60.9 % | -- | $p_z$ | 28.6 % | bonding analogue of 73A |
| 64A | **$yz/xy/p_{acen}$** | a'' | yz | 46.4 % | $\pi^{n.b.}$(a) | -- | -- | (bonding analogue of 70A) |
| | | | xy | 21.0 % | $p_\sigma(O/N)_a$ | | | |
| 63A [a] | **$x^2$-$y^2$/$p_\sigma$** | a' | $x^2$-$y^2$ | 62.4 % | $p_\sigma(O/N)_s$ | -- | -- | bonding analogue of 69A |
| 62A [a] | **$\pi_2$** | a'' | yz | 11.6 % | $\pi_2$(a) | -- | -- | *acen* π-orbital |
| **β spin** | | | | | | | | |
| 81B [a] | **$\pi_2$*** | a'' | yz | 13.4 % | $\pi_2$*(a) | -- | -- | *acen* π*-orbital, $\pi_2$*(a) |
| 80B [a] | **$\pi_2$*** | a' | -- | -- | $\pi_2$*(s) | -- | -- | *acen* π*-orbital, $\pi_2$*(a) |
| 79B | **$\pi_2$*** | a' | $z^2$ | 15.1 % | $\pi_2$*(s) | -- | -- | *acen* π*-orbital, $\pi_2$*(a) |
| 76B | **xy** | | xy | 77.5 % | $p_\sigma(O/N)_a$ | -- | -- | metal d-orbital (d*xy*), antibonding |
| 75B | **xz/π*** | a' | xz | 55.5 % | $\pi_1$*(s) | -- | -- | metal d-orbital (d*xz*), antibonding |
| 74B | **$z^2$/xy($\pi_1$*)** | a'' | $z^2$ | 41.7 % | $\pi_1$*(a) | $p_z$ | 12.2 % | partly bonding/antibonding interaction |
| | | | xy | 21.1 % | | | | |
| 73B | **$z^2/p_z$** | a'' | $z^2$ | 61.3 % | $\pi_1$*(a) | $p_z$ | 18.5 % | antibonding interaction, formerly symmetric metal d-orbital combined with antisymmetric π*-orbital |
| | | | xy | 16.6 % | | | | |
| | | | yz | 11.9 % | | | | |
| | | | $x^2$-$y^2$ | 11.3 % | | | | |
| 72B | **yz** | a'' | yz | 78.3 % | $\pi^{n.b.}$(a) | $p_y$ | 11.4 % | metal d-orbital (d*yz*), antibonding |
| 71B | **$x^2$-$y^2$/$p_\sigma$** | a' | $x^2$-$y^2$ | 79.9 % | $p_\sigma(O/N)_s$ | -- | -- | metal d-orbital (d$x^2$-$y^2$), antibonding |

| | | | | | | | | |
|---|---|---|---|---|---|---|---|---|
| | | | ($z^2$) | (9.2 %) | | | | |
| 70B | **xz/π*** | a' | xz | 60.8 % | $\pi_1$*(s) | $p_x$ | 15.2 % | metal d-orbital (d*xz*), π-bonding, $p_x$: antibonding |
| | | | $x^2$-$y^2$ | 10.2 % | | | | |
| 69B | **$p_y$** | a'' | -- | — | $\pi^{n.b.}$(a) | $p_y$ | 48.5 % | ligand p-orbital ($p_y$) |
| 68B | **$p_x$** | a' | xz | 16.4 % | $\pi_1$*(s) | $p_x$ | 49.6 % | ligand p-orbital ($p_x$) |
| 67B | **π/$z^2$** | a' | $z^2$ | 21.0 % | $\pi^{n.b.}$(s) | $p_z$ | 15.4 % | *acen* π-orbital, $\pi^{n.b.}$(s), bonding analogue of MO 73B |
| | | | (yz) | (9.7 %) | | -- | -- | |
| 66B | **π/yz** | a'' | yz | 19.5 % | $\pi^{n.b.}$(a) | $p_y$ | 14.5 % | *acen* π-orbital, $\pi^{n.b.}$(a), bonding analogue of MO 72B |
| | | | ($z^2$) | (9.5 %) | | -- | -- | |
| 65B | **$p_z$/$z^2$** | a' | $z^2$ | 21.7 % | $\pi^{n.b.}$(s) | $p_z$ | 42.7 % | bonding analogue of MO 73B, ligand p-orbital ($p_z$) |
| 64B | **$p_\sigma$($x^2$-$y^2$)** | a' | $x^2$-$y^2$ | 17.7 % | $p_\sigma(O/N)_s$ | -- | -- | bonding analogue of MO 71B |
| 63B [a] | **$p_\sigma$(xy)** | a'' | xy | 20.7 % | $p_\sigma(O/N)_a$ | -- | -- | bonding analogue of MO 73B |
| 62B [a] | **$\pi_2$** | a'' | -- | -- | $\pi_2$(a) | -- | -- | *acen* π-orbital |

[a] not shown in Figure 4.17

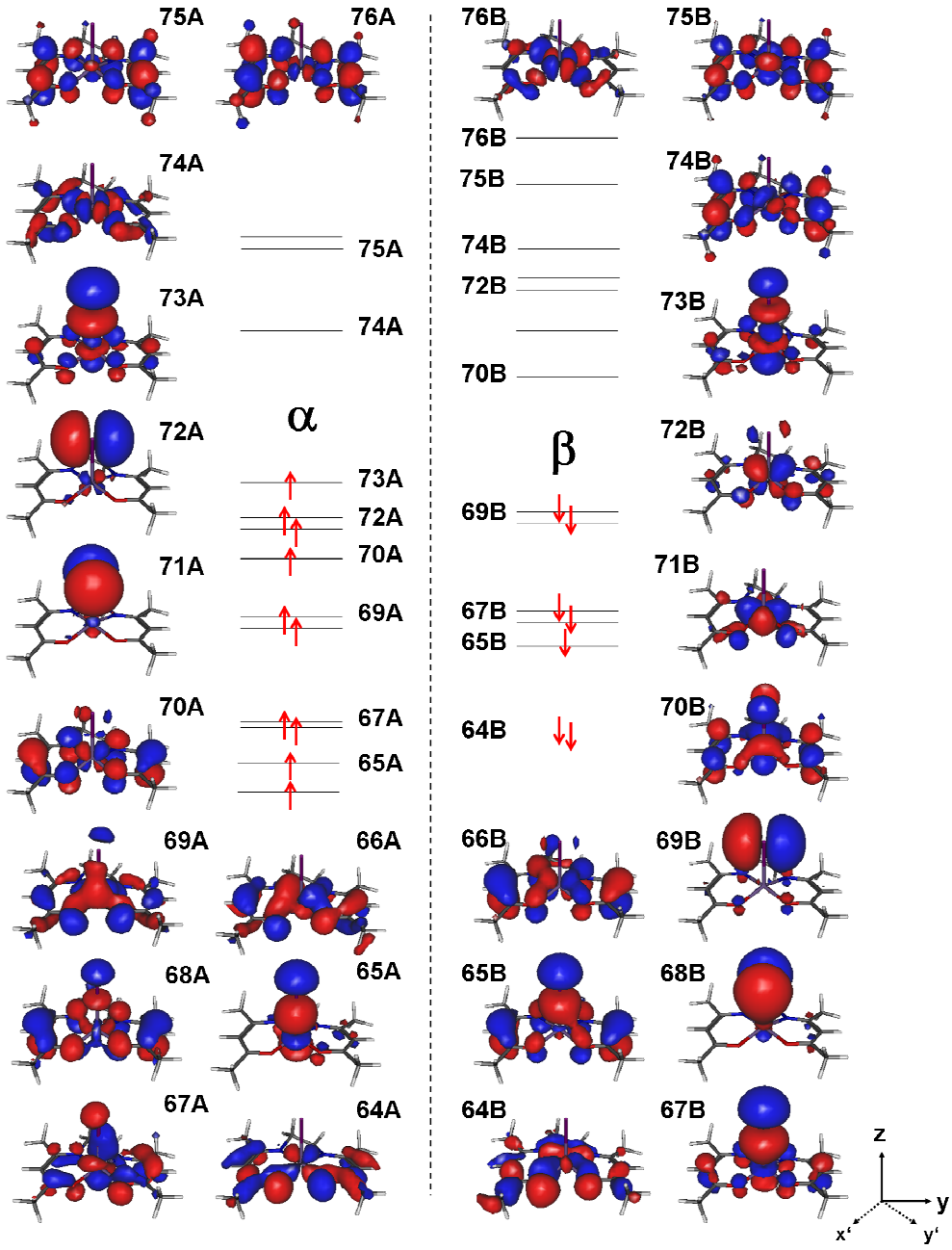


**Figure 4.18.** Molecular orbitals of [Mn(*acen*)I] (BP86/LANL2DZ).

**Table 4.9.** Molecular orbitals of [Mn(*acen*)I] (BP86/LANL2DZ). Only atomic orbital contributions greater than 10 % are listed.

| α spin | | sym. ($C_S$) | $Mn^{3+}$ | | *acen*$^{2-}$ | axial ligand ($I^-$) | | description |
|---|---|---|---|---|---|---|---|---|
| 81A [a] | $\pi_2$* | a'' | -- | -- | $\pi_2$*(a) | -- | -- | *acen* π*-orbital, $\pi_2$*(a) |
| 80A [a] | $\pi_2$* | a' | -- | -- | $\pi_2$*(s) | -- | -- | *acen* π*-orbital, $\pi_2$*(s) |
| 79A | $\pi_2$* | a' | -- | -- | $\pi_2$*(s) | -- | -- | *acen* π*-orbital, $\pi_2$*(s) |
| 76A | $\pi_1$* | a'' | xy | 26.8 % | $\pi_1$*(a) | -- | -- | *acen* π*-orbital, $\pi_1$*(a) (antibonding interaction) |
| | | | yz | 22.3 % | | | | |
| 75A | $\pi_1$* | a' | xz | 16.5 % | $\pi_1$*(s) | -- | -- | *acen* π*-orbital, $\pi_1$*(s) (antibonding interaction) |

| | | | | | | | | |
|---|---|---|---|---|---|---|---|---|
| | | | ($z^2$) | (9.5 %) | | | | |
| 74A | **xy** | a'' | xy | 66.1 % | $p_\sigma(O/N)_a$ | -- | -- | metal d-orbital (d*xy*), antibonding, LUMO |
| | | | yz | 23.2 % | | | | |
| 73A | **$z^2/p_z$** | a' | $z^2$ | 42.5 % | $\pi^{n.b.}(s)$ | $p_z$ | 38.8 % | metal d-orbital (d$z^2$), antibonding, HOMO |
| | | | xz | 22.5 % | | $p_x$ | 11.9 % | |
| 72A | **$p_y$(yz)** | a'' | yz | 20.8 % | -- | $p_y$ | 50.9 % | ligand p-orbital ($p_y$) |
| 71A | **$p_x$(xz)** | a' | xz | 14.3 % | -- | $p_x$ | 49.3 % | ligand p-orbital ($p_x$) |
| | | | | | | $p_z$ | 14.9 % | |
| 70A | **yz/π** | a'' | yz | 37.2 % | $\pi^{n.b.}(a)$ | $p_y$ | 9.9 % | metal d-orbital (dy*z*), antibonding |
| | | | $x^2$-$y^2$ | 13.5 % | | | | |
| 69A | **$x^2$-$y^2$/$p_\sigma$** | a' | $x^2$-$y^2$ | 46.6 % | $p_\sigma(O/N)_s$ | $p_z$ | 11.8 % | metal d-orbital (d$x^2$-$y^2$), antibonding |
| | | | xz | 14.4 % | | | | |
| | | | $z^2$ | 12.0 % | | | | |
| 68A | **$\pi^{n.b.}$** | a' | $x^2$-$y^2$ | 20.6 % | $\pi^{n.b.}(s)$ | $p_z$ | 14.3 % | non-bonding *acen* π-orbital, $\pi^{n.b.}(s)$ |
| 67A | **xz/yz(π)** | a'' | xz | 49.1 % | $\pi_2(s)$ | ($p_z$) | (9.0 %) | xz/yz hybrid orbital |
| | | | $z^2$ | 43.9 % | $p_\sigma(O, N)_a$ | | | |
| | | | yz | 17.7 % | | | | |
| | | | $x^2$-$y^2$ | 10.8 % | | | | |
| 66A | **xz/yz(π)** | a'' | yz | 41.7 % | $\pi_2(s)$ | -- | -- | xz/yz hybrid orbital |
| | | | xy | 27.0 % | $p_\sigma(O, N)_a$ | | | |
| | | | xz | 21.6 % | | | | |
| | | | $z^2$ | 16.0 % | | | | |
| 65A | **$z^2/p_z$** | a' | $z^2$ | 45.3 % | -- | $p_z$ | 23.3 % | bonding analogue of 73A |
| | | | xz | 50.8 % | | | | |
| 64A | **yz(xy)/$p_{acen}$** | a'' | yz | 49.5 % | $\pi^{n.b.}(a)$ | -- | -- | bonding interaction |
| | | | | | $p_\sigma(O/N)_a$ | | | |
| 63A [a] | **$x^2$-$y^2$/$p_\sigma$** | a' | $x^2$-$y^2$ | 62.1 % | $p_\sigma(O/N)_s$ | -- | -- | bonding analogue of 69A |
| | | | xz | 10.7 % | | | | |
| 62A [a] | **$\pi_2$** | a'' | yz | 11.0 % | $\pi_2(a)$ | -- | -- | *acen* π-orbital |
| **β spin** | | | | | | | | |
| 81B [a] | **$\pi_2$*** | a'' | yz | 12.4 % | $\pi_2$*(a) | -- | -- | *acen* π*-orbital, $\pi_2$*(a) |
| 80B [a] | **$\pi_2$*** | a' | -- | -- | $\pi_2$*(s) | -- | -- | *acen* π*-orbital, $\pi_2$*(s) |
| 79B | **$\pi_2$*** | a' | $z^2$ | 10.7 % | $\pi_2$*(s) | -- | -- | *acen* π*-orbital, $\pi_2$*(s) |
| | | | (xz) | (9.2 %) | | | | |
| 76B | **xy** | a'' | xy | 72.8 % | $p_\sigma(O/N)_a$ | -- | -- | metal d-orbital (d*xy*), antibonding |
| | | | yz | 28.2 % | | | | |
| 75B | **xz/π*** | a' | xz | 43.5 % | $\pi_1$*(s) | -- | -- | metal d-orbital (d*xz*), antibonding |
| | | | $z^2$ | 28.8 % | | | | |
| | | | $x^2$-$y^2$ | 18.8 % | | | | |
| 74B | **$z^2$/xy(π*)** | a'' | xy | 25.5 % | $\pi_1$*(a) | -- | -- | partly bonding/antibonding interaction |

| | | | | | | | | |
|---|---|---|---|---|---|---|---|---|
| | | | $z^2$ | 20.3 % | | | | |
| | | | xz | 11.0 % | | | | |
| 73B | **$z^2$** | (a') | $z^2$ | 61.0 % | $\pi^{n.b.}$(s) | $p_z$ | 21.0 % | metal d-orbital ($dz^2$), antibonding |
| | | | xz | 30.2 % | | | | |
| | | | $x^2$-$y^2$ | 16.6 % | | | | |
| | | | xy | 12.4 % | | | | |
| 72B | **yz** | a'' | yz | 74.4 % | $\pi^{n.b.}$(a) | $p_y$ | 10.3 % | metal d-orbital (d*yz*), antibonding |
| | | | xy | 23.8 % | | | | |
| 71B | **$x^2$-$y^2$** | a' | $x^2$-$y^2$ | 76.7 % | $p_\sigma(O/N)_s$ | -- | -- | metal d-orbital ($dx^2$-$y^2$), antibonding |
| | | | xz | 23.6 5 | | | | |
| 70B | **xz/π*** | a' | xz | 54.0 % | $\pi_1$*(s) | $p_x$ | 14.8 % | metal d-orbital (d*xz*), bonding, $p_x$: antibonding |
| | | | $z^2$ | 28.9 % | | | | |
| 69B | **$p_y$** | a'' | -- | -- | $\pi^{n.b.}$(a) | $p_y$ | 50.6 % | ligand p-orbital ($p_y$) |
| 68B | **$p_x$** | a' | xz | 13.9 % | $\pi_1$*(s) | $p_x$ | 47.9 % | ligand p-orbital ($p_x$) |
| | | | | | | $p_z$ | 14.5 % | |
| 67B | **$p_z/z^2$** | a' | $z^2$ | 27.8 % | $\pi^{n.b.}$(s) | $p_z$ | 36.6 % | *acen* π-orbital, $\pi^{n.b.}$(s), bonding analogue of MO 73B |
| | | | xz | 17.1 % | | $p_x$ | 10.1 % | |
| 66B | **π/yz** | a'' | yz | 19.9 % | $\pi^{n.b.}$(a) | ($p_y$) | (9.9 %) | *acen* π-orbital, $\pi^{n.b.}$(a), bonding analogue of MO 72B |
| 65B | **π/($z^2$)/$p_z$** | a' | ($z^2$) | -- | $\pi^{n.b.}$(s) | $p_z$ | 24.6 % | ligand p-orbital ($p_z$), bonding analogue of MO 73B |
| 64B | **$p_\sigma$($x^2$-$y^2$)** | a' | $x^2$-$y^2$ | 19.3 % | $p_\sigma(O/N)_s$ | -- | -- | bonding analogue of MO 71B |
| 63B [a] | **$p_\sigma$(xy)** | a'' | xy | 16.9 % | $p_\sigma(O/N)_a$ | -- | -- | bonding analogue of MO 79B |
| | | | yz | 13.4 % | | | | |
| 62B [a] | **$\pi_2$** | a'' | -- | -- | $\pi_2$(a) | -- | -- | *acen* π-orbital |

[a] not shown in Figure 4.18

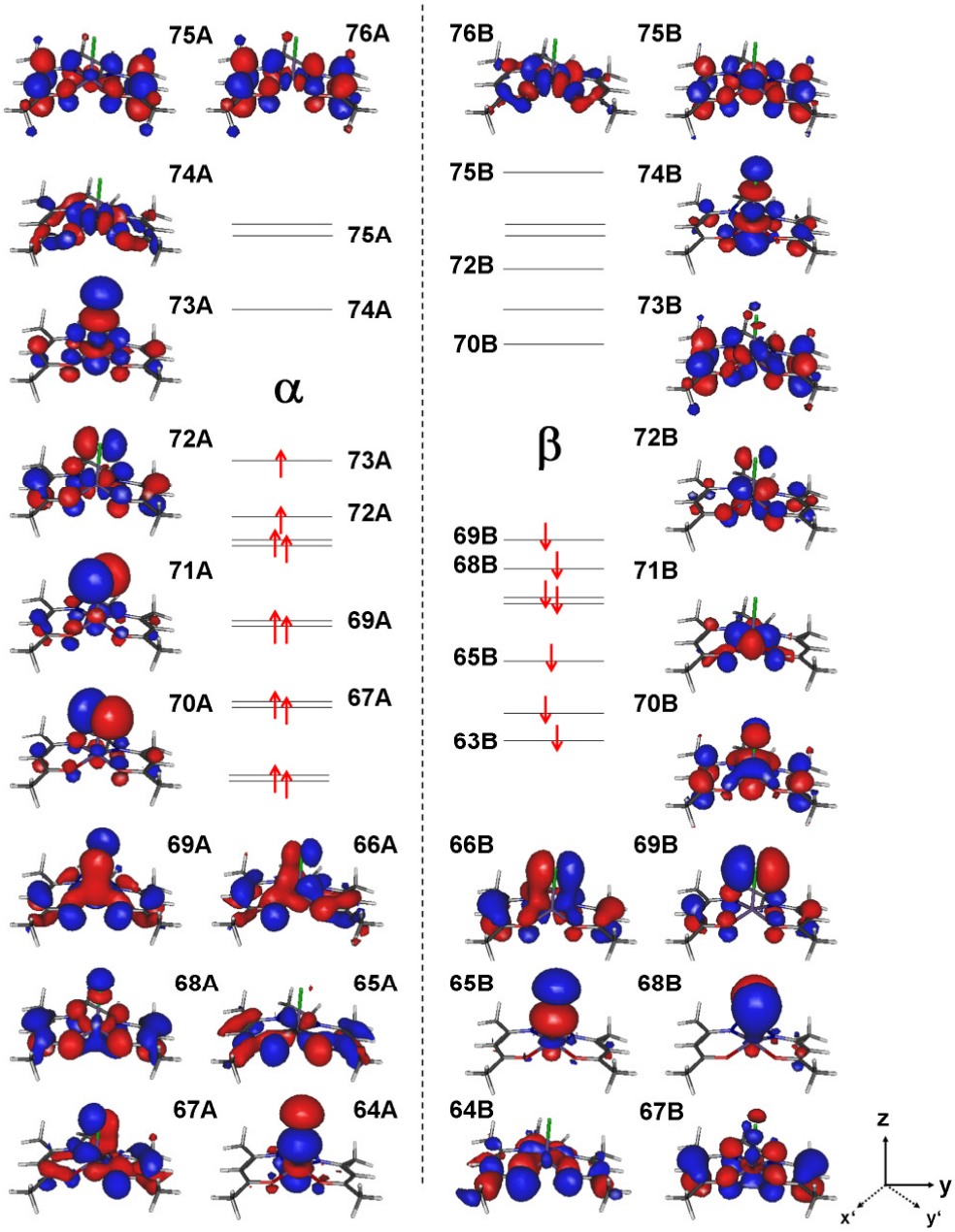


**Figure 4.19.** Molecular orbitals of [Mn(*acen*)Cl] (BP86/LANL2DZ).

**Table 4.10.** Molecular orbitals of [Mn(*acen*)Cl] (BP86/LANL2DZ). Only atomic orbital contributions greater than 10 % are listed.

| α spin | | sym. ($C_S$) | $Mn^{3+}$ | | *acen*$^{2-}$ | axial ligand ($Cl^-$) | | description |
|---|---|---|---|---|---|---|---|---|
| 81A [a] | $\pi_2$* | a'' | -- | -- | $\pi_2$*(a) | -- | -- | *acen* π*-orbital, $\pi_2$*(a) |
| 80A [a] | $\pi_2$* | a' | -- | -- | $\pi_2$*(s) | -- | -- | *acen* π*-orbital, $\pi_2$*(s) |
| 79A | $\pi_2$* | a' | ($z^2$) | (9.8 %) | $\pi_2$*(s) | -- | -- | *acen* π*-orbital, $\pi_2$*(s) |
| 76A | $\pi_1$* | a'' | xy | 26.6 % | $\pi_1$*(a) | -- | -- | *acen* π*-orbital, $\pi_1$*(s) |
| 75A | $\pi_1$* | a' | yz | 20.0 % | $\pi_1$*(s) | -- | -- | *acen* π*-orbital, $\pi_1$*(s) |
| 74A | xy | a'' | xy | 70.5 % | $p_\sigma(O/N)_a$ | -- | -- | metal d-orbital (d*xy*), antibonding, LUMO |
| 73A | $z^2/p_z$ | a' | $Z^2$ | 56.2 % | $\pi^{n.b.}$(s) | $p_z$ | 33.5 % | metal d-orbital ($dz^2$), antibonding, HOMO |

| | | | | | | | | |
|---|---|---|---|---|---|---|---|---|
| 72A | **yz/π** | a'' | yz | 48.9 % | $\pi^{n.b.}$(a) | $p_y$ | 21.2 % | metal d-orbital (d*yz*), antibonding |
| 71A | **$p_x$/$p_y$** | a' | xz | 29.4 % | -- | $p_x$ | 36.7 % | ligand p-orbital ($p_x$) |
| | | | | | | $p_y$ | 24.8 % | |
| 70A | **$p_y$/$p_x$** | a'' | xz | 19.4 % | $\pi^{n.b.}$(a) | $p_y$ | 36.1 % | ligand p-orbital ($p_y$) |
| | | | | | | $p_x$ | 28.0 % | |
| 69A | **$x^2$-$y^2$/$p_\sigma$** | a' | $x^2$-$y^2$ | 34.8 % | $p_\sigma(O/N)_s$ | $p_x$ | 17.1 % | metal d-orbital (d$x^2$-$y^2$), antibonding |
| | | | xz | 23.0 % | | $p_z$ | 10.2 % | |
| | | | ($z^2$) | (9.5 %) | | | | |
| 68A | **$\pi^{n.b.}$** | a' | $x^2$-$y^2$ | 25.2 % | $\pi^{n.b.}$(s) | $p_z$ | 11.8 % | non-bonding *acen* π orbital, $\pi^{n.b.}$(s) |
| | | | $z^2$ | 16.3 % | | | | |
| 67A | **xz/yz(π)** | a'' | xz | 47.3 % | $\pi_2$(s) | $p_x$ | 10.0 % | xz/yz hybrid metal d-orbital |
| | | | yz | 28.1 % | $p_\sigma(O, N)_a$ | ($p_y$) | (9.7 %) | |
| | | | $x^2$-$y^2$ | 26.6 % | | | | |
| 66A | **xz/yz(π)** | a'' | xz | 39.3 % | $\pi_2$(s) | $p_y$ | 10.3 % | xz/yz hybrid metal d-orbital |
| | | | yz | 36.7 % | $p_\sigma(O, N)_a$ | | | |
| | | | $x^2$-$y^2$ | 16.2 % | | | | |
| | | | xy | 12.2 % | | | | |
| 65A | **yz/xy/$p_\sigma$** | a'' | yz | 46.4 % | $\pi^{n.b.}$(a) | -- | -- | (bonding analogue of 74A) |
| | | | xy | 22. % | $p_\sigma(O/N)_a$ | | | |
| 64A | **$z^2$/$p_z$** | a'' | $z^2$ | 55.4 % | $\pi^{n.b.}$(a) | $p_z$ | 31.9 % | bonding analogue of 73A |
| | | | | | $p_\sigma(O/N)_a$ | | | |
| 63A [a] | **$x^2$-$y^2$/$p_\sigma$** | a' | $x^2$-$y^2$ | 60.4 % | $p_\sigma(O/N)_s$ | -- | -- | bonding analogue of 69A |
| | | | (xz) | (9.6 %) | | | | |
| 62A [a] | **$\pi_2$** | a'' | $x^2$-$y^2$ | 17.9 % | $\pi_2$(a) | -- | -- | *acen* π orbital |
| | | | $z^2$ | 14.2 % | | | | |
| | | | (yz) | (9.0 %) | | | | |
| **β spin** | | | | | | | | |
| 81B [a] | **$\pi_2$*** | a'' | yz | 13.7 % | $\pi_2$*(a) | -- | -- | *acen* π* orbital, $\pi_2$*(a) |
| 80B [a] | **$\pi_2$*** | a' | -- | -- | $\pi_2$*(s) | -- | -- | *acen* π* orbital, $\pi_2$*(s) |
| 79B | **$\pi_2$*** | a' | $z^2$ | 17.6 % | $\pi_2$*(s) | -- | -- | *acen* π* orbital, $\pi_2$*(s) |
| 76B | **xy** | a'' | xy | 78.8 % | $p_\sigma(O/N)_a$ | -- | -- | metal d-orbital (d*xy*), antibonding |
| 75B | **xz/π*** | a' | xz | 58.0 % | $\pi_1$*(s) | -- | -- | metal d-orbital (d*xz*), antibonding |
| 74B | **$z^2$** | a'' | $z^2$ | 70.1 % | $\pi^{n.b.}$(s) | $p_z$ | 19.3 % | metal d-orbital (d$z^2$), antibonding |
| 73B | **$z^2$/xy/yz(π*)** | a'' | $z^2$ | 23.9 % | $\pi_1$*(a) | -- | -- | antibonding interaction |
| | | | xy | 21.8 % | | | | |
| | | | yz | 21.7 % | | | | |
| 72B | **yz** | a'' | yz | 76.8 % | $\pi^{n.b.}$(a) | $p_y$ | 11.7 % | metal d-orbital (d*yz*), antibonding |
| 71B | **$x^2$-$y^2$** | a' | $x^2$-$y^2$ | 80.0 % | $p_\sigma(O/N)_s$ | -- | -- | metal d-orbital (d$x^2$-$y^2$), antibonding |
| 70B | **xz/π*** | a' | xz | 58.1 % | $\pi_1$*(s) | $p_x$ | 14.8 % | metal d-orbital (d$x^z$), bonding, $p_x$: antibonding |
| | | | $x^2$-$y^2$ | 11.9 % | | | | |

| | | | | | | | | |
|---|---|---|---|---|---|---|---|---|
| 69B | $\mathbf{p_y}$ | a'' | -- | -- | $\pi^{n.b.}$(a) | $p_y$ | 41.9 % | ligand p orbital ($p_y$) |
| 68B | $\mathbf{p_x}$ | a' | xz | 16.0 % | ($\pi_1$*(s)?) | $p_x$ | 47.4 % | ligand p orbital ($p_x$) |
| 67B | $\boldsymbol{\pi/z^2}$ | a' | $z^2$ | 17.0 % | $\pi^{n.b.}$(s) | -- | -- | *acen* π-orbital, $\pi^{n.b.}$(s), bonding analogue of MO 74BB |
| 66B | $\boldsymbol{\pi/yz(p_y)}$ | a'' | yz | 23.3 % | $\pi^{n.b.}$(a) | $p_y$ | 25.9 % | *acen* π-orbital, $\pi^{n.b.}$(a), bonding analogue of MO 72B |
| 65B | $\mathbf{p_z/z^2}$ | a' | $z^2$ | 24.8 % | $\pi^{n.b.}$(s) | $p_z$ | 44.2 % | ligand p-orbital ($p_z$), bonding analogue of MO 66B |
| 64B | $\boldsymbol{p_\sigma(x^2\text{-}y^2)}$ | a' | $x^2$-$y^2$ | 16.4 % | $p_\sigma(O/N)_s$ | -- | -- | bonding analogue of MO 71B |
| 63B [a] | $\boldsymbol{p_\sigma(xy)}$ | a'' | xy | 20.5 % | $p_\sigma(O/N)_a$ | -- | -- | bonding analogue of MO 79B |
| 62B [a] | $\boldsymbol{\pi_2}$ | a'' | -- | -- | $\pi_2$(a) | -- | -- | *acen* π-orbital |

[a] not shown in Figure 4.19

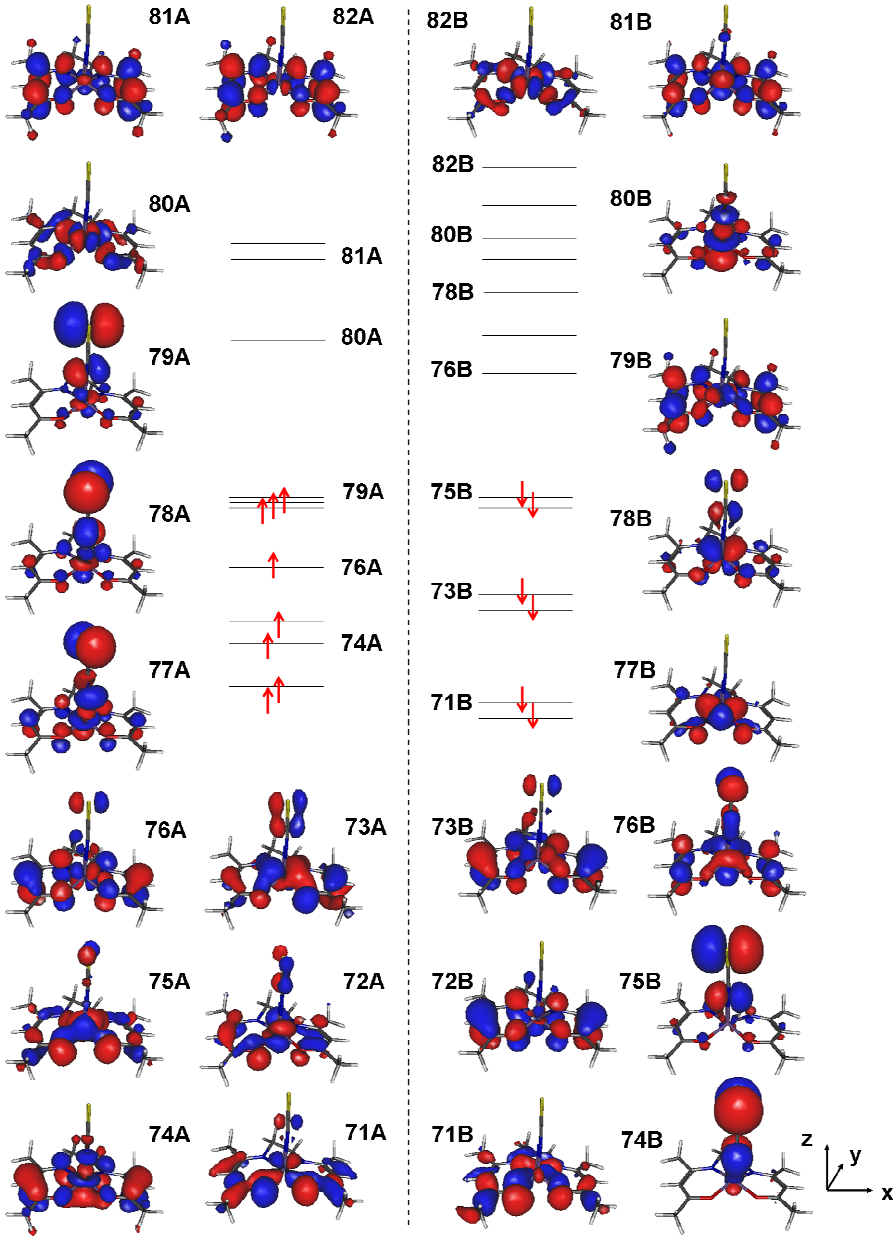


**Figure 4.20.** Molecular orbitals of [Mn(*acen*)NCS] (BP86/LANL2DZ).

**Table 4.11.** Molecular orbitals of [Mn(*acen*)NCS] (BP86/LANL2DZ). Only atomic orbital contributions greater than 10 % are listed.

| α spin | | sym. ($C_S$) | $Mn^{3+}$ | | *acen*$^{2-}$ | axial ligand ($SCN^-$) | | description |
|---|---|---|---|---|---|---|---|---|
| 89A [a] | $\pi_2$* | a' | -- | -- | $\pi_2$*(s) | $p_y$(N) | 23.4 % | *acen* π*-orbital, $\pi_2$*(a), $p_y(NCS)_a$ |
| | | | | | | $p_y$(C) | 31.0 % | |
| | | | | | | $p_y$(S) | 10.3 % | |
| 88A [a] | $\pi_2$* | a'' | yz | 13.9 % | $\pi_2$*(a) | $p_y$(N) | 39.9 % | *acen* π*-orbital, $\pi_2$*(a), $p_y(NCS)_a$ |
| | | | | | | $p_y$(C) | 53.2 % | |
| | | | | | | $p_y$(S) | 18.8 % | |
| 87A [a] | $\pi_2$* | a' | -- | -- | $\pi_2$*(s) | $p_x$(N) | 28.8 % | *acen* π*-orbital, $\pi_2$*(s), $p_x(NCS)_a$ |

| | | | | | | | | |
|---|---|---|---|---|---|---|---|---|
| | | | | | | $p_x$(C) | 40.4 % | |
| | | | | | | $p_x$(S) | 13.8 % | |
| 86A [a] | **$\pi_2$*** | a' | | -- | $\pi_2$*(s) | $p_x$(N) | 32.5 % | *acen* π*-orbital, $\pi_2$*(s), $p_x(NCS)_a$ + ~9 % $p_y$ (N, C) |
| | | | | | | $p_x$(C) | 43.0 % | |
| | | | | | | $p_x$(S) | 15.7 % | |
| 82A | **$\pi_1$*** | a'' | xy | 23.0 % | $\pi_1$*(a) | -- | -- | *acen* π*-orbital, $\pi_1$*(a) (antibonding) |
| 81A | **$\pi_1$*** | a' | xz | 18.0 % | $\pi_1$*(s) | -- | -- | *acen* π*-orbital, $\pi_1$*(a) (antibonding) |
| 80A | **xy** | a'' | xy | 68.8 % | $p_\sigma(O/N)_a$ | -- | -- | metal d-orbital (d*xy*), antibonding, LUMO |
| | | | yz | 15.5 % | | | | |
| 79A | **$p_y$/yz** | a'' | yz | 24.2 % | $\pi^{n.b.}$(s) | $p_y$(N) | 34.1 % | metal-ligand hybrid orbital, antibonding ($p_y$ non-bonding), HOMO |
| | | | $z^2$ | 19.1 % | | $p_y$(S) | 42.2 % | |
| | | | (xz) | (9.6 %) | | | | |
| 78A | **$p_x$/$z^2$** | a' | $z^2$ | 34.7 % | $\pi^{n.b.}$(s) | $p_x$(N) | 31.4 % | metal ligand hybrid orbital, antibonding ($p_x$ non-bonding) |
| | | | $x^2$-$y^2$ | 21.4 % | | $p_x$(S) | 36.6 % | |
| 77A | **$z^2$/$p_z$** | a' | $z^2$ | 40.6 % | $\pi^{n.b.}$(s) | $p_x$(N) | 19.3 % | metal-ligand hybrid orbital, antibonding interaction |
| | | | xz | 27.3 % | | $p_z$(N) | 17.8 % | |
| | | | | | | $p_y$(N) | 11.4 % | |
| | | | | | | $p_x$(S) | 27.0 % | |
| | | | | | | $p_y$(S) | 13.0 % | |
| 76A | **yz/π** | a'' | yz | 36.3 % | $\pi^{n.b.}$(a) | ($p_y$(N)) | (8.2 %) | non-bonding *acen* π–orbital/ metal d-orbital (dyz), antibonding |
| | | | xy | 10.3 % | | $p_y$(S) | 11.2 % | |
| 75A | **$x^2$-$y^2$/$p_\sigma$** | a' | $x^2$-$y^2$ | 48.3 % | $p_\sigma(O/N)_s$ | ($p_x$(S)) | (9.4 %) | metal d-orbital (d$x^2$-$y^2$), antibonding |
| | | | xz | 20.8% | | | | |
| 74A | **$\pi^{n.b.}$/$z^2$** | a' | $z^2$ | 37.4 % | $\pi^{n.b.}$(s) | ($p_z$(N)) | (9.2 %) | non-bonding *acen* π-orbital, $\pi^{n.b.}$(s) |
| | | | $x^2$-$y^2$ | 14.2 % | | | | |
| 73A | **yz/π** | a'' | yz | 46.4 % | $\pi_2$(s) | $p_y$(C) | 14.4 % | bonding analogue of 76A |
| | | | xy | 21.4 % | $p_\sigma(O, N)_a$ | $p_y$(S) | 10.4 % | |
| | | | xz | 17.2 % | | | | |
| 72A | **xz/π** | a' | xz | 67.4 % | $\pi_2$(s) | $p_x$(C) | 11.9 % | metal d-orbital (d*xz*), bonding |
| | | | $z^2$ | 17.3 % | $p_\sigma(O, N)_a$ | | | |
| | | | yz | 13.0 % | | | | |
| | | | ($x^2$-$y^2$) | (9.4 %) | | | | |
| 71A | **yz(xy)/$p_\sigma$** | a'' | yz | 44.8 % | $\pi^{n.b.}$(a) | $p_y$(C) | 10.9 % | (bonding analogue of 80A) |
| | | | xy | 15.1 % | $p_\sigma(O/N)_a$ | | | |
| 70A [a] | **$x^2$-$y^2$/$p_\sigma$** | a' | $x^2$-$y^2$ | 56.2 % | $\pi_2$(s) | -- | -- | bonding analogue of 75A |
| | | | $z^2$ | 26.2 % | $p_\sigma(O/N)_s$ | | | |
| 69A [a] | **π** | a'' | -- | -- | $\pi_2$(a) | $p_y$(C) | 10.1 % | *acen* π-orbital |
| 68A [a] | **π/$p_x$** | a' | $x^2$-$y^2$ | 20.7 % | $\pi_2$(s) | $p_x$(N) | 28.8 % | bonding interaction, $p_x(NCS)_{bind.}$ + ~ 10 % $p_y$ |
| | | | | | | $p_x$(C) | 40.4 % | |
| | | | | | | $p_x$(S) | 13.8 % | |

| | | | | | | | | |
|---|---|---|---|---|---|---|---|---|
| 67A [a] | **$\pi/p_y$** | a'' | yz | 16.1 % | $\pi_1$(a) | $p_y$(N) | 36.9 % | bonding interaction, $p_y(NCS)_{bind.}$ + ~ 10 % $p_x$ |
| | | | xy | 12.7 % | | $p_y$(C) | 39.8 % | |
| | | | | | | $p_y$(S) | 14.2 % | |
| **β spin** | | | | | | | | |
| 89B [a] | **$\pi_2$*** | a'' | yz | 22.2 % | $\pi_2$*(a) | $p_y$(N) | 34.9 % | *acen* π*-orbital, $\pi_2$*(a), $p_y(NCS)_a$ + ~ 20 % $p_x$ |
| | | | (xz) | (9.0 %) | | $p_y$(C) | 44.4 % | |
| | | | | | | $p_y$(S) | 15.4 % | |
| 88B [a] | **$\pi_2$*** | a'' | -- | -- | $\pi_2$*(a) | $p_x$(N) | 32.1 % | *acen* π*-orbital, $\pi_2$*(a), $p_x(NCS)_a$ + ~ 15 % $p_y$ |
| | | | | | | $p_x$(C) | 42.1 % | |
| | | | | | | $p_x$(S) | 14.1 % | |
| 87B [a] | **$\pi_2$*** | a'' | xz | 16.3 % | $\pi_2$*(a) | $p_x$(N) | 35.6 % | *acen* π*-orbital, $\pi_2$*(a), $p_x(NCS)_a$ |
| | | | | | | $p_x$(C) | 47.3 % | |
| | | | | | | $p_x$(S) | 16.7 % | |
| 86B [a] | **$\pi_2$*** | a' | -- | -- | $\pi_2$*(s) | $p_x$(C) | 11.3 % | *acen* π*-orbital |
| 82B | **xy** | a'' | xy | 74.4 % | $p_\sigma(O/N)_a$ | -- | -- | metal d-orbital (d*xy*), antibonding |
| | | | yz | 22.1 % | | | | |
| 81B | **xz/π*** | a' | xz | 45.9 % | $\pi_1$*(s) | -- | -- | metal d-orbital (d*xz*), antibonding |
| | | | $x^2$-$y^2$ | 25.1 % | | | | |
| | | | $z^2$ | 12.4 % | | | | |
| 80B | **$z^2$** | a'' | $z^2$ | 65.3 % | $\pi_1$*(a)? | -- | -- | metal d-orbital (d$z^2$), antibonding |
| | | | xz | 28.1 % | $\pi^{n.b.}$(s)? | | | |
| | | | $x^2$-$y^2$ | 27.0 % | | | | |
| 79B | **$z^2$/xy(π*)** | a'' | xy | 27.9 % | $\pi_1$*(a) | -- | -- | partly bonding/antibonding interaction |
| | | | $z^2$ | 12.4 % | | | | |
| 78B | **yz** | a'' | yz | 74.7 % | $\pi^{n.b.}$(a) | $p_y$(N) | 5.9 % | metal d-orbital (d*yz*), antibonding, $p_y(NCS)_a$ |
| | | | xy | 18.0 % | | $p_y$(C) | 16.4 % | |
| | | | | | | $p_y$(S) | 12.2 % | |
| 77B | **$x^2$-$y^2$** | a' | $x^2$-$y^2$ | 70.9 % | $p_\sigma(O/N)_s$ | -- | -- | metal d-orbital (d$x^2$-$y^2$), antibonding |
| | | | $z^2$ | 35.4 % | | | | |
| | | | xz | 14.7 % | | | | |
| 76B | **xz/π*** | a' | xz | 57.2 % | $\pi_1$*(s) | $p_x$(N) | 11.6 % | metal d-orbital (d*xz*), bonding, $p_x(NCS)_a$ |
| | | | $z^2$ | 16.8 % | | $p_x$(C) | 13.7 % | |
| | | | $x^2$-$y^2$ | 10.2 % | | $p_x$(S) | 15.7 % | |
| 75B | **$p_y$** | a'' | (yz) | (9.5) | $\pi^{n.b.}$(a) | $p_y$(N) | 35.8 % | ligand p-orbital ($p_y$ non-bonding) |
| | | | | | | $p_y$(S) | 44.5 % | |
| 74B | **$p_x$** | a' | xz | 18.5 % | $\pi_1$*(s) | $p_x$(N) | 34.2 % | ligand p-orbital ($p_x$ non-bonding) |
| | | | $x^2$-$y^2$ | 6.5 % | | $p_x$(S) | 43.8 % | |
| 73B | **π/yz** | a'' | yz | 19.5 % | $\pi^{n.b.}$(a) | $p_y$(C) | 7.7 % | *acen* π-orbital, $\pi^{n.b.}$(a), bonding analogue of MO 78BB |
| | | | | | | $p_y$(S) | 10.4 % | |
| 72B | **π/$z^2$** | a' | $z^2$ | 10.3 % | $\pi^{n.b.}$(s) | -- | -- | *acen* π-orbital, $\pi^{n.b.}$(s), bonding analogue of MO 80B |

| | | | | | | | | |
|---|---|---|---|---|---|---|---|---|
| 71B | $\mathbf{p_\sigma(x^2\text{-}y^2)}$ | a' | $x^2\text{-}y^2$ | 16.4 % | $p_\sigma(O/N)_s$ | -- | -- | bonding analogue of MO 77B, ~ 5 % xy, xz and yz |
| 70B [a] | $\mathbf{p_\sigma(xy)}$ | a'' | xy | 18.2 % | $p_\sigma(O/N)_a$ | -- | -- | bonding analogue of MO 82B |
| | | | yz | 12.9 % | | | | |
| 69B [a] | $\boldsymbol{\pi}$ | a'' | -- | -- | $\pi_2(a)$ | $p_x(C)$ | 10.7 % | *acen* π-orbital, $\pi_2(a)$ |
| 68B [a] | $\boldsymbol{\pi}$ | a' | -- | -- | $\pi_2(s)$ | $p_y$, $p_x$ | 15-20 % | *acen* π-orbital, $\pi_2(s)$, $p(NCS)_{bind.}$ |
| 67B [a] | $\boldsymbol{\pi}$ | a' | -- | -- | $\pi_2(s)$ | $p_y$, $p_x$ | 20-30 % | *acen* π-orbital, $\pi_2(s)$, $p(NCS)_{bind.}$ |

[a] not shown in Figure 4.20

Comparing the molecular orbitals of the three halogenido complexes, the relative energies of the unoccupied *alpha* and *beta* spin orbitals are virtually not affected by the exchange of the axial ligand X (Figure 4.21). An exception is the antibonding $z^2/p_z$ orbital which is more and more lifted in energy with the increased ligand field strength. In contrast, the energies of occupied molecular orbitals are definitely affected by the exchange of the axial ligand.

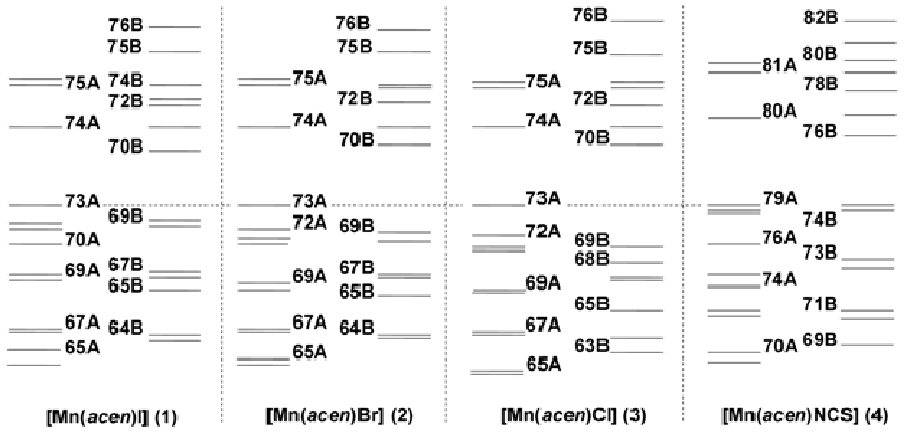


**Figure 4.21.** [Mn(*acen*)X]: the relative energies of the calculated molecular orbitals are shown for comparison (BP86/LANL2DZ). The description of the individual orbitals is given in Table 4.12. Within the halogenido complexes the bonding $p_z/z^2$ orbital and the p-orbitals of the axial ligands are more and more stabilized with the increased ligand field strength from the iodido to the chlorido complex.

A comparison the iodido and the bromido complexes results in the same sequence of *alpha* and *beta* spin orbitals is obtained - with the only exception of the *beta* spin orbitals 65 - 67B. As already mentioned, the increasing ligand field strength within the [Mn(*acen*)X] series going from $X = I^-$ to $X = NCS^-$ is generally associated with an increased displacement of the manganese(III) ion from the equatorial plane (*vide supra*, chapter 4.2). One consequence of this is that the bonding metal-ligand orbitals along the Mn-X axis (*z*) as well as the p-orbitals of the axial ligand X ($p_x$ and $p_y$) are consistently lowered in energy from [Mn(*acen*)I] to [Mn(*acen*)Cl] (Figure 4.21). The antibonding $p_z/z^2$ *beta* spin orbital on the other hand is more

and more lifted in energy with the increased ligand field strength. It generally has two bonding equivalents, 65B and 67B. In the case of [Mn(*acen*)I] the MO 67B clearly exhibits bonding $p_z/z^2$ Mn-X metal-ligand hybrid character, while the MO 65B is identified as the symmetric non-bonding *acen* π-orbital $\pi^{n.b.}(s)/z^2$ (Figure 4.18, Table 4.9). However, proceeding to [Mn(*acen*)Br] and [Mn(*acen*)Cl] these two orbitals are inverted, as MO 65B is now the bonding $p_z/z^2$ orbital being significantly lowered in energy compared to the iodido complex, while MO 67B is made out as the symmetric non-bonding $\pi/z^2$ ligand π-orbital in the case of the bromido and chlorido complex.

The molecular orbitals of [Mn(*acen*)NCS] have to be discussed separately. For the three-atomic $NCS^-$ ligand, bonding $(p(NCS)_{bind.})$, antibonding $(p(NCS)_{antibond.})$ and non-bonding linear combinations of the N, C and S $p_x$ and $p_y$ orbitals are obtained. Note that among the occupied molecular orbitals the relevant *N*CS p-orbitals (78/79A, 74/75B) are all of a non-bonding type (Figure 4.20). Within the singly occupied *alpha* spin orbitals they do not follow the described tendency of being lowered with the increased ligand field strength but appear higher in energy (78/79A) than the highest occupied metal d-orbital ($z^2/p_z$, 77A). The other molecular orbitals are in most parts identical, except of the d*yz*/π and d*xz*/π metal d-orbitals (72/73A) which are not mixed in contrast to the three haloganido complexes. Besides, no bonding $z^2/p_z$ analogue of MO 80B is observed in the case of [Mn(*acen*)NCS]. The relative energies of the *alpha* and *beta* orbitals are therefore probably not really comparable to the three halogenido complexes. In consequence, they are not included in the further argumentation. Only the qualitative trends which have been worked out on the haloganido complexes are considered instead.

**Table 4.12.** Molecular orbitals of the [Mn(*acen*)X] complexes for comparison (BP86/LANL2DZ). The relative energies are depicted in Figure 4.21.

| **α spin** | **sym. ($C_S$)** | **[Mn(*acen*) I]** | | **[Mn(*acen*$^{\#}$)Br]** | **[Mn(*acen*)Br]** | **[Mn(*acen*)Cl]** | | **[Mn(*acen*)NCS]** |
|---|---|---|---|---|---|---|---|---|
| 76A | **a"** | $\pi_1$* | 69A | $\pi_1$* | $\pi_1$* | $\pi_1$* | 82A | $\pi_1$* |
| 75A | **a'** | $\pi_1$* | 68A | $\pi_1$* | $\pi_1$* | $\pi_1$* | 81A | $\pi_1$* |
| 74A | **a"** | xy | 67A | xy | xy | xy | 80A | xy |
| 73A | **a'** | $z^2/p_z$ | 66A | $z^2/p_z$ | $z^2/p_z$ | $z^2/p_z$ | 79A | $p_y$ |
| 72A | **a"** | $p_y$ | 65A | $p_y$ | $p_y$ | yz/π | 78A | $p_x$ |
| 71A | **a'** | $p_x$ | 64A | $p_x$ | $p_x$ | $p_x/p_y$ | 77A | $z^2/p_z$ |
| 70A | **a"** | yz/π | 63A | yz/π | yz/π | $p_y/p_x$ | 76A | yz/π |
| 69A | **a'** | $x^2$-$y^2/p_\sigma$ | 62A | $x^2$-$y^2/p_\sigma$ | $x^2$-$y^2/p_\sigma$ | $x^2$-$y^2/p_\sigma$ | 75A | $x^2$-$y^2/p_\sigma$ |
| 68A | **a'** | $\pi^{n.b.}$(s) | 61A | $\pi^{n.b.}$(s) | $\pi^{n.b.}$(s) | $\pi^{n.b.}$(s) | 74A | $\pi^{n.b.}/z^2$ |
| 67A | **a"** | xz/yz(π) | 60A | xz/π | xz/yz(π) | xz/yz(π) | 73A | yz/π |
| 66A | **a"** | xz/yz(π) | 59A | $xy/p_\sigma$ (a') | xz/yz(π) | xz/yz(π) | 72A | xz/π (a') |
| 65A | **a"** | $z^2/p_z$ (a') | 58A | $z^2/p_z$ (a') | $z^2/p_z$ (a') | $yz/xy/p_{acen}$ | 71A | $yz(xy)/p_{acen}$ |
| 64A | **a"** | $yz(xy)/p_{acen}$ | 57A | yz/π | $yz/xy/p_{acen}$ | $z^2/p_z$ (a') | | -- |
| 63A | **a'** | $x^2$-$y^2/p_\sigma$ | 56A | $x^2$-$y^2/p_\sigma$ | $x^2$-$y^2/p_\sigma$ | $x^2$-$y^2/p_\sigma$ | 70A | $x^2$-$y^2/p_\sigma$ |
| 62A | **a'** | $\pi_2$(a) | 55A | $\pi_2$(a) | $\pi_2$(a) | $\pi_2$(a) | 69A | $\pi_2$(a) |
| **β spin** | | | | | | | | |
| 76B | **a"** | xy | 69B | xy | xy | xy | 82B | xy |
| 75B | **a'** | xz/π* | 68B | xz/π* | xz/π* | xz/π* | 81B | xz/π* |
| 74B | **a"** | $z^2/xy(\pi^*)$ | 67B | yz/π* | $z^2/xy(\pi^*)$ | $z^2/p_z$ | 80B | $z^2$ |
| 73B | **a'** | $z^2/p_z$ | 66B | $z^2/p_z$ | $z^2/p_z$ | $z^2/xy/yz/\pi^*$ | 79B | $z^2/xy(\pi^*)$ |
| 72B | **a"** | yz | 65B | yz/π | yz | yz | 78B | yz |
| 71B | **a'** | $x^2$-$y^2$ | 64B | $x^2$-$y^2$ | $x^2$-$y^2$ | $x^2$-$y^2$ | 77B | $x^2$-$y^2$ |
| 70B | **a'** | xz/π* | 63B | xz/π* | xz/π* | xz/π* | 76B | xz/π* |
| 69B | **a"** | $p_y$ | 62B | $p_y$ | $p_y$ | $p_y$ | 75B | $p_y$ |
| 68B | **a'** | $p_x$ | 61B | $p_x$ | $p_x$ | $p_x$ | 74B | $p_x$ |
| 67B | **a'** | $p_z/z^2$ | 60B | $p_z/z^2$ | $\pi/z^2$ | $\pi/z^2$ | 73B | π/yz |
| 66B | **a"** | π/yz | 59B | π/yz | π/yz | $\pi/yz(p_y)$ | 72B | $\pi/z^2$ |
| 65B | **a'** | $\pi/z^2$ | 58B | $\pi/z^2$ | $p_z/z^2$ | $p_z/z^2$ | -- | -- |
| 64B | **a'** | $p_\sigma(x^2$-$y^2)$ | 57B | $p_\sigma(x^2$-$y^2)$ | $p_\sigma(x^2$-$y^2)$ | $p_\sigma(x^2$-$y^2)$ | 71B | $p_\sigma(x^2$-$y^2)$ |
| 63B | **a'** | $p_\sigma$(xy) | 56B | $p_\sigma$(xy) | $p_\sigma$ (xy) | $p_\sigma$(xy) | 70B | $p_\sigma$(xy) |
| 62B | **a'** | $\pi_2$(a) | 55B | $\pi_2$(a) | $\pi_2$(a) | $\pi_2$(a) | 69B | $\pi_2$(a) |

## 4.9 Time-dependent DFT Calculation of the Electronic Transitions (TDDFT)

The electronic transitions of the [Mn(*acen*)X] complexes were calculated using time-dependent DFT (Figure 4.22, Table 9). Comparing the overall shape of the calculated UV/Vis spectra of the halogenido complexes, no distinct absorption maxima between 15 000 $cm^{-1}$ and 40 000 $cm^{-1}$are obtained as they are observed in the experimental spectra. For [Mn(*acen*)NCS], two absorption maxima are obtained in the calculated spectrum which, however, do not correspond to the energies of any of the experimental absorption bands. In the following presentation of the TDDFT calculations only the energies of the electronic transitions will be discussed first without considering the signs of the corresponding MCD bands.

Considering metal-centered ligand field transitions, only spin-allowed d → d bands can generally be calculated with TDDFT methods. First, the three quintet transitions which are theoretically expected according to the ligand field diagram (band I – III, Scheme 4.1) three ligand field transitions are also obtained from the TDDFT calculations for all [Mn(*acen*)X] complexes. Depending on the axial ligand X they are centered at 10 200 - 12 700 $cm^{-1}$, 16 100 - 16 700 $cm^{-1}$ and 22 900 - 25 100 $cm^{-1}$ and exhibit very low intensities. The calculated energies for the first ligand field transition, $z^2/p_z$ → xy (HOMO → LUMO), assort well with the results of the AOM ligand field calculations (*vide supra*, chapter 4.7) and not with the energy of 8 000 $cm^{-1}$ reported in the literature.[188] In contrast, the correlation between the literature and the calculated energies of the observed UV/Vis band A or its corresponding MCD transition is very good as the second d → d transition is found at ~ 16 000 $cm^{-1}$ ($yz/\pi^{n.b.}(a)$ → xy, band II).[188] The $x^2$-$y^2/p_\sigma$ → xy transition (band III) is identified at around 25 000 $cm^{-1}$ and shows very low intensities in the calculated UV/Vis spectra of the halogenido complexes, however. In contrast, it shows a very high intensity in the calculated spectrum of [Mn(*acen*)NCS] at 22 900 $cm^{-1}$. *Alpha* spin transitions from the bonding d*xz*/d*yz* hybrid orbitals into the unoccupied d*xy* orbital should in fact also be considered as metal centered ligand field transitions. They are found between 28 000 $cm^{-1}$ and 31 300 $cm^{-1}$ in the calculated UV/Vis spectra with their energies lowered with increasing ligand field strength from [Mn(*acen*)I] to [Mn(*acen*)NCS]. Additionally, the $yz/xy/p_{acen}$ → xy transition may also be considered as another ligand field transition. Actually it is a $xy/p_{acen}$ bonding → antibonding

transition, as the starting orbital is the bonding analogue of the unoccupied d*xy* orbital (74A). In the calculated spectra, this transition is found between 34 200 $cm^{-1}$ and 35 200 $cm^{-1}$. From its energy it might be assigned to the positive band 15 in the MCD spectra of [Mn(*acen*)Cl] and [Mn(*acen*)NCS] which is shifted towards lower energies with decreased ligand field strengths and thus might correspond to the MCD band 14 in the MCD spectrum of [Mn(*acen*)Br].

The most intense transition between 20 000 $cm^{-1}$ and 25 000 $cm^{-1}$ in the calculated UV/Vis spectra of the halogenido complexes are the $\pi^{n.b.} \rightarrow$ xy ligand-to-metal charge transfer transitions (68A → 74A) around 23 800 $cm^{-1}$. Again, the energy of the *N*CS complex differs as in the calculated spectrum of [Mn(*acen*)NCS] it is found at 25 300 $cm^{-1}$ (74A → 80A) and shows a very low intensity. This LMCT transition is assigned to the UV/Vis absorption band C which might be centered at around 22 500 $cm^{-1}$ and corresponds to the MCD band 9 around 23 300 $cm^{-1}$ in the MCD spectra of the bromido, the chlorido and the *N*CS complex and to band 8 at 23 900 $cm^{-1}$ in the case of the iodido complex. The latter is finally also considered to be a positive band centered between the two negative MCD bands 7 and 9 (*vide supra*, chapter 4.6). An alternative assignment for the UV/Vis band C as well as the MCD band 9 or 8 could be the $z^2/p_z \rightarrow \pi_1^*$ transition which appears at 24 900 $cm^{-1}$and 27 700 $cm^{-1}$ in the calculated UV/Vis spectra of the halogenido complexes (73A (HOMO) → 75/76A) and at 24 600 $cm^{-1}$ in the case of [Mn(*acen*)NCS] (78A → 81A).

The LMCT transitions from the $p_x$ and $p_y$ orbitals of the axial ligands into the d*xz* and d*yz* orbitals are observed at 16 800 – 19 100 $cm^{-1}$ (68B → 70B) and 23 600 – 27 700 $cm^{-1}$ (69B → 72B) in the calculated UV/Vis spectra. They show moderate to high intensities for the halogenido complexes and very high intensities in the case of [Mn(*acen*)NCS]. The first energy corresponds to the very broad and low-intensity absorption band A. The second energy may correspond to the UV/Vis absorption band B and could also be assigned to the MCD bands 8 and 10 at least for the chlorido and the *N*CS complex. Probably the same is true for the bromido complex, as the negative MCD band 10 could also be considered as a positive transition.

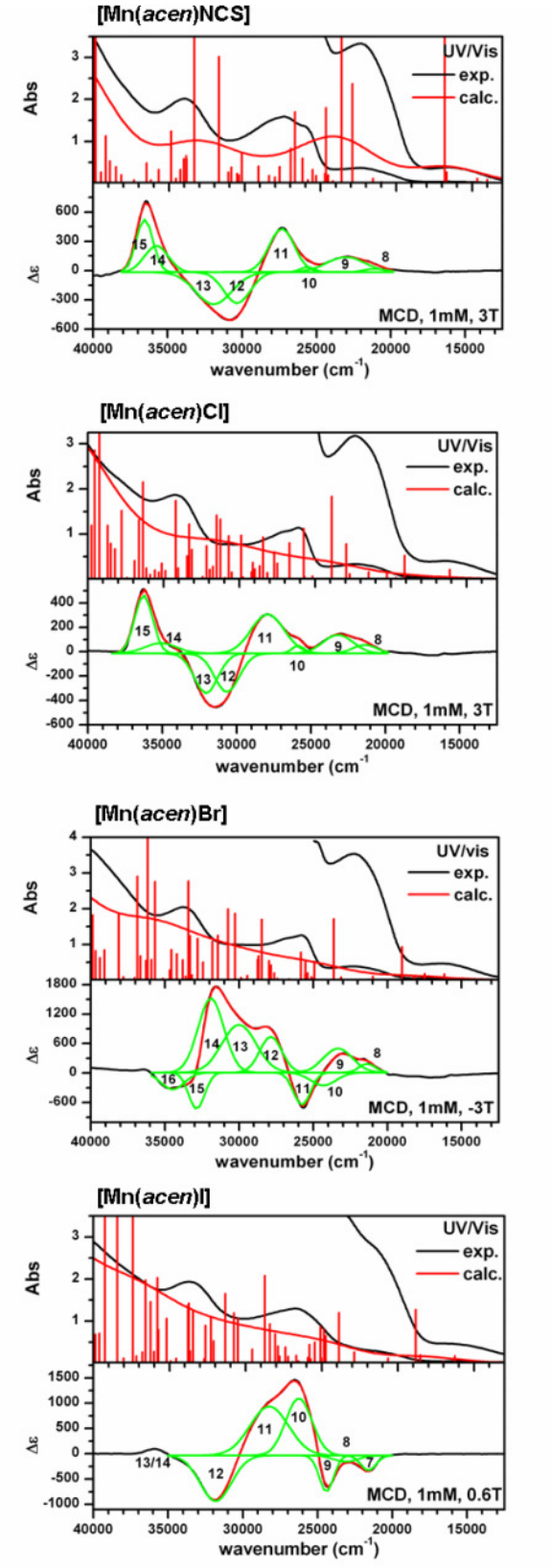


**Figure 4.22.** Comparison of the low-temperature MCD spectra and the experimental and calculated UV/Vis spectra of the [Mn(*acen*)X] complexes; MCD spectra: 1mM, $CH_2Cl_2$/polystyrene, T = 2 K, UV/Vis spectra: 2mM, $CH_2Cl_2$, calc.: TDDFT, B3LYP/LANL2DZ.

| [Mn(*acen*)I] | | | | [Mn(*acen*)Br] | | | | [Mn(*acen*)Cl] | | | | [Mn(*acen*)NCS] | | | |
|---|---|---|---|---|---|---|---|---|---|---|---|---|---|---|---|
| $cm^{-1}$ | | | | $cm^{-1}$ | | | | $cm^{-1}$ | | | | $cm^{-1}$ | | | |
| 10 200 | 0.0007 | 73A → 74A | $z^2/p_z \rightarrow xy$ | 11 700 | 0.0005 | 73A → 74A | $z^2/p_z \rightarrow xy$ | 11 900 | 0.0005 | 73A → 74A | $z^2/p_z \rightarrow xy$ | 12 700 | 0.0002 | 76A → 80A | $yz/\pi \rightarrow xy$ |
| 16 300 | 0.0017 | 70A → 74A | $yz/\pi \rightarrow xy$ | 16 200 | 0.0017 | 70A → 74A | $yz/\pi \rightarrow xy$ | 16 100 | 0.0021 | 72A → 74A | $yz/\pi \rightarrow xy$ | 14 000 | 0.0009 | 79A → 80A | $p_y/yz \rightarrow xy$ |
| **18 800** | 0.0127 | 68B → 70B | $p_x \rightarrow xz/\pi^*$ | **19 000** | 0.0093 | 68B → 70B | $p_x \rightarrow xz/\pi^*$ | **19 100** | 0.0052 | 70/71A→74A | $p_y/p_x \rightarrow xy$ | 16 700 | 0.0026 | 77A → 80A | $z^2/p_z \rightarrow xy$ |
| **23 900** | 0.0120 | 68A → 74A | $\pi^{n.b.} \rightarrow xy$ | **23 600** | 0.0171 | 68A → 74A | $\pi^{n.b.} \rightarrow xy$ | 22 900 | 0.0078 | 68B → 70B | $p_x \rightarrow xz/\pi^*$ | **16 800** | 0.0437 | 74B → 76B | $p_x \rightarrow xz/\pi^*$ |
| **24 700** | 0.0065 | 69B → 72B | $p_y \rightarrow yz$ | **24 900** | 0.0050 | 69B → 72/73B | $p_y \rightarrow yz, z^2$ | **23 900** | 0.0183 | 68A → 74A | $\pi^{n.b.} \rightarrow xy$ | **22 900** | 0.0237 | 75A → 80A | $x^2\text{-}y^2/p_\sigma \rightarrow xy$ |
| **24 900** | 0.0080 | 73A → 76A | $z^2/p_z \rightarrow \pi_1^*$ | 25 000 | 0.0004 | 69A → 74A | $x^2\text{-}y^2/p_\sigma \rightarrow xy$ | 25 200 | 0.0007 | 69A → 74A | $x^2\text{-}y^2/p_\sigma \rightarrow xy$ | **23 600** | 0.0714 | 75B→78/79B | $p_y \rightarrow yz, z^2/xy(\pi^*)$ |
| **25 100** | 0.0086 | 69B → 73B | $p_y \rightarrow z^2$ | **25 800** | 0.0078 | 73A → 76A | $z^2/p_z \rightarrow \pi_1^*$ | **25 800** | 0.0112 | 67B → 70B | $\pi/z^2 \rightarrow xz/\pi_1^*$ | **24 600** | 0.0180 | 78A → 81A | $p_x/z^2 \rightarrow \pi_1^*$ |
| **25 500** | 0.0050 | 69B → 74B | $p_y \rightarrow z^2/xy(\pi)$ | **26 000** | 0.0116 | 73A → 75A<br>65B → 70B | $z^2/p_z \rightarrow \pi_1^*$, $p_z/z^2 \rightarrow xz/\pi^*$ | **26 700** | 0.0080 | 66B → 70B | $\pi/yz \rightarrow xz/\pi^*$ | 25 300 | 0.0018 | 74A → 80A | $\pi^{n.b.} \rightarrow xy$ |
| 25 700 | 0.0009 | 69A → 74A | $x^2\text{-}y^2/p_\sigma \rightarrow xy$ | **28 000** | 0.0054 | 67B → 73B | $\pi/z^2 \rightarrow z^2$ | **27 700** | 0.0060 | 73A → 75A<br>69B → 72B | $z^2/p_z \rightarrow \pi_1^*$, $p_y \rightarrow yz/\pi$ | **26 200** | 0.0059 | 73B→76/77B | $\pi/yz \rightarrow xz/\pi^*$, $x^2\text{-}y^2$ |
| **28 100** | 0.0069 | 72A → 76A | $p_y \rightarrow \pi_1^*$ | **28 500** | 0.0107 | 70/72A→76A<br>65B → 70B | $yz/p_y \rightarrow \pi_1^*$, $p_z/z^2 \rightarrow xz/\pi^*$ | **28 400** | 0.0093 | 69B → 73B | $p_y \rightarrow z^2/xy/yz(\pi^*)$ | **26 700** | 0.0170 | 72B → 76B | $\pi/z^2 \rightarrow xz/\pi^*$ |
| **28 400** | 0.0093 | 71A → 76A | $p_x \rightarrow \pi_1^*$ | **28 700** | 0.0067 | 71/72A → 76A | $p_y, p_x \rightarrow \pi_1^*(xy)$ | **29 900** | 0.0097 | 67A → 74A | $xz/yz(\pi) \rightarrow xy$ | **26 900** | 0.0083 | 73B → 77B | $\pi/yz \rightarrow x^2\text{-}y^2$ |
| **28 700** | 0.0208 | 70A → 76A<br>66B → 72B | $yz/\pi \rightarrow \pi_1^*, \pi/yz \rightarrow yz$ | **28 700** | 0.0058 | 66A → 74A | $xz/yz(\pi) \rightarrow xy$ | **30 700** | 0.0096 | 67B → 73B | $\pi/z^2 \rightarrow z^2/xy/yz(\pi^*)$ | 28 000<br>29 100 | 0.0014<br>0.0040 | 72/73A → 80A | $xz/\pi$, $yz//\pi \rightarrow xy$ |
| **30 500** | 0.0106 | 66B → 73B | $\pi/yz \rightarrow z^2$ | **30 300** | 0.0186 | 67B→72/73B | $\pi/z^2 \rightarrow yz, z^2$ | **31 200** | 0.0133 | 68B → 72B | $p_x \rightarrow yz$ | **30 200** | 0.0071 | 73B → 79B<br>74B → 81B | $\pi/yz \rightarrow z^2/xy(\pi^*)$, $p_x \rightarrow xz/\pi^*$ |
| **30 800** | 0.0119 | 65/66B → 71/73B | $\pi \rightarrow x^2\text{-}y^2, z^2$ | **30 700** | 0.0199 | 67A → 74A<br>67B → 74B | $xz/yz(\pi) \rightarrow xy$<br>$\pi/z^2 \rightarrow z^2/xy(\pi^*)$ | **31 500** | 0.0142 | 66B → 73B | $\pi/yz \rightarrow z^2/xy/yz(\pi^*)$ | **31 700** | 0.0302 | 72B→78/79B | $\pi/z^2 \rightarrow yz, z^2/xy(\pi^*)$ |
| **31 300** | 0.0165 | 67A → 74A<br>67B → 74B | $xz/yz(\pi) \rightarrow xy$, $p_z/z^2 \rightarrow z^2/xy(\pi^*)$ | **31 400** | 0.0125 | 67B → 74B | $\pi/z^2 \rightarrow z^2/xy(\pi^*)$ | **32 200** | 0.0074 | 66B → 73B | $\pi/yz \rightarrow z^2$ | **33 300** | 0.0536 | 78A → 82A | $p_x/z^2 \rightarrow \pi_1^*$ |
| **32 300** | 0.0108 | 67B → 74B | $p_z/z^2 \rightarrow z^2/xy(\pi^*)$ | **31 800** | 0.0109 | 66B/67B →<br>73/74B | $\pi \rightarrow z^2(\pi^*)$ | **33 100** | 0.0066 | 66B → 74B | $\pi/yz \rightarrow z^2/xy/yz(\pi^*)$ | **33 800**<br>**33 900** | 0.0057<br>0.0065 | 74B → 82B | $p_x \rightarrow xy$ |
| **32 600** | 0.0089 | 67B → 72B<br>69B → 75B | $p_z/z^2 \rightarrow yz, p_y \rightarrow xz/\pi^*$ | **32 400** | 0.0050 | 67B → 72B | $\pi/yz \rightarrow yz$ | **33 300** | 0.0122 | 66/67B → 72/74B | $\pi \rightarrow yz, z^2/xy/yz(\pi^*)$ | **34 000** | 0.0058 | 72B → 78B | $\pi/z^2 \rightarrow yz$ |
| **33 500** | 0.0124 | 70A → 76A<br>64B → 70B | $yz/\pi \rightarrow \pi_i^*$, $p_\sigma(x^2\text{-}y^2) \rightarrow xz/\pi^*$ | **33 300** | 0.0124 | 65B → 73B<br>67B → 73B | $p_z/z^2 \rightarrow z^2$, $\pi/z^2 \rightarrow z^2(\pi^*)$ | **33 400** | 0.0051 | 67B → 72B | $\pi/z^2 \rightarrow yz$ | **34 300** | 0 0032 | 71A → 80A | $yz(xy)/p_{acen} \rightarrow xy$ |
| **33 700** | 0.0142 | 65/67B→73B | $p_z/z^2, \pi/z^2 \rightarrow z^2$ | **33 400** | 0.0277 | 70A → 76A<br>66B → 72B | $yz/\pi \rightarrow \pi_i^*, \pi/yz \rightarrow yz(\pi^*)$ | **34 200** | 0.0174 | 66B → 72B | $\pi/yz \rightarrow yz$ | **34 900** | 0.0124 | 73B → 80B | $\pi/yz \rightarrow z^2$ |
| **33 800** | 0.0137 | 70A → 76A<br>68B → 75B | $yz/\pi \rightarrow \pi^*, p_x \rightarrow xz/\pi^*$ | **33 800** | 0.0056 | 64B → 70B | $p_\sigma(x^2\text{-}y^2) \rightarrow xz/\pi^*$ | **36 400**<br>**36 600** | 0.0215<br>0.0132 | 68/69A→75A | $x^2\text{-}y^2/p_\sigma, \pi^{n.b.} \rightarrow \pi_1^*$ | **38 900** | 0.0053 | 74A → 81A<br>71B → 77B | $\pi^{n.b.}/z^2 \rightarrow \pi_1^*$, $p_\sigma(x^2\text{-}y^2) \rightarrow x^2\text{-}y^2$ |
| **35 200** | 0.0109 | 64A → 74A<br>65B→72/74B | $yz(xy)p_{acen} \rightarrow xy$, $\pi/z^2 \rightarrow yz, z^2/xy(\pi^*)$ | **34 200** | 0.0073 | 65B → 74B<br>64A → 74A | $p_z/z^2 \rightarrow z^2/xy(\pi^*)$, $yz/xy/p_{acen} \rightarrow xy$ | **37 800** | 0.0152 | 65B → 72B | $p_z/z^2 \rightarrow yz$ | **39 200** | 0.0113 | 69B → 76B | $\pi_2 \rightarrow xz/\pi^*$ |
| **35 700** | 0.0079 | 65B→72B | $\pi/z^2 \rightarrow yz$ | **34 600** | 0.0085 | 65B → 72B | $p_z/z^2 \rightarrow yz$ | **38 200** | 0.0067<br>0.0079 | 69B → 76B | $p_y \rightarrow xy$ | | | | |
| **35 800** | 0.0203 | 69A → 75A | $x^2\text{-}y^2/p_\sigma \rightarrow \pi_1^*$ | **35 700** | 0.0276 | 69A → 75A | $x^2\text{-}y^2/p_\sigma \rightarrow \pi_1^*$ | **38 700** | 0.0119 | 69B → 76B | $p_y \rightarrow xy$ | | | | |
| **36 200** | 0.0146 | 69B → 76B | $p_y \rightarrow xy$ | **35 900** | 0.0057 | 68A → 76A | $\pi^{n.b.} \rightarrow \pi_1^*$ | **39 200** | 0.0073 | 62B → 70B | $\pi_2 \rightarrow xz/\pi^*$ | | | | |
| **36 600** | 0.0197 | 68A → 75A | $\pi^{n.b.} \rightarrow \pi_1^*$ | **36 200** | 0.0535 | 65B → 74B | $p_z/z^2 \rightarrow z^2/xy/\pi^*$ | **39 600** | 0.0286 | 67B → 75B | $\pi/z^2 \rightarrow xz/\pi^*$ | | | | |
| **37 400** | 0.0646 | 64B → 71B<br>65B → 73B | $p_\sigma(x^2\text{-}y^2) \rightarrow x^2\text{-}y^2, \pi/z^2 \rightarrow z^2$ | **36 300** | 0.0055 | 69B → 76B | $p_y \rightarrow xy$ | **39 800** | 0.0119 | 68B → 76B | $p_x \rightarrow xy$ | | | | |
| **38 400** | 0.0485 | 67B → 75B | $p_z/z^2 \rightarrow xz/\pi^*$ | **36 700**<br>**36 900** | 0.0067<br>0.0290 | 68B → 76B | $p_x \rightarrow xy$ | **40 100** | 0.0474 | 65B → 74B<br>66B → 75B | $p_z/z^2 \rightarrow z^2/xy/yz$ (π*), $\pi/z^2 \rightarrow xz/\pi^*$ | | | | |
| | | | | **38 100** | 0.0186 | 67B → 75B | $\pi/z^2 \rightarrow xz/\pi^*$ | | | | | | | | |

**Table 4.13.** Electronic transitions of the [Mn(*acen*)X] complexes obtained from TDDFT calculations (B3LYP/LANL2DZ).

A reasonable assignment of the negative MCD band 7 in the case of [Mn(*acen*)I] can unfortunately not directly be extracted from the corresponding TDDFT calculation. However, one should keep in mind that the $p_z/z^2$ *beta* spin orbitals 67B and 73B are the only orbitals that are significantly affected by the exchange of the axial ligand X. In consequence, the negative MCD band 7 might be tentatively assigned to the $p_z/z^2$ bonding → antibonding transition (67B → 73B). As already mentioned, the bonding $p_z/z^2$ orbital is more and more stabilized with an increasing ligand field strength while the energy of the antibonding $p_z/z^2$ orbital is more and more raised at the same time. This negative band would therefore shift towards higher energies upon the exchange of the axial ligand and could then be assigned to the negative MCD band 10 in the case of [Mn(*acen*)Br], if this band is indeed considered to be a negatively signed transition. In the cases of [Mn(*acen*)Cl] and [Mn(*acen*)NCS], this band would be further shifted towards higher energies. It would not be resolved in the MCD spectra of the latter two complexes as it would be superimposed by the very intense negative bands 12 and 13.

The most dominant feature of the MCD spectra is a double *pseudo-A*-term which corresponds to the UV/Vis absorption bands D, E and F. In the literature d*xz*, d*yz* → π* metal-to-ligand charge transfer (MLCT) has been suggested for the absorption band D while band F was assigned to ligand-centered π → π* excitations.[188] From the TDDFT calculations ligand-to-metal charge transfer transitions arising from the $\pi^{n.b.}$(a)/yz and $\pi^{n.b.}$(s)/$z^2$ *beta* spin orbitals or metal-to-ligand charge transfer arising from the *alpha* spin manganese d-orbitals into the *acen* π* orbitals could be suggested, because these two types are the most intense transitions within the considered spectral regions of the calculated UV/Vis spectra. However, as the TDDFT calculations give no explanation for the positive or negative signs of the individual MCD transitions, an unambiguous assignment of the double *pseudo-A*-terms is not possible without further molecular orbital and symmetry considerations. Especially the change of sign within the double *pseudo-A*-terms of the different [Mn(*acen*)X] complexes has to be explained as well, which is the topic of the following section.

## 4.10 Assignment of the Double *Pseudo-A*-Terms Based on Molecular Orbital and Symmetry Considerations.

Two corresponding *pseudo-A*-terms, i.e. a "double *pseudo-A*-term", are made out as the most dominant features in the MCD spectra of all studied [Mn(*acen*)X] complexes. This implies that the starting orbitals of the two *pseudo-A*-terms correspond to the symmetric and antisymmetric linear combinations of atomic orbitals with respect to the mirror plane *xz*. Additionally, the individual transitions must be polarized in different directions resulting in oppositely signed transition dipole moments. The protocol of calculating MCD *C*-term intensities and determining the individual signs from the corresponding transition dipole moments which has been described by Neese and Solomon[8] could already successfully be applied for the $C_S$ symmetric molybdenum(V) $d^1$ complex [Mo(O)$Cl_3$*dppe*] (*dppe* = 1,2-bis(diphenylphosphino)ethane, chapter 4).

In general, three types of – in parts formerly degenerate – pairs of orbitals showing different symmetries with respect to the mirror plane *xz* are identified in the molecular orbital schemes of the [Mn(*acen*)X] complexes which are

(i) the symmetric and antisymmetric *acen* $\pi_1$* orbitals (75/76A – (I, Br, Cl); 81/82A – (*N*CS)),

(ii) the $p_x$ and $p_y$ orbitals of the axial ligand X (71/72A and 68/69B - (I, Br, Cl); 78/79A and 74/75B – (*N*CS)) and

(iii) the bonding and antibonding linear combinations of the symmetric and antisymmetric non-bonding *acen* π-orbitals with $dz^2$ and d*yz* (73/70A – (I, Br); 73/72A – (Cl); 77/76A – (*N*CS) and 65/66B – (I), 67/66B - (Br, Cl), 73/72B - (*N*CS)).

Note that the formerly degenerate manganese d-orbitals d*yz* and d*xz* (Scheme 4.1) are combined with different types of *acen* π-orbitals in the case of the symmetrized [Mn(*acen*$^{\#}$)X] complexes while they are mixed to give two xz/yz hybrid orbitals without a clear symmetry in the case of the unsymmetrized complexes. However, in both cases they no longer fit into the described pattern of corresponding orbitals showing opposite symmetries and are therefore neither considered as starting orbitals nor as target orbitals for the observed (double) *pseudo-*

*A*-terms in the MCD spectra of any of the [Mn(*acen*)X] complexes. As already mentioned, d*yz* and d$z^2$ instead have to be considered as corresponding metal d-orbitals in the molecular orbital schemes of [Mn(*acen*)X], as they are combined with the same type of *acen* ligand orbitals which are the symmetric and antisymmetric non-bonding π-orbitals, $\pi^{n.b.}$(s, a).

The LMCT transitions arising from the $p_x$ and $p_y$ orbitals of the axial ligand (68/69B → 70/72B – (I, Br, Cl) and 74/75B → 76/78B – (*N*CS)) would all be *z*-polarized resulting in equally signed transition dipole moments which cannot lead to oppositely signed MCD bands. These orbitals are therefore also ruled out as starting orbitals for the observed (double) *pseudo-A*-term features.

In consequence, the double *pseudo-A*-term can only arise from metal-to-ligand charge transfer from the yz/$\pi^{n.b.}$(a) and $\pi^{n.b.}$(s)/$z^2$ orbitals into the $\pi_1$* orbitals among the *alpha* spin orbitals or from ligand-to-metal charge transfer, i.e. the bonding → antibonding transitions from the occupied $\pi^{n.b.}$(a)/yz and $\pi^{n.b.}$(s)/$z^2$ orbitals into the unoccupied yz and $z^2$ orbitals among the *beta* spin orbitals.

Considering the corresponding transition dipole moments, electronic transitions into the $\pi_1$* orbitals cannot give rise to a (double) *pseudo-A*-term, because transitions into the antisymmetric $\pi_1$* orbitals do not have electric dipole character.

Based on the particular symmetries of the involved *beta* spin orbitals, it can therefore be concluded that the only possibility left for a reasonable assignment of the observed double *pseudo-A*-term in the MCD spectra of the [Mn(*acen*)X] complexes are the $\pi^{n.b.}$(a)/yz, $\pi^{n.b.}$(s)/$z^2$ → yz(π), $z^2$(π) LMCT *beta* spin transitions. Considering the relative energies of these orbitals, the most important trends within the calculated MO schemes are again shortly summarized in the following.

The iodido ligand has the weakest ligand field effect of all studied axial ligands. The energy gap between the bonding and the antibonding $z^2/p_z$ (*beta* spin) orbitals therefore is the smallest within the [Mn(*acen*)X] series. In consequence, the bonding $z^2/p_z$ orbital (67B) appears above the non-bonding *acen* π-orbitals, so that the symmetric π-orbital $\pi^{n.b.}$(s) (65B) is found <u>below</u> the antisymmetric π-orbital $\pi^{n.b.}$(a) (66B) in the case of the iodido complex

(Figure 4.18, Table 4.9). An increasing ligand field strength leads to an increased displacement of the manganese(III) ion from the equatorial plane in positive *z* direction for different axial ligands X. This is clearly associated with the energetic stabilization of the bonding $z^2/p_z$ orbital which is thus found below the non-bonding *acen* π-orbitals. The symmetric π-orbital $\pi^{n.b.}$(s) (67B) now appears above the antisymmetric π-orbital $\pi^{n.b.}$(a) (66B) as it is observed in the calculated MO schemes of the bromido and the chlorido complex (Figure 4.21, Table 4.12). At the same time the antibonding $z^2/p_z$ orbital (73B) is more and more lifted in energy (Figure 4.21). The sequence of the considered target orbitals d*yz* (72B) and d$z^2$ (73B) is unchanged for all [Mn(*acen*)X] complexes (Figure 4.21, Table 4.12). Note, however, that only the symmetry of the starting orbitals determines the signs within a double *pseudo-A*-term while the symmetry of the target orbitals has no influence on these signs.[8]

Beginning with [Mn(*acen*)I] the $\pi^{n.b.}$(s)/$z^2$, $\pi^{n.b.}$(a)/yz → yz(π), $z^2$(π) LMCT transitions involve the *beta* spin orbitals 66/65B and 72/73B. The d$z^2$ and d*yz* manganese d-orbitals interact through spin-orbit coupling via $L_x$.

The $\pi^{n.b.}$(a)/yz → yz transition is *z*-polarized in the negative direction:

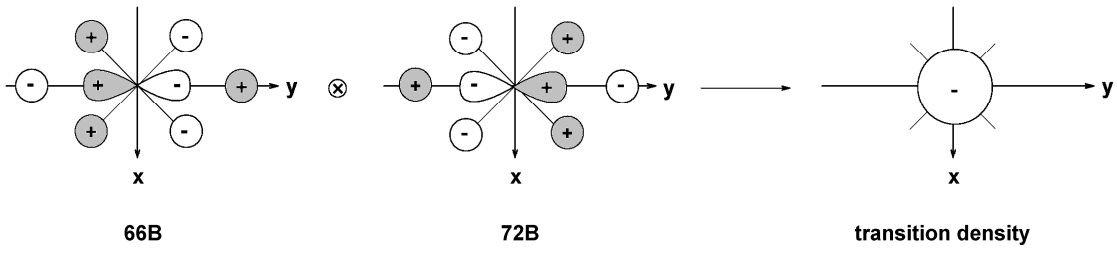


Note that the only contribution to the transition density arises from a yz/$p_y$ bonding → antibonding transition along the *z* axis and not from the *acen* π-orbitals (Figure 4.18).

The $\pi^{n.b.}$(a)/yz → $z^2$ transition is *y*-polarized in the positive direction:

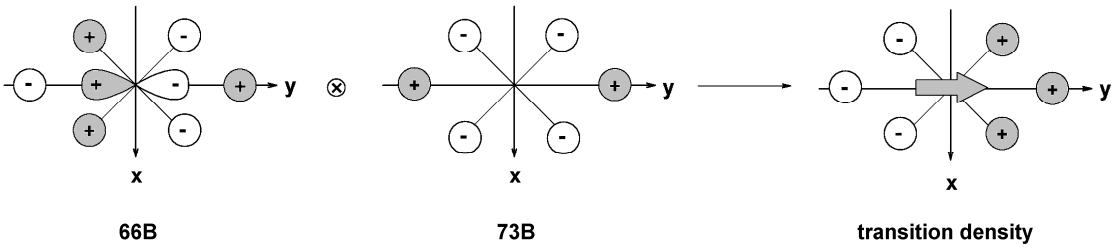


In general the MCD *C*-term intensity of *yz* polarized transitions is given by

$$C_0 \sim -\sum_{K\neq A,J} \frac{1}{\Delta_{KJ}} \{\langle A|\mu_y|K\rangle\langle A|\mu_z|J\rangle\langle K|L_x|J\rangle - \langle A|\mu_z|K\rangle\langle A|\mu_y|J\rangle\langle K|L_x|J\rangle\}$$

as for only $M_{yz}^{eff}$ has to be considered:

$$M_{yz}^{eff} = \sum_{K\neq A,J} \left(\vec{D}_y^{AK}\,\vec{D}_z^{AJ} - \vec{D}_z^{AK}\,\vec{D}_y^{AJ}\right)\frac{\overline{L}_x^{KJ}}{\Delta_{KJ}} + \left(\vec{D}_y^{AJ}\,\vec{D}_z^{JK} - \vec{D}_z^{AJ}\,\vec{D}_y^{JK}\right)\frac{\overline{L}_x^{KA}}{\Delta_{KA}}$$

*J* and *K* are the excited states which are coupled through spin-orbit coupling via $L_x$. The LMCT transitions considered here are type I electronic transitions[117] among <u>*beta*</u> spin orbitals, so that an additional negative coefficient has to be introduced here, as the spin-orbit coupling matrix elements of two *beta* spin orbitals can generally be written as

$$\langle\beta_1|L_x|\beta_2\rangle = (-1)\langle\alpha_1|L_x|\alpha_2\rangle$$

As a result, the MCD *C*-term intensity of the $\pi^{n.b.}$(a)/yz → yz transition (*A* → *J* (66B → 72B); *K*: $z^2$ (73B)) has a negative sign. It is given by

$$C_0 \sim \frac{1}{\Delta_{KJ}} \{\langle\pi^{n.b.}(a)|\mu_y|z^2\rangle\langle\pi^{n.b.}(a)|\mu_z|yz\rangle\,\mathrm{Im}(\langle z^2|l_x|yz\rangle) - \langle\pi^{n.b.}(a)|\mu_z|z^2\rangle\langle\pi^{n.b.}(a)|\mu_y|yz\rangle\,\mathrm{Im}(\langle z^2|l_x|yz\rangle)\}$$

$$= \frac{1}{\Delta_{KJ}} \{(+1)|\langle\pi^{n.b.}(a)|\mu_y|z^2\rangle|\cdot(-1)|\langle\pi^{n.b.}(a)|\mu_z|yz\rangle|\cdot(+1)\cdot\mathrm{Im}(\langle z^2|l_x|yz\rangle) - 0\} < 0$$

with $\Delta_{KJ} = E_K - E_J > 0$.

On the contrary, MCD *C*-term intensity of the corresponding $\pi^{n.b.}$(a)/yz → $z^2$ transition (*A* → *J* (66B → 73B); *K*: yz (72B)) has a positive sign:

$$C_0 \sim \frac{1}{\Delta_{KJ}}\{\langle \pi^{n.b.}(a)|\mu_y|yz\rangle\langle \pi^{n.b.}(a)|\mu_z|z^2\rangle \mathrm{Im}(\langle yz|l_x|z^2\rangle) - \langle \pi^{n.b.}(a)|\mu_z|yz\rangle\langle \pi^{n.b.}(a)|\mu_y|z^2\rangle \mathrm{Im}(\langle yz|l_x|z^2\rangle)\}$$

$$= \frac{1}{\Delta_{KJ}}\{0-(-1)|\langle \pi^{n.b.}(a)|\mu_z|yz\rangle|\cdot(+1)|\langle \pi^{n.b.}(a)|\mu_y|z^2\rangle|\cdot(-1)\cdot \mathrm{Im}(\langle yz|l_x|z^2\rangle)\} > 0$$

with $\Delta_{KJ} = E_K - E_J < 0$.

Taken together, the $\pi^{n.b.}$(a)/yz → yz, $z^2$ ligand-to-metal charge transfer transitions (66B → 72/73B) thus give rise to a positive *pseudo-A*-term. In consequence, they can be assigned to the MCD bands 9 and 10 in the case of [Mn(*acen*)I] which also correspond to band 11 and 12 in the MCD spectrum of [Mn(*acen*)Br].

For the corresponding $\pi^{n.b.}$(s)/$z^2$ → yz, $z^2$ LMCT transitions (65B → 72/73B) a negative *pseudo-A*-term is obtained in the MCD spectra. The $z^2/\pi^{n.b.}$(s) → yz transition is *y*-polarized in the positive direction

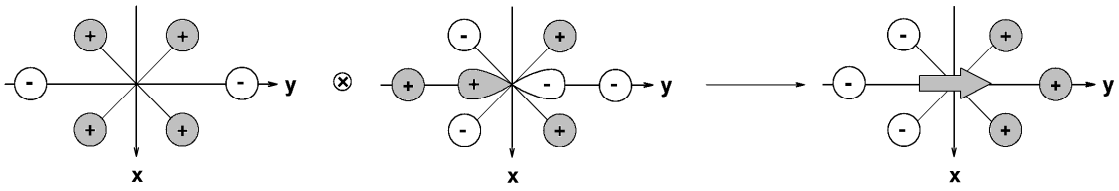


and the $\pi^{n.b.}$(s)/$z^2$ → $z^2$ transition is *z*-polarized in the negative direction:

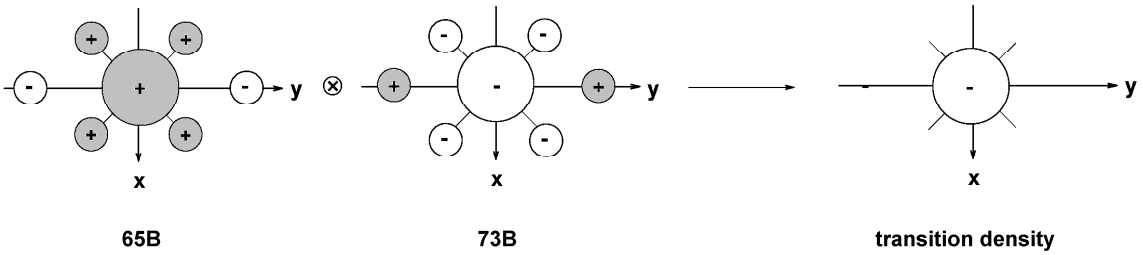

Thus the only contribution to the transition density, corresponding to the $\pi^{n.b.}$(a)/yz → yz transition, here does not involve the *acen* π-orbitals but actually arises from a $z^2/p_z$ bonding → antibonding transition along the *z* axis (Figure 4.18).

A positive MCD intensity is then obtained for the $\pi^{n.b.}$(s)/$z^2$ → yz transition (*A* → *J* (65B → 72B); *K*: $z^2$ (73B)):

$$C_0 \sim \frac{1}{\Delta_{KJ}}\{\langle\pi^{n.b.}(s)|\mu_y|z^2\rangle\langle\pi^{n.b.}(s)|\mu_z|yz\rangle \mathrm{Im}(\langle z^2|l_x|yz\rangle) - \langle\pi^{n.b.}(s)|\mu_z|z^2\rangle\langle\pi^{n.b.}(s)|\mu_y|yz\rangle \mathrm{Im}(\langle z^2|l_x|yz\rangle)\}$$

$$= \frac{1}{\Delta_{KJ}}\{0-(-1)|\langle\pi^{n.b.}(s)|\mu_z|z^2\rangle|\cdot(+1)|\langle\pi^{n.b.}(s)|\mu_y|yz\rangle|\cdot(+1)\cdot\mathrm{Im}(\langle z^2|l_x|yz\rangle)\} > 0$$

with $\Delta_{KJ} = E_K - E_J > 0$.

The corresponding $\pi^{n.b.}$(s)/$z^2$ → $z^2$ transition (65B → 73B (*A* → *J*); *K*: yz (72B)) results in a negative signed MCD band:

$$C_0 \sim \frac{1}{\Delta_{KJ}}\{\langle\pi^{n.b.}(s)|\mu_y|yz\rangle\langle\pi^{n.b.}(s)|\mu_z|z^2\rangle \mathrm{Im}(\langle yz|l_x|z^2\rangle) - \langle\pi^{n.b.}(s)|\mu_z|yz\rangle\langle\pi^{n.b.}(s)|\mu_y|z^2\rangle \mathrm{Im}(\langle yz|l_x|z^2\rangle)\}$$

$$= \frac{1}{\Delta_{KJ}}\{(+1)|\langle\pi^{n.b.}(s)|\mu_y|yz\rangle|\cdot(-1)|\langle\pi^{n.b.}(s)|\mu_z|z^2\rangle|\cdot(-1)\cdot\mathrm{Im}(\langle yz|l_x|z^2\rangle) - 0\} < 0$$

with $\Delta_{KJ} = E_K - E_J < 0$.

In total, the $\pi^{n.b.}$(s)/$z^2$ → yz, $z^2$ LMCT transitions (65B → 72/73B) thus give rise to a negative *pseudo-A*-term which is assigned to band 11 and 12 in the MCD spectrum of [Mn(*acen*)I] as well as to band 13 and 15 in the MCD spectrum of [Mn(*acen*)Br].

To sum up, our symmetry-based analysis identifies a positive *pseudo-A*-term centered at ~ 26 000 $cm^{-1}$ followed by a negative *pseudo-A*-term at higher energies in the MCD spectra of

[Mn(*acen*)I] and [Mn(*acen*)Br], which can be taken together as double *pseudo-A*-terms arising from the $\pi^{n.b.}(s)/z^2$, $\pi^{n.b.}(a)/yz \rightarrow z^2$, yz ligand-to-metal charge transfer transitions.

As already mentioned, the symmetric π-orbital $\pi^{n.b.}(s)/z^2$ (67B) and the antisymmetric π-orbital $\pi^{n.b.}(a)/yz$ are inverted in energy in the case of the bromido, the chlorido and the *N*CS complexes (Figure 4.21, Table 4.12). In consequence, the symmetry of the starting orbitals of the two *pseudo-A*-terms is inverted which leads to a change of signs within the double *pseudo-A*-term. In the MCD spectra of [Mn(*acen*)Cl] and [Mn(*acen*)NCS] the negative *pseudo-A*-term (band 11 + 12) is indeed centered at ~ 29 000 $cm^{-1}$ and followed by the positive *pseudo A*-term at higher energies (*vide supra*, Figure 4.14). Based on the calculated MO scheme, a change of signs within the *pseudo-A*-term would also be expected for [Mn(*acen*)Br] but is not observed within the MCD spectrum. This implies that the relative energies of the symmetric and antisymmetric $\pi^{n.b.}$ orbitals (65B - 67B) are not correctly reproduced by the quantum chemical computation of the molecular orbitals.

The assignment of the double *pseudo-A*-terms to the $\pi^{n.b.}(a)/yz$, $\pi^{n.b.}(s)/z^2 \rightarrow yz, z^2$ LMCT transitions is shown in Figure 4.23.

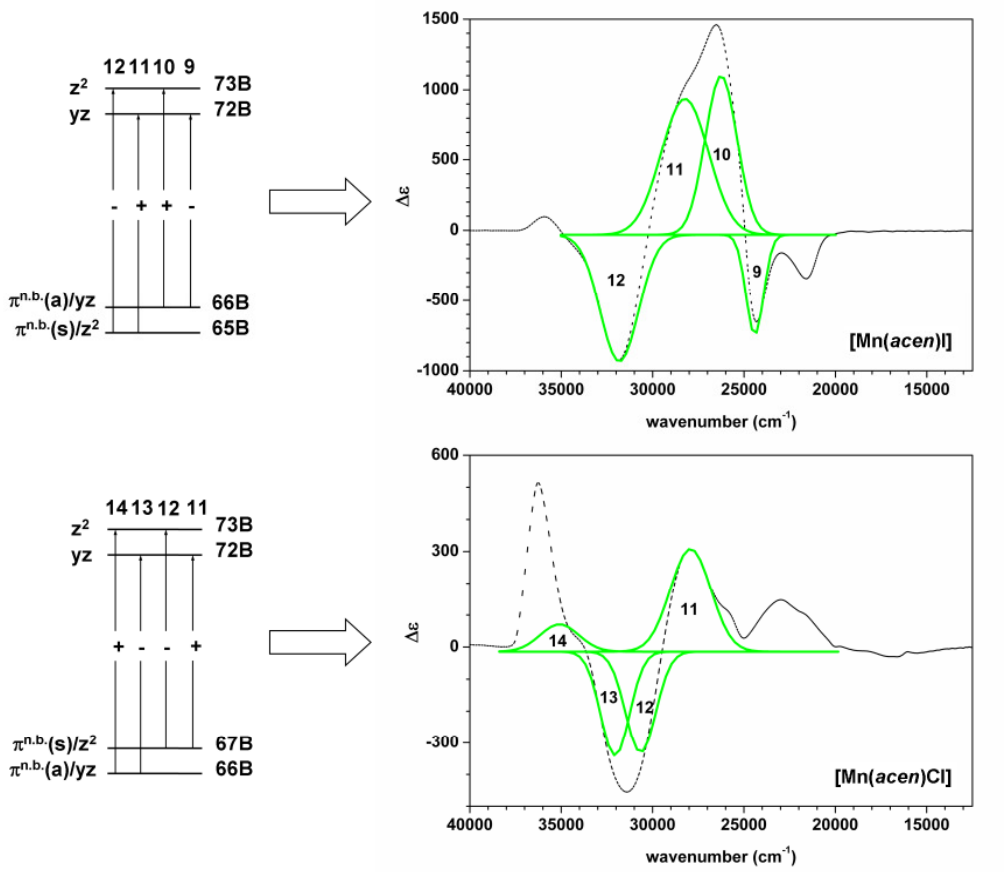


**Figure 4.23.** Assignment of the double *pseudo-A*-terms in the low-temperature MCD spectra of [Mn(*acen*)I] (**top**) and [Mn(*acen*)Cl] (**bottom**) to the $\pi^{n.b.}(a)/yz$, $\pi^{n.b.}(s)/z^2 \rightarrow yz(\pi)$, $z^2(\pi)$ LMCT transitions.

The suggested assignment of all UV/Vis and MCD transitions of the [Mn(*acen*)X] complexes is summarized in Table 4.14. The analysis is based on the combined results of the AOMX ligand field calculations as well as the (TD)DFT calculations of the molecular orbitals and electronic transitions.

The spin-forbidden triplet transitions and the spin-allowed d → d band II could be identified from the AOMX results. In contrast, the energy of the third spin-allowed ligand field transition band III is still unclear as the results of the AOMX and the TDDFT calculations do not agree. Also, the assignments of the p → d charge transfer transitions from the p-orbitals of the axial ligand X into the manganese d-orbitals ($L_{ax}$MCT) may rather be considered to be tentative suggestions than definite assignments. However, the most intense transitions which dominate the MCD spectra of all [Mn(*acen*)X] complexes could be identified as double *pseudo-A*-term features arising from $\pi^{n.b.}(s)/z^2$, $\pi^{n.b.}(a)/yz \rightarrow yz, z^2$ ligand-to-metal charge transfer (LMCT). Furthermore, the change of signs which has been observed within these

*pseudo-A*-terms could be explained by the stabilization of the bonding $p_z/z^2$ orbital which leads to the inversion of the symmetric and antisymmetric non-bonding π–orbitals with increased ligand field strength of the axial co-ligand

**Table 4.14.** Assignment of the MCD (and UV/Vis) transitions of the [Mn(*acen*)X] complexes based on AOMX and (TD)DFT calculations as well as on molecular orbital and symmetry considerations.

| **UV/Vis** | **MCD** | | | | **assignment** |
|---|---|---|---|---|---|
| | **[Mn(*acen*)I]** | **[Mn(*acen*)Br]** | **[Mn(*acen*)Cl]** | **[Mn(*acen*)NCS]** | |
| | -- | (1) 14 800 (-) | (1) 14 900 (-) | (1) 14 800 (-) | |
| | -- | (2) 15 200 (-) | (2) 15 400 (-) | (2) 15 500 (-) | spin-forbidden triplet transitions (d → d)[a] |
| | (1) 15 600 (-) | (3) 15 500 (-) | (3) 15 700 (-) | (3) 16 100 (-) | |
| (A) 16 400 | (2) 16 400 (-) | (4) 16 400 (-) | (4) 16 500 (-) | (4) 16 900 (-) | $^5B_1 \rightarrow {}^5B_2$ spin-allowed ligand field transition (d → d) [a, b] |
| | (3) 16 900 (-) | (5) 17 200 (-) | (5) 17 200 (-) | (5) 17 300 (-) | $^5B_1 \rightarrow {}^5E$ spin-allowed ligand field transitions (d → d) [a] **or** low-energy $L_{ax}MCT$ [b] |
| | (4) 18 200 (-) | (6) 18 200 (-) | (6) 17 600 (-) | (6) 17 900 (-) | |
| | (5) 18 800 (-) | (7) 18 900 (-) | (7) | (7) 18 700 (-) | spin-forbidden triplet transition (d → d)[a] |
| | (6) 19 700 (-) | | | | low-energy $L_{ax}MCT$ [b] |
| | (7) 21 600 (-) | | | | $p_x \rightarrow xz/\pi^*$ ($L_{ax}MCT$ ) [b] |
| (B, C) 22 300 | -- | (8) 21 400 (+) | (8) 21 400 (+) | (8) 21 400 (+) | $L_{ax}MCT$ [b] |
| | (8) 23 300 (-) | (9) 23 300 (+) | (9) 23 200 (+) | (9) 23 200 (+) | $\pi^{n.b.}(s) \rightarrow xy$ (LMCT)[b] |
| | -- | (10) 24 300 (-) | (10) 25 900 (+) | (10) 25 300 (+) | $L_{ax}MCT$ [b] |
| (D) 25 000 - 27 000 | (9) 24 400 (-) | (11) 25 800 (-) | (11) 27 900 (+) | (11) 27 500 (+) | |
| | (10) 26 200 (+) | (12) 27 900 (+) | (12) 30 700 (-) | (12) 30 700 (-) | **$\pi^{n.b.}(s)/z^2$, $\pi^{n.b.}(a)/yz \rightarrow yz, z^2$** (LMCT)[b, c] |
| ((E) 30 500*) | (11) 28 000 (+) | (13) 30 000 (+) | (13) 32 100 (-) | (13) 32 800 (-) | The change of signs with the double pseudo-A-term: is explained by the inversion of the symmetric and antisymmetric non-bonding π–orbitals with the increased ligand field strength of the axial co-ligand [c] |
| | (12) 31 800 (-) | * | (14) 35 100 (+) | (14) 35 800 (+) | |
| | | (15) 32 900 (-) | | | |
| (F) 33 500 | (13/14) | (16) 34 500 (-) | | | |
| | | *(14) 31 900 (+) | (15) 36 300 (+) | (15) 36 400 (+) | $xy/p_{acen}$ bonding → antibonding transition |

[a] AOMX

[b] TDDFT (B3LYP/LANL2DZ)

[c] molecular orbital and symmetry considerations

As UV/Vis and MCD intensities of electronic transitions are due to completely different mechanisms, they actually cannot really be compared. However, looking at the UV/Vis assignment reported in the literature,[188] the situation is obviously more complex. Band

assignment is more difficult if not only the observed shifts in the UV/Vs spectra but also the calculated molecular orbitals are taken as a basis.

As a concluding remark it should be noted, that in the case of [$Mo^{V}(O)Cl_3$*dppe*] the double *pseudo-A*-term arose from type III electronic transitions, i.e. transitions from doubly occupied ligand orbitals into unoccupied metal d-orbitals. To describe the involved excited states, multi-determinant expressions[117] had to be employed to describe the MCD mechanism properly (*vide supra*, chapter 3). In the case of the [Mn(*acen*)X] complexes the $\pi^{n.b.}$(a)/yz, $\pi^{n.b.}$(s)/$z^2$ → yz($\pi$), $z^2$($\pi$) transitions, which give rise to the double *pseudo-A*-terms in the corresponding MCD spectra, are type I transitions, i.e. transitions from doubly occupied ligand orbitals into singly occupied manganese d-orbitals. Considering the resulting excited states, the spin states are represented by single determinants. In consequence, the description of the MCD mechanisms of these type I transitions is much easier compared to the type III electronic transitions which dominate the MCD spectra of [$Mo^{V}(O)Cl_3$*dppe*].

## 4.11 Summary

The [Mn(*acen*)X] Schiff base complexes (X = $I^-$, $Br^-$, $Cl^-$, *N*$CS^-$) have firstly been thoroughly characterized by vibrational spectroscopy. The molecular vibrations were completely correlated to the observed transitions based on quantum chemical computations of the corresponding IR and Raman spectra. As a result, the DFT optimized complex structures were verified as reliable for further calculations.

The study on the [Mn(*acen*)X] low-temperature parallel mode cw X-band EPR spectra achieved excellent results with respect to the quality of the recorded spectra as well as of the spectral simulations using the XSophe simulation software.[1] From this study it could be concluded, that discrete, mononuclear manganese(III) species are present in solution even at high concentrations. This is a prerequisite for the UV/Vis and MCD study of the electronic transitions.

The UV/Vis absorption spectra of the [Mn(*acen*)X] complexes which have already been reported in the literature[188] were further studied within this work with respect to different solvents, different media (polystyrene film spectra vs. solution spectra) and the low-

temperature spectra. It could be confirmed that a varying ligand field strength of the axial ligands X ($I^- < Br^- < Cl^- < NCS^-$) almost has no effect on the UV/Vis absorption spectrum.

In contrast, the variation of X was found to have a huge effect on the corresponding low-temperature MCD spectra. They are all dominated by very intense double *pseudo-A*-term features which change their signs from [Mn(*acen*)I] and [Mn(*acen*)Br] to [Mn(*acen*)Cl] and [Mn(*acen*)NCS]. For the assignment of the observed UV/Vis and MCD bands the molecular orbitals and the electronic transitions were computed using (TD)DFT calculations. The description of the molecular orbitals turned out to be rather difficult due to the high covalence of the metal-ligand bonds. It could be managed with the help of MO calculations for the symmetrized [Mn($acen^{\#}$)X] complexes ($C_S$ symmetry) first. Two pairs of almost degenerate E states were identified among the *beta* spin orbitals which could give rise to a double *pseudo-A*-terms in the MCD spectra. From the considered transition densities, this feature was indeed assigned to the ligand-to-metal charge transfer transitions from the doubly occupied non-bonding π-orbitals $\pi^{n.b.}$(a)/yz and $\pi^{n.b.}$(s)/$z^2$ into the singly occupied manganese d-orbitals d$yz$ and d$z^2$. In addition, an explanation was also presented for the observed change of signs of the *pseudo-A*-terms within the [Mn(*acen*)X] series. Upon the variation of the axial ligand X the non-bonding π-orbitals shift within the MO schemes leading to an inverted symmetry in the case of [Mn(*acen*)Cl] and [Mn(*acen*)NCS] compared to [Mn(*acen*)Br] and [Mn(*acen*)Br]. As they determine the signs of the considered *pseudo-A*-term transitions this clearly results in a change of signs within the observed double *pseudo-A*-terms. Suggestions for the assignments of the remaining UV/Vis and MCD bands could also be made from AOMX ligand field and TDDFT calculations.

From the study on the UV/Vis and MCD spectra of the [Mn(*acen*)X] series of complexes it is concluded that MCD spectroscopy must definitely be considered superior to conventional UV/Vis absorption spectroscopy with respect to its sensitivity. Even small changes of the ligand field strength, like the variation of an axial ligand, which cannot be followed by UV/Vis spectroscopy can be studied by MCD spectroscopy as they may lead to dramatic changes in the corresponding MCD spectra.

# 5 Electronic Structure of Facially Coordinated Molybdenum(III) *Tripod* Complexes

The UV/Vis absorption spectra which are analyzed in this chapter were recorded by Jan Krahmer and Henning Broda.

## 5.1 $[MoBr_3P_3]$

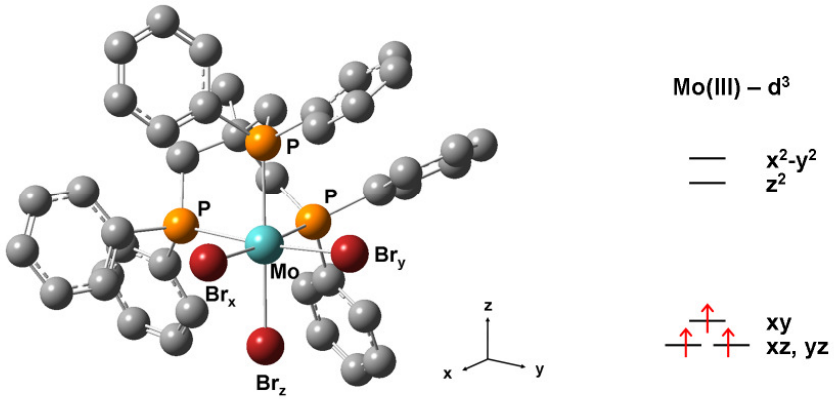


**Figure 5.1. left:** Structure of $[MoBr_3P_3]$ obtained from X-ray single crystal analysis[6, 196] with the hydrogen atoms omitted for clarity. This structure was used for the (TD)DFT calculation without further optimisation. **right:** Schematic ligand field splitting of the metal d-orbitals in an elongated octahedral coordination geometry, molybdenum(III): $d^3$

The uncharged molybdenum(III) complex $[MoBr_3P_3]$ ($P_3$ = 1,1,1-tris(diphenylphosphino-methyl)ethane, *tdppme*) was the first molybdenum-phosphorus *tripod* complex synthesized by the Tuczek group.[196] It serves as a precursor for Chatt type molybdenum(0)-dinitrogen complexes (**C1**, chapter 1.2.3) like $[Mo(N_2)P_3$*dppm*$]$ (*dppm* = diphenylphosphinomethane) or $[Mo(N_2)P_3$*dmpm*$]$ (*dmpm* = dimethylphosphinomethane).[6, 196] These are obtained from $[MoBr_3P_3]$ by sodium amalgam reduction in the presence of the *dppm* or *dmpm* co-ligands under a dinitrogen atmosphere. The Mo(0) center of these complexes is facially coordinated to the tripodal $P_3$ ligand. The axial position *trans* to the $N_2$ ligand is therefore protected by a coordinating phosphorus atom and is thus no longer accessible for ligand exchange. This is an important improvement on the way to catalytic $N_2$ fixation, as undesired side-reactions involving the position *trans* to $N_2$ can be avoided. The $N_2$ ligand of the $[Mo(N_2)P_3$*dmpm*$]$ complex shows a moderate activation and can be protonated to give the hydrazido complex $[Mo(NNH_2)P_3$*dmpm*$]$.[6, 196] This represents one of the first intermediates (**C3**, chapter 1.2.3)

of the Chatt cycle and eventually could lead to ammonia formation by true catalytic dinitrogen reduction.

The synthesis of $[MoBr_3P_3]$ has already been described.[196] The tripodal $P_3$ ligand ($P_3$ = 1,1,1-tris(diphenylphosphinomethyl)ethane) is facially coordinated to the molybdenum(III) center leading to a distorted octahedral complex geometry of trigonal symmetry with a slightly elongated *z* axis (Figure 5.1). The atomic coordinates of the $[MoBr_3P_3]$ obtained by X-ray crystallography[196] were used for the quantum chemical (TD)DFT calculations of the molecular orbitals and electronic transitions without performing any further geometry optimization. Considering the ligand field splitting of the molybdenum d-orbitals, a slight splitting should be expected within the $t_{2g}$ and $e_g$ orbitals (Figure 5.1, right). The title complex has a high-spin $d^3$ configuration, so the $t_{2g}$ orbitals are singly occupied.

### 5.1.1 UV/Vis Absorption Spectrum and Ligand Field Calculations (AOM)

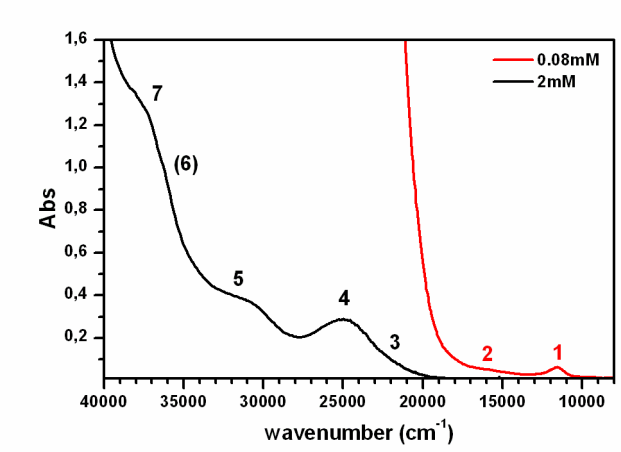


**Figure 5.2.** UV/Vis absorption spectra of $[MoBr_3P_3]$ measured in $CH_2Cl_2$ (d = 10 mm) at two different concentrations (0.08/2 mM).

Solutions of $[MoBr_3P_3]$ in $CH_2Cl_2$ have a yellow color. Two distinct absorption features at 25 000 $cm^{-1}$ ($\varepsilon$ = 3 600 $mol^{-1}cm^{-1}$, band (3 +) 4) and 31 300 $cm^{-1}$ ($\varepsilon$ = 4 800 $mol^{-1}cm^{-1}$, band 5) and a clear shoulder at 37 500 $cm^{-1}$ (band 7) are observed in the UV/Vis absorption spectrum of $[MoBr_3P_3]$ at low concentrations (0.08 mM). In addition, a very weak shoulder is eventually made out at ~ 36 000 $cm^{-1}$ (band 6). At a higher concentration (2 mM) a distinct, low-intensity absorption band at 11 600 $cm^{-1}$ ($\varepsilon$ = 30 $mol^{-1}cm^{-1}$, band 1) and a tiny shoulder

around 16 000 $cm^{-1}$ (band 2) are additionally observed in the low energy region of the UV/Vis spectrum (Figure 5.2).

The UV/Vis spectra of three molybdenum(III) high-spin systems have already been studied in detail. In the case of the meridionally coordinated trispyridine and trispicoline Mo(III) complexes [$MoBr_3py_3$] and [$MoBr_3$(4-*pic*)$_3$] two low-intensity bands were observed at 8 800 $cm^{-1}$ and ~ 14 500 $cm^{-1}$.[109] These were assigned to the spin-forbidden doublet transitions $^4A_{2g} \rightarrow {}^2E_g$, $^2T_{1g}$(G) and $^4A_{2g} \rightarrow {}^2T_{2g}$(G). Additionally, an intense absorption band at 27 200 - 27 600 $cm^{-1}$ has been assigned to a spin-allowed ligand field transition ($^4A_{2g} \rightarrow {}^4T_{2g}$) for these two complexes which gains its high intensity by being mixed with a more intense Mo → *py*/4-*pic* metal-to-ligand charge transfer transition.

In the UV/Vis spectrum of the facially coordinated [$Mo^{III}Br_3(NH_3)_3$] complex, the $^4A_{2g} \rightarrow {}^4T_{2g}$ and $^4A_{2g} \rightarrow {}^4T_{1g}$ quartet transitions were observed at 23 800 $cm^{-1}$ and 28 100 $cm^{-1}$.[197] Additionally, a weak absorption feature at 15 100 $cm^{-1}$ was assigned to the $^4A_{2g} \rightarrow {}^2T_{2g}$(G) doublet transition.

**Scheme 5.1.** Ligand field diagram of Mo(III) extracted from the Tanabe-Sugano diagram of an octahedral $d^3$ high spin system[102] and confirmed by ligand field calculations based on the *angular overlap model* (AOM).

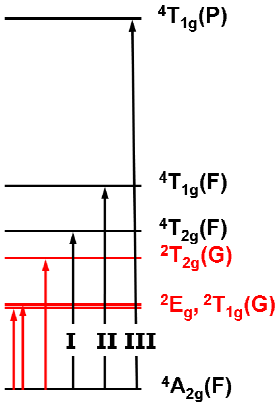


Transferring these assignments to the UV/Vis spectrum of [$MoBr_3P_3$] and in accordance with the ligand field diagram of an octahedral $d^3$ high spin system[95, 102] (Scheme 5.1), the absorption band 4 at 25 000 $cm^{-1}$ and band 5 at 31 300 $cm^{-1}$ would then also intuitively be assigned to the first two spin-allowed ligand field transitions, $^4A_{2g} \rightarrow {}^4T_{2g}$ (band I) and $A_{2g} \rightarrow {}^4T_{1g}$ (band II). However, the extinction coefficients are actually too high to support

these assignments. The absorption features below 20 000 $cm^{-1}$ are expected to originate from spin-forbidden transitions due to their very low intensities.

To verify these assignments ligand field calculations based on the *angular overlap model* were employed using the AOMX program.[169, 170] The input geometry (*xyz*) of the coordinating ligand atoms, i.e. bond lengths and bond angles, was taken from the single crystal X-ray structure.[196] One set of σ- and π-bonding parameters $e_\sigma$ and $e_\pi$ was chosen for the bromido ligands ($e_\sigma 1/e_\pi 1$) and one set for the $P_3$ ligand ($e_\sigma 2/e_\pi 2$). Starting values of $e_\sigma$ and $e_\pi$ were taken based on typical values taken from a previously published data.[168] The π-back-bonding from the molybdenum d-orbitals into unoccupied p-orbitals of the three coordinating phosphorus atoms is reflected by the negative π-bonding parameter of the $P_3$ ligand ($e_\pi 2$ = -1 500 $cm^{-1}$). As a result of that the electron density at the metal center is reduced, so that in consequence the Mo-Br bond strength might be increased, resulting in a significantly increased value of the corresponding σ-bonding parameter $e_\sigma 1$. The π-bonding parameter $e_\pi 1$, however, shows no variation during the calculation (Table 5.1).

**Table 5.1. left:** Experimental and calculated (AOMX) ligand field transitions of $[MoBr_3P_3]$. **right:** overview of the corresponding AOM parameters. All parameters and energies are given in $cm^{-1}$.

| | UV/Vis | calc. |
|---|---|---|
| $^4A_{2g}$ **(F)** | 0 | 0 |
| $^2E_g$ **(G)** | (1) 11 600 | 11 600 |
| $^2T_{1g}$ **(G)** | | 12 100 |
| $^2T_{2g}$ **(G)** | (2) ~ 16 000 | 18 300 |
| $^4T_{2g}$ **(F)** | (4) 25 000 | 25 000 |
| $^4T_{1g}$ **(F)** | (5) 31 300 | 31 500 |
| $^4T_{1g}$ **(P)** | -- | > 50 000 |

| | input | fit |
|---|---|---|
| $e_\sigma 1$ | 5 050 | 8 400 |
| $e_\pi 1$ | 690 | 690 |
| $e_\sigma 2$ | 7 500 | 7 500 |
| $e_\pi 2$ | -1 500 | -1 500 |
| **B** | 500 | 610 |
| **C** | 2 300 | 2 300 |
| $\|D\|$ | -- | 4.2 |

Overall, the AOMX calculation confirms the ligand field diagram of Mo(III) which has been extracted from the Tanabe-Sugano diagram of an octahedral $d^3$ high spin system (Scheme 5.1).[95, 102] The results of this calculation are shown in Table 5.1. The electronic ground state is represented by a non-degenerate $^4A_{2g}$ term originating from the splitting of the $^4F$ ground term in octahedral symmetry. The first three electronic transitions are spin-forbidden, as three low lying doublet states, $^2E_g$, $^2T_{1g}$ and $^2T_{2g}$, arise from the ligand field splitting of the excited $^2G$ term. If the weak absorption band at 11 600 $cm^{-1}$ is assigned to the $^4A_{2g} \rightarrow {}^2E_g(G)$ doublet transition in the AOM calculation, the other two spin-forbidden transitions, $^4A_{2g} \rightarrow {}^2T_{1g}(G)$

and $^4A_{2g} \rightarrow {}^2T_{2g}(G)$, are expected to appear at 12 100 $cm^{-1}$ and 18 300 $cm^{-1}$. In the experimental UV/Vis spectrum of the 2 mM complex solution, the $^4A_{2g} \rightarrow {}^2T_{1g}(G)$ transition might cause the asymmetry of band 1 at 11 600 $cm^{-1}$ without being resolved as an distinct absorption feature. However, the calculated energy of the $^4A_{2g} \rightarrow {}^2T_{2g}(G)$ transition does not really match the observed shoulder at 16 000 $cm^{-1}$ (band 2). On the other hand, if positioned at 18 300 $cm^{-1}$, this transition would be hard to detect next to the very intense band 4 at 25 000 $cm^{-1}$. If this absorption band is assigned to the first spin-allowed quartet transition (band I, $^4A_{2g} \rightarrow {}^4T_{2g}$) the second quartet transition (band II, $^4A_{2g} \rightarrow {}^4T_{1g}$) appears at 31 500 $cm^{-1}$ in the AOM calculation. This is in a very good agreement with the experimentally observed energy of band 5 at 31 300 $cm^{-1}$. The third spin-allowed transition, $^4A_{2g} \rightarrow {}^4T_{1g}(P)$, is then expected at an energy larger than 50 000 $cm^{-1}$ and thus is not observed in the experimental spectrum. In consequence, the UV/Vis bands 6 + 7 at 36 000 $cm^{-1}$ and 37 500 $cm^{-1}$ cannot be assigned to another d → d transition and must be associated with charge transfer processes instead. Here, especially the possibility of phenyl $\pi \rightarrow \pi^*$ transitions has to be considered as well.

Note that the interelectronic repulsion parameter (Racah-Parameter) of B = 610 $cm^{-1}$ obtained from the AOM calculation of the ligand field states (Table 5.1) is very high compared to the literature. In the case of the *fac*-[$Mo^{III}Br_3(NH_3)_3$] complex, a value of B = 377 $cm^{-1}$ has been determined for the molybdenum(III) ion from the UV/Vis absorption spectra.[197] However, if values of B < 500 $cm^{-1}$ were chosen in the AOM calculations, no reasonable results considering the energies of the ligand field states of [$MoBr_3P_3$] could be obtained anymore.

Including spin-orbit coupling into the ligand field calculations ($\zeta_{Mo(III)}$ = 820 $cm^{-1}$ [105]) an axial zero-field splitting value of $|D| = 4.2\ cm^{-1}$ is obtained for the $^4A_{2g}$ ground state. As the negative spin-orbit coupling of the three bromido ligands has not been included, this value appears to be too high. The sign of *D* cannot be extracted from the ligand field calculation in the case of an S = 3/2 system.

### 5.1.2 Low-temperature MCD Spectrum

The low-temperature MCD spectrum of [$MoBr_3P_3$] (Figure 5.3) shows relatively low intensities. In consequence, baseline subtraction was difficult. Nevertheless, two very broad, but partly structured, positive absorption features without zero-crossings are observed between 20 000 $cm^{-1}$ and 38 000 $cm^{-1}$ at positive magnetic field strengths. By spectral deconvolution, these could be modeled by two sets of three and four Gaussian curves, respectively (Figure 5.3, right).

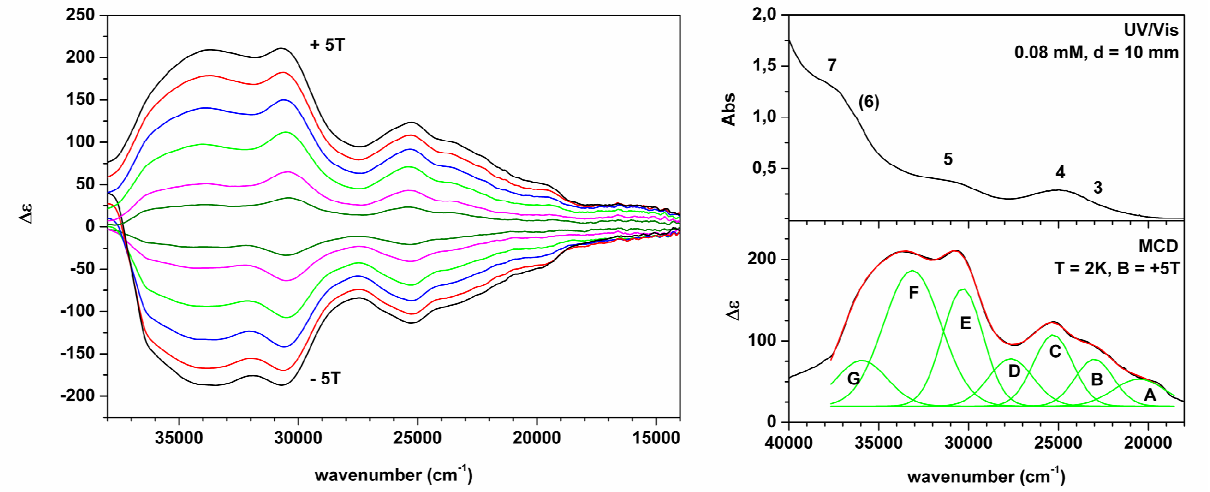


**Figure 5.3. left:** Low-temperature MCD spectrum of [$MoBr_3P_3$], measured in a thin film of polystryrene/$CH_2Cl_2$ at T = 2 K and magnetic field strengths varied from B = -5 T to +5 T. The sample was prepared from a 1 mM complex solution. **right:** Gaussian curve fit of the low-temperature MCD spectrum at B = 5 T between 20 000 $cm^{-1}$ and 38 000 $cm^{-1}$ and UV/Vis absorption spectrum ($CH_2Cl_2$, 0.08 mM, d = 10 mm) for comparison.

The MCD bands A – D roughly correspond to the first UV/Vis absorption feature (band 3; 4) between 20 000 $cm^{-1}$ and 28 000 $cm^{-1}$. The MCD band C shows a higher intensity than the bands A, B and D and is found in the spectral region of the UV/Vis absorption maximum at 25 000 $cm^{-1}$ (band 4). Note that the energy of the MCD band B might correspond to a possible low-intensity absorption band 3 at around 22 500 $cm^{-1}$ which is not resolved as an individual transition in the UV/Vis spectrum (Figure 5.2). The other three positive MCD bands E – G show comparatively high intensities. The MCD bands E and G correspond to the observed UV/Vis absorption band 5 at 31 300 $cm^{-1}$ and band 6 at 36 000 $cm^{-1}$. In contrast, the absorption band corresponding to the MCD band F is not observed but probably hidden beneath the strong absorbance in the high-energy region of the UV/Vis spectrum. An MCD band corresponding to the UV/Vis absorption band 7 at 37 500 $cm^{-1}$ is only observed as a very

small shoulder in the corresponding MCD spectrum and was not included in the Gaussian curve fits.

A detailed assignment of the observed MCD bands (and UV/Vis absorption features) to the individual electronic transitions was developed based on time-dependent DFT calculations and molecular orbital considerations and will be described in the following.

### 5.1.3 DFT Calculation of the Molecular Orbitals

*Molecular orbitals of [$MoBr_3P_3^H$]*

The molecular orbitals of [$MoBr_3P_3$] were first constructed from MO calculation of a simplified model complex in which the phenyl groups of the $P_3$ ligand were abbreviated by hydrogen atoms. This truncated complexes will be denoted as [$MoBr_3P_3^H$] in the following.[2]

As expected, three singly occupied (d*xz*, d*yz*, d*xy*, 47A – 49A, $t_{2g}$) and two unoccupied ($dz^2$, $dx^2$-$y^2$, 50/51A, $e_g$) molybdenum d-orbitals were obtained among the *alpha* spin orbitals. In contrast to the schematic ligand field diagram shown in Figure 5.1 (right) both the $t_{2g}$ and the $e_g$ molybdenum d-orbitals are almost degenerate in the molecular orbital scheme of [$MoBr_3P_3^H$]. Nearly no spin polarization is observed between the *alpha* and *beta* spin orbitals, so only the *alpha* spin orbitals are depicted in Figure 5.4.

Using the simplified [$MoBr_3P_3^H$] model complex, it can be seen that the bromido ligand MOs of a trigonal complex are generally constructed by combining two p-orbitals of two of the three bromido ligands, $Br_x$, $Br_y$ and $Br_z$ (Figure 5.4, Table 5.2). In consequence, three symmetric and three antisymmetric $p_\pi$ orbitals, $p_{xy}$, $p_{xz}$ and $p_{yz}$, i.e. one in each molecular plane, are obtained. To some extent they can be derived from and still correlated with the symmetric and antisymmetric in-plane and out-of-plane chlorido p-orbitals of the $C_S$

[2] Note that no DFT geometry optimization was performed for the truncated [$MoBr_3P_3^H$] model complex before the DFT calculation of the molecular orbitals. Instead, atom coordinates obtained from the X-ray crystal structure were used.

symmetric [Mo(O)$Cl_3$*dppe*] (*vide supra*, chapter 3), which is a molybdenum(V) complex but also facially coordinated by three halogenido ligands.

**Table 5.2.** DFT calculation of the molecular orbitals of the truncated [$MoBr_3P_3^H$] complex (BP86/LANL2DZ).

| | orbital | $Mo^{3+}$ | $Br_x$ | $Br_y$ | $Br_z$ | description | ligand $C_S$ |
|---|---|---|---|---|---|---|---|
| 51 | $x^2$-$y^2$ | d$x^2$-$y^2$ | $\sigma_2$(Br + P) | | -- | σ–antibonding, unoccupied metal d-orbital | $\sigma_2(Br_{eq}$ + P) |
| 50 | $z^2$ | d$z^2$ | $\sigma_{sym}$(Br + P) | | | σ–antibonding, unoccupied metal d-orbital | $\sigma_{sym.}(Br_{eq, ax}$ + P) |
| 49 | ***xy*/$p_{xy}$(s)** | d*xy* | $p_{xy}$(s) | | ($p_y$) | π–antibonding, singly occupied metal d-orbital | $p_{in\text{-}plane}$(s) |
| 48 | ***yz*/$p_{yz}$(s)** | d*yz* | ($p_y$) | $p_{yz}$(s) | | π–antibonding, singly occupied metal d-orbital | $p_{out\text{-}of\text{-}plane}$(a) |
| 47 | ***xz*/$p_{xz}$(s)** | d*xz* | $p_{xz}$(s) | ($p_x$) | $p_{xz}$(s) | π–antibonding, singly occupied metal d-orbital | $p_{out\text{-}of\text{-}plane}$(s) |
| 46 | **$p_{xz}$(a)** | -- | $p_z$ | ($p_z$) | $p_x$ | bromido p-orbital, antisymm. linear combination | $p_{out\text{-}of\text{-}plane}$(s) |
| 45 | **$p_{yz}$(a)** | -- | ($p_z$) | $p_z$ | $p_y$ | bromido p-orbital, antisymm. linear combination | $p_{out\text{-}of\text{-}plane}$(a) |
| 44 | **$p_{xy}$(a)** | -- | $p_y$ | $p_x$ | $p_y$ | bromido p-orbital, antisymm. linear combination | $p_{in\text{-}plane}$(a) |
| 43 | **$p_{xz}$(s)/*xz*** | d*xz* | $p_z$ | $p_z$ | $p_x$ | $p_{out\text{-}of\text{-}plane}$(s), π–bonding analogue of MO 47 | **$p_{out\text{-}of\text{-}plane}$(s)** |
| 42 | **$p_{yz}$(s)/*yz*** | d*yz* | $p_z$ | $p_z$ | $p_y$ | $p_{out\text{-}of\text{-}plane}$(a), π–bonding analogue of MO 48 | **$p_{out\text{-}of\text{-}plane}$(a)** |
| 41 | **$p_{xy}$(s)/*xy*** | d*xy* | $p_y$ | $p_x$ | $p_y$ | $p_{in\text{-}plane}$(s), π–bonding analogue of MO 49 | **$p_{in\text{-}plane}$(s)** |
| 40 | **$p_{\sigma 1}$** | -- | $\sigma_1$(Br + P) | | $p_y$ | bromido p-orbital, $p_y(Br_z)$ bonding | -- |
| 39 | **$p_{xy}(s)_{px}$** | -- | $p_{xy}(s)p_x$ | | $p_x$ | $p_{in\text{-}plane}$(s), $p_x$ ($Br_z$) antibonding | **$p_{in\text{-}plane}$(s)** |
| 38 | **$p_{xy}(s)_{px}$** | (d*xy*) | $p_{xy}(s)p_x$ | | $p_x$ | $p_{in\text{-}plane}$(s), $p_x$ ($Br_z$) bonding | **$p_{in\text{-}plane}$(s)** |
| 37 | $z^2/\sigma_{sym}$ | d$z^2$ | $\sigma_{sym}$(Br + P) | | | σ–bonding, bonding analogue of MO 50 | $\sigma_{sym.}(Br_{eq, ax}$ + P) |
| 36 | $x^2$-$y^2/\sigma_2$ | d$x^2$-$y^2$ | $\sigma_2$(Br + P) | | -- | σ–bonding, bonding analogue of MO 51 | $\sigma_2(Br_{eq}$ + P) |

The symmetric $p_\pi$ orbitals, $p_{xy}$(s), $p_{xz}$(s) and $p_{yz}$(s), are observed both in bonding (41 – 43, occupied) and antibonding (47 – 49, singly occupied) linear combinations with the appropriate $t_{2g}$ molybdenum d-orbitals. They can also be described as the symmetric and antisymmetric in-plane and out-of-plane p-orbitals, $p_{out\text{-}of\text{-}plane}$(s) (43, 47), $p_{out\text{-}of\text{-}plane}$(a) (42, 48) and $p_{in\text{-}plane}$(s) (41, 49), of the equatorial bromido ligands. In contrast, the antisymmetric $p_{xy}$(a), $p_{xz}$(a) and $p_{yz}$(a) orbitals are not stabilized by the metal d-orbitals and thus show pure bromido p-character (44 - 46). In addition, three $p_\sigma$ orbitals with zero ($\sigma_{sym}$), one ($\sigma_1$) and two ($\sigma_2$) nodal planes are expected. The all-symmetric $\sigma_{sym}$ orbital and the antisymmetric $\sigma_2$ orbital are observed in bonding and antibonding linear combinations with the d$z^2$ orbital (37, 50) and the d$x^2$-$y^2$ orbital (36, 51), respectively. The antisymmetric $\sigma_1$ ligand orbital is found in a bonding combination with the $p_y$ orbital of the axial bromido ligand $Br_z$ (40) but cannot be stabilized by any of the molybdenum d-orbitals. The molecular orbitals 38 and 39 are symmetric in-plane bromido p-orbitals, $p_{xy}(s)_{px}$, in the bonding and antibonding linear

combination with the $p_x$ orbital of the axial bromido ligand $Br_z$, which show a kind of trigonal symmetry.

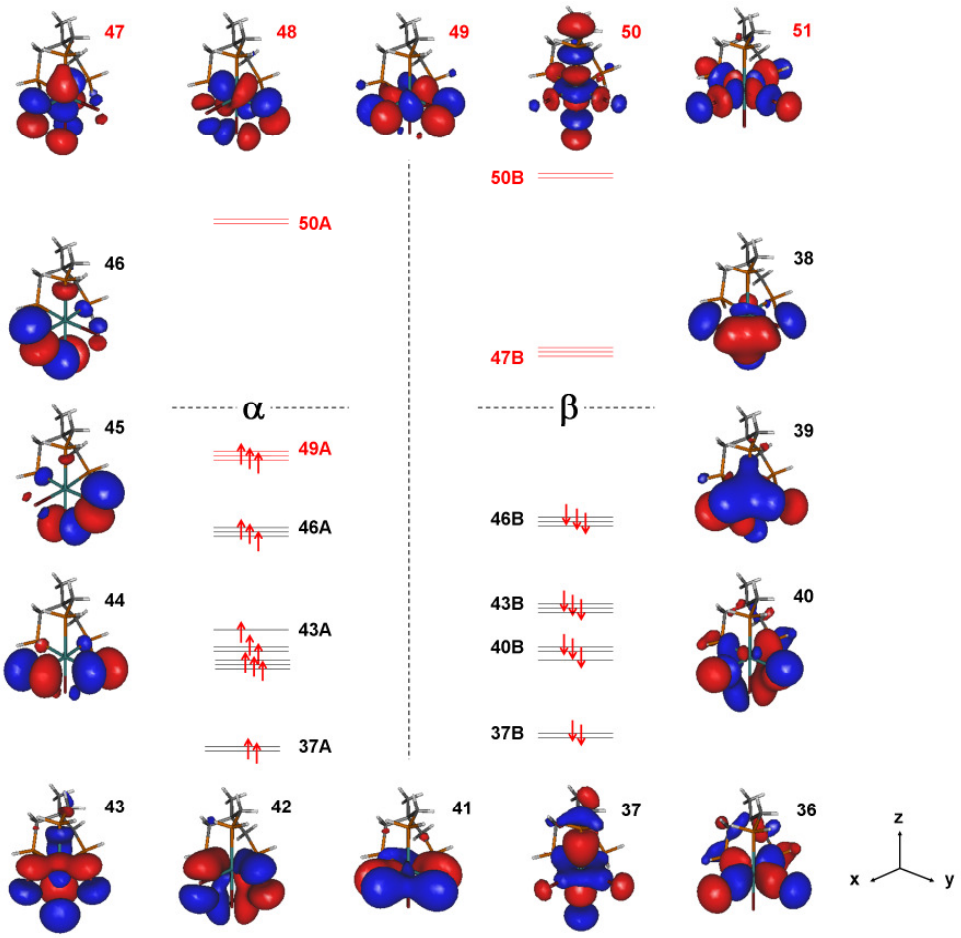


**Figure 5.4.** Molecular orbitals of the simplified [$MoBr_3P_3^H$] model complex (BP86/LANL2DZ). The phenyl groups of the $P_3$ ligand are abbreviated by hydrogen atoms.

*Molecular orbitals of [$MoBr_3P_3$]*

If the phenyl groups of the $P_3$ ligand are *not* abbreviated by hydrogen atoms, the description of the molecular orbitals obtained for the original, non-simplified [$MoBr_3P_3$] complex is quite difficult (Figure 5.5, Table 5.3).

.

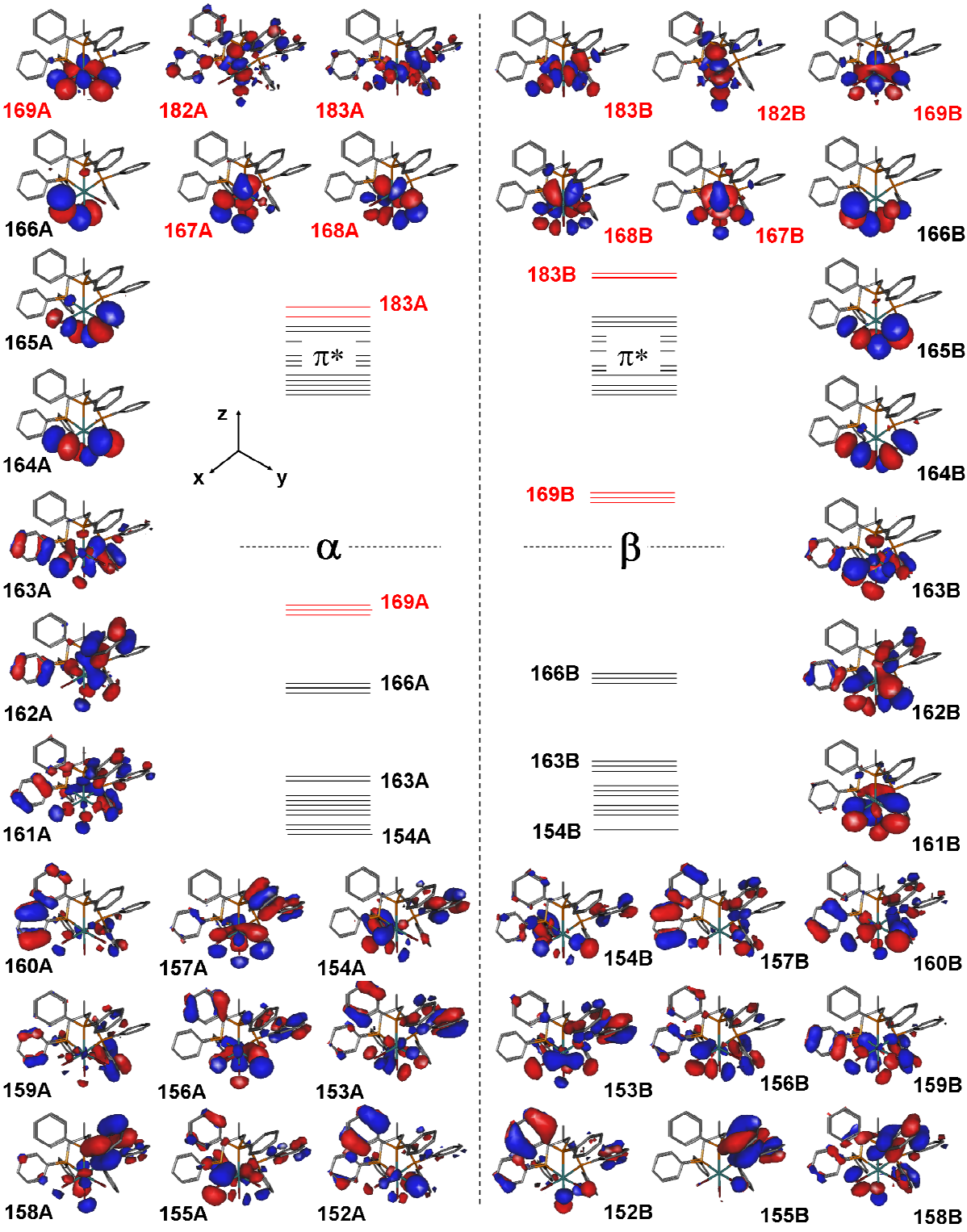


**Figure 5.5.** Molecular orbitals of [$MoBr_3P_3$], (BP86/LANL2DZ). Hydrogen atoms are omitted for clarity.

**Table 5.3.** Molecular orbitals of the non-simplified [$MoBr_3P_3$] complex (BP86/LANL2DZ).

| α/β spin | | $Mo^{3+}$ | $Cl_x$ | $Cl_y$ | $Cl_z$ | description |
|---|---|---|---|---|---|---|
| 177, 183 | $x^2$-$y^2$ | d$x^2$-$y^2$ | $\sigma_2$(Cl + P) | | -- | σ–antibonding, unoccupied metal d-orbital |
| 176, 182 | $z^2$ | d$z^2$ | ($\sigma_{sym}$.(Cl + P)) | | $p_z$ | σ–antibonding, unoccupied metal d-orbital |
| 170-181 [b] | π* | (d$x^2$-$y^2$, d$z^2$) | -- | -- | -- | phenyl π* orbitals with small contributions of the molybdenum d$z^2$ and d$x^2$-$y^2$ orbitals |
| 169 | **$xy/p_{xy}$(s)** | d$xy$ | $p_{xy}$(s) | | -- | π–antibonding, singly occupied metal d-orbital |
| 168 | **$yz/p_{yz}$(s)** | d$yz$ | ($p_y$) | $p_{yz}$(s) | | π–antibonding, singly occupied metal d-orbital |
| 167 | **$xz/p_{xz}$(s)** | d$xz$ | $p_{xz}$(s) | ($p_x$) | $p_{xz}$(s) | π–antibonding, singly occupied metal d-orbital |
| 166 | **$p_{xz}$(a)** | -- | $p_z$ | -- | $p_x$ | bromido p-orbital, antisymm. linear combination |
| 165 | **$p_{yz}$(a)** | -- | ($p_y$) | $p_z$ | $p_y$ | bromido p-orbital, antisymm. linear combination |
| 164 | **$p_{xy}$(a)** | -- | $p_y$ | $p_x$ | ($p_y$) | bromido p-orbital, antisymm. linear combination |
| 163A [a] | π | -- | -- | -- | -- | phenyl π-orbital, $p_{\sigma 1}$ |
| 163B [a] | **$p_{xz}$(s)/$xz$** | d$xz$ | | $p_{out\text{-}of\text{-}plane}$(s) | | π–bonding analogue of MO 167, $p_{out\text{-}of\text{-}plane}$(s) |
| 162A [a] | π | -- | -- | -- | -- | phenyl π-orbital, $p_{\sigma 1}$ |
| 162B [a] | **$p_{yz}$(s)/$yz$** | d$yz$ | | $p_{out\text{-}of\text{-}plane}$(a) | | π– bonding analogue of MO 168, $p_{out\text{-}of\text{-}plane}$(a) |
| 161A [a] | π | -- | -- | -- | -- | phenyl π-orbital, $p_{\sigma 1}$ |
| 161B [a] | **$p_{xy}$(s)/$xy$** | d$xy$ | | $p_{in\text{-}plane}$(s) | | π–bonding analogue of MO 169, $p_{in\text{-}plane}$(s) |
| 160A [a] | π | -- | -- | -- | -- | phenyl π-orbital |
| 160B [a] | π | -- | -- | -- | -- | phenyl π-orbital, $p_{\sigma 1}$ |
| 159A [a] | π | -- | -- | -- | -- | phenyl π-orbital |
| 159B [a] | π | -- | -- | -- | | phenyl π-orbital, $p_{\sigma 1}$ |
| 158A [a] | π | d$xz$ | | $p_{out\text{-}of\text{-}plane}$(s) | | π–bonding analogue of MO 167, phenyl π-orbital |
| 158B [a] | π | -- | -- | -- | -- | $p_{xz}$(s), phenyl p-orbital |
| 157A [a] | π | d$xz$ | | $p_{out\text{-}of\text{-}plane}$(s) | | π–bonding analogue of MO 167, phenyl π-orbital |
| 157B [a] | π | -- | -- | -- | -- | phenyl π-orbital |
| 156A [a] | π | d$xy$ | | $p_{in\text{-}plane}$(s) | | phenyl π-orbital (π–bonding analogue of MO 169) |
| 156B [a] | π | d$yz$ | | $p_{out\text{-}of\text{-}plane}$(a) | | phenyl π-orbital (π– bonding analogue of MO 168) |
| 155A [a] | π | d$yz$ | | $p_{out\text{-}of\text{-}plane}$(a) | | phenyl π-orbital (π– bonding analogue of MO 168) |
| 155B [a] | π | -- | -- | -- | -- | phenyl π-orbital |
| 154A [a] | π | d$yz$ | | $p_{out\text{-}of\text{-}plane}$(a) | | phenyl π-orbital (π– bonding analogue of MO 168) |
| 154B [a] | π | -- | -- | -- | -- | phenyl π-orbital (???) |
| 153A [a] | π | d$yz$ | | $p_{out\text{-}of\text{-}plane}$(a) | | phenyl π-orbital (π– bonding analogue of MO 168) |
| 153B [a] | π | -- | | $p_{in\text{-}plane}$(s) | | phenyl π-orbital ($p_{in\text{-}plane}$(s)) |
| 152A [a] | π | -- | -- | -- | -- | phenyl π-orbital |
| 152B [a] | π | -- | -- | -- | -- | phenyl p-orbital ($p_{yz}$(s)) |
| 145 [b] | $x^2$-$y^2$ | d$x^2$-$y^2$ | $\sigma_2$(Cl + P) | | -- | σ– bonding analogue of MO 183 |
| 144 [b] | $z^2$ | d$z^2$ | -- | $\sigma_{sym}$.(Cl + P) | | σ– bonding analogue of MO 182 |

[a] molecular orbitals lower than MO 164: mixed metal-ligand orbitals and pure bromido p-orbitals with very large contributions of phenyl π orbitals → theoretical assignment corresponding to [$MoBr_3P_3^H$] (MO 36 - 43)

[b] not shown in Figure 5.5

Again, the unoccupied molybdenum d$z^2$ and d$x^2$-$y^2$ orbitals ($e_g$, 182/183A) and the singly occupied d*xz*, d*yz* and d*xy* orbitals ($t_{2g}$, 167A – 169A), which all appear in antibonding linear combinations with the appropriate $p_\sigma$ and $p_\pi$ ligand orbitals, are almost degenerate. Corresponding to the truncated [$MoBr_3P_3^H$] complex, the highest occupied ligand orbitals are the three antisymmetric bromido $p_\pi$ orbitals $p_{xz}$(a), $p_{yz}$(a) and $p_{xy}$(a) (166 - 164). However, in the case of the non-simplified complex these are the only ligand orbitals which can be unambiguously identified within the molecular orbital scheme, as the molecular orbitals below MO number 164 show large contributions of the phenyl π-orbitals. A large extent of mixing, especially of the different ligand orbitals, and additional splittings are also observed here. In consequence, most of the individual ligand orbitals can no longer be determined systematically as demonstrated for the truncated [$MoBr_3P_3^H$] model complex above. However, as estimated mainly from the *beta* spin orbitals, they should also be assigned to the π-bonding analogues of the singly occupied $t_{2g}$ orbitals, i.e. the bonding symmetric metal-ligand orbitals $p_{xz}$(s)/*xz*, $p_{yz}$(s)/*yz* and $p_{xy}$(s)/*xy* as well as to the symmetric (trigonal) in-plane $p_{xy}(s)_{px}$ bromido p-orbitals in analogy to the simplified [$MoBr_3P_3^H$] model complex. The σ-bonding analogues of the unoccupied $e_g$ orbitals (MO 144/145, not shown in Figure 5.5) are not mixed with phenyl π-orbitals. The unoccuppied molecular orbitals 170 – 181, also not shown in Figure 5.5, mainly show phenyl π* character and have only very small contributions of d$z^2$ and d$x^2$-$y^2$

### 5.1.4 Calculation of the Electronic Transitions (UV/Vis) and Assignment of the MCD Spectrum

*Electronic transitions of [$MoBr_3P_3^H$]*

For a systematic assignment of the electronic transitions, a theoretical UV/Vis spectrum was again first calculated for the truncated [$MoBr_3P_3^H$] complex. The results are listed in Table 5.4. The calculated UV/Vis spectrum of [$MoBr_3P_3^H$] is depicted in Figure 5.6.

As the singly occupied $t_{2g}$ orbitals are almost degenerate in the molecular orbital scheme of [$MoBr_3P_3^H$] (*vide supra*, Figure 5.4), the metal-centered ligand field transitions are very close in energy (22 000 – 24 700 $cm^{-1}$). Very low intensities are predicted for these d → d bands. In consequence, the intense absorption bands 4 and 5, which are observed in the experimental

UV/Vis absorption spectrum at 25 000 $cm^{-1}$ and 31 000 $cm^{-1}$ and correlated with the MCD bands C and E (Figure 5.3, right) should with a great probability *not* be ascribed to d → d ligand field transitions. On the other hand, this has been indicated by the results of the AOMX ligand field calculations (*vide supra*).

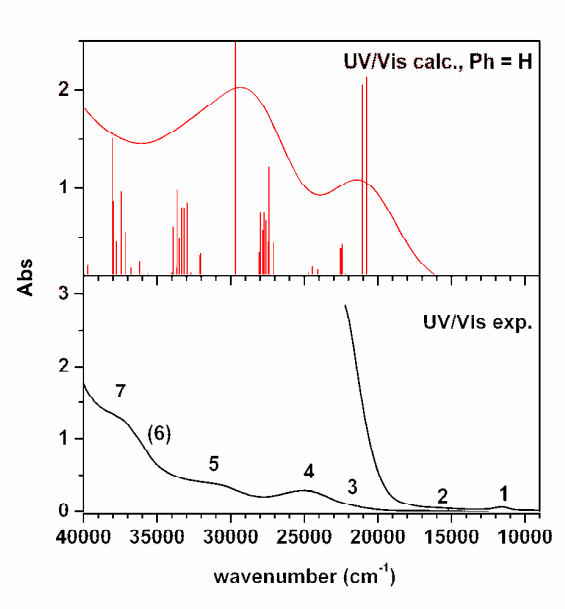


**Figure 5.6**. Experimental UV/Vis absorption spectra (**bottom**) of [$MoBr_3P_3$] ($CH_2Cl_2$, 0.08/2 mM, d = 10 mm) and calculated UV/Vis spectrum (**top**) of [$MoBr_3P_3^H$]. The calculated UV/Vis spectrum was computed with time-dependent DFT (B3LYP/LANL2DZ).

**Table 5.4.** TDDFT calculation of the electronic transitions of the simplified [$MoBr_3P_3^H$] model complex (B3LYP/LANL2DZ). Only d → d ligand field transitions and charge transfer transitions with oscillator strengths > 0.0020 are listed.

| energy ($cm^{-1}$) | oscillator strength | description | |
|---|---|---|---|
| **20 800** | 0.0214 | $p_{xy}$(a) → xy, $p_{xz}$(a) → yz | 44/46B → 48/49B |
| **21 100** | 0.0205 | $p_{xy}$(a) → yz | 44B → 48B |
| 22 200 | 0.0012, 0.0042 | yz, xy → $z^2$, xy → $x^2$-$y^2$ | 48/49A → 50A, 49A → 51A |
| **22 500** | 0.0038 | xz → $z^2$, $x^2$-$y^2$ | 47A → 50/51A |
| 24 100 | 0.0016 | yz, xy → $z^2$ | 48/49A → 50A |
| 24 400 | 0.0019 | xz → $z^2$, yz, xy → $x^2$-$y^2$ | 47-49A → 50/51A |
| 24 700 | 0.0013 | xz → $x^2$-$y^2$ | 47A → 51A |
| **27 100** | 0.0044 | $p_{xz}$(s)/xz → xz, xy | 43B → 47/48B |
| **27 400** | 0.0121 | $p_{xz}$(s)/xz → yz, xy | 43B → 48/49B |
| **27500** | 0.0044 | $p_{xz}$(s)/xz → xz, xy | 43B → 47/49B |
| **27 600** | 0.0066 | $p_{xy}$(s)/xy → yz, $p_{yz}$(s)/yz → xz, yz | 41/42B → 47-49B |
| **27 700** | 0.0074 | $p_{xy}$(s)/xy → xz, xy | 41B → 47/49B |
| **27 800** | 0.0057 | $p_{yz}$(s)/yz → xz | 42B → 47B |

| | | | |
|---|---|---|---|
| **28 000** | 0.0074 | $p_{yz}(s)/yz \rightarrow yz$ | 42B → 48B |
| **28 100** | 0.0034 | $p_{xy}(s)/xy \rightarrow yz$ | 41B → 48B |
| **29 700** | 0.0471 | $p_{xy}(s)/xy \rightarrow yz$ | 41B → 48B |
| **32 000** | 0.0033 | $p_{xz}(a) \rightarrow z^2, x^2\text{-}y^2$ | 46A → 50/51A |
| **32 100** | 0.0031 | $p_{xy}(s) \rightarrow xz, xy$ | 39B → 47/49B |
| **33 000** | 0.0085 | $p_{xy}(s) \rightarrow yz, xy$ | 39B → 48/49B |
| **33 200** | 0.0079 | $p_{xz}(a) \rightarrow z^2$ | 46A → 51A |
| **33 300** | 0.0080 | $p_{xy}(a) \rightarrow x^2\text{-}y^2$, $p_{xy}(s) \rightarrow xy$ | 44A → 51A, 38B → 49B |
| **33 500** | 0.0049 | $p_{xy}(a)$, $p_{yz}(a) \rightarrow z^2, x^2\text{-}y^2$ | 44/45A → 50/51A |
| **33 600** | 0.0098 | $p_{xy}(s) \rightarrow xz$, $p_{xy}(a) \rightarrow x^2\text{-}y^2$ | 38B → 47B, 44A → 51A |
| **33 900** | 0.0060 | $p_{xy}(s) \rightarrow xy$ | 38B → 49B |
| **36 200** | 0.0025 | $xz \rightarrow P$ | 47A → 52A |
| **37 200** | 0.0055 | $p_{xz}(a) \rightarrow x^2\text{-}y^2$ | 46B → 51B |
| **37 400** | 0.0096 | $p_{yz}(a) \rightarrow z^2$ | 45B → 50B |
| **37 800** | 0.0045 | $p_{yz}(a) \rightarrow x^2\text{-}y^2$ | 45B → 51B |
| **38 000** | 0.0086, 0.0151 | $p_{xy}(a)$, $p_{yz}(a) \rightarrow z^2, x^2\text{-}y^2$ | 44/45B → 50/51B |
| **39 700** | 0.0020 | $yz \rightarrow p_{phosphorus}$ (MLCT) | 48A → 53A |
| **40 800** | 0.0098 | $xy \rightarrow p_{phosphorus}$ (MLCT) | 49A → 54/56A |
| **41 400** | 0.0146 | $yz, xy \rightarrow p_{phosphorus}$ (MLCT) | 48/49A → 56A |
| **41 600** | 0.0023 | $p_{yz}(a) \rightarrow p_{phosphorus}$ (MLCT) | 45B → 52B |
| **41700** | 0.0024 | $xy \rightarrow p_{phosphorus}$ (MLCT) | 49A → 56A |
| **42 000** | 0.0022 | $p_{yz}(a)$, $xz \rightarrow p_P$ (MLCT) | 45 → 52, 47A → 55A |
| **42 700** | 0.0060 | $x^2\text{-}y^2/\sigma, z^2/\sigma \rightarrow xz, yz, xy$ | 36/37B → 47-49B |
| **42 900** | 0.0078 | $z^2/\sigma \rightarrow yz$, $p_{yz}(s)/yz \rightarrow z^2$ | 37B → 48B, 42A → 50A |
| **43 300** | 0.0084 | $x^2\text{-}y^2/\sigma \rightarrow xz$ | 36B → 47B |
| **43 600** | 0.0104 | $z^2/\sigma \rightarrow xy$ | 37B → 49B |

Considering the overall shape of the theoretical UV/Vis spectrum two very intense absorption features are found at 21 000 $cm^{-1}$ and 29 000 $cm^{-1}$ for the simplified model complex $[MoBr_3P_3^H]$. The first energy does not correspond to the first experimental UV/Vis absorption maximum at 25 000 $cm^{-1}$ (band 4) nor to the first positive signed MCD feature (band A - D). In the calculated UV/Vis spectrum, the 21 000 $cm^{-1}$ band arises from p → d ligand-to-metal charge transfer transitions from the different antisymmetric bromido $p_\pi$ orbitals (44B - 46B) into the singly occupied molybdenum d*yz* and d*xy* orbitals (48B, 49B). This would also correspond to the energy of the MCD band A quite well. Also the spin-allowed d → d ligand field transitions between the $t_{2g}$ and $e_g$ orbitals are made out within this spectral region. They are found at 22 500 $cm^{-1}$ and 24 400 $cm^{-1}$ in the calculated UV/Vis spectrum and could be

assigned to the low-intensity absorption band 3 which corresponds to the MCD band B. The transitions from the bonding metal-ligand orbitals (41B – 43B) into their antibonding $t_{2g}$ analogues (47B – 49B) appear at 27 700 – 29 700 $cm^{-1}$ which corresponds to the energy of the MCD band D or E. They are mainly predicted to show only moderate intensities and should be considered as an own type of electronic transitions ($t_{2g}$ bonding → antibonding) rather than being referred to as ordinary charge transfer. However, the most intense of these transitions, $p_{xy}(s)/xy \rightarrow dyz$ (41B → 48B), is found at 29 700 $cm^{-1}$. This rather supports the assignment of the MCD band E as a $t_{2g}$ bonding → antibonding transition.

Transitions from the symmetric (trigonal) in-plane bromido $p_{xy}(s)_{px}$ orbitals (38, 39) into the molybdenum $t_{2g}$ orbitals (47 - 49) appear between 33 000 $cm^{-1}$ and 33 900 $cm^{-1}$ in the theoretical spectrum of $[MoBr_3P_3^H]$ which would correspond to the MCD band F. Transitions in the spectral region of the MCD band G (35 900 $cm^{-1}$) have low to moderate intensities and arise from metal-to-ligand charge transfer from the singly occupied metal d-orbitals into unoccupied phosphorus p-orbitals The last type of transitions obtained in the calculated UV/Vis spectra below 40 000 $cm^{-1}$ is a ligand-to-metal charge transfer from the antisymmetric bromido $p_\pi$ orbitals (44B - 46B) into the unoccupied $e_g$ molybdenum d-orbitals (50/51B) between 37 100 $cm^{-1}$ and 37 500 $cm^{-1}$. LMCT transitions from the bonding $e_g$ metal-ligand orbitals 36B and 37B into the $t_{2g}$ molybdenum d-orbitals are predicted at energies greater than 42 000 $cm^{-1}$ with moderate intensities.

In general, transitions at energies greater than 40 000 $cm^{-1}$ mainly arise from metal-to-ligand charge transfer (MLCT) from the $t_{2g}$ molybdenum d-orbitals into unoccupied phosphorus p-orbitals and are only partly listed in Table 5.4.

*Electronic transitions of [$MoBr_3P_3$]*

As in the case of the truncated $[MoBr_3P_3^H]$ model complex, a distinct absorption maximum can be made out in the calculated UV/Vis spectrum of the non-simplified $[MoBr_3P_3]$ complex around 22 000 $cm^{-1}$ (Figure 5.7). This is the spectral region of the first experimental UV/Vis absorption bands 3 and 4 and the MCD bands A - D. Some of the most intense transitions in

the calculated UV/Vis spectrum are made out at 21 700 $cm^{-1}$ which corresponds the energy of MCD band A. They arise from ligand-to-metal charge transfer from the antisymmetric $p_{xy}(a)$, $p_{yz}(a)$ and $p_{xz}(a)$ bromido p-orbitals (164B - 166B) into the $t_{2g}$ molybdenum d-orbitals (167B - 169B). However, these are the only charge transfer transitions that can definitely be extracted from the TDDFT calculation of the non-simplified [$MoBr_3P_3$] complex, because the antisymmetric $p_\pi$ orbitals are the only ligand orbitals that can be clearly identified in the corresponding molecular orbital scheme (Figure 5.5). The metal centered ligand field transitions are observed at 23 200 $cm^{-1}$ with moderate intensities matching the position of MCD band B which possibly corresponds to a potential UV/Vis absorption band 3 (*vide supra*).

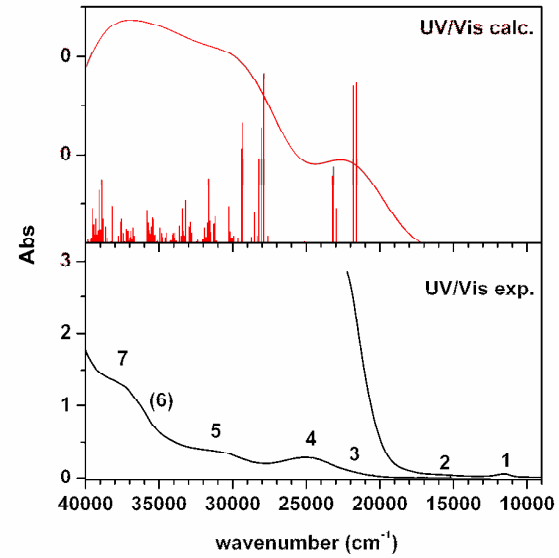


**Figure 5.7.** UV/Vis absorption spectra of [$MoBr_3P_3$]. The experimental UV/Vis spectra (**bottom**) were measured in $CH_2Cl_2$ (0.08/2 mM, d = 10 mm). The calculated UV/Vis spectrum (**top**) was computed using TDDFT (B3LYP/LANL2DZ).

As the molecular orbitals below MO number 164 cannot be clearly identified due to their strong mixing and the large contributions of the phenyl π and π∗ orbitals, the individual electronic transitions at calculated energies greater than 25 000 $cm^{-1}$ cannot really be assigned. Nevertheless, a very large number of transitions with low to moderate intensities is obtained between 30 000 $cm^{-1}$ and 40 000 $cm^{-1}$. Based on the MO scheme of the non-simplified complex they are mostly associated with $\pi \rightarrow d$ and $d \rightarrow \pi^*$ transitions, but do not provide more detailed information regarding UV/Vis and MCD band assignment.

**Table 5.5.** TDDFT calculation of the electronic transitions of (B3LYP/LANL2DZ). Only d → d ligand field transitions and charge transfer transitions with oscillator strengths > 0.0020 are listed.

| energy ($cm^{-1}$) | oscillator strength | description | |
|---|---|---|---|
| **21 600** | 0.0173 | $p_{xz}(a) \rightarrow xz/p_{xz}(s)$ | 166B → 168B |
| **21 800** | 0.0170 | $p_{xy}(a) \rightarrow xy/p_{xy}(s)$ | 164B → 169B |
| **23 000** | 0.0045 | yz → π*/d | 168A → 176A |
| **23 200** | 0.0087 | xz → π*/d | 167A → 171/173A, 180A |
| | 0.0078 | xy → π*/d | 169A → 172/177A |
| **27 900** | 0.0183 | $p_{out\text{-}of\text{-}plane}(s, a) \rightarrow yz, xz$ | 163B → 168B, 162B → 167B |
| **28 000** | 0.0127 | $p_{out\text{-}of\text{-}plane}(a), p_{in\text{-}plane}(s) \rightarrow xz, yz$ | 161/162B → 167/168B |
| **28 500** | 0.0040 | $p_{out\text{-}of\text{-}plane}(s) \rightarrow xy$ | 163B → 169B |
| **29 300** | 0.0132 | $xy \rightarrow \pi^*/d, p_{in\text{-}plane}(s) \rightarrow xy$ | 169A →171A, 161B →169B |
| **29 400** | 0.0106 | $xy \rightarrow \pi^*/d, p_{out\text{-}of\text{-}plane}(a) \rightarrow yz$ | 169A → 171A, 162B → 168B |
| **30 200** | 0.0021 | yz → π*/d | 168A → 172A |
| **30 300** | 0.0047 | xz/yz → π*/d | 167/168A → 174A |
| **31 200** | 0.0036, 0.0024 | $xy \rightarrow \pi^*/d, \pi/p_{\sigma 1} \rightarrow xz/yz$ | 169A → 173/174/177A, 159/160B → 167/168B |
| **31 300** | 0.0029 | $\pi/p_{\sigma 1} \rightarrow xz/yz$, xz → π*/d | 160B → 167/168B, 167A → 174A |
| | 0.0027 | xz/yz → π*/d | 167/168A → 173/174/177A |
| **31 500** | 0.0021 | xz → π*/d | 167A → 173A |
| **31 600** | 0.0032 | $\pi/p_{\sigma 1} \rightarrow xy$ | 160B → 169B |
| **31 600** | 0.0075 | $xz/xy \rightarrow \pi^*/d, \pi/p_{\sigma 1} \rightarrow xy$ | 167/169A → 174/175/176A, 160B → 169B |
| **31 700** | 0.0030 | xy → π*/d | 169A → 175A |
| **31 900** | 0.0025 | $p_{xz}(s)/\pi/p_{\sigma 1} \rightarrow xz/xy$ | 158/159B → 167/169B |
| **32 800** | 0.0020 | $p_{xy}(a) \rightarrow \pi^*/d$ | 164B → 170B |
| **32 900** | 0.0031 | $p_{xz}(s) \rightarrow xy, p_{xz}(a) \rightarrow \pi^*/d$ | 158B → 169B, 166A → 171A |
| **33 000** | 0.0026 | $p_{xy}(a)/p_{yz}(a) \rightarrow \pi^*/d$ | 164/165A → 171/173A |
| **33 200** | 0.0053 | $xy \rightarrow \pi^*/d, p_{xy}(a)/p_{yz}(a) \rightarrow \pi^*/d$ | 169A → 178A, 164/165B → 171B |
| **33 400** | 0.0022, 0.0045 | $p_{yz}(a) \rightarrow \pi^*/d$, xy → π*/d | 165B → 171B, 169A → 178A |
| **33 500** | 0.0028 | $xz/yz \rightarrow \pi^*/d, p_{yz}(a) \rightarrow \pi^*/d$ | 166/167A → 172/178A, 165B → 171B |
| **33 600** | 0.0027 | yz → π*/d | 168A → 178A |
| **33 900** | 0.0020 | xz → π*/d | 167A → 178A |
| **34 000** | 0.0020 | xy → π*/d | 169A → 176/178/180A |
| **34 500** | 0.0020 | phenyl π → xz/yz | 156/157B → 167/168B |
| **34 800** | 0.0020 | phenyl π → yz | 157B → 168B |
| **35 000** | 0.0025 | phenyl π → xz/yz/xy | 153/157/158B → 167-169B |
| **35 400** | 0.0033 | $p_{xz}(a)$, xz, xy → π*/d | 166/167/169A → 172/174/181/183A |
| **35 500** | 0.0022-0.0035 | $xz \rightarrow \pi^*/d, p_{xy}(a), p_{xz}(a) \rightarrow \pi^*/d$, phenyl π → xz/xy | 167A → 181A, 164/166B → 175B, 153/155B → 167/169B |
| **35 700** | 0.0022, 0.0030 | phenyl π → xz, $p_{xy}(a), p_{yz}(a) \rightarrow \pi^*/d$ | 155B → 167B, 164/165B → 174/175B |
| **35 800** | 0.0024, 0.0043 | $p_{xy}(a), p_{yz}(a) \rightarrow \pi^*/d$, xy → $z^2$ | 164/165A → 172/174A, 169A → 182A |

However, compared to the truncated [$MoBr_3P_3^H$] complex, the remaining UV/Vis and MCD bands should also very likely be ascribed to the different LMCT transitions (*vide supra*). Some of the most intense transitions in the calculated UV/Vis spectrum of [$MoBr_3P_3$] can be assigned to the bonding → antibonding transitions into the singly occupied $t_{2g}$ orbitals if the molecular orbitals 161B – 163B are in fact assigned to be the bonding $t_{2g}$ metal-ligand orbitals. They are found at 29 400 $cm^{-1}$ which is the same energy as obtained previously for such transitions in the case of the truncated [$MoBr_3P_3^H$] complex and corresponds to the UV/Vis absorption band 5 at 31 300 $cm^{-1}$ as well as to the MCD band E at 30 300 $cm^{-1}$. The calculated electronic transitions of the non-simplified [$MoBr_3P_3$] complex are listed in Table 5.5. An assignment of the MCD bands F and G cannot directly be extracted from this calculation.

In conclusion, the assignment of a larger number of the observed UV/Vis and MCD bands based on TDDFT calculation of electronic transitions is only possible with the help of the molecular orbital scheme of the simplified [$MoBr_3P_3^H$] model. For the complete, non-simplified, complex [$MoBr_3P_3$], the (TD)DFT calculations yield only very little convincing information concerning UV/Vis and MCD band assignment as most of the molecular orbitals cannot clearly be identified due to the strong mixing of the metal and ligand orbitals with phenyl $\pi/\pi^*$ orbitals.

*Assignment of the electronic transitions based on molecular orbital considerations*

For both the truncated model complex [$MoBr_3P_3^H$] and the non-simplified [$MoBr_3P_3$] complex, the intensities that are predicted for the metal-centered ligand field transitions are not very high. However, the slight splitting within the $t_{2g}$ and the $e_g$ orbitals which is expected for an axially elongated coordination geometry, is not reflected in the calculated molecular orbital schemes of [$MoBr_3P_3^H$] and [$MoBr_3P_3$]. Nevertheless, the first two spin-allowed d → d transitions, bands I and II, should not have the same energies according to the ligand field diagram (Scheme 5.1) and are most likely separated by even more than 2 000 $cm^{-1}$ as has been calculated for [$MoBr_3P_3^H$]. From the TDDFT calculations, they are found at 22 500 $cm^{-1}$ and 24 400 $cm^{-1}$ for the truncated [$MoBr_3P_3^H$] model complex and at 23 200 $cm^{-1}$ in the case of the non-simplified [$MoBr_3P_3$] complex. The latter energy approximately matches the energy of

the MCD band B at 23 000 $cm^{-1}$. Assigning this MCD band to the first spin-allowed ligand field transition (band I) and having in mind that this MCD band might correspond to a low-intensity UV/Vis absorption band 3 at around 22 500 $cm^{-1}$, the AOMX ligand field calculation was repeated. From the new results the second spin-allowed d → d transition (band II) is now expected around 26 700 $cm^{-1}$ ($\Delta E$ = 3 700 $cm^{-1}$, Table 5.6) and can be assigned to the MCD band D at 27 000 $cm^{-1}$. Another argument in favor of this assignment is that the MCD bands B and D ($\Delta E$ = 4 700 $cm^{-1}$) show similar intensities. It is also supported by the literature, as the first two spin-allowed ligand field transitions of the facially coordinated molybdenum(III) complex *fac*-[$MoBr_3(NH_3)_3$] had been reported at 23 800 $cm^{-1}$ and 28 100 $cm^{-1}$.[197]

The results of the second AOMX ligand field calculation in general seem to be more reasonable. An overview is given in Table 5.6. The variation of the σ-bonding parameter for the bromido ligands ($e_\sigma$1) is not as large when compared to the previous calculation (Table 5.1) and also the Racah interelectronic repulsion parameter of B = 350 $cm^{-1}$ is now in the range of what was reported in the literature (*vide supra*).[197] However, there are still some differences between experimental and calculated energies (Table 5.6, left). They might probably be explained by structural differences between the crystal structure (used for the calculation) and the actual complex structure in $CH_2Cl_2$ solutions (used for recording the experimental UV/Vis spectra).

If the assignment of the MCD bands B and D as d → d transitions is correct, the MCD bands A and C – G must arise from the various (ligand-to-metal) charge transfer transitions. According to the molecular orbital scheme of the simplified model complex [$MoBr_3P_3^H$] the lowest energy ligand-to-metal charge transfer should be the $p_\pi(a) \rightarrow t_{2g}$ transition. According to the TDDFT calculated energies the MCD band A can indeed clearly be assigned as $p_{xy}(a)/p_{yz}(a)/p_{xz}(a) \rightarrow t_{2g}$ LMCT transitions, although much higher intensities are predicted for these transitions in the theoretical spectra. However, if a splitting of the $t_{2g}$ orbitals takes place for an axial elongated octahedral complex geometry, not only the d → d transitions are expected to be split into more than one band, but also the individual charge transfer transitions should be split. Based on that, an additional band is also expected for the $p_\pi(a) \rightarrow t_{2g}$ transitions. Within this spectral region this can only be band C. Band A therefore should be assigned to the $p_{xz}(a), p_{yz}(a) \rightarrow d_{xy}$ transition, while band C, corresponding to the UV/Vis

absorption band 4 at 25 000 $cm^{-1}$, is assigned to the $p_{xy}(a) \rightarrow dxy$ transition. As the second transition completely occurs within the *xy*-plane it is expected to show a higher intensity than the first one and this is just what is observed in the MCD spectrum, as band C shows a significantly higher intensity than band A.

The assignment of the MCD bands E - G is not as easy, though. Strictly following the molecular orbital scheme of the simplified [$MoBr_3P_3^H$] model complex and based on the corresponding TDDFT calculation, the MCD band E must be assigned to the bonding → antibonding transitions from the bonding $t_{2g}$ metal-ligand orbitals $p_{xy}(s)$/xy, $p_{yz}(s)$/yz and $p_{xz}(s)$/xz into their singly occupied antibonding analogues. The MCD band F then is suggested to be assigned to LMCT transitions from the two symmetric in-plane bromido $p_{xy}(s)_{px}$ orbitals (38B, 39B) into the singly occupied molybdenum d-orbitals. Note that this is the most intense transition in the MCD spectrum of [$MoBr_3P_3$]. For the assignment of the MCD band G corresponding to the UV/Vis absorption band 6 or 7 at 35 500 - 37 500 $cm^{-1}$, ligand-to-metal charge transfer from the antisymmetric bromido $p_\pi$ orbitals $p_{xz}(a)$, $p_{yz}(a)$ and $p_{xy}(a)$ into the unoccupied molybdenum d orbitals ($dz^2$, $dx^2$-$y^2$, $e_g$) could be suggested.

As no unoccupied phosphorus p-orbitals are obtained from the DFT calculations of the molecular orbitals in the case of the non-simplified [$MoBr_3P_3$] complex, MLCT transitions from the singly occupied molybdenum d-orbitals into phosphorus p-orbitals are not considered as a probable assignment of the MCD band G. The bonding → antibonding transitions from the bonding $dz^2/\sigma_{sym}$ and $\sigma_2/dx^2$-$y^2$ orbitals into the unoccupied $e_g$ molybdenum d-orbitals should be expected at significantly higher energies and are therefore also excluded here for the assignment of band 6 and 7.

A complete assignment of the UV/Vis and MCD transitions is summarized in Table 5.6 (left). The final assignment of the UV/Vis and MCD spectra of [$MoBr_3P_3$] will be presented in comparison with the electronic transitions of the [$MoCl_3P_3$] and [$MoCl_3SiP_3$] complexes discussed below.

**Table 5.6.** [$MoBr_3P_3$]: **left**: Assignment of the UV/Vis and MCD bands based on the AOMX calculation of the ligand field states as well as TDDFT calculations electronic transitions. **Right:** Overview of the corresponding AOM parameters. All parameters and energies are given in $cm^{-1}$.

| | UV/Vis | MCD | calc. |
|---|---|---|---|
| $^4A_{2g}$ **(F)** | 0 | -- | 0 |
| $^2E_g$ **(G)** | (1) 11 600 | -- | 10 500 |
| $^2T_{1g}$ **(G)** | | -- | 10 700 |
| $^2T_{2g}$ **(G)** | (2) ~ 16 000 | -- | 16 500 |
| | | (A) 20 500 [a] | |
| $^4T_{2g}$ **(F)** | (3) ~ 22 500 | (B) 23 000 | 23 000 |
| | (4) 25 000 | (C) 25 300 [a] | -- |
| $^4T_{1g}$ **(F)** | | (D) 27 700 | 26 800 |
| | (5) 31 300 | (E) 30 300 [a] | -- |
| | | (F) 33 100 [a] | -- |
| | (6) ~ 36 000 | (G) 35 900 [a] | -- |
| | (7) 37 500 | -- | -- |
| $^4T_{1g}$ **(P)** | -- | -- | 47 900 |

[a] (LM)CT transitions are assigned from TDDFT (*vide supra*)

| | input | fit |
|---|---|---|
| $e_\sigma$**1** | 5 050 | 6930 |
| $e_\pi$**1** | 690 | 690 |
| $e_\sigma$**2** | 7 500 | 7 500 |
| $e_\pi$**2** | -1 500 | -1 500 |
| **B** | 350 [b] | 350 |
| **C** | 1500 | 2250 |

[b] Lit.[197]: B = 377 $cm^{-1}$

### 5.1.5 EPR Spectra

The low-temperature cw X-band EPR spectrum of [$MoBr_3P_3$] shows the two signals which are characteristic for a $d^3$ high spin (S = 3/2) system (Figure 5.8). Based on the splitting scheme shown in Figure 5.8 (right) they can be assigned to the $|-3/2\rangle \rightarrow |+3/2\rangle$ (signal I, absorption band shape) and $|-1/2\rangle \rightarrow |+1/2\rangle$ (signal II, derivative band shape) transitions at the $B_0 \parallel z$ orientation of the applied magnetic field. As the axial zero-field splitting is larger than the X-band microwave frequency (~ 9 GHz ≙ 0.3 $cm^{-1}$)[164] a transition *between* the two Kramers doublets is <u>not</u> possible. An additional signal would be expected arising from the $|-1/2\rangle \rightarrow |+1/2\rangle$ transition in the $B_0 \parallel x$ orientation of the applied magnetic field,[164] but it is hidden beneath the asymmetric tail of signal I. A non-zero rhombic zero-field splitting parameter ($E \neq 0$) results in a slight splitting of signal I[164] which is also observed here (Figure 5.8). Unfortunately a simulation of the low-temperature EPR spectrum using the XSophe simulation software[1] was not successful so far, so that absolute values of $D$ and $E$ cannot be given at this stage.

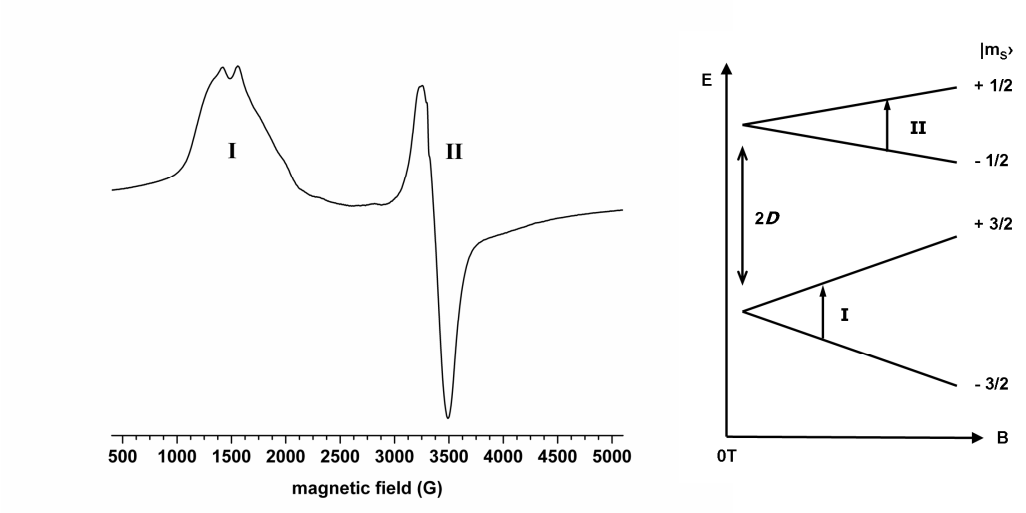


**Figure 5.8.** l**eft**: Low-temperature cw X-band EPR spectrum of [$MoBr_3P_3$], measured in a frozen $CH_2Cl_2$ solution, T = 3.7 K (microwave frequency 9.386 GHz, microwave power 2 mW, modulation amplitude 10 G. modulation frequency 100 kHz). **right**: axial zero-field splitting of the two Kramers doublets of an S = 3/2 system ($D < 0$, $|D| > 0.3$ cm$^{-1}$, $E = 0$)

At room temperature, only the $|-1/2\rangle \rightarrow |+1/2\rangle$ transition is observed in the X-band EPR spectrum of [$MoBr_3P_3$]. While no hyperfine splitting is observed in the low-temperature EPR spectrum, a well-resolved quartet is obtained in the solution spectrum at room temperature (Figure 5.9). This spectral signature arises from the coupling of the electron spin with the nuclear spin of the three phosphorus atoms of the $P_3$ ligand ($\boldsymbol{I}(^{31}P) = 3/2$). It is not very well resolved in the experimental spectrum, but can clearly be made out in the spectral simulation. The parameters for the best match obtained from a spectral simulation using the XSophe simulation software suite[1] are $A_{iso}(^{95/97}Mo) = 35$ G and $A_{iso}(^{31}P) = 24\text{G} \triangleq 22.3 \cdot 10^{-4}\text{cm}^{-1}$ (anisotropic simulation: $A_{xx} = 25$ G, $A_{yy} = 15$ G $A_{zz} = 35$ G). The isotropic hyperfine splitting parameter of the $^{95/97}$Mo coupling is close to other Mo(III) complexes (*vide infra*, chapter 6). Also the $A(^{31}P)$ value is within the typical range (10 - 25 G) of $^{31}$P hyperfine coupling in molybdenum complexes containing phosphorus ligands.[165]

The correlation between the experimental and simulated spectrum is not very good with respect to the intensity ratios within the observed signal, but could not be further improved so far. The room temperature EPR measurement should be repeated with modified parameters. Especially a lower modulation amplitude and frequency could lead to a better resolution of the $^{31}$P hyperfine coupling. In this way a better correlation between experimental and simulated spectra could be achieved.

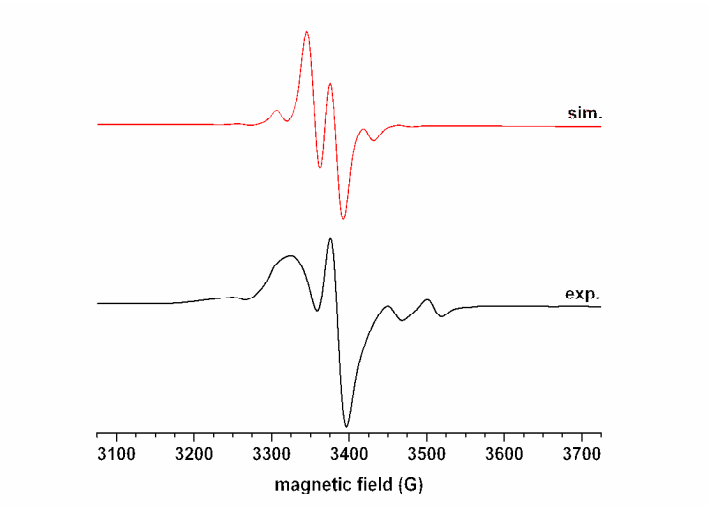


**Figure 5.9.** Room temperature cw X-band EPR spectrum of $[MoBr_3P_3]$, measured in $CH_2Cl_2$ (microwave frequency 9.366 GHz, microwave power 2 mW, modulation amplitude 10 G, modulation frequency 100 kHz) and spectral simulation (XSophe, g = 1.99, $A_{iso}(^{95/97}Mo)$ = 35 G, $A_{iso}(^{31}P)$ = 24 G ($A_{xx}$ = 25 G, $A_{yy}$ = 15 G $A_{zz}$ = 35 G), line width 10 G).

## 5.2 $[MoCl_3P_3]$

To provide a comparison to the UV/Vis and EPR spectra of $[MoBr_3P_3]$, the UV/Vis and EPR data of the corresponding chlorido analogue, $[MoCl_3P_3]$, was analyzed. The DFT geometry optimized complex structure of $[MoCl_3P_3]$ shown in Figure 5.10 was used for the (TD)DFT calculations of the molecular orbitals and electronic transitions as well as for the ligand arrangement of the AOMX input geometry. Virtually no differences are obtained compared to $[MoBr_3P_3]$ with respect to bond distances and bond angles, except for the Mo-X ($X = Cl^-, Br^-$) bond lengths, of course.

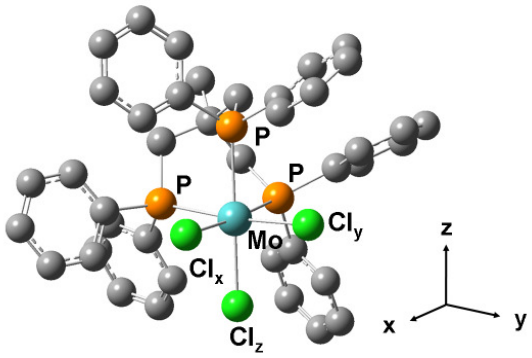


**Figure 5.10.** Complex structure of $[MoCl_3P_3]$ obtained from a DFT quantum chemical geometry optimization (B3LYP/LANL2DZ), hydrogen atoms are omitted for clarity.

### 5.2.1 UV/Vis Absorption Spectrum and Ligand Field Calculations (AOM)

The UV/Vis absorption spectrum of $[MoCl_3P_3]$ shows some differences compared to the UV/Vis spectrum of the corresponding bromido complex with respect to the energies and the intensities of particular absorption bands (Figure 5.11). Of course, this is somewhat expected, as the ligand field splitting is different in both complexes. Especially the d → d ligand field transitions should shift towards higher energies upon the increased ligand field strength of the halogenido ligands from $[MoBr_3P_3]$ to $[MoCl_3P_3]$.

In the UV/Vis spectrum of $[MoCl_3P_3]$, two very intense absorption bands at 28 000 $cm^{-1}$ (band 4) and 36 200 $cm^{-1}$ (band 6) and a clear shoulder at 33 200 $cm^{-1}$ (band 5) are made out at low concentrations. Band 6 clearly shows a vibrational structure ($\Delta E \sim 1\,000$ $cm^{-1}$) which has not been observed in the UV/Vis spectrum of the bromido complex. In the case of

$[MoCl_3P_3]$, absorption band 4 is clearly asymmetric indicating that another band could be hidden beneath resulting in the weak shoulder found at around 29 000 $cm^{-1}$. An additional absorption band of lower intensity is observed at 24 000 $cm^{-1}$ (band 3). At very high concentrations the spin-forbidden $^4A_{2g} \rightarrow {}^2E_g$, $^2T_{2g}$ and $^4A_{2g} \rightarrow {}^2T_{1g}$ doublet transitions are observed at 11 900 $cm^{-1}$ (band 1) and 17 000 $cm^{-1}$ (band 2), respectively. Compared to $[MoBr_3P_3]$ the latter is made out more clearly as the following absorption band 3 (centered at 24 000 $cm^{-1}$) shows less intensity in the UV/Vis spectrum of $[MoCl_3P_3]$. This band should be assigned to the first spin-allowed ligand field transition, $^4A_{2g} \rightarrow {}^2T_{2g}$, (band I). In the case of the bromido complex, it has been assigned to the MCD band B at 23 000 $cm^{-1}$ which might correspond to a potential UV/Vis absorption band 3 at ~ 22 500 $cm^{-1}$.

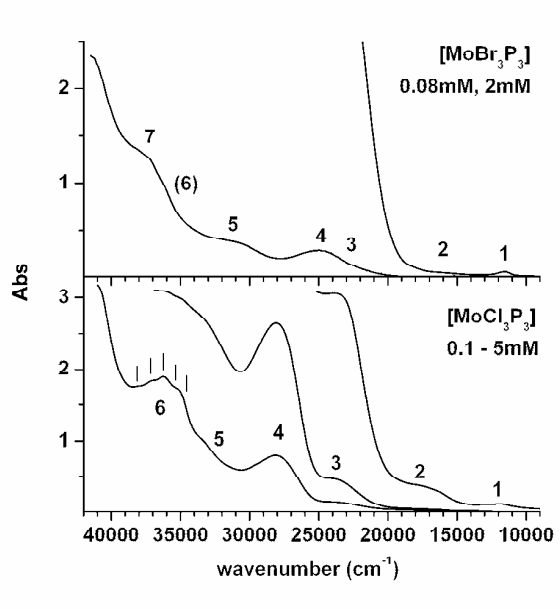


**Figure 5.11.** UV/Vis absorption spectra of $[MoCl_3P_3]$ (**bottom**) and $[MoBr_3P_3]$ (**top**), measured in $CH_2Cl_2$ (d = 10 mm) at different concentrations ($[MoBr_3P_3]$: 0.08/2 mM; $[MoCl_3P_3]$: 0.1/0.5/5 mM).

AOMX calculations of the ligand field states support these assignments of the ligand field transitions (Table 5.7). Similar to the bromido complex, the Racah interelectronic repulsion parameter B again had to be chosen significantly higher (> 500 $cm^{-1}$) than that reported in the literature for the *fac*-$[Mo^{III}Cl_3(NH_3)_3]$ complex (B = 408 $cm^{-1}$).[197]

If band 3 at 24 000 $cm^{-1}$ is assigned to the spin-allowed $^4A_{2g} \rightarrow {}^4T_{2g}$ transition (band I), the second ligand field transition (band II, $^4A_{2g} \rightarrow {}^4T_{1g}$) is expected at around 30 000 $cm^{-1}$ in the case of $[MoCl_3P_3]$. It can probably be identified with a weak shoulder around 29 000 $cm^{-1}$ at

the high energy side of the asymmetric absorption band 4 at 28 000 $cm^{-1}$. As for the bromido complex, the third quartet transition, $^4A_{2g} \rightarrow {}^4T_{1g}(P)$ (band III), is expected at ~ 50 000 $cm^{-1}$ and therefore cannot be observed experimentally here. The experimental and calculated energies of the d → d ligand field transitions of $[MoCl_3P_3]$ are listed in Table 5.7 together with the corresponding AOM parameters. Compared to the first AOMX calculation of the electronic ligand field states of the bromido complex (Table 5.1), the Racah parameter B is increased which would be expected as the chlorido ligands are significantly smaller and less polarizing than the bromido ligands according to the nephaulexetic series.[93]

**Table 5.7. left**: Experimental and calculated (AOMX) ligand field transitions of $[MoCl_3P_3]$. **right:** overview of the corresponding AOM parameters. All parameters and energies are given in $cm^{-1}$.

| | UV/Vis | calc. |
|---|---|---|
| $^4A_{2g}$ **(F)** | 0 | 0 |
| $^2E_g$ **(G)** | (1) 11 900 | 11 900 |
| $^2T_{1g}$ **(G)** | | 12 400 |
| $^2T_{2g}$ **(G)** | (2) 17 000 | 18 300 |
| $^4T_{2g}$ **(F)** | (3) 24 000 | 24 000 |
| $^4T_{1g}$ **(F)** | (29 000) | 30 400 |
| $^4T_{1g}$ **(P)** | -- | ~ 50 000 |

| | input | fit |
|---|---|---|
| $e_\sigma$**1** | 6 800 | 8 767 |
| $e_\pi$**1** | 1 440 | 1 440 |
| $e_\sigma$**2** | 7 500 | 7 497 |
| $e_\pi$**2** | -1 500 | -1 493 |
| **B** | 500 | 658 |
| **C** | 2 300 | 2 311 |
| $\|D\|$ | -- | 4.3 |

In the UV/Vis absorption spectrum of the facially coordinated ammine complex $[Mo^{III}Cl_3(NH_3)_3]$ the $^4A_{2g} \rightarrow {}^4T_{2g}$ and the $^4A_{2g} \rightarrow {}^4T_{1g}$ quartet transitions were reported to be found at 24 700 $cm^{-1}$ and 29 300 $cm^{-1}$,[197] which supports the assignments of the spin-allowed ligand field transitions given above. In the case of the trispyridine and trispicoline complexes $[Mo^{III}Cl_3py_3]$ and $[Mo^{III}Cl_3(4\text{-}pic)_3]$ which both show a meridional coordination of the three chlorido ligands, the two spin-forbidden transitions $^4A_{2g} \rightarrow {}^2E_g$, $^2T_{1g}(G)$ and $^4A_{2g} \rightarrow {}^2T_{2g}(G)$ have been observed at 8 800 $cm^{-1}$ and 13 000 - 14 500 $cm^{-1}$. Corresponding to the bromido analogues a mixed d – d ($^4A_{2g} \rightarrow {}^4T_{2g}$)/MLCT transition is additionally observed at ~ 27 000 $cm^{-1}$.[109]

Considering the assignment of the various charge transfer transitions which have been worked out for the bromido complex, band 4 at 28 000 $cm^{-1}$ in the UV/Vis spectrum of $[MoCl_3P_3]$ should be assigned to the LMCT transitions from the antisymmetric ligand $p_\pi$ orbitals ($p_{xy}(a)$, $p_{yz}(a)$ and $p_{xz}(a)$) into the singly occupied molybdenum $t_{2g}$ orbitals. As expected, these transitions are clearly shifted towards higher energies compared to $[MoBr_3P_3]$ (*vide infra*).

The shoulder at 33 200 $cm^{-1}$ (band 5) then could be assigned to the bonding → antibonding transitions from the bonding metal-ligand orbitals into their antibonding $t_{2g}$ analogues. They are shifted towards higher energies in the case of $[MoCl_3P_3]$ as well and correspond to the absorption band 5 at 31 300 $cm^{-1}$ and to band E at 30 300 $cm^{-1}$ in the UV/Vis and MCD spectra of the bromido complex. The absorption band 6 observed at 36 200 $cm^{-1}$ in the UV/Vis spectrum of $[MoCl_3P_3]$ is only made out as a small shoulder which is hardly visible in the UV/Vis spectrum of $[MoBr_3P_3]$. In contrast, the shoulder that is observed in the UV/Vis spectrum of the bromido complex at 37 500 $cm^{-1}$ cannot be identified in the UV/Vis spectrum of $[MoCl_3P_3]$. However, probably the absorption bands 6 and 7 in the UV/Vis spectrum of the bromido complex should not be considered as two different transitions but taken together as one structured band in analogy to the UV/Vis band 6 of the chlorido complex. It has been assigned to the LMCT transitions from the antisymmetric bromido $p_\pi$ orbitals into the unoccupied molybdenum $e_g$ orbitals in the case of $[MoBr_3P_3]$ based on molecular orbital considerations.

### 5.2.2 DFT and Time-dependent DFT Calculations and Assignment of the Electronic Transitions

*DFT calculation of the molecular orbitals*

Compared to the bromido complex the same molecular orbitals are obtained for the simplified, truncated $[MoCl_3P_3^H]$ complex with the phenyl groups of the $P_3$ ligand being abbreviated by H atoms (not shown). The only difference is that the d*xy* and d*yz* orbitals (48, 49) and the bonding $p_\pi$(s)/d*xy*, d*yz* metal-ligand orbitals (41, 42) are inverted in energy in the case of $[MoCl_3P_3^{(H)}]$ (Table 5.8).

As far as they can be identified, the same molecular orbitals are also obtained for the non-simplified $[MoCl_3P_3]$ complex (Figure 5.12, Table 5.9). The degenerate $t_{2g}$ orbitals (d*xz*, d*yz*, d*xy*, 167A - 169A) are singly occupied, the degenerate $e_g$ orbitals (d$z^2$, d$x^2$-$y^2$, 182/183A) are unoccupied and the highest occupied ligand orbitals are the antisymmetric chlorido $p_\pi$ orbitals, $p_{xy}$(a), $p_{yz}$(a) and $p_{xz}$(a) (164 - 166) with the $p_{xy}$(a) and $p_{yz}$(a) orbitals being inverted in energy compared to $[MoBr_3P_3]$. As in the case of the bromido complex, there are the same

difficulties to identify the individual molecular orbitals below MO number 164 due to the strong mixing of different orbitals and the large contributions of the phenyl π-orbitals.

**Table 5.8.** Molecular orbitals (*alpha* spin) of the simplified [$MoCl_3P_3^H$] model complex obtained from DFT calculations (BP86/LANL2DZ).

| | orbital | $Mo^{3+}$ | $Cl_x$ | $Cl_y$ | $Cl_z$ | description | ligand $C_S$ |
|---|---|---|---|---|---|---|---|
| 51 | $x^2$-$y^2$ | d$x^2$-$y^2$ | $\sigma_2$(Br + P) | | -- | σ–antibonding, unoccupied metal d-orbital | $\sigma_2(Br_{eq} + P)$ |
| 50 | $z^2$ | d$z^2$ | $\sigma_{sym}$(Br + P) | | | σ–antibonding, unoccupied metal d-orbital | $\sigma_{sym.}(Br_{eq,\ ax} + P)$ |
| 49 | $yz/p_{yz}$(s) | d$yz$ | ($p_y$) | $p_{yz}$(s) | | π–antibonding, singly occupied metal d-orbital | $p_{out\text{-}of\text{-}plane}$(a) |
| 48 | $xy/p_{xy}$(s) | d$xy$ | $p_{xy}$(s) | | ($p_y$) | π–antibonding, singly occupied metal d-orbital | $p_{in\text{-}plane}$(s) |
| 47 | $xz/p_{xz}$(s) | d$xz$ | $p_{xz}$(s) | ($p_x$) | $p_{xz}$(s) | π–antibonding, singly occupied metal d-orbital | $p_{out\text{-}of\text{-}plane}$(s) |
| 46 | $p_{xz}$(a) | -- | $p_z$ | ($p_z$) | $p_x$ | bromido p-orbital, antisymm. linear combination | $p_{out\text{-}of\text{-}plane}$(s) |
| 45 | $p_{yz}$(a) | -- | ($p_z$) | $p_z$ | $p_y$ | bromido p-orbital, antisymm. linear combination | $p_{out\text{-}of\text{-}plane}$(a) |
| 44 | $p_{xy}$(a) | -- | $p_y$ | $p_x$ | $p_y$ | bromido p-orbital, antisymm. linear combination | $p_{in\text{-}plane}$(a) |
| 43 | $p_{xz}$(s)/$xz$ | d$xz$ | $p_z$ | $p_z$ | $p_x$ | $p_{out\text{-}of\text{-}plane}$(s), π–bonding analogue of MO 47 | **$p_{out\text{-}of\text{-}plane}$(s)** |
| 42 | $p_{xy}$(s)/$xy$ | d$xy$ | $p_y$ | $p_x$ | $p_y$ | $p_{in\text{-}plane}$(s), π–bonding analogue of MO 49 | **$p_{in\text{-}plane}$(s)** |
| 41 | $p_{yz}$(s)/$yz$ | d$yz$ | $p_z$ | $p_z$ | $p_y$ | $p_{out\text{-}of\text{-}plane}$(a), π–bonding analogue of MO 48 | **$p_{out\text{-}of\text{-}plane}$(a)** |
| 40 | $p_{\sigma 1}$ | -- | $\sigma_1$(Br + P) | | $p_y$ | bromido p-orbital, $p_y(Br_z)$ bonding | -- |
| 39 | $p_{xy}(s)_{px}$ | -- | $p_{xy}(s)_{px}$ | | $p_x$ | $p_{in\text{-}plane}$(s), $p_x$ ($Br_z$) antibonding | **$p_{in\text{-}plane}$(s)** |
| 38 | $p_{xy}(s)_{px}$ | (d$xy$) | $p_{xy}(s)_{px}$ | | $p_x$ | $p_{in\text{-}plane}$(s), $p_x$ ($Br_z$) bonding | **$p_{in\text{-}plane}$(s)** |
| 37 | $z^2/\sigma_{sym}$ | d$z^2$ | $\sigma_{sym}$(Br + P) | | | σ–bonding, bonding analogue of MO 50 | $\sigma_{sym.}(Br_{eq,\ ax} + P)$ |
| 36 | $x^2$-$y^2/\sigma_2$ | d$x^2$-$y^2$ | $\sigma_2$(Br + P) | | -- | σ–bonding, bonding analogue of MO 51 | $\sigma_2(Br_{eq} + P)$ |

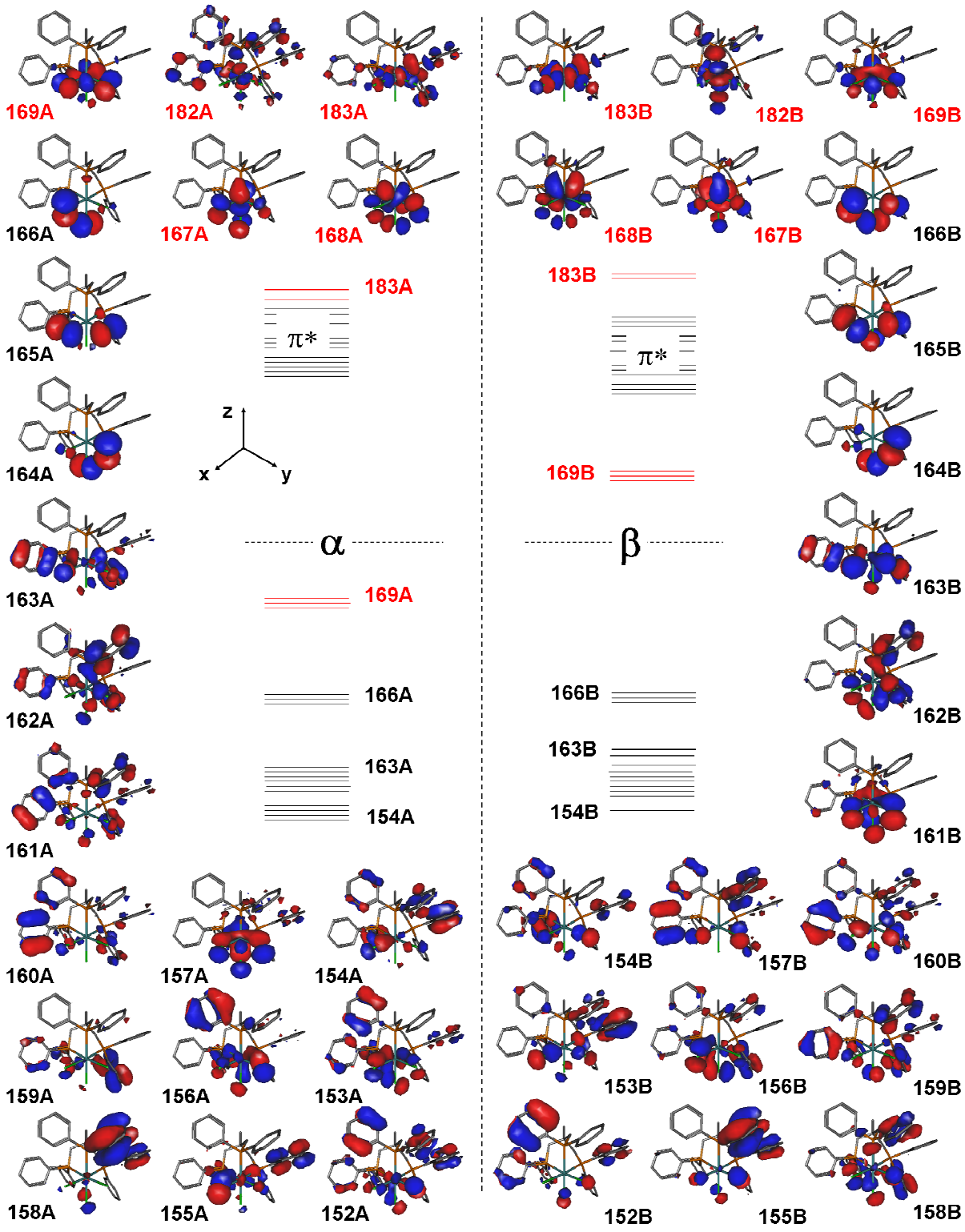


**Figure 5.12.** DFT computation of the molecular orbitals of $[MoCl_3P_3]$ (BP86/LANL2DZ. Hydrogen atoms are omitted for clarity.

**Table 5.9.** DFT calculation of the molecular orbitals of $[MoCl_3P_3]$ (BP86/LANL2DZ).

| α/β spin | | $Mo^{3+}$ | $Cl_x$ | $Cl_y$ | $Cl_z$ | description |
|---|---|---|---|---|---|---|
| 177, 183 | $x^2$-$y^2$ | d$x^2$-$y^2$ | $\sigma_2$(Cl + P) | | -- | σ–antibonding, unoccupied metal d-orbital |
| 176, 182 | $z^2$ | d$z^2$ | ($\sigma_{sym}$.(Cl + P)) | | $p_z$ | σ–antibonding, unoccupied metal d-orbital |
| 170 - 181 [b] | **π*** | (d$x^2$-$y^2$, d$z^2$) | -- | -- | -- | phenyl π* orbitals with small contributions of the molybdenum d$z^2$ and d$x^2$-$y^2$ orbitals |
| 169 | ***xy*/$p_{xy}$(s)** | d*xy* | $p_{xy}$(s) | | -- | π–antibonding, singly occupied metal d-orbital |
| 168 | ***yz*/$p_{yz}$(s)** | d*yz* | ($p_y$) | $p_{yz}$(s) | | π–antibonding, singly occupied metal d-orbital |
| 167 | ***xz*/$p_{xz}$(s)** | d*xz* | $p_{xz}$(s) | ($p_x$) | $p_{xz}$(s) | π–antibonding, singly occupied metal d-orbital |
| 166 | **$p_{xz}$(a)** | -- | $p_z$ | -- | $p_x$ | bromido p-orbital, antisymm. linear combination |
| 165 | **$p_{xy}$(a)** | -- | $p_y$ | $p_x$ | ($p_y$) | bromido p-orbital, antisymm. linear combination |
| 164 | **$p_{yz}$(a)** | -- | ($p_y$) | $p_z$ | $p_y$ | bromido p-orbital, antisymm. linear combination |
| 163A [a] | **π** | -- | -- | -- | -- | phenyl π-orbital, $p_{\sigma 1}$ |
| 163B [a] | **$p_{xy}$(s)/*xy*** | d*xy* | | $p_{in\text{-}plane}$(s) | | π–bonding analogue of MO 169, $p_{in\text{-}plane}$(s) |
| 162A [a] | **π** | -- | -- | $p_{yz}$ | | phenyl π-orbital, $p_{yz}$ |
| 162B [a] | **$p_{yz}$(s)/*yz*** | d*yz* | | $p_{out\text{-}of\text{-}plane}$(a) | | π– bonding analogue of MO 168, $p_{out\text{-}of\text{-}plane}$(a) |
| 161A [a] | **π** | -- | -- | -- | -- | phenyl π-orbital |
| 161B [a] | **$p_{xz}$(s)/*xz*** | d*xz* | | $p_{out\text{-}of\text{-}plane}$(s) | | π–bonding analogue of MO 167, $p_{out\text{-}of\text{-}plane}$(s) |
| 160A [a] | **π** | -- | -- | -- | -- | phenyl π-orbital |
| 160B [a] | **π** | -- | | $p_{xy}(s)_{px}$ | | phenyl p-orbital, $p_{xy}(s)_{px}$ |
| 159A [a] | π | -- | -- | -- | -- | phenyl p-orbital |
| 159B [a] | π | -- | -- | $p_{yz}$(s) | | phenyl π-orbital, $p_{yz}$(s) |
| 158A [a] | **π** | -- | -- | -- | -- | phenyl π-orbital |
| 158B [a] | **π** | -- | | $p_{xy}(s)_{px}$ | | phenyl p-orbital, $p_{xy}(s)_{px}$ |
| 157A [a] | **π** | d*xz* | | $p_{out\text{-}of\text{-}plane}$(s) | | π–bonding analogue of MO 167, phenyl π-orbital |
| 157B [a] | **π** | -- | | ($p_{xy}(s)_{px}$) | | phenyl p-orbital ($p_{xy}(s)_{px}$) |
| 156A [a] | **π** | d*yz* | | $p_{out\text{-}of\text{-}plane}$(a) | | π–bonding analogue of MO 168, phenyl π-orbital |
| 156B [a] | **π** | d*yz* | | $p_{out\text{-}of\text{-}plane}$(a) | | π– bonding analogue of MO 168, phenyl π-orbital |
| 155A [a] | **π** | d*xy*? | | $p_{in\text{-}plane}$(s) | | π– bonding analogue of MO 169?, phenyl π-orbital |
| 155B [a] | **π** | -- | | ($p_{xy}(s)_{px}$) | | phenyl p-orbital ($p_{xy}(s)_{px}$) |
| 154A [a] | **π** | -- | -- | -- | -- | phenyl π-orbital, $p_{\sigma 1}$ |
| 154B [a] | **π** | -- | -- | -- | -- | phenyl π-orbital ($p_{\sigma 1}$?) |
| 153A [a] | **π** | d*yz* | | $p_{out\text{-}of\text{-}plane}$(a) | | phenyl π-orbital (π– bonding analogue of MO 168) |
| 153B [a] | **π** | -- | -- | -- | -- | phenyl π-orbital, $p_{\sigma 1}$ |
| 152A [a] | **π** | d*xy* | | $p_{in\text{-}plane}$(s) | | phenyl π-orbital (π– bonding analogue of MO 169) |
| 152B [a] | **π** | -- | -- | -- | -- | phenyl p-orbital ($p_{yz}$(s)?) |
| 145 [b] | ***x*²-*y*²** | d$x^2$-$y^2$ | $\sigma_2$(Cl + P) | | -- | σ– bonding analogue of MO 183 |
| 144 [b] | ***z*²** | d$z^2$ | -- | $\sigma_{sym}$.(Cl + P) | | σ– bonding analogue of MO 182 |

[a] molecular orbitals lower than MO 164: mixed metal-ligand orbitals and pure bromido p-orbitals with very large contributions of phenyl π orbitals → theoretical assignment corresponding to $[MoCl_3P_3{}^H]$ (MO 36 - 43)

[b] not shown in Figure 5.12

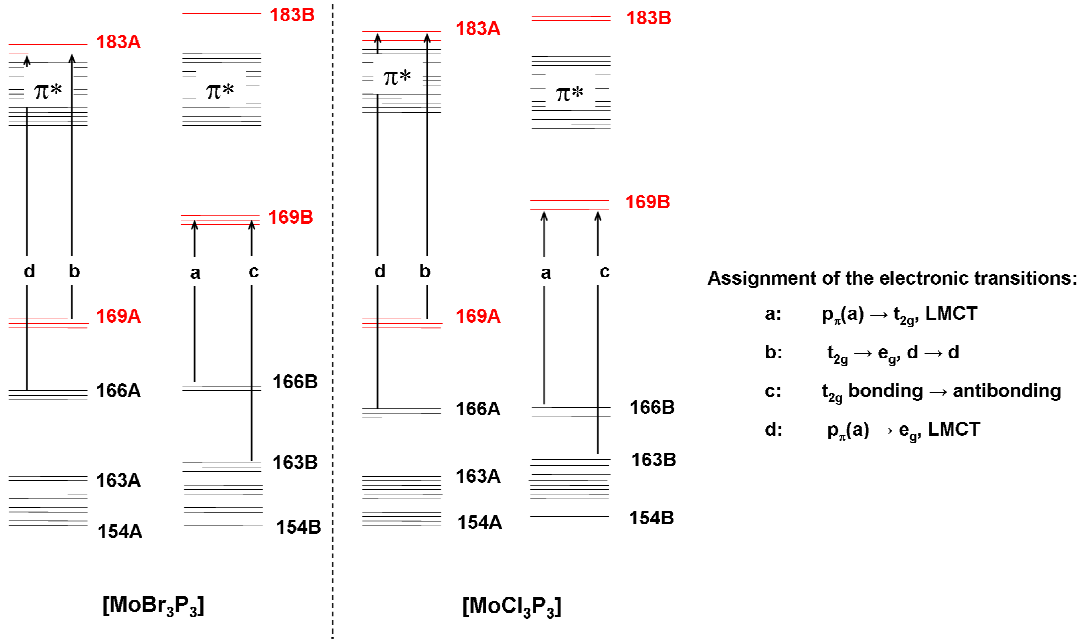


**Figure 5.13.** Comparison of the relative MO energies for $[MoBr_3P_3]$ and $[MoCl_3P_3]$ obtained from the DFT calculation of the molecular orbitals (BP86/LANL2DZ).

Comparing the relative MO energies of $[MoCl_3P_3]$ and $[MoBr_3P_3]$ (Figure 5.13) only very small differences are expected for the energies of the calculated d → d ligand field transitions. In contrast, the $p_\pi(a) \rightarrow t_{2g}$ LMCT transitions should be shifted towards higher energies in the case of the chlorido complex as the antisymmetric $p_\pi$ orbitals (164 - 166) are relatively lowered in their energies compared to $[MoBr_3P_3]$. The same should theoretically be expected for the bonding symmetric metal ligand orbitals (161 - 163) leading to increased energies for the $t_{2g}$ bonding → antibonding transitions as well. Note that two different types of complex structures were used in the TDDFT calculations ($[MoBr_3P_3]$: single crystal X-ray structure; $[MoCl_3P_3]$: DFT-optimized complex structure), so a direct comparison of the MO energies etc. probably should not be taken too seriously for further argumentation.

*TDDFT calculation and assignment of the electronic transitions*

As in the case of the bromido complex TDDFT was used to calculate the electronic transitions first for the simplified $[MoCl_3P_3^H]$ model complex in which the $P_3$ phenyl groups are abbreviated by H atoms. The assignment of individual transitions to particular spectral regions turns out to be easier for the chlorido complex than for the bromido complex (Figure 5.14, Table 5.10).

**Table 5.10.** TDDFT calculation of the electronic transitions of the truncated [$MoCl_3P_3^H$] complex (B3LYP/LANL2DZ). Only d → d transitions and transitions with oscillator strengths > 0.0020 are listed.

| energy ($cm^{-1}$) | oscillator strength | description | |
|---|---|---|---|
| **24 700** | 0.0154 | LMCT, $p_{xz}(a)/p_{yz}(a)/p_{xy}(a) \rightarrow xz, yz, xy\ (t_{2g})$ | 46B → 49B |
| **24 900 - 25 400** | 0.0025 - 0.0090 | $t_{2g} \rightarrow e_g$, d → d ligand field transitions | 48A → 50A |
| **29 700 - 30 300** | 0.0045 – 0.0082 | $p_{xz}(s)/p_{yz}(s)/p_{xy}(s) \rightarrow xz, yz, xy\ (t_{2g})$ | 41-43B → 47 – 49B |
| **32 100** | 0.0532 | $p_{xy}(s)/xy \rightarrow xy$, bonding → antibonding | 41B → 49B |
| **~ 35 500** | 0.0010 | $p_{xy}(s)_{px} \rightarrow xz, yz, xy\ (t_{2g})$ | 38/39B →47-49B |
| **35 800** | 0.0093 | | |
| **36 100** | 0.059 | | |
| **36 200** | 0.0216 | $p_{xz}(a)/p_{yz}(a)/p_{xy}(a) \rightarrow z^2, x^2\text{-}y^2\ (e_g)$ | 44-46A → 50/51A |
| **36 000** | 0.0053 | | |
| **36 800** | 0.0060 | | |
| **41 100** | 0.0101 | | |

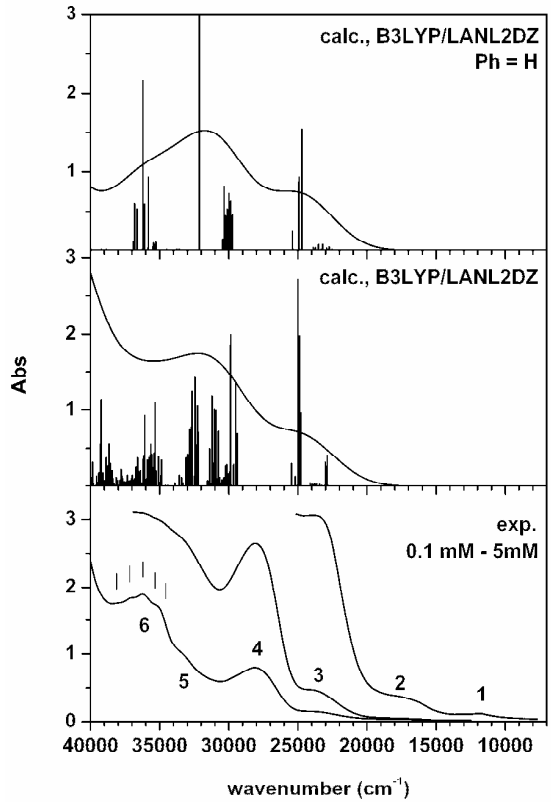


**Figure 5.14.** Experimental UV/Vis absorption spectra of [$MoCl_3P_3$] and calculated UV/Vis absorption spectra (TDDFT, B3LYP/LANL2DZ) of the truncated [$MoCl_3P_3^H$] complex (**top**) and the non-simplified [$MoCl_3P_3$] complex (**middle**). The experimental UV/Vis absorption spectra were measured in $CH_2Cl_2$ (d = 10 mm) at different concentrations.

Considering the overall shape of the calculated UV/Vis spectrum, again no acceptable agreement could be found between the experimental and calculated spectra. Absorption maxima are obtained at 25 000 $cm^{-1}$ and 32 000 $cm^{-1}$ in both calculations which do not really

correspond to any of the experimentally observed absorption bands in the UV/Vis spectrum of $[MoCl_3P_3]$ (Figure 5.14).

The calculated spectra of $[MoCl_3P_3^H]$ predicts moderate intensities for the d → d ligand field transitions which are found around 24 900 $cm^{-1}$. This energy corresponds to the low-intensity band 3 at 24 000 $cm^{-1}$ quite well. As for the truncated bromido complex, the LMCT transitions from the antisymmetric $p_\pi$ orbitals, $p_{xz}(a)$, $p_{yz}(a)$ and $p_{xy}(a)$, into the singly occupied $t_{2g}$ molybdenum d-orbitals are also very intense in the calculated UV/Vis spectra of $[MoCl_3P_3^H]$. They are made out at 24 700 $cm^{-1}$, but this does not really correspond to the energy of the experimentally observed absorption band 4. The bonding → antibonding $p_\pi(s)/d \rightarrow t_{2g}$ transitions are expected around 30 000 $cm^{-1}$. The most intense of these transitions in the calculated spectrum is the $p_{xy}(s)/dxy \rightarrow dxy$ transition at 32 100 $cm^{-1}$ which matches the experimental energy of the UV/Vis band 5 at 33 200 $cm^{-1}$ of $[MoCl_3P_3]$ very well. The $p_{xy}(s)_{px} \rightarrow t_{2g}$ LMCT transitions are found around 35 500 $cm^{-1}$, but are predicted to have very low intensities in the theoretical UV/Vis spectrum. LMCT transitions from the antisymmetric $p_\pi$ orbitals into the unoccupied $e_g$ molybdenum d-orbitals are centered at 35 800 $cm^{-1}$and 36 200 $cm^{-1}$ exactly corresponding to the absorption band 6 at 36 200 $cm^{-1}$ in the experimental UV/Vis spectrum.

For the non-simplified complex $[MoCl_3P_3]$ the d → d ligand field transitions are clearly made out at 22 900 - 24 700 $cm^{-1}$ and 31 000 – 32 800 $cm^{-1}$ ($t_{2g}/p_\pi$(bind.) → π*/d, Table 5.11) in the calculated UV/Vis spectrum with moderate intensities. This again supports the assignment of the UV/Vis absorption band 3 at 24 000 $cm^{-1}$ to the first quartet transition, $^4A_{2g} \rightarrow {}^2T_{2g}$ (band I). As already suggested by the results of the AOMX ligand field calculations, the second spin-allowed ligand field transition, $^4A_{2g} \rightarrow {}^1T_{2g}$ (band II) may be assigned to a low-intensity absorption feature which is hidden beneath the absorption band 4, but made out as a weak shoulder at 29 000 $cm^{-1}$.

**Table 5.11.** Electronic transitions of $[MoCl_3P_3]$ (TDDFT, B3LYP/LANL2DZ). Only the d → d ligand field transitions and transitions with oscillator strengths > 0.0020 are listed.

| energy ($cm^{-1}$) | oscillator strength | description | |
|---|---|---|---|
| **22 900** | 0.0027 | $yz/p_{yz}(s) \rightarrow \pi^*/d$ | 168A → 173/176A |
| **23 000** | 0.0021 | $xy/p_{xy}(s)$, $xz/p_{xz}(s) \rightarrow \pi^*/d$ | 169A → 174/177A, 167A → 173/176A |
| **24 800** | 0.0064 | $xy/p_{xy}(s) \rightarrow \pi^*/d$, $p_{xz}(a) \rightarrow yz/p_{yz}(s)$ | 169A → 173A, 166B → 168B |
| **24 900** | 0.0132 | $p_{xy}(a) \rightarrow xy/p_{xy}(s)$ | 165B → 169B, 169A → 173/176A |
| **25 000** | 0.0181 | $p_{yz}(a)$, $p_{xz}(a) \rightarrow t_{2g}/p_\pi$(antibond.) | 164B → 168/169B, 166B → 167B |
| **25 500** | 0.0020 | $xz/p_{xz}(s) \rightarrow \pi^*/d$ | 167A → 172/174/177A |
| **29 400** | 0.0046 | $p_{xy}(s)/xy \rightarrow xz/p_{xz}(s)$ | 163B → 167B |
| **29 500** | 0.0090 | $t_{2g}/p_\pi$(bind.) → $xz/p_{xz}(s)$, $yz/p_{yz}(s)$ | 160-163B → 167/168B |
| **29 900** | 0.0133, 0.0124 | $p_{xz}(s)/xz$, $p_{xy}(s)/xy \rightarrow yz/p_{yz}(s)$, $xy/p_{xy}(s)$ | 161/163B → 168/169B |
| **30 800** | 0.0048 | $xz/p_{xz}(s) \rightarrow \pi^*/d$, $p_{xz}(s)/xz \rightarrow xy/p_{xy}(s)$ | 167A → 170A, 161B → 169B |
| **31 000** | 0.0067 | $yz/p_{yz}(s) \rightarrow \pi^*/d$ | 168A → 171/173A |
| **31 100** | 0.0020 | $yz/p_{yz}(s)$, $xy/p_{xy}(s) \rightarrow \pi^*/d$ | 168/169A → 172/173A |
| **31 200** | 0.0079 | $yz/p_{yz}(s) \rightarrow \pi^*/d$, $p_{xz}(s)/xz$, $p_{xy}(s)/xy \rightarrow yz/p_{yz}(s)$, $xy/p_{xy}(s)$ | 168A → 171/173A, 161/163B → 168/169B |
| **31 400** | 0.0033 | $xy/p_{xy}(s) \rightarrow \pi^*/d$, $p_{yz}(s)/yz$, $p_{xy}(s)/xy \rightarrow xz/p_{xz}(s)$, $yz/p_{yz}(s)$ | 169A → 172A, 162/163B → 167/168B |
| **32 200** | 0.0047 | $p_{xy}(s)_{px} \rightarrow yz/p_{yz}(s)$ | 158/160B → 168B |
| **32 300** | 0.0070, 0.0036 | $t_{2g}/p_\pi$(bind.), $p_{xy}(s)_{px} \rightarrow t_{2g}/p_\pi$(antibond.) | 155/156/158/160B → 167B |
| **32 500** | 0.0095 | | 155/158/159/160B → 168/169B |
| **32 700** | 0.0083, 0.0052 | $p_{yz}(s)$, $p_{xy}(s)_{px} \rightarrow t_{2g}/p_\pi$(antibond.), $xz/p_{xz}(s)$, $yz/p_{yz}(s) \rightarrow \pi^*/d$ | 158/159B → 167-169B, 168/169A → 174/176/177A |
| **32 800** | 0.0025, 0.0050 | $yz/p_{yz}(s)$, $xy/p_{xy}(s) \rightarrow \pi^*/d$ | 168/169A → 174/176A |
| **33 000** | 0.0028 | $xz/p_{xz}(s)$, $yz/p_{yz}(s) \rightarrow \pi^*/d$, $p_{yz}(s)$, $p_{xy}(s)_{px} \rightarrow xy/p_{xy}(s)$ | 167/168A → 173/174A, 158/159B → 169B |
| **33 100** | 0.0025 | $xz/p_{xz}(s)$, $xy/p_{xy}(s) \rightarrow \pi^*/d$, $p_{yz}(s) \rightarrow yz/p_{yz}(s)$ | 167/169A → 174/175/177A, 159B → 168B |
| **34 900** | 0.0023 | $xy/p_{xy}(s) \rightarrow \pi^*/d$, $p_{yz}(s)/yz$, $p_{xz}(s)/xz \rightarrow yz/p_{yz}(s)$ | 169A → 178A, 156B, 161B → 168B |
| **35 100** | 0.0026 | $yz/p_{yz}(s) \rightarrow \pi^*/d$ | 168A → 178A |
| **35 300** | 0.0073 | $xz/p_{xz}(s) \rightarrow \pi^*/d$ | 167A → 178A |
| **35 400** | 0.0029 | $xy/p_{xy}(s) \rightarrow \pi^*/d$ | 169A → 178/180A |
| **35 600** | 0.0037 | $yz/p_{yz}(s) \rightarrow \pi^*/d$ | 168A → 180A |
| **35 700** | 0.0027 | $xy/p_{xy}(s) \rightarrow \pi^*/d$ | 169A → 177/179/181A |
| **35 800** | 0.0025 | $yz/p_{yz}(s)$, $xy/p_{xy}(s) \rightarrow \pi^*/d$ | 168/169A → 179A, 155/157B → 167B |
| **35 900** | 0.0023 | $yz/p_{yz}(s) \rightarrow \pi^*/d$, $p_{yz}(a) \rightarrow \pi^*/d$ | 168A → 179A, 164B → 170B |
| **36 100** | 0.0062, 0.0027 | $p_{yz}(a)$, $p_{xy}(a) \rightarrow \pi^*/d$ | 165A → 117/172/177A, 164B → 170B |
| **36 200** | 0.0024 | $xz/p_{xz}(s) \rightarrow \pi^*/d$ | 167A → 177/179/181B |
| **36 600** | 0.0025 | $p_{yz}(a) \rightarrow \pi^*/d$ | 164A → 172/177A, 164B → 171B |
| **38 600** | 0.0020 | $p_{xz}(a) \rightarrow \pi^*/d$ | 166A → 171/173A, 166B → 174B |
| **38 900** | 0.0025 | phenyl $\pi \rightarrow xy/p_{xy}(s)$ | 154B → 169B |

| energy ($cm^{-1}$) | oscillator strength | description | |
|---|---|---|---|
| **39 200** | 0.0076 | $p_{yz}(a) \rightarrow \pi^*/d$ | 164B → 175/176B |
| **39 300** | 0.0037 | phenyl $\pi \rightarrow xy/p_{xy}(s)$, $p_{xy}(a)$, $p_{xz}(a) \rightarrow \pi^*/d$ | 153B → 169B, 165/166B → 174/175B |
| **39 900** | 0.0021 | phenyl $\pi \rightarrow xy/p_{xy}(s)$ | 148/150B → 169B |
| **40 700** | 0.0043 | phenyl $\pi \rightarrow yz/p_{yz}(s)$, $yz/p_{yz}(s) \rightarrow \pi^*/d$ | 147 B → 168B,168B → 177B |

Furthermore, the $p_\pi(a) \rightarrow t_{2g}$ LMCT transitions can also be assigned from the TDDFT calculations of the non-simplified $[MoCl_3P_3]$ complex (Table 5.11). They are found at 24 900 – 29 900 $cm^{-1}$ in the calculated UV/Vis spectrum and thus match the observed UV/Vis absorption band 4 at 28 000 $cm^{-1}$ quite well. The energy of this band is shifted by ~ 3 000 $cm^{-1}$ compared to the corresponding bromido complex, which would be expected as the antisymmetric $p_\pi(a)$ orbitals are relatively lowered in energy upon the increased ligand field strength going from bromido to chlorido ligands (*vide supra*, Figure 5.13). Almost the same shift is expected for the $p_\pi(s)/d \rightarrow t_{2g}$ bonding → antibonding transitions, which have been observed at 31 300 $cm^{-1}$ (UV/Vis band 5) and 30 300 $cm^{-1}$ (MCD band E) for the bromido complex and is assigned to the absorption shoulder at 33 200 $cm^{-1}$ (band 5) in the UV/Vis spectrum of $[MoCl_3P_3]$ (UV/Vis calc.: 29 900 - 32 700 $cm^{-1}$). The absorption band 6 at 36 200 $cm^{-1}$ in the UV/Vis spectrum of the chlorido complex is assigned to the $p_\pi(a) \rightarrow e_g$ LMCT transitions corresponding to the UV/Vis bands 6 and 7 of the bromido complex. A convincing argument in favor of this assignment is the vibrational structure with $\Delta E$ = ~ 1 000 $cm^{-1}$. It might originate from the symmetric aromatic ring breathing vibration which is associated with a symmetric C-$P_{phenyl}$ stretch observed at 1 029 $cm^{-1}$ (FT-Raman) and might be excited upon electronic transitions into the σ–antibonding $e_g$ molybdenum d-orbitals

In summary, the proposed assignments of the individual electronic transitions of $[MoCl_3P_3]$ and $[MoBr_3P_3]$ are shown in Table 5.12.

**Table 5.12.** Assignment of the electronic transitions of $[MoCl_3P_3]$ and $[MoBr_3P_3]$ (in $cm^{-1}$).

| $[MoCl_3P_3]$ | $[MoBr_3P_3]$ | | assignment |
|---|---|---|---|
| | UV/Vis | MCD | |
| (1) 11 900 | (1) 11600 | -- | spin-forbidden d → d ligand field transition ($^4A_{2g} \rightarrow {}^2E_g$, $^2T_{1g}$) |
| (2) 17 000 | (2) ~ 16 000 | -- | spin-forbidden d → d ligand field transition ($^4A_{2g} \rightarrow {}^2T_{2g}$) |
| -- | -- | (A) 20 500 | LMCT, $p_\pi(a) \rightarrow xz, yz, xy\ (t_{2g})$ |
| (3) 24 000 | (3) ~ 22 500 | (B) 23 000 | d → d ligand field transition ($^4A_{2g} \rightarrow {}^4T_{2g}$, band I) |
| (4) 28 000 | (4) 25 000 | (C) 25 300 | LMCT, $p_\pi(a) \rightarrow xz, yz, xy\ (t_{2g})$ |
| (29 000) | -- | (D) 27 700 | d → d ligand field transition ($^4A_{2g} \rightarrow {}^4T_{1g}$, band II) |
| (5) 33 200 | (5) 31 300 | (E) 30 300 | LMCT, $p_\pi(s)/t_{2g} \rightarrow xz, yz, xy\ (t_{2g})$ |
| -- | -- | (F) 33 100 | LMCT, $p_{xy}(s)_{px} \rightarrow xz, yz, xy\ (t_{2g})$ |
| (6) 36 200 [a] | (6) (36 000) | (G) 35 900 | LMCT, $p_\pi(a) \rightarrow z^2, x^2\text{-}y^2\ (e_g)$ |
| -- | (7) 37 500 | -- | |

[a] vibrational progression: $\Delta E = 1000\ cm^{-1}$

### 5.2.3 EPR Spectra of $[MoCl_3P_3]$

The low-temperature cw X-band EPR spectrum of $[MoCl_3P_3]$ also shows two signals (Figure 5.15) in analogy to the corresponding bromido complex. They are assigned to the $|-3/2\rangle \rightarrow |+3/2\rangle$ (signal I) and the $|-1/2\rangle \rightarrow |+1/2\rangle$ (signal II) spin transitions at the $B_0 \parallel z$ orientation of the applied magnetic field (*vide supra*). In the EPR spectrum of the chlorido complex the overall shape and the intensity ratio of the two signals is somewhat different, however, as signal I here shows a significantly higher intensity compared to signal II. This cannot only be explained with the higher temperature during the measurement which was only increased by ~ 1 K at measurement of $[MoCl_3P_3]$. In addition, signal I is not as asymmetric and shows no splitting compared to the low-temperature EPR spectrum of $[MoBr_3P_3]$, which indicates a very small rhombic zero-field-splitting value $E$ ($E \sim 0$) in the case of the chlorido complex. As a simulation of the spectrum was not successful so far, a further interpretation is not possible at the moment.

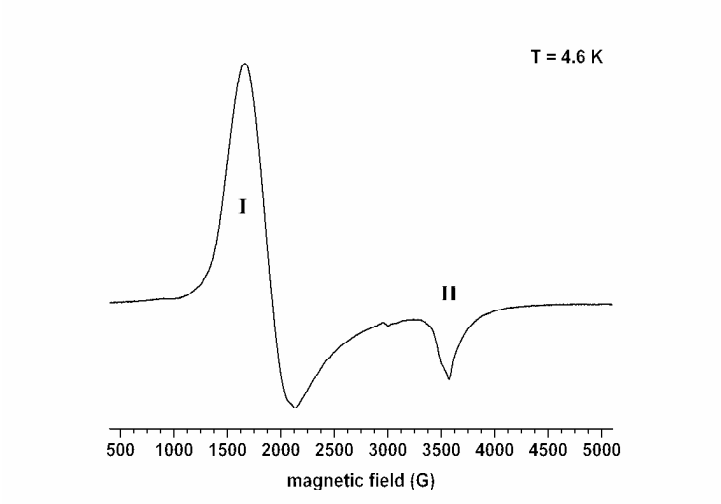


**Figure 5.15.** Low-temperature cw X-band EPR spectrum of $[MoCl_3P_3]$, measured in a frozen $CH_2Cl_2$ solution at T = 4.6 K, microwave frequency 9.642 GHz, microwave power 2 mW, modulation amplitude 10 G., modulation frequency 100 kHz.

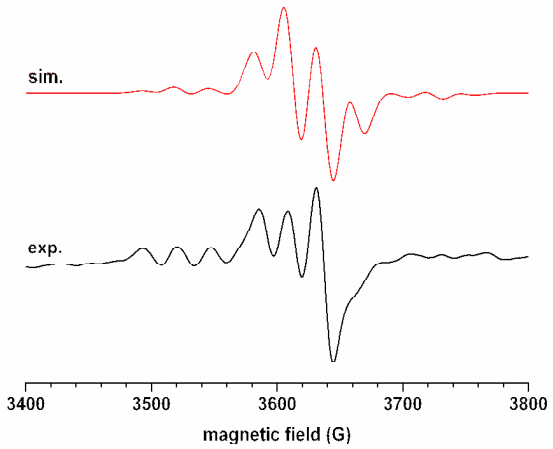


**Figure 5.16.** Room temperature cw X-band EPR spectrum of $[MoCl_3P_3]$, measured in a $CH_2Cl_2$ solution (microwave frequency: 9.874 GHz, microwave power 2 mW, modulation amplitude 10 G., modulation frequency 100 kHz) and spectral simulation (EasySpin[198] (garlic), g = 1.95, $A(^{95/97}Mo)$ = 34 G, $A_{iso}(^{31}P)$ = 23 G ($A_{xx}$ = 26 G, $A_{yy}$ = 23 G $A_{zz}$ = 21 G, line width 7 G). The spectral simulation was performed by Henning Broda.

The signal arising from the $|-1/2\rangle \rightarrow |+1/2\rangle$ transition in the room temperature EPR spectrum of $[MoCl_3P_3]$ shows a better resolution of the $^{31}P$ hyperfine splitting compared to the EPR spectrum of the bromido complex. In the spectral simulation using the simulation software EasySpin[198] the "molybdenum satellites" arising from hyperfine coupling between the electron spin and the nuclear spin of the $^{95}Mo$ and $^{97}Mo$ isotopes show significantly higher intensities compared to the XSophe simulation of the EPR spectrum of $[MoBr_3P_3]$. The g-value of $g_{iso}$ = 1.95 in the case of $[MoCl_3P_3]$ is significantly lower compared to $[MoBr_3P_3]$ ($g_{iso}$ = 1.99). Considering the hyperfine coupling constants, however, no significant

differences are obtained between the chlorido and the bromido complex. For both complexes an A-value of $A(^{95/97}Mo) = 35$ G is obtained for the $^{95/97}Mo$ hyperfine coupling. In fact, no difference would have been expected here as both complexes have the same oxidation state (Mo(III)). The $^{31}P$ hyperfine coupling constant, however, is minimally decreased from $22.3 \cdot 10^{-4}$ cm$^{-1}$ (≙ 24 G) in the case of $[MoBr_3P_3]$ to $21.1 \cdot 10^{-4}$ cm$^{-1}$ (≙ 23 G) in the case of $[MoCl_3P_3]$. From the decreased covalence of the metal-ligand bonds going from bromido to chlorido ligands within the $[MoX_3P_3]$ complexes probably a much stronger decrease of the $^{31}P$ hyperfine coupling constant would have been expected for $[MoCl_3P_3]$.

### 5.2.4 Conclusion

The electronic transitions of the $[MoX_3P_3]$ complexes have been successfully assigned based AOM ligand field calculation and the (TD)DFT calculations of molecular orbitals and electronic transitions (Table 5.12). All of these methods could only be applied with certain limitations. In the case of the AOMX calculations, the obtained results for both the energies of the ligand field states and the specific AOM parameters, which especially are the $e_\sigma$ and $e_\pi$ bonding parameters as well as the interelectronic repulsion parameters (Racah parameters), should always be compared to the literature so avoid erroneous band assignments. However, from their very low intensities the spin-forbidden ligand field transitions even could be assigned *without* AOMX calculations.

In the case of the quantum chemical DFT and TDDFT calculations, the electronic transitions could be assigned based on molecular orbital considerations, but only with the help of the simplified $[MoX_3P_3^H]$ complexes, as for the non-simplified complexes the identification of the molecular orbitals was rather difficult due to the strong mixing of metal and ligand orbitals with the π- and π*-orbitals of the $P_3$ phenyl groups.

Whether the proposed assignments of the remaining UV/Vis and MCD bands to the individual d → d and charge transfer transitions are correct and whether the observed trends and shifts within the optical spectra have been explained in the right way should be verified by extending this study to other tripodal molybdenum(III) $P_3$ complexes. The most obvious candidate for further investigations, of course, would be the analogous iodido complex

[$MoI_3P_3$]. Compared to the chlorido and bromido complexes, a further decreased ligand field strength should be expected in the case of the iodido ligands leading to further shifts of the electronic transitions in the optical spectra. The same is also true for the analysis of the EPR spectra. Due to the increased covalence of the Mo-I bonds, an increased $^{31}P$ hyperfine coupling constant, compared to [$MoBr_3P_3$] and [$MoCl_3P_3$], would be expected. However, the iodido $P_3$ molybdenum(III) complex [$MoI_3P_3$] still has to be synthesized.

## 5.3 [$MoCl_3SiP_3$]

For further investigations on the optical spectra of facially coordinated molybdenum(III) *tripod* complexes and to verify the proposed assignments of the electronic transitions, [$MoCl_3SiP_3$] has additionally been analyzed. The $SiP_3$ ligand and the [$MoCl_3SiP_3$] complex have been synthesized by Henning Broda.[199] The DFT optimized complex structure] is shown in Figure 5.17. The tripodal $SiP_3$ ligand is an aliphatic ligand ($SiP_3$ = tris(dimethyl-phosphinomethyl)methylsilane, *tdmpmms*) and does *not* contain any phenyl groups in contrast to the aromatic $P_3$ ligand ($P_3$ = 1,1,1-tris(diphenylphosphinomethyl)ethane). In consequence, the analysis of the molecular orbitals is expected to be less difficult in the case of [$MoCl_3SiP_3$] compared to the [$MoX_3P_3$] complexes and should therefore lead to a more reliable assignment of the electronic transitions.

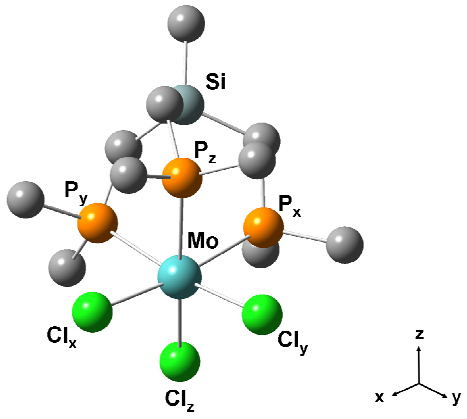


**Figure 5.17.** DFT optimized complex structure of [$MoCl_3SiP_3$] (B3LYP/LANL2DZ). Hydrogen atoms are omitted for clarity.

### 5.3.1 UV/Vis Absorption Spectrum

Compared to the UV/Vis absorption spectrum of [$MoCl_3P_3$], three absorption bands at 24 500 $cm^{-1}$ (band 3), 28 900 $cm^{-1}$ (band 4) and around 36 000 $cm^{-1}$ (band 6) also observed in the UV/Vis spectrum of [$MoCl_3SiP_3$]. Additionally, also a clear shoulder is identified at 33 400 $cm^{-1}$ (band 5). Analogous to band 6 in the UV/Vis spectrum of [$MoCl_3P_3$], the absorption band 6 at 36 000 $cm^{-1}$ also shows a vibrational structure with $\Delta E \sim 1\,000$ $cm^{-1}$. In the case of [$MoCl_3P_3$], the vibrational frequency of 1 000 $cm^{-1}$ has been assigned to the symmetric phenyl ring-breathing vibrations which cannot be transferred to [$MoCl_3SiP_3$]

complex, of course. However, very intense P - $C_{methyl}$ bending vibrations are observed in the IR spectrum of the $SiP_3$ complex at 900 - 1 000 $cm^{-1}$. This indicates that again the σ-antibonding $e_g$ orbitals might be involved in these (LMCT) transition.

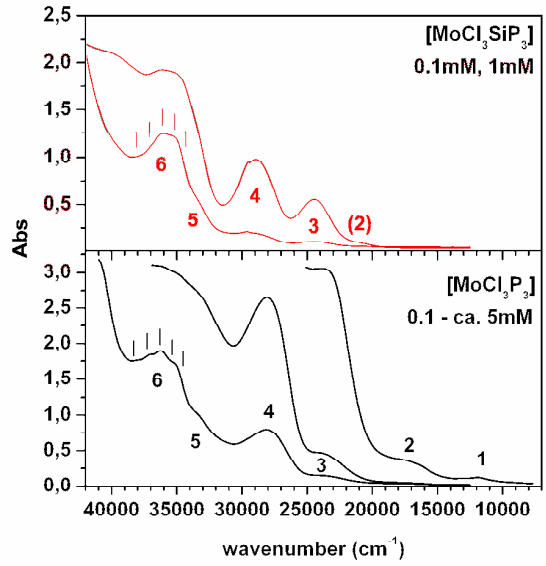


**Figure 5.18.** UV/Vis spectra of $[MoCl_3P_3]$ (**bottom**) and $[MoCl_3SiP_3]$ (**top**), measured in $CH_2Cl_2$ at different concentrations ($[MoCl_3P_3]$: 0.1 – 5 mM; $[MoCl_3SiP_3]$: 0.1/1 mM).

The absorption bands 3 and 4 at 24 500 $cm^{-1}$ and 28 900 $cm^{-1}$ show a different intensity ratio in the UV/Vis spectrum of $[MoCl_3SiP_3]$ when compared to $[MoCl_3P_3]$ (Figure 5.18).

Additionally, a low-intensity absorption band 2 might probably be made out at around 21 500 $cm^{-1}$ in the UV/Vis spectrum of $[MoCl_3SiP_3]$ which may be assigned to the $^4A_{2g} \rightarrow {}^4T_{2g}$ ligand field transition (band I).

### 5.3.2 DFT calculations of the Molecular Orbitals

Considering the molybdenum d-orbitals of $[MoCl_3SiP_3]$, they are found in antibonding linear combinations with the corresponding ligand $p_\pi$ and $p_\sigma$ orbitals as obtained for the $[MoX_3P_3]$ complexes (*vide supra*). The unoccupied $dz^2$ and $dx^2\text{-}y^2$ orbitals are observed in antibonding linear combinations with the $\sigma_{sym}$ and $\sigma_2$ orbitals and are almost degenerate ($e_g$, 73/74A). Compared to the $[MoX_3P_3]$ complexes, however, a different sequence of the singly occupied molybdenum $t_{2g}$ orbitals is obtained. In the case of $[MoCl_3SiP_3]$ the d*xy* and d*xz* + d*yz* orbitals

(70A - 72A) which observed in antibonding linear combinations with the symmetric chlorido $p_\pi$ orbitals $p_{xy}$, $p_{xz}$ and $p_{yz}$ are inverted in energy.

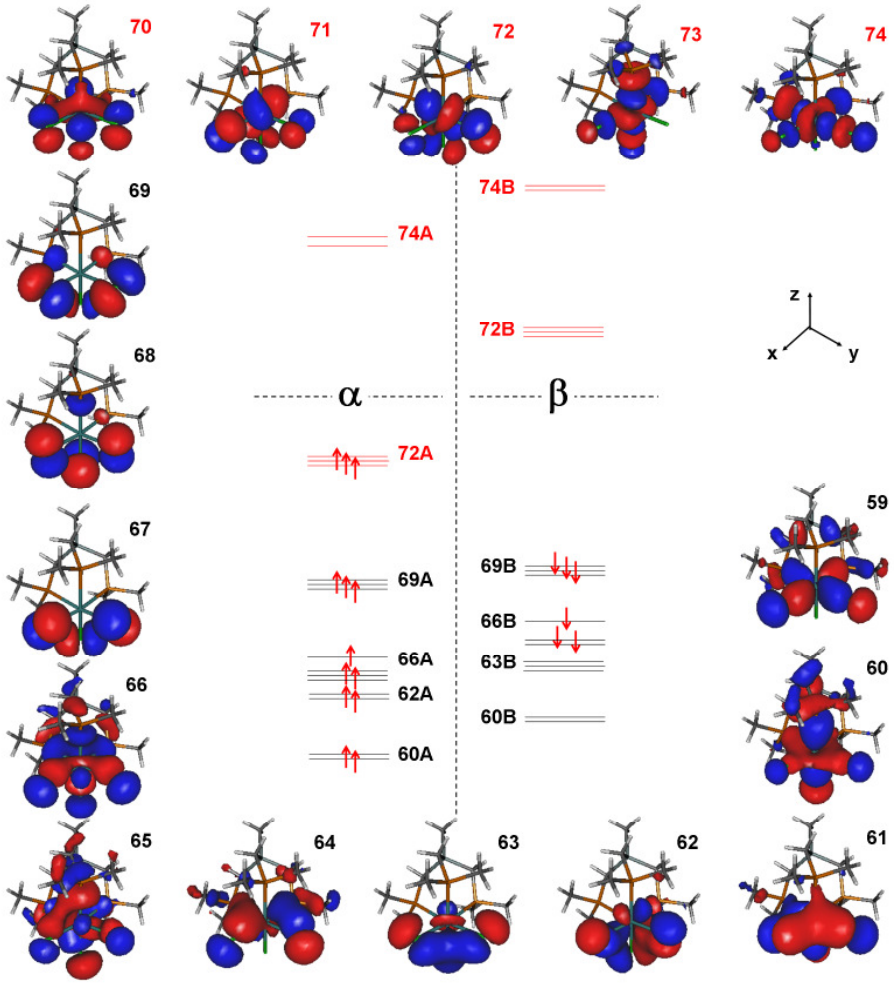


**Figure 5.19.** Molecular orbitals of [$MoCl_3SiP_3$] (*alpha* spin orbitals), BP86/LANL2DZ.

The highest occupied ligand orbitals (67A – 69A) rather remind of the antibonding in-plane and out-of-plane chlorido p-orbitals as obtained for the $C_S$ symmetric molybdenum(V) complex [Mo(O)$Cl_3$*dppe*] (*dppe*: 1,2-bis(diphenyl-phosphino)ethane, chapter 3) than of the corresponding orbitals of the [$MoX_3P_3$] complexes. However, their bonding counterparts are not as easily identified (61A - 63A). The same is true for the bonding analogues of the singly occupied $t_{2g}$ orbitals (64A - 66A) due to the large extent of mixing of different metal or ligand orbitals.

Within the antibonding $p_\pi$(s) orbitals, the bonding d*xy*/$p_{xy}$(s) orbital is relatively lifted in its energy compared to the d*xz*/$p_{xz}$(s) and d*yz*/$p_{yz}$(s) orbitals as the former is additionally mixed

with the $\sigma_1$ orbital (66A) here. The molecular orbitals 59A and 60A are the bonding analogues of the unoccupied $d_{x^2-y^2}/\sigma_2$ and $d_{z^2}/\sigma_{sym}$ $e_g$ molybdenum d-orbitals. Molecular orbitals above MO 74 predominantly show phosphorus p-character. As nearly no spin-polarization is observed between the *alpha* and *beta* spin orbitals, only the *alpha* spin orbitals are depicted in Figure 5.19 and described in Table 5.13.

**Table 5.13.** Molecular orbital (*alpha* spin orbitals) of $[MoCl_3SiP_3^H]$, BP86/LANL2DZ.

| | orbital | $Mo^{3+}$ | $Cl_x$ | $Cl_y$ | $Cl_z$ | description |
|---|---|---|---|---|---|---|
| 74 | $x^2$-$y^2$ | $dx^2$-$y^2$ | $\sigma_2$(Br + P) | | -- | σ–antibonding, unoccupied metal d-orbital |
| 73 | $z^2$ | $dz^2$ | $\sigma_{sym}$(Br + P) | | | σ–antibonding, unoccupied metal d-orbital |
| 72 | $yz/p_{yz}(s)$ | $dyz$ | $p_x$ | $p_{yz}(s)$ | | π–antibonding, singly occupied metal d-orbital |
| 71 | $xz/p_{xz}(s)$ | $dxz$ | $p_{xz}(s)$ | ($p_x$) | $p_{xz}(s)$ | π–antibonding, singly occupied metal d-orbital |
| 70 | $xy/p_{xy}(s)$ | $dxy$ | $p_{xy}(s)$ | | $p_x$ | π–antibonding, singly occupied metal d-orbital |
| 69 | $p_{out\text{-}of\text{-}plane}(a)$ | -- | $p_{out\text{-}of\text{-}plane}(a)$ | | | chlorido p-orbital, antibonding linear combination |
| 68 | $p_{out\text{-}of\text{-}plane}(s)$ | -- | $p_{out\text{-}of\text{-}plane}(s)$ | | | chlorido p-orbital, antibonding linear combination |
| 67 | $p_{in\text{-}plane}(a)$ | -- | $p_{in\text{-}plane}(a)$ | | | chlorido p-orbital, antibonding linear combination |
| 66 | $p_{\sigma 1} + p_{xy}(s)/xy$ | $dxy$ | $p_{\sigma 1} + xy/p_{xy}(s)$ | | | bonding metal-ligand hybrid orbital (π–bonding analogue of MO 70) |
| 65 | $p_{xz}(s)/xz$ | ($dxz$) | $p_{out\text{-}of\text{-}plane}(a)$,($p_{xz}(s)$) | | | π–bonding analogue of MO 71 |
| 64 | $p_{yz}(s)/yz$ | $dyz$ | $p_x$ | $p_{yz}(s)$ | | π–bonding analogue of MO 72 |
| 63 | $p_{out\text{-}of\text{-}plane}(s)$ | ($dxy$) | $p_{out\text{-}of\text{-}plane}(s)$ | | | chlorido p-orbital, π–bonding analogue of MO 68 |
| 62 | $p_{out\text{-}of\text{-}plane}(a)$ | $dxz$ | $p_{out\text{-}of\text{-}plane}(a)$ | | | chlorido p-orbital, π–bonding analogue of MO 69 |
| 61 | $p_{in\text{-}plane}(s)$ | ($dxy$) | $p_{in\text{-}plane}(s)$ | | | chlorido p-orbital, bonding analogue of MO 67 |
| 60 | $z^2/\sigma_{sym}$ | $dz^2$ | $\sigma_2$(Br + P) | | -- | σ–bonding, bonding analogue of MO 74 |
| 59 | $x^2$-$y^2/\sigma_2$ | $dx^2$-$y^2$ | $\sigma_{sym}$(Br + P) | | | σ–bonding, bonding analogue of MO 73 |

The relative MO energies of $[MoCl_3SiP_3]$ and the $[MoX_3P_3]$ complexes are shown in Figure 5.20. It is obvious at the first sight that the ligand field splitting is reduced in the case of $[MoCl_3SiP_3]$. This implies that lower energies are expected for the $d \rightarrow d$ ligand field transitions compared to the $[MoX_3P_3]$ complexes. In contrast, the antisymmetric $p_\pi$ ligand orbitals and the bonding $t_{2g}/p_\pi(s)$ orbitals are relatively lowered in energy in the case of $[MoCl_3SiP_3]$. This should lead to increased energies of the $p_\pi(a) \rightarrow t_{2g}$ LMCT as well as the $t_{2g}$ bonding → antibonding transitions, for example.

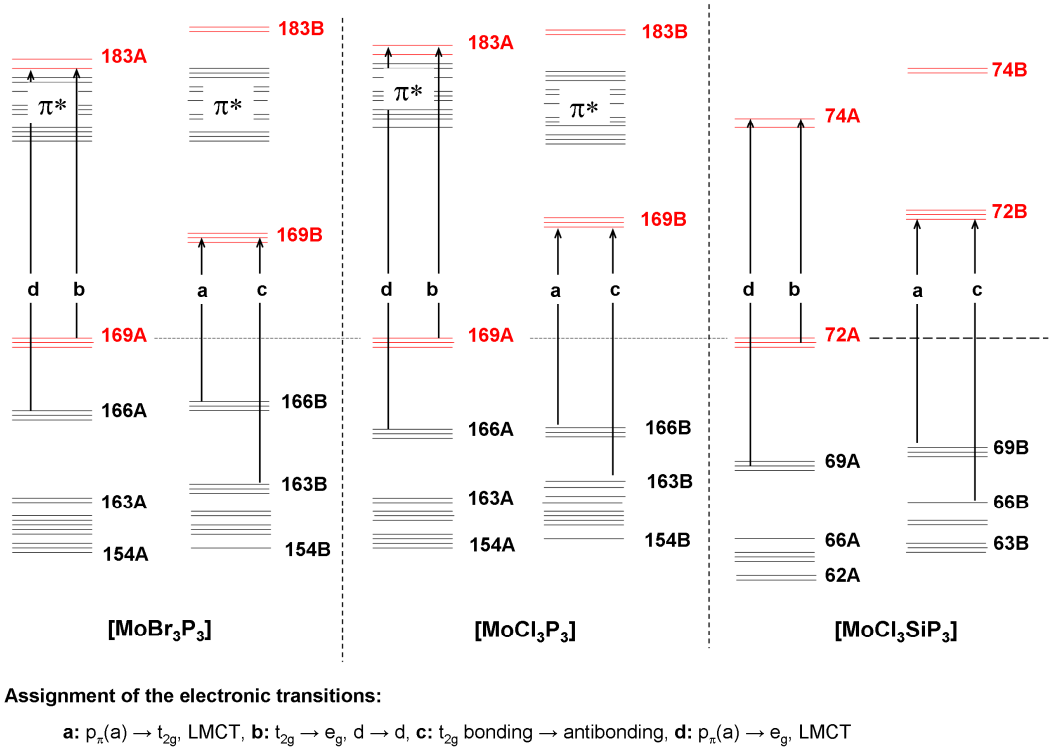


**Figure 5.20.** The relative MO energies of $[MoBr_3P_3]$, $[MoCl_3P_3]$ and $[MoCl_3SiP_3]$ obtained from DFT calculations (BP86/LANL2DZ) are shown for comparison.

### 5.3.3 TDDFT Calculations of the Electronic Transitions and Assignment of the UV/Vis Spectrum

The overall shape of the theoretical UV/Vis spectrum of $[MoCl_3SiP_3]$ obtained from the TDDFT calculation of the electronic transitions shows one very broad absorption band at 33 000 $cm^{-1}$. It does not match any of the observed bands in the experimental UV/Vis spectrum (Figure 5.21). However, the calculated energies of the most intense transitions seem to match the experimental absorption features at 28 900 $cm^{-1}$ and 36 000 $cm^{-1}$. As it can hardly be distinguished between the bonding in-plane and out-of-plane chlorido $p_\pi$ orbitals and the bonding analogues of the molybdenum $t_{2g}/p_\pi(s)$ orbitals, a definite assignment of the individual electronic transitions turns out to be quite difficult. Nevertheless, some trends considering the different types of electronic transitions within the particular spectral regions of the experimental UV/Vis spectrum can be extracted from the TDDFT calculation.

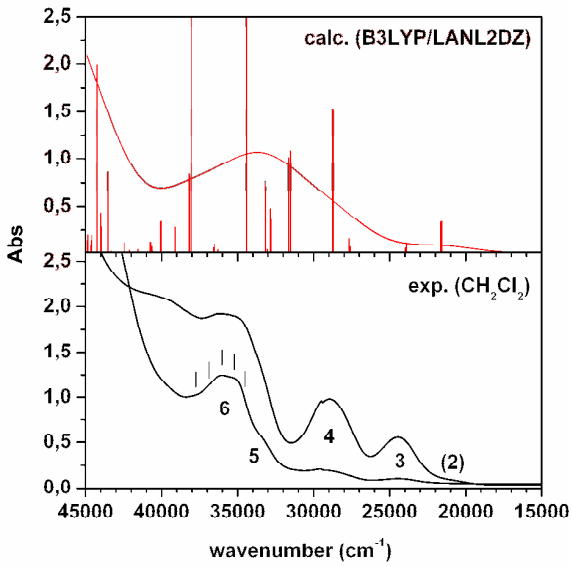


**Figure 5.21.**Experimental (**bottom**) and calculated (**top**) UV/Vis spectrum of [$MoCl_3SiP_3$]. The experimental spectra were measured in $CH_2Cl_2$ (d = 10 mm, ~ 0.1/1 mM). Electronic transitions were computed by time-dependent DFT (B3LYP/LANL2DZ).

In the theoretical UV/Vis spectrum, the $t_{2g} \rightarrow e_g$ ligand field transitions are calculated around 21 600 $cm^{-1}$ and 24 000 $cm^{-1}$ and show low to moderate intensities. The first energy perfectly matches the energy of the assumed low-intensity band 2 in the experimental spectrum. It is therefore assigned to the $^4A_{2g} \rightarrow {}^4T_{2g}$, transition (band I). The second energy matches the experimental absorption band 3 at 24 500 $cm^{-1}$. However, although the $^4A_{2g} \rightarrow {}^4T_{1g}$ transition (band II) would also be expected at significantly lower energies compared to the [$MoX_3P_3$] complexes, this band should probably rather not be assigned to a ligand field transition due to its relatively high intensity. However, in the case of [$MoCl_3P_3$], the $^4A_{2g} \rightarrow {}^4T_{1g}$ transition has been identified as a small shoulder next to the high intensity LMCT transition ($p_\pi(a) \rightarrow t_{2g}$, band 4) on the other hand. This means that, in general, the intensity of this ligand field transition cannot be too low. In consequence, the UV/Vis band 3 might probably indeed be assigned to the second spin-allowed quartet transition (band II) in the case of [$MoCl_3SiP_3$], especially as no other reasonable assignment is suggest by the molecular orbital and TDDFT calculations.

LMCT transitions from the in-plane and the out-of-plane chlorido $p_\pi$ orbitals into the singly occupied $t_{2g}$ molybdenum d-orbitals are found between 27 600 $cm^{-1}$ and 28 800 $cm^{-1}$ in the calculated UV/Vis spectrum of [$MoCl_3SiP_3$]. Again, they show very low intensities in the calculated spectrum. The only exception is the $p_{in\text{-}plane}(a) \rightarrow dxz, dyz$ transition at 28 800 $cm^{-1}$

which exactly matches the experimental absorption band 4 at 28 900 $cm^{-1}$. In the theoretical UV/Vis spectrum of $[MoCl_3SiP_3]$, the $t_{2g}$ bonding → antibonding transitions are found between 31 500 $cm^{-1}$ and 34 400 $cm^{-1}$. The most intense of these transitions is are the $p_{xz}(s)/xz_{bind.} \rightarrow yz/p_{yz}(s)_{antibond.}$ transitions (65A → 72A) at 34 400 $cm^{-1}$. They might be assigned to the experimental absorption band 5 at 33 000 $cm^{-1}$.

**Table 5.14.** TDDFT calculations of the electronic transitions of $[MoCl_3SiP_3]$ (B3LYP/LANL2DZ). Only the d → d transitions and transitions with oscillator strengths > 0.0020 are listed.

| energy ($cm^{-1}$) | oscillator strength | description | |
|---|---|---|---|
| 21 500 | 0.0001 | d → d, d*xz*, d*yz* → d$x^2$-$y^2$ | 71/72A → 73A |
| **21 600** | 0.0034 | d → d, d*xz*, d*yz* → d$x^2$-$y^2$, d$z^2$ | 71/72A → 73/74A |
| **21 600** | 0.0033 | d → d, d*xy* → d$z^2$ | 70A → 74A |
| **23 900** | 0.0033 | d → d, d*xz* → d$z^2$ | 71A → 74A |
| 24 000 | 0.0006 | d → d, d*xy* → d$x^2$-$y^2$ | 70A →73A |
| 27 600 | 0.0007 | LMCT, $p_{out\text{-}of\text{-}plane}$(a) → d*xy*, d*yz* | 69B → 70/72B |
| 27 700 | 0.0015 | LMCT, $p_{in\text{-}plane}$(a) → d*xz* | 67B → 71B |
| 27 700 | 0.0016 | LMCT, $p_{in\text{-}plane}$(a), $p_{out\text{-}of\text{-}plane}$(a) → d*xy*, d*xz*, d*yz* | 67/68B → 70-72B |
| **28 700-28 800** | 0.0152 | LMCT, $p_{in\text{-}plane}$(a) → d*xz*, d*yz* | 67B → 71/72B |
| **31 500, 31700** | 0.0101-0.0108 | $\sigma_1$ + $p_{xy}$/*xy* (hybrid) → d*xy*, d*xz*, d*yz* | 66B → 70-72B |
| **32 800** | 0.0036-0.0048 | $p_{yz}(s)/yz \rightarrow yz/p_{yz}(s)$, $p_{xz}(s)/xz \rightarrow$ d*xz* | 64/65B → 71/72B |
| **33 200** | 0.0071-0.0076 | $p_{yz}(s)/yz$, $p_{xz}(s)/xz \rightarrow$ d*xy* | 64/65B → 70B |
| **34 400** | 0.0534 | $p_{xz}(s)/xz \rightarrow yz/p_{yz}(s)$ | 65B → 72B |
| **38 000** | 0.0276 | $p_{out\text{-}of\text{-}plane}$(a) → d$z^2$ | 69A → 74A |
| **38 200** | 0.0083 | $p_{out\text{-}of\text{-}plane}$(s) → d$z^2$, d$x^2$-$y^2$ | 68A → 73/74A |
| **39 100** | 0.0028 | $p_{in\text{-}plane}$(a) → d$z^2$, d$x^2$-$y^2$ | 67A → 73/74A |
| **40 100** | 0.0034 | d$x^2$-$y^2$/$\sigma_2$ (bind.) → d*xy* | 59B → 70B, |
| | 0.0033 | d$z^2$/$\sigma_{sym.}$ (bind.) → d*xy*, d*yz* | 60B → 70/72B |
| **43 500** | 0.0086 | $p_{out\text{-}of\text{-}plane}$(s, a) → d$z^2$, d$x^2$-$y^2$ | 68/69B → 73/74B |
| **44 000** | 0.0028, 0.0042 | $p_{in\text{-}plane}$(a) → d$z^2$, d$x^2$-$y^2$ | 67B → 73/74B |
| **44 300** | 0.0197 | $\sigma_1$ + $p_{xy}$/*xy* (hybrid) → d$z^2$, d$x^2$-$y^2$ | 66A → 73/74A |

The vibrational progression of band 6 of $\Delta E \sim 1\,000\ cm^{-1}$ corresponds to the energy of P-$C_{methyl}$ bending vibrations. This implies that the unoccupied σ-antibonding $e_g$ orbitals might be involved in these transitions. In analogy to the $[MoX_3P_3]$ complexes, this band should therefore be assigned to the LMCT transitions from the chlorido $p_\pi$ orbitals into the unoccupied d$x^2$-$y^2$ and d$z^2$ molybdenum d-orbitals. In the calculated UV/Vis spectrum they are found at 38 000 – 39 100 $cm^{-1}$. Transitions above 45 000 $cm^{-1}$ are predicted to be MLCT

transitions from the singly occupied $t_{2g}$ orbitals into phosphorus p-orbitals from TDDFT calculation of $[MoCl_3SiP_3]$.

As no spin-forbidden ligand field transitions are observed in the UV/Vis spectrum at the used concentrations of max. 1 mM, no AOMX ligand field calculations were performed in the case of $[MoCl_3SiP_3]$.

In summary a complete assignment of the electronic transitions of the $P_3$ and $SiP_3$ molybdenum(III) *tripod* complexes is shown in Table 5.15.

**Table 5.15.** Assignment of the electronic transitions of $[MoX_3P_3]$ (X = $Cl^-$, $Br^-$) and $[MoCl_3SiP_3]$. The energies are given in $cm^{-1}$.

| $[MoCl_3P_3]$ | $[MoCl_3SiP_3]$ | $[MoBr_3P_3]$ | | assignment |
|---|---|---|---|---|
| | | UV/Vis | MCD | |
| (1) 11 900 | -- | (1) 11600 | -- | spin-forbidden d → d ligand field transition ($^4A_{2g} \rightarrow {}^2E_g$, $^2T_{1g}$) |
| (2) 17 000 | -- | (2) ~ 16 000 | -- | spin-forbidden d → d ligand field transition ($^4A_{2g} \rightarrow {}^2T_{2g}$) |
| -- | -- | -- | (A) 20 500 | LMCT, $p_\pi(a) \rightarrow$ xz, yz, xy ($t_{2g}$) |
| (3) 24 000 | ((2) 21 500) | (3) ~ 22 500 | (B) 23 000 | d → d ligand field transition ($^4A_{2g} \rightarrow {}^4T_{2g}$, band I) |
| | (3) 24 000 | | | assignment unclear[b] |
| (4) 28 000 | (4) 28 900 | (4) 25 000 | (C) 25 300 | LMCT, $p_\pi(a) \rightarrow$ xz, yz, xy ($t_{2g}$) |
| (29 000) | ??? | -- | (D) 27 700 | d → d ligand field transition ($^4A_{2g} \rightarrow {}^4T_{1g}$, band II) |
| (5) 33 200 | (5) ~ 33 000 | (5) 31 300 | (E) 30 300 | LMCT, $p_\pi(s)/t_{2g} \rightarrow$ xz, yz, xy ($t_{2g}$) |
| -- | -- | -- | (F) 33 100 | LMCT, $p_{xy}(s)_{px} \rightarrow$ xz, yz, xy ($t_{2g}$) |
| (6) 36 200 [a] | (6) 36 000 [a] | (6) (36 000) | (G) 35 900 | LMCT, $p_\pi(a) \rightarrow z^2$, $x^2$-$y^2$ ($e_g$) |
| -- | -- | (7) 37 500 | -- | |

[a] vibrational progression: $\Delta E = 1000\ cm^{-1}$

[b] from the TDDFT calculation the $^4A_{2g} \rightarrow {}^4T_{1g}$ ligand field transition (band II) could be suggested

### 5.3.4 Conclusion

As expected the molecular orbitals of the $[MoCl_3SiP_3]$ complex with its aliphatic $SiP_3$ ligand could directly be calculated without any abbreviations. The identification of the individual MOs is quite easy compared to $[MoX_3P_3]$ as the $P_3$ ligand bearing several phenyl groups. Compared to the MO calculations of the truncated $[MoX_3P_3{}^H]$ complexes, a larger extent of mixing of different metal and/or ligand orbitals is observed in the case of $[MoCl_3SiP_3]$. Comparing the UV/Vis spectra of $[MoCl_3SiP_3]$ and $[MoCl_3P_3]$ apparently the same absorption bands are obtained with only little differences considering the energies and the intensity ratios

of the individual bands. However, the assignment of the various electronic transitions cannot directly be transferred from $[MoCl_3P_3]$ to $[MoCl_3SiP_3]$. Especially the energies of the d → d ligand field transitions and thus the assignment of the absorption band 3 remain somewhat unclear in the case of the $SiP_3$ complex. From the TDDFT calculation the latter could indeed be assigned to the $^4A_{2g} \rightarrow {}^4T_{1g}$ ligand field transition in the case of $[MoCl_3SiP_3]$, but the intensity of this band is actually too high compared to the other absorption bands. Compared to the $[MoX_3P_3]$ complexes (slight) shifts of the various LMCT transitions towards higher energies are predicted for $[MoCl_3SiP_3]$ from the comparison of the relative MO energies as well as from the TDDFT calculation of the electronic transitions. These shifts are throughout confirmed by the experimental energies. In consequence, the assignment of the LMCT transitions is considered to be correct for all three complexes (Table 5.15).

Nevertheless, the proposed assignments should be verified by further studies on the UV/Vis (and MCD) spectra as well as on the corresponding DFT and TDDFT calculations of a larger number of different facially coordinated aliphatic, aromatic, heteroatom containing etc. molybdenum(III) *tripod* complexes.

# 6 EPR Spectroelectrochemistry of [Mo(NCMe)(NEt)*depe*$_2$]$^{2+}$

Considering the Chatt cycle for catalytic $N_2$ reduction one important intermediate is the Mo/W(IV)-imido intermediate **C6** (*vide supra*, chapter 1.2.3). After the first equivalent of $NH_3$ has been eliminated **C6** is generated from the Mo/W(IV)-nitrido intermediate **C5** by protonation. For the generation of the second equivalent of ammonia this Mo/W(IV)-imido complex has first to be reduced by two electrons to the corresponding Mo/W(II)-imido stage **C7** before being protonated in two further steps. During the two-electron reduction the anionic *trans* ligand is eliminated. As the Mo/W(IV)-imido complex **C6** is able to protonate itself in a cross- reaction during the reduction resulting in the instant formation of the Mo/W(II)-amido complex **C8** the Mo/W(II)-imido intermediate **C7** cannot be studied. However, this self-protonation reaction can be avoided using alkylated imido complexes, which was the synthetic strategy employed in previous work by the Tuczek group.[3, 89]

An example of such an alkyl imido Chatt type molybdenum(IV) complex is [Mo(NCMe)(NEt)*depe*$_2$]$^{2+}$ (NEt = ethyl imide, *depe* = 1,2-Bis(diethylphosphino)ethane), where the molybdenum(IV) center bears an acetonitrile solvent molecule *trans* to the ethyl imido ligand in addition to two equatorially coordinated *depe* ligands (Figure 6.1). Beside some other Mo(IV) ethyl imido complexes it has already been used to study the reduction of the Mo(IV)-imido intermediate[89] to compare the results to a previous study on the reduction of the corresponding Mo(IV) alkyl imido *dppe* complexes (*dppe* = 1,2-Bis-(diphenyl-phosphino)ethane).[200]

The [Mo(NCMe)(NEt)*depe*$_2$]$^{2+}$ complex was synthesized, characterized and intensively studied with respect to its redox behavior by Ameli Dreher. One of the key observations of that work was that the neutral acetonitrile ligand *trans* to the imido moiety cannot be eliminated during electrochemical reductions and that only one electron could be transferred, even when strongly reducing potentials (E ~ -2 V vs. $Fc/Fc^+$) where applied. Thus only a paramagnetic Mo(III)-imido species (S = 1/2) was prepared instead of the Mo(II)-imido complex **C7**.[89] The starting Mo(IV)-imido complex itself is diamagnetic (S = 0) and thus EPR silent. However, the paramagnetic complex obtained from the one-electron reduction of [$Mo^{IV}$(NCMe)(NEt)*depe*$_2$]$^{2+}$ can be detected by EPR spectroscopy (S = 1/2). The same is true for the product of a one-electron oxidation (Mo(IV) → Mo(V), S = 1/2), which of course is not part of the catalytic cycle of $N_2$ reduction and was only studied for comparison.

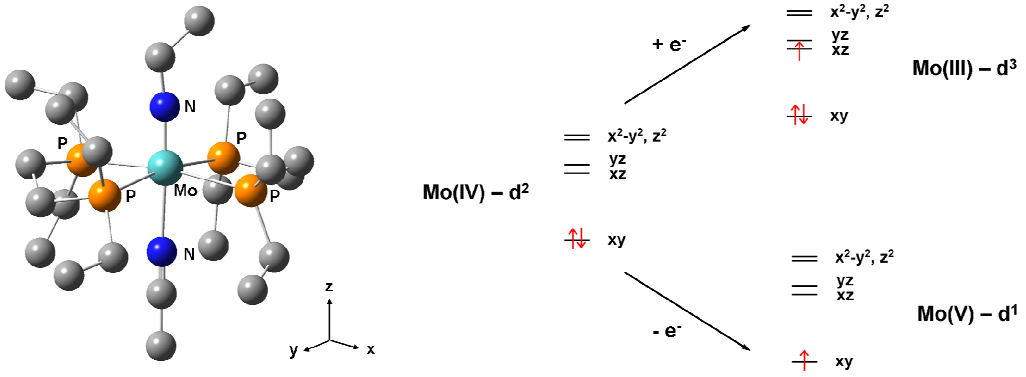


**Figure 6.1:** Optimized complex structure of [Mo(NCMe)(NEt)*depe*$_2$]$^{2+}$ and schematic ligand field splitting of the molybdenum d orbitals as obtained from DFT calculation of the molecular orbitals.[89] Hydrogen atoms are omitted for clarity. The DFT geometry optimization was carried out by Sven Meyer (B3LYP/6-311G, Mo: LANL2DZ).

As, so far, only very few and rare examples are reported in the literature considering the EPR spectra of mononuclear Mo(III) complexes, the room temperature EPR spectra obtained after the electrochemical reduction and oxidation of [Mo(NCMe)(NEt)*depe*$_2$]$^{2+}$ were also used as test spectra for isotropic spectral simulations with the XSophe simulation software suite.[1]

Samples were prepared under argon atmosphere by Sven Meyer. Using an appropriate EPR tube with two platiunum electrodes the EPR spectra were measured at room temperature in 10 mM acetonitrile solutions (1 mL) containing $NBu_4PF_6$ as electrolyte (0.1 M). As no reference electrode or internal standard was used, reduction or oxidation potentials were slowly changed until a current of 30 - 40 µA was reached. The samples were then electrolyzed over several minutes until significant intensities of the EPR spectra were obtained.

## 6.1 Reduction of [Mo(NCMe)(NEt)*depe*$_2$]$^{2+}$

After the electrochemical reduction of the EPR silent molybdenum(IV) complex [Mo(NCMe)(NEt)*depe*$_2$]$^{2+}$ (S = 0) a symmetric hyperfine split quintet at g = 2.01 is detected in the room temperature EPR spectrum (Figure 6.2). The color of the solution changes during electrolysis from violet to yellow (and ultimately red at very high concentrations).[3] According

[3] Note that in the case of the molybdenum(III) complexes containing the tripodal $P_3$ ($P_3$ = 1,1,1-tris(diphenylphosphinomethyl)ethane) and $SiP_3$ ($SiP_3$ = tris(dimethylphosphinomethyl)methylsilane) ligands (*vide supra*, chapter 5), diluted complex solutions are yellow as well.

to previous coulometric measurements, only one electron is transferred during the electrochemical reduction,[89] so the EPR signal should arise from the $|-1/2\rangle \rightarrow |+1/2\rangle$ transition of a (low spin) Mo(III) species (S = 1/2).

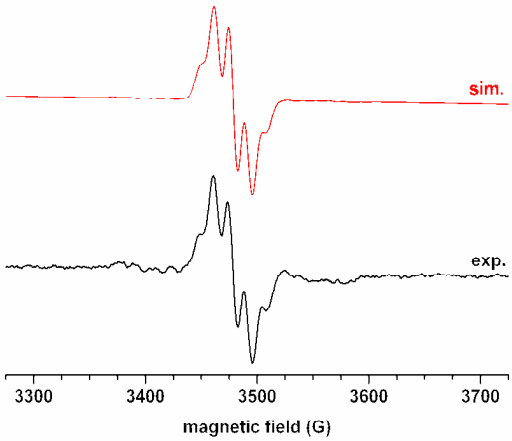


**Figure 6.2.** Experimental and simulated cw X-band EPR spectrum of the Mo(III) complex, that was obtained after reduction of [Mo(NCMe)(NEt)*depe*$_2$]$^{2+}$ (10 mM) in MeCN containing $NBu_4PF_6$ (0.1 M) at ~-2.2 to -2.5V. Experimental: room temperature, microwave frequency 9.781 GHz, microwave power 6.3 mW, modulation amplitude 4 G, modulation frequency 100 kHz, simulation: $g_{iso}$ = 2.01, $A_{iso}(^{95/97}Mo)$ = 35.5 G, $A_{iso}(^{31}P)$ = 12.3 G, (line width 6.5G)

The hyperfine splitting is due to the coupling of the unpaired electron with the four equivalent P atoms ($^{31}$P: I = 1/2) of the two equatorial *depe* ligands. In addition, "molybdenum satellites" are observed on both sides of the actual signal resulting from the hyperfine coupling with the molybdenum isotopes $^{95}$Mo and $^{97}$Mo (both I = 5/2, natural abundance 15.9 % and 9.6 %, respectively). The overall signal width is about 200 G. From the simulation of the spectrum (Figure 6.2, top) an isotropic hyperfine coupling constant of 12.3 G ($11.5 \cdot 10^{-4}$ cm$^{-1}$) is obtained for $^{31}$P. The isotropic hyperfine coupling of $^{95/97}$Mo could best be simulated using 35.5 G ($33.3 \cdot 10^{-4}$ cm$^{-1}$). The accordance between the calculated and simulated spectrum is very good considering the position, the relative intensities and the overall width of the signal. For so far unknown reasons the signals arising from the molybdenum hyperfine coupling at the wings of the signal are found at the right position but with much too low intensities in the simulated spectrum.

In contrast to a previous study on the EPR spectra of the methyl imido molybdenum(III) complex [MoCl(NMe)*dppe*]$^{2+}$,[165] which also has only one unpaired electron, the hyperfine coupling with $^{14}$N and the alkyl protons ($A_{iso}(^{14}N)$ = 3.4 G, $A_{iso}(^{1}H)$ = 3.6 G) is not resolved in

the EPR spectrum of [Mo(NCMe)(NEt)*depe*$_2$]$^{2+}$. A reason might be that the modulation amplitude was chosen too high in our experiment.[4] No hyperfine coupling constant is given in the report for the $^{95/97}$Mo center of [MoCl(NMe)*dppe*]$^{2+}$. The phosphorus hyperfine splitting parameter of $A_{iso}(^{31}P)$ = 20.2 G (18.7·10$^{-4}$ cm$^{-1}$) is markedly higher for the *dppe* complex. This could be explained by the lower covalence considering the metal-ligand bonds of [MoCl(NMe)*dppe*]$^{2+}$ compared to the [Mo(NCMe)(NEt)*depe*$_2$]$^{2+}$ complex.

## 6.2 Reduction of [Mo(NCMe)(NEt)depe$_2$]$^{2+}$ in the presence of phenol

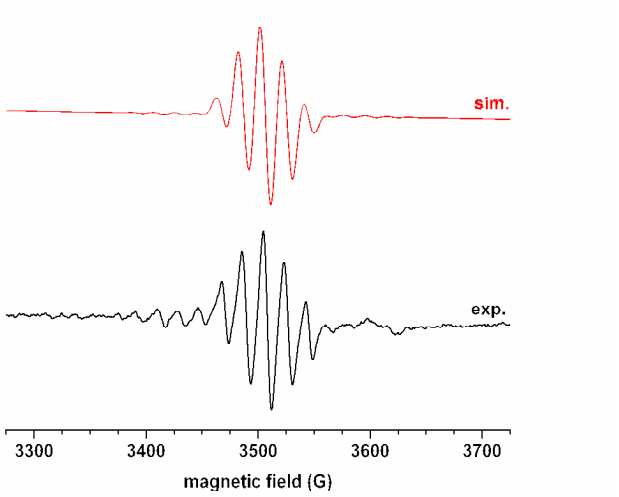


**Figure 6.3.** Experimental and simulated cw X-band EPR spectrum of [Mo(NCMe)(NEt)*depe*$_2$]$^{2+}$ (10 mM), reduced in MeCN containing $NBu_4PF_6$ (0.1 M) at -2.2 - -2.5V in the presence of phenol. Experimental: room temperature, microwave frequency: 9.78 GHz, microwave power 6.3 mW, modulation amplitude 4 G, modulation frequency 100 kHz, simulation: $g_{iso}$ = 1.99, $A_{iso}(^{95/97}Mo)$ = 35.5 G, $A_{iso}(^{31}P)$ = 19.1 G, (line width 6.1 G)

After the reduction of [Mo(NCMe)(NEt)*depe*$_2$]$^{2+}$ in the presence of phenol serving as a potential proton-source a different EPR spectrum is obtained showing a significantly larger hyperfine splitting (Figure 6.3) compared to the previous measurement in the absence of PhOH. Again, electrolysis causes a clear color change, in this case from violet to red. The product of the reduction in the presence of phenol is not stable, as the EPR signal and the red

[4] For comparison: A modulation amplitude of only 0.1 mT (microwave power of 20 mW) was used for the EPR measurements reported in ref.[165] D. L. Hughes, D. J. Lowe, M. Y. Mohammed, C. J. Pickett, N. M. Pinhal, *J. Chem. Soc. Dalton Trans.* **1990**, 2021.

color completely disappear within very few minutes but can be reproduced by repeated reductions.

Compared to the reduction experiment without phenol (*vide supra*) the g value of 1.99 is now slightly decreased and an increased phosphorus hyperfine splitting parameter of $A_{iso}(^{31}P) = 19.1$ G ($17.7 \cdot 10^{-4}$ cm$^{-1}$) is obtained from the spectral simulation. This clearly indicates that changes within the complex structure which result in significant changes of the electronic structure of the reaction product occur as a consequence of the reduction in the presence of phenol. This could be explained by the two scenarios that a possible protonation of the imido ligand might give an amido or amino ligand and the acetonitrile *trans* ligand is exchanged by phenolate.[89] The molybdenum hyperfine coupling of $A_{iso}(^{95/97}Mo) = 33.5$ G ($32.9 \cdot 10^{-4}$ cm$^{-1}$) is identical to the preceding measurement (same oxidation state: Mo(III)).

Phenol is used to provide $H^+$ for the protonation of the imido ligand, so the initial compound being formed during the reduction might be a Mo(III)-alkyl amido species. This could probably be further reduced (and protonated) right away forming a Mo(II)-alkyl amido (or amino) species or disproportionate to give Mo(IV) and Mo(II). Both possible reaction pathways could explain the disappearance of the EPR signal after a few minutes, as Mo(IV) is EPR silent. Mo(II), which could be an S = 0 or an S = 1 integer spin system, can also not be detected at least not in the "normal" (perpendicular) detection mode.

After the reduction of [Mo(NCMe)(NEt)*depe*$_2$]$^{2+}$ in the presence of phenol further protonation steps could lead to the formation of ethylamine, which could in the end be detected by UV/Vis spectroscopy (colorimetry) using a 2,4-Dinitrofluorobenzene assay.[201]

## 6.3 Oxidation of [Mo(NCMe)(NEt)*depe*$_2$]$^{2+}$

After the electrochemical oxidation of [Mo(NCMe)(NEt)*depe*$_2$]$^{2+}$ a symmetric hyperfine split quintet is observed in the EPR spectrum at g = 2.00 (Figure 6.4), indicating that a stable paramagnetic oxidation product must have been formed, which could only be a Mo(V)

species. This is also confirmed by the change of color during the oxidation turning from violet to green.[5]

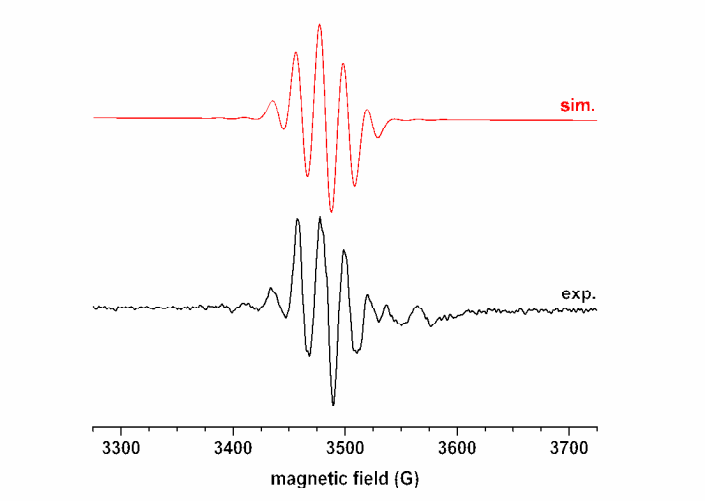


**Figure 6.4.** Experimental and simulated cw X-band EPR spectrum of [Mo(NCMe)(NEt)*depe*$_2$]$^{2+}$ (10 mM), oxidized in MeCN containing $NBu_4PF_6$ (0.1 M) at +2.2 - +2.5V. experimental: room temperature, microwave frequency: 9.78 GHz, microwave power 6.3 mW, modulation amplitude 4 G, modulation frequency 100 kHz, simulation: $g_{iso}$ = 2.00, $A_{iso}(^{95/97}Mo)$ = 27.0 G, $A_{iso}(^{31}P)$ = 20.5 G, (line width 6.6 G).

As we now have a different oxidation state compared to the preceding two measurements a different molybdenum hyperfine coupling constant is expected for the Mo(V) oxidation product. From the spectral simulation a value of $A_{iso}(^{95/97}Mo)$ = 27.0 G ($25.2 \cdot 10^{-4}$ cm$^{1}$) is obtained, which is significantly lower than compared to the Mo(III) reduction products. The overall signal width now is thus only about 180 G. On the other hand, the phosphorus hyperfine splitting parameter $A_{iso}(^{31}P)$ is as expected very similar to the previous Mo(III) spectra, as a value of 20.5 G ($19.1 \cdot 10^{-4}$ cm$^{-1}$) is derived from the simulation of the EPR spectrum.

## 6.4 Summary

The paramagnetic reaction products that were obtained from the electrochemical reduction and oxidation of the diamagnetic [Mo(NCMe)(NEt)*depe*$_2$]$^{2+}$ complex all show symmetric S = ±1/2 signals in the room-temperature EPR spectra, which could be successfully simulated

[5] Note that the molybdenum(V)´complex [Mo(O)Cl$_3$*dppe*] (*dppe* = 1,2-Bis(diphenylphosphino)ethane, *vide supra*, chapter 3) also is green in the solid state as well as in solution.

with isotropic parameters using the XSophe simulation software suite.[1] The accordance between the experimental and simulated spectra is excellent for all electrochemically generated compounds with respect to the positions, the relative intensities and the overall widths of the EPR signals. Only the "molybdenum satellites" on both sides of the very intense quintets that arise from the phosphorus hyperfine coupling are reproduced with very low amplitudes in all simulated spectra, which seems to be an intrinsic implementation problem of the XSophe package.

When comparing the EPR spectra of the oxidation product and the reduction products, different molybdenum hyperfine splitting parameters are obtained for the different oxidation states. Beyond that the two reduction experiments result in two different phosphorus hyperfine splitting parameters indicating the formation of two different Mo(III) species at the different reaction conditions. As no structural information can directly be extracted from the EPR spectra suggestions of possible complex geometries and/or reactions pathways are of course only speculative and have to be proven by other spectroscopic and theoretical methods. Further information about the different oxidation and reduction products would also be gained from the corresponding low-temperature EPR spectra.

# 7 General Conclusion and Future Prospects

Molybdenum and manganese complexes are studied by the Tuczek and Kurz groups as potential catalytic model systems for the reductive nitrogen fixation (Chatt cycle) and oxidative water-splitting, respectively. For the spectroscopic characterization of the electronic structures of different mononuclear molybdenum and manganese complexes, magnetic circular dichroism (MCD) and electron paramagnetic resonance (EPR) spectroscopy were used in addition to UV/Vis absorption spectroscopy in this work. Within the scope of this thesis, also new procedures for the general analysis of MCD *C*-term intensities and signs of electronic transitions have been developed. At this, double *pseudo-A*-terms were identified to be the dominant spectral features in the MCD spectra of $C_S$ symmetric transition metal complexes. Most of the studies were accompanied by (TD)DFT and AOMX ligand field calculations.

On the example of the molybdenum(V) complex [Mo(O)$Cl_3$*dppe*], it has been worked out how MCD *C*-term transitions and especially (double) *pseudo-A*-terms are analyzed based on molecular orbital and symmetry considerations (chapter 3). At the same time it was shown that, in the case of type III electronic transitions,[117] the multi-determinant character of the excited doublet states explicitly has to be considered to correctly describe the MCD *C*-term mechanism, as only configuration interaction between the sing-doublet and the trip-doublet excited states gives rise to a non-zero *C*-term intensity. Based on the derived equations, it was possible to determine the positive and negative signs of these transitions from the considered transition densities according to the protocol of Neese and Solomon[8] and to unambiguously assign the double *pseudo-A*-term in the MCD spectrum of [Mo(O)$Cl_3$*dppe*]. This procedure now has to be verified by transferring it to other $d^1$ systems in the future. Considering other molybdenum(V) complexes the most obvious choice would be a series of molybdenum(V) oxido-trichlorido complexes containing other bidentate phosphine ligands instead of *dppe* or Mo(V) oxido *dppe* complexes with other halogenido co-ligands like the bromido analogue [Mo(O)$Br_3$*dppe*]. Significant shifts of the *pseudo-A*-term transitions would be expected in the MCD spectra for such a series as the involved molecular orbitals are the out-of-plane $p_\pi$ orbitals of the equatorial ligands. Also, the oxidized and reduced forms of the [Mo(NCMe)(NEt)*depe*$_2$]$^{2+}$ complex (chapter 6) may be suitable candidates for an MCD study of the electronic transitions, as they are assumed to be S = 1/2 systems as well. In addition,

MCD *C*-terms intensities will have to be determined quantitatively in future studies. Suitable candidates for that might be the vanadyl, copper and cobalt porphyrin complexes that have already been studied by Gouterman and co-worker with respect to their excited states by luminescence spectroscopy.[187]

The MCD spectra of (pseudo-)$C_S$ symmetric multi-electron systems have been systematically analyzed as well, in form of the [$Mn^{III}$(*acen*)X] series of complexes (chapter 4). These MCD spectra are also dominated by double *pseudo-A*-terms. By the variation of the axial ligand X (X = $I^-$, $Br^-$, $Cl^-$, *N*$CS^-$), small changes of the ligand field were induced within the square-pyramidal complex geometry. This has a huge impact on the signs of the *pseudo-A*-terms as the involved molecular orbitals energetically shift due to the increasing ligand field strength going from the iodido to the *N*CS complex. As a larger number of the observed MCD bands could not clearly be assigned in the case of [Mn(*acen*)X] other manganese(III) complexes, probably exhibiting higher symmetries, should be chosen and systematically analyzed in the next step. Future studies should then be extended to manganese(IV) complexes with the long-term goal to fully describe the MCD spectra of the important class of *di*nuclear manganese complexes including the signs of the observed transitions.

In addition, a study on the optical absorption spectra of different molybdenum(III) *tripod* complexes has been presented within this thesis (chapter 5). The assignment of the electronic transitions was based on AOMX ligand field as well as TDDFT calculations. The description of the molecular orbitals turned out to be rather difficult in the case of the [$MoX_3P_3$] complexes (X = $Cl^-$, $Br^-$) containing the aromatic $P_3$ ligand ($P_3$ = 1,1,1-tris(diphenyl-hosphinomethyl)ethane) but could be managed with the help of a truncated [$MoX_3P_3^H$] model. To verify the suggested band assignments, this study should be extended to a larger number of different facially coordinated aliphatic, aromatic and heteroatom containing molybdenum(III) *tripod* complexes. Only on a broader basis of UV/Vis (and probably MCD) data a further and more profound analysis of the observed bands will be successful.

One thing that was not part of any of the presented MCD studies is the VTVH analysis of the recorded MCD spectra. In the case of $d^{>1}$ complexes, this will be necessary in the future to gain further ground state information which could be compared to the properties obtained from the simulations of the corresponding EPR spectra as well as to directly get the polarization of the considered electronic transitions. Therefore it should be included in future

studies on any MCD spectra. However, for that purpose probably a suitable multi-electron system (other than [$Mn^{III}$(*acen*)X]!) will have to be chosen first to develop and test an appropriate procedure for the correct VTVH analysis.

After some initial studies on the cw X-band EPR spectra and spectral simulations of different mononuclear molybdenum and manganese complexes the most promising field for future studies are the EPR spectra of high spin molybdenum(III) complexes (S = 3/2) which are also important for the Chatt cycle. In a first step, the present study will have to be extended to a larger number of molybdenum(III) *tripod* complexes, before the differences between meridional and facial coordination geometries should be explored systematically. In addition, also the corresponding low-temperature EPR spectra will have to be analyzed.

Considering the low-temperature parallel mode EPR spectra of the [$Mn^{III}$(*acen*)X] complexes, which have been presented in a comprehensive study within this work (chapter 4.4), the excellent quality of the recorded spectra should be stressed at this point.

In the case of the spectroelectrochemistry of [Mo(NCMe)(NEt)*depe*$_2$]$^{2+}$ (chapter 6) also the low-temperature EPR spectra of the different oxidation and reduction products should be measured to further characterize the resulting species.

In summary, this work has shown that EPR and MCD spectroscopy are very powerful techniques for the characterization of mononuclear molybdenum and manganese complexes. Some of the presented studies may also be taken as starting points for future work in the Tuczek/Kurz groups. In addition, especially by the theoretical analysis of the *C*-term intensities and signs for multi-determinant excited doublet states this work has made an important contribution to a more advanced understanding of MCD spectra in general.

# 8 Experimental

## 8.1 Synthesis and Preparation

The synthesis of the *$H_2$acen* ligand (*$H_2$acen* = *N,N'*-ethylenebis(acetylacetone)imine) and the preparation of the [Mn(*acen*)X] complexes (X = $I^-$, $Br^-$, $Cl^-$, *N*$CS^-$) were carried out according to literature procedures.[189] [188] Starting reagents and solvents were used as obtained from the provider without purification.

The preparation of the [$MoX_3P_3$] complexes ($P_3$ = 1,1,1-tris(diphenylphosphino-methyl)ethane, X = $Cl^-$, $Br^-$) has already been decribed.[6, 196] The synthesis of the $SiP_3$ ligand ($SiP_3$ = tris(dimethylphosphinomethyl)methylsilane, *tdmpmms*) and the preparation of [$MoCl_3SiP_3$] will be described elsewhere.[199]

The molybdenum [Mo(O)$Cl_3$*dppe*] complex (*dppe* = 1,2-bis(diphenylphosphino)ethane) was synthesized by Henning Broda according to a previously published literature procedure.[186]

The synthesis [Mo(NCMe)(NEt)*depe*$_2$]$^{2+}$ has already been reported.[89]

For sample preparations, solvents of the *pro analysi* (p.a.) grade were used and, where necessary, dried and destilled under $N_2$ atmosphere.

## 8.2 CHNS Elemental Analysis and Atomic Absorption Spectroscopy (AAS)

Elemental analyses were performed with a Euro Vector CHNS-O element analyzer (Euro EA 3000). The solid samples were burned in sealed tin pots in a stream of oxygen.

The percentage of halides was determined after the incineration of the solid samples by titration versus silver nitrate (potentiometric death stop method).

Manganese atomic absorption spectroscopy (AAS) measurements were performed on an AAnalyst spectrometer system by Perkin Elmer. 1 mL of AAS sample solutions were added to 1 mL of conc. $HNO_3$ and left at room temperature for at least 24 h before being diluted to 25 mL with ultra pure water.

## 8.3 Vibrational Spectroscopy

*Infrared Spectroscopy*

Infrared spectra (MIR) of the solid samples were measured in KBr between 400 $cm^{-1}$ and 4 000 $cm^{-1}$ using a Bruker IFS v66/S FT-IR spectrometer.

Far infrared IR spectra (FIR) were recorded between 100 $cm^{-1}$ and 550 $cm^{-1}$ using a Bruker IFS 66 FIR spectrometer. The solid compounds were lubricated with silicon and halogen free grease (Apiezon) between thin PE sheets.

*FT-Raman Spectroscopy*

FT-Raman spectra of the solid samples were recorded with a Bruker IFS 666/CS NIR FT-Raman spectrometer. A Nd:YAG laser with an excitation wavelength of 1064 nm was used as a light source. The spectral resolution was 2 $cm^{-1}$.

*Resonance Raman Spectroscopy*

Resonance Raman spectra were recorded with a DILOR XY-multichannel Raman spectrometer with a triple monochromator and a CCD detector. Excitation wavelengths between 454.5 nm and 647.1 nm were generated by an $Ar^+/Kr^+$ laser. A spectral resolution between 0.8 $cm^{-1}$ and 2.5 $cm^{-1}$ was obtained dependent on the excitation energy.

## 8.4 UV/Visible Absorption (UV/Vis) Spectroscopy

The UV/Vis absorption spectra of the complex solutions and polystyrene film samples were recorded with a Cary 5 000 NIR spectrometer at wavelengths between 1 500 nm and 200 nm using different concentrations and path lengths. Low-temperature UV/Vis spectra of thin polystyrene film samples were recorded at 100 K using a KONTI cryostat associated with a TIC-300 MA temperature controller (CryoVac).

## 8.5 Magnetic Circular Dichroism (MCD) Spectroscopy

Low-temperature MCD data were recorded at T = 2 K using a JASCO J810 CD spectro-polarimeter associated with an OXFORD SM 4 000-9 magnetocryostat, as previously described.[122, 147] Magnetic field strengths were varied between 0 T and (up to) ±7 T. Using two interchangeable head-on photomultiplier tubes MCD spectra for a combined wavelength range of 200 - 1 100 nm (50 000 - 9 000 $cm^{-1}$) could be recorded. Thin polystyrene film samples were prepared by the evaporation of 200 µL of dichloromethane complex solutions (1 mM, 5 mM) containing a sufficient amount of polystyrene. After the subtraction of the B = 0 T reference spectra the resulting MCD spectra were deconvoluted by Gaussian curve fits to resolve the individual MCD *C*-term transitions.

## 8.6 Electrochemistry

Cyclic voltammetry measurements of [Mn(*acen*)X] complex solutions (1 mM in $CH_2Cl_2$) were performed with an EG&G 273A Potentiostat/Galvanostat (Princeton Applied Research). Tetrabutylammoniumhexafluorophosphat ($NBu_4PF_6$, $TBAPF_6$) was used as electrolyte (0.1 M). Cyclic voltammograms were recorded at scanning rates of 0.1 $V \cdot s^{-1}$ using a 1 mm platinum disk as working electrode, a platinum counter electrode and a silver reference electrode. Ferrocene ($Fc/Fc^+$) was used as internal reference.

## 8.7 Electron Paramagnetic Resonance (EPR) Spectroscopy and Spectroelectrochemistry

Low-temperature cw X-band EPR spectra were collected at temperatures between 4 and 25 K using a Bruker EMX*plus* spectrometer with a PremiumX microwave bridge equipped with an Oxford Instrument ESR 900 cryostat, an Oxford ITC-4 temperature controller and a dual mode cavity (Bruker ER-4116DM). Samples were prepared as frozen manganese and molybdenum complex solutions (200 µL) in 1 mm quartz tubes. EPR spectra of the manganese complexes were recorded both in the parallel and in the perpendicular detection mode. EPR data collection was managed using the Bruker Xenon 1.0 software package.

Room temperature EPR spectra of molybdenum complex solutions were recorded in small capillaries using a HQ cavity.

EPR samples of the molybdenum complexes were prepared under a protective Ar or $N_2$ atmosphere.

Room temperature EPR spectroelectrochemistry measurements of acetonitrile complex solutions (10 mM) were recorded in a 4 mm quartz tube which contains a platinum working and a platinum counter electrode. $NBu_4PF_6$ was used (0.1 M) as electrolyte. As no reference electrode or internal standard was used, reduction and oxidation potentials were slowly changed using a conventional power supply unit until a current of 30 - 40 µA was reached. The samples were then electrolyzed over several minutes until significant intensities of the EPR spectra were obtained.

Spectral simulations of the EPR spectra were performed using the EPR simulation software packages XSophe[1] or EasySpin.[198]

## 8.8 Ligand Field Calculations (AOMX)

Ligand field (AOM) calculations were carried out using the AOMX program developed by H. Adamsky.[169], [170] Input coordinates of the coordinating ligand atoms (bond distances and bond angles) were taken from DFT optimized complex structures unless stated otherwise. The calculations were carried out without an effective symmetry assignment. The AOM parameters were fitted to experimental energies taken from the UV/Vis and/or MCD spectra (Gaussian curve fits). The σ- and π-bonding parameters $e_\sigma$ and $e_\pi$ can be interpreted as a measure of the donor and acceptor properties of the corresponding ligands. Starting parameters were taken from a previously published data.[168]

## 8.9 Quantum Chemical DFT Calculations

Spin-unrestricted DFT calculations were performed using Gaussian03.[202] The B3LYP hybrid functional[172-174] was employed for the geometry optimization of complex structures, the calculation of vibrational spectra and for the time-dependent DFT (TDDFT) calculations of the electronic transitions. The computation of molecular orbitals was done using the BP86 functional.[175-177] The LANL2DZ basis set was always used for all types of atoms.[178] [179-181]

Optimized complex structures and calculated spectra were displayed with GaussView 5.0.[203] The molecular orbitals were plotted with Gabedit.[204]

# 9 References


[1] G. R. Hanson, K. E. Gates, C. J. Noble, M. Griffin, A. Mitchell, S. Benson, *J. Inorg. Biochem.* **2004**, *98*, 903.

[2] R. Römer, G. Stephan, C. Habeck, C. Hoberg, G. Peters, C. Näther, F. Tuczek, *Eur. J. Inorg. Chem.* **2008**, 3258.

[3] A. Dreher, K. Mersmann, C. Näther, I. Ivanovic-Burmazovic, R. van Eldik, F. Tuczek, *Inorg. Chem.* **2009**, *48*, 2078.

[4] R. Römer, C. Gradert, A. Bannwarth, G. Peters, C. Näther, F. Tuczek, *Dalton Trans.* **2011**, *40*, 3229.

[5] L. Söncksen, R. Römer, C. Näther, G. Peters, F. Tuczek, *Inorg. Chim. Acta* **2011**, *374*, 472.

[6] J. Krahmer, H. Broda, C. Näther, G. Peters, W. Thimm, F. Tuczek, *Eur. J. Inorg. Chem.* **2011**, *48*, 4377.

[7] M. Wiechen, H. M. Berends, P. Kurz, *Dalton Trans.* **2011**.

[8] F. Neese, E. I. Solomon, *Inorg. Chem.* **1999**, *38*, 1847.

[9] I. Batinić-Haberle, J. S. Reboucas, I. Spasojevic, *Antioxid. Redox Signal.* **2010**, *13*, 877.

[10] T. R. Golden, M. Patel, *Antioxid. Redox Signal.* **2009**, *11*, 555.

[11] I. Fridovich, *Annu. Rev. Biochem.* **1995**, *64*, 97.

[12] I. A. Abreu, D. E. Cabelli, *Biochim. Biophys. Acta* **2010**, *1804*, 263.

[13] G. E. O. Borgstahl, H. E. Parge, M. J. Hickey, W. F. Beyer, R. A. Hallewell, J. A. Tainer, *Cell* **1992**, *71*, 107.

[14] R. A. Edwards, H. M. Baker, M. M. Whittaker, J. W. Whittaker, G. B. Jameson, E. N. Baker, *J. Biol. Inorg. Chem.* **1998**, *3*, 161.

[15] R. J. Dennis, E. Micossi, J. McCarthy, E. Moe, E. J. Gordon, S. Kozielski-Stuhrmann, G. A. Leonard, S. McSweeney, *Acta Crystallogr.* **2006**, *62*, 325.

[16] C. Bull, E. C. Niederhoffer, T. Yoshida, J. A. Fee, *J. Am. Chem. Soc.* **1991**, *113*, 4069.

[17] V. Oliveri, A. Puglisi, G. Vecchio, *Dalton Trans* **2011**, *40*, 2913.

[18] V. Oliveri, G. Vecchio, *Eur. J. Med. Chem.* **2011**, *46*, 961.

[19] C. Beauchamp, I. Fridovich., *Anal. Biochem.* **1971**, *44*, 276.

[20] N. Metzler-Nolte, U. Schatzschneider, *Bioinorganic Chemistry - A Practical Course*, de Gruyter, Berlin, New York, **2009**.

[21] G. C. Dismukes, *Chem. Rev.* **1996**, *96*, 2909.

[22] S. V. Antonyuk, V. R. Melik-Adamyan, A. N. Popov, V. S. Lamzin, P. D. Hempstead, P. M. Harrison, P. J. Artymyuk, V. V. Barynin, *Crystallogr. Reports* **2000**, *45*, 105.

[23] V. V. Barynin, M. M. Whittaker, S. V. Antonyuk, V. S. Lamzin, P. M. Harrison, P. J. Artymiuk, J. W. Whittaker, *Structure* **2001**, *9*, 725.

[24] M. M. Whittaker, V. V. Barynin, S. V. Antonyuk, J. Whittaker, *Biochemistry* **1999**, *38*, 9126.

[25] A. J. Wu, J. E. Penner-Hahn, V. L. Pecoraro, *Chem. Rev.* **2004**, *104*, 903.

[26] H. M. Berends. *PhD Thesis*, Christian-Albrechts-Universität zu Kiel, 2011.

[27] G. S. Waldo, J. E. Penner-Hahn, *Biochemistry* **1995**, *34*, 1507.

[28] J. W. de Boer, W. R. Browne, B. L. Feringa, R. Hage, *C. R. Chimie* **2007**, *10*, 341.

[29] Y. Kono, I. Fridovich, *J. Biol. Chem.* **1983**, *258*, 3646.

[30] A. E. Meier, M. M. Whittaker, J. W. Whittaker, *Biochemistry* **1996**, *35*, 348.

[31] Y. Naruta, M. Sasayama, T. Sasaki, *Angew. Chem., Int. Ed. Engl.* **1994**, *33*, 1839.

[32] Y. Naruta, M. Sasayama, K. Ichihara, *J. Mol. Cat. A* **1997**, *117*, 115.

[33] M. U. Triller, W. Y. Hsieh, V. L. Pecoraro, A. Rompel, B. Krebs, *Inorg. Chem.* **2002**, *41*, 5544.

[34] L. Dubois, J. Pecaut, M. F. Charlot, C. Baffert, M. N. Collomb, A. Deronzier, J. M. Latour, *Chem. Eur. J.* **2008**, *14*, 3013.

[35] A. Zouni, H. T. Witt, J. Kern, P. Fromme, N. Krauss, W. Saenger, P. Orth, *Nature* **2001**, *409*, 739.

[36] K. N. Ferreira, T. M. Iverson, K. Maghlaoui, J. Barber, S. Iwata, *Science* **2004**, *303*, 1831.

[37] A. Guskov, J. Kern, A. Gabdulkhakov, M. Broser, A. Zouni, W. Saenger, *Nat. Struct. Mol. Biol.* **2009**, *16*, 334.

[38] Y. Umena, K. Kawakami, J. R. Shen, N. Kamiya, *Nature* **2011**, *473*, 55.

[39] B. Loll, J. Kern, W. Saenger, A. Zouni, J. Biesiadka, *Nature* **2005**, *438*, 1040.

[40] J. Yano, J. Kern, K. Sauer, M. J. Latimer, Y. Pushkar, J. Biesiadka, B. Loll, W. Saenger, J. Messinger, A. Zouni, V. K. Yachandra, *Science* **2006**, *314*, 821.

[41] K. Sauer, J. Yano, V. K. Yachandra, *Coord. Chem. Rev.* **2008**, *252*, 318.

[42] K. Kawakami, Y. Umena, N. Kamiya, J. R. Shen, *J. Photochem. Photobiol. B* **2011**, *104*, 9.

[43] B. Kok, B. Forbush, M. Mcgloin, *Photochem. Photobiol.* **1970**, *11*, 457.

[44] H. Dau, C. Limberg, T. Reier, M. Risch, S. Roggan, P. Strasser, *ChemCatChem.* **2010**, *2*, 724.

[45] T. J. Meyer, M. H. Huynh, H. H. Thorp, *Angew. Chem. Int. Ed. Engl.* **2007**, *46*, 5284.

[46] W. Lubitz, E. J. Reijerse, J. Messinger, *Energy Environ. Sci.* **2008**, *1*, 15.

[47] E. M. Sproviero, J. A. Gascon, J. P. McEvoy, G. W. Brudvig, V. S. Batista, *Coord. Chem. Rev.* **2008**, *252*, 395.

[48] S. Mukhopadhyay, S. K. Mandal, S. Bhaduri, W. H. Armstrong, *Chem. Rev.* **2004**, *104*, 3981.

[49] C. S. Mullins, V. L. Pecoraro, *Coord. Chem. Rev.* **2008**, *252*, 416.

[50] C. W. Cady, R. H. Crabtree, G. W. Brudvig, *Coord. Chem. Rev.* **2008**, *252*, 444.

[51] J. Limburg, J. S. Vrettos, L. M. Liable-Sands, A. L. Rheingold, G. W. Brudvig, R. H. Crabtree, *Science* **1999**, *283*, 1524.

[52] J. Limburg, J. S. Vrettos, H. Y. Chen, J. C. de Paula, G. W. Brudvig, R. H. Crabtree, *J. Am. Chem. Soc.* **2001**, *123*, 423.

[53] N. S. Lewis, D. G. Nocera, *Proc. Natl. Acad. Sci. USA* **2006**, *103*, 15729.

[54] M. Kirch, J. M. Lehn, J. P. Sauvage, *Helv. Chim. Acta* **1979**, *62*, 1345.

[55] V. Balzani, A. Credi, M. Venturi, *ChemSusChem* **2008**, *1*, 26.

[56] R. Ramaraj, A. Kira, M. Kaneko, *Chem. Lett.* **1987**, 261.

[57] M. Yagi, K. Narita, *J. Am. Chem. Soc.* **2004**, *126*, 8084.

[58] M. Yagi, K. Narita, S. Maruyama, K. Sone, T. Kuwabara, K. Shimizu, *Biochim. Biophys. Acta* **2007**, *1767*, 660.

[59] H. M. Berends, T. Homburg, I. Kunz, P. Kurz, *Appl. Clay Sci.* **2011**, *53*, 174.

[60] M. M. Najafpour, T. Ehrenberg, M. Wiechen, P. Kurz, *Angew. Chem. Int. Ed.* **2010**, *49*, 2233.

[61] I. Zaharieva, M. M. Najafpour, M. Wiechen, M. Haumann, P. Kurz, H. Dau, *Energy Environ. Sci.* **2011**, *4*, 2400.

[62] A. F. Hollemann, E. Wiberg, *Lehrbuch der Anorganischen Chemie*, 101. Auflage ed., Walter de Gruyter Verlag & Co., Berlin - New York, **1984-1995**.

[63] T. A. Bazhenova, A. E. Shilov, *Coord. Chem. Rev.* **1995**, *144*, 69.

[64] G. Ertl, M. Huber, S. B. Lee, Z. Paal, M. Weiss, *Appl. Surf. Sci.* **1981**, *8*, 373.

[65] G. Ertl, *Akademie-Journal* **2003**, 14.

[66] J. S. Kim, D. C. Rees, *Nature* **1992**, *360*, 553.

[67] O. Einsle, F. A. Tezcan, S. L. A. Andrade, B. Schmid, M. Yoshida, J. B. Howard, D. C. Rees, *Science* **2002**, *297*, 1696.

[68] K. M. Lancaster, M. Roemelt, P. Ettenhuber, Y. L. Hu, M. W. Ribbe, F. Neese, U. Bergmann, S. DeBeer, *Science* **2011**, *334*, 974.

[69] T. Le Gall, S. K. Ibrahim, C. A. Gormal, B. E. Smith, C. J. Pickett, *Chem. Comm.* **1999**, 773.

[70] B. Hinnemann, J. K. Norskov, *Top. Catal.* **2006**, *37*, 55.

[71] R. N. F. Thorneley, D. J. Lowe, *Molybdenum Enzymes*, John Wiley, New York, **1985**.

[72] D. J. Lowe, R. N. F. Thorneley, *Biochem. J.* **1984**, *224*, 877.

[73] D. J. Lowe, R. N. F. Thorneley, *Biochem. J.* **1984**, *224*, 895.

[74] R. N. F. Thorneley, D. J. Lowe, *Biochem. J.* **1984**, *224*, 887.

[75] R. N. F. Thorneley, D. J. Lowe, *Biochem. J.* **1984**, *224*, 903.

[76] I. Dance, *J. Am. Chem. Soc.* **2007**, *129*, 1076.

[77] I. Dance, *Dalton Trans.* **2008**, 5977.

[78] I. Dance, *Dalton Trans.* **2008**, 5992.

[79] B. M. Hoffman, D. R. Dean, L. C. Seefeldt, *Accounts Chem. Res.* **2009**, *42*, 609.

[80] D. V. Yandulov, A. L. Rheingold, C. Ceccarelli, W. M. Davis, R. R. Schrock, *Inorg. Chem.* **2003**, *42*, 796.

[81] D. V. Yandulov, R. R. Schrock, *Science* **2003**, *301*, 76.

[82] D. V. Yandulov, R. R. Schrock, *Inorg. Chem.* **2005**, *44*, 1103.

[83] R. R. Schrock, *Accounts Chem. Res.* **2005**, *38*, 955.

[84] F. Studt, F. Tuczek, *Angew. Chem.* **2005**, *117*, 5783.

[85] J. Chatt, G. A. Heath, R. L. Richards, *J. Chem. Soc. Chem. Comm.* **1972**, 1010.

[86] J. Chatt, A. J. Pearman, R. L. Richards, *Nature* **1975**, *253*, 39.

[87] N. Lehnert, F. Tuczek, *Inorg. Chem.* **1999**, *38*, 1671.

[88] K. Mersmann, A. Hauser, N. Lehnert, F. Tuczek, *Inorg. Chem.* **2006**, *45*, 5044.

[89] A. Dreher. *PhD Thesis*, Christian-Albrechts-Universität zu Kiel, **2010**.

[90] C. J. Pickett, J. Talarmin, *Nature* **1985**, *317*, 652.

[91] F. A. Cotton, G. Wilkinson, *Anorganische Chemie - eine zusammenfassende Darstellung für Fortgeschrittene*, 4., völlig neu bearbeitete Auflage ed., Verlag Chemie, Weinheim; Deerfield Beach, Florida; Basel, **1982**.

[92] J. Huheey, E. Keiter, R. Keiter, *Anorganische Chemie - Prinzipien von Struktur und Reaktivität*, de Gruyter, Berlin, New York, **2003**.

[93] L. H. Gade, *Koordinationschemie*, 1. Auflage ed., Weinheim, New York, Chichester, Brisbane, Singapore, Toronto, **1998**.

[94] *Inorganic Electronic Structure and Spectroscopy,* Vol. I, Whiley Interscience, Hoboken, New Jersey, **2006**.

[95] B. N. Figgis, *Introduction to Ligand Fields*, Wiley, New York, **1966**.

[96] A. B. P. Lever, *Inorganic Electronic Spectroscopy*, Elsevier, Amsterdam, **1986**.

[97] H. A. Jahn, E. Teller, *Proc. R. Soc. Lond. A* **1937**, *161*, 220.

[98] B. Albela, R. Carina, C. Policar, S. Poussereau, J. Cano, J. Guilhem, L. Tchertanov, G. Blondin, M. Delroisse, J. J. Girerd, *Inorg. Chem.* **2005**, *44*, 6959.

[99] C. Bellitto, A. A. G. Tomlinson, C. Furlani, *J. Chem. Soc. A* **1971**, 3267.

[100] L. J. Boucher, M. O. Farrell, *J. Inorg. Nucl. Chem.* **1973**, *35*, 3731.

[101] M. U. Triller, D. Pursche, W. Y. Hsieh, V. L. Pecoraro, A. Rompel, B. Krebs, *Inorg. Chem.* **2003**, *42*, 6274.

[102] E. König, S. Kremer, *Ligand Field Diagrams*, Plenum Press, New York, **1977**.

[103] V. Chin Quee-Smith, L. DelPizzo, S. H. Jureller, J. L. Kerschner, R. Hage, *Inorg. Chem.* **1996**, *35*, 6461.

[104] A. Westphal, unpublisched work, Christian-Albrechts-Universität zu Kiel, **2010**.

[105] T. M. Dunn, *Trans. Faraday Soc.* **1961**, *57*, 1441.

[106] H. Hartmann, H. J. Schmidt, *Z. Phys. Chem.* **1957**, *11*, 234.

[107] R. J. Irving, M. C. Steele, *Aust. J. Chem.* **1957**, *10*, 490.

[108] W. Wardlaw, A. J. I. Harding, *J. Chem. Soc.* **1926**, 1592.

[109] C. Furlani, O. Piovesana, *Mol. Phys.* **1965**, *9*, 341.

[110] S. Pal, J. W. Gohdes, W. C. A. Wilisch, W. H. Armstrong, *Inorg. Chem.* **1992**, *31*, 713.

[111] D. R. Gamelin, M. L. Kirk, T. L. Stemmler, S. Pal, W. H. Armstrong, J. E. Pennerhahn, E. I. Solomon, *J. Am. Chem. Soc.* **1994**, *116*, 2392.

[112] P. J. Stephens, *J. Chem. Phys.* **1970**, *52*, 3489.

[113] P. J. Stephens, *Annu. Rev. Chem. Phys.* **1974**, *25*, 201.

[114] P. N. Schatz, A. J. McCafferty, *Q. Rev.* **1969**, *23*, 552.

[115] W. R. Mason, *A Practical Guide to Magnetic Circular Dichroism Spectroscopy*, John Wiley & Sons, Inc., Hoboken, New Jersey, **2007**.

[116] N. Lehnert, S. DeBeer George, E. I. Solomon, *Curr. Opin. Chem. Biol.* **2001**, *5*, 176.

[117] F. Neese. *PhD Thesis*, Universität Konstanz, 1997.

[118] E. I. Solomon, E. G. Pavel, K. E. Loeb, C. Campochiaro, *Coord. Chem. Rev.* **1995**, *144*, 369.

[119] J. A. Farrar, F. Neese, P. Lappalainen, P. M. H. Kroneck, M. Saraste, W. G. Zumft, A. J. Thomson, *J. Am. Chem. Soc.* **1996**, *118*, 11501.

[120] F. Neese, E. I. Solomon, *J. Am. Chem. Soc.* **1998**, *120*, 12829.

[121] D. R. Gamelin, D. W. Randall, M. T. Hay, R. P. Houser, T. C. Mulder, G. W. Canters, S. de Vries, W. B. Tolman, Y. Lu, E. I. Solomon, *J. Am. Chem. Soc.* **1998**, *120*, 5246.

[122] F. Paulat, N. Lehnert, *Inorg. Chem.* **2008**, *47*, 4963.

[123] F. B. Johansson, A. D. Bond, U. G. Nielsen, B. Moubaraki, K. S. Murray, K. J. Berry, J. A. Larrabee, C. J. McKenzie, *Inorg. Chem.* **2008**, *47*, 5079.

[124] J. A. Larrabee, W. R. Johnson, A. S. Volwiler, *Inorg. Chem.* **2009**, *48*, 8822.

[125] T. C. Brunold, D. R. Gamelin, T. L. Stemmler, S. K. Mandal, W. H. Armstrong, J. E. Penner-Hahn, E. I. Solomon, *J. Am. Chem. Soc.* **1998**, *120*, 8724.

[126] R. A. Geiger, S. Chattopadhyay, V. W. Day, T. A. Jackson, *J. Am. Chem. Soc.* **2010**, *132*, 2821.

[127] S. Chattopadhyay, R. A. Geiger, G. C. Yin, D. H. Busch, T. A. Jackson, *Inorg. Chem.* **2010**, *49*, 7530.

[128] T. A. Jackson, J. Xie, E. Yikilmaz, A. F. Miller, T. C. Brunold, *J. Am. Chem. Soc.* **2002**, *124*, 10833.

[129] T. A. Jackson, T. C. Brunold, *Acc. Chem. Res.* **2004**, *37*, 461.

[130] J. W. Whittaker, M. M. Whittaker, *J. Am. Chem. Soc.* **1991**, *113*, 5528.

[131] T. C. Brunold, D. R. Gamelin, E. I. Solomon, *J. Am. Chem. Soc.* **2000**, *122*, 8511.

[132] J. A. Larrabee, C. H. Leung, R. L. Moore, T. Thamrong-Nawasawat, B. S. Wessler, *J. Am. Chem. Soc.* **2004**, *126*, 12316.

[133] J. A. Larrabee, S. A. Chyun, A. S. Volwiler, *Inorg. Chem.* **2008**, *47*, 10499.

[134] J. A. Larrabee, W. R. Johnson, A. S. Volwiler, *Inorg. Chem.* **2009**, *48*, 8822.

[135] D. Ganyushin, F. Neese, *J. Chem. Phys.* **2008**, *128*.

[136] M. Sundararajan, D. Ganyushin, S. F. Ye, F. Neese, *Dalton Trans.* **2009**, 6021.

[137] M. Seth, T. Ziegler, A. Banerjee, J. Autschbach, S. J. A. van Gisbergen, E. J. Baerends, *J. Chem. Phys.* **2004**, *120*, 10942.

[138] M. Seth, T. Ziegler, *J. Chem. Phys.* **2006**, *124*.

[139] M. Krykunov, M. Seth, T. Ziegler, J. Autschbach, *J. Chem. Phys.* **2007**, *127*.

[140] G. A. Peralta, M. Seth, H. Zhekova, T. Ziegler, *Inorg. Chem.* **2008**, *47*, 4185.

[141] M. Seth, T. Ziegler, J. Autschbach, *J. Chem. Phys.* **2008**, *129*, 104105.

[142] E. Hernandez-Marin, M. Seth, T. Ziegler, *Inorg. Chem.* **2010**, *49*, 1566.

[143] D. M. Sabel, A. A. Gewirth, *Inorg. Chem.* **1994**, *33*, 148.

[144] M. D. Carducci, C. Brown, E. I. Solomon, J. H. Enemark, *J. Am. Chem. Soc.* **1994**, *116*, 11856.

[145] F. E. Inscore, R. McNaughton, B. L. Westcott, M. E. Helton, R. Jones, I. K. Dhawan, J. H. Enemark, M. L. Kirk, *Inorg. Chem.* **1999**, *38*, 1401.

[146] M. L. Kirk, K. Peariso, *Polyhedron* **2004**, *23*, 499.

[147] F. Paulat. *PhD*, Christian-Albrechts-Universität zu Kiel, 2007.

[148] R. Kirmse, J. Stach, *ESR-Spektroskopie: Grundlagen und Anwendungen*, Akademie Verlag, Berlin, **1985**.

[149] G. Jeschke, *Einführung in die ESR-Spektroskopie*, Vorlesungsskript, MPI Mainz, **1998**.

[150] J. A. Weil, J. R. Bolton, *Electron Paramagnetic Resonance, Elementary Theory and Practical Application*, John Wiley & Sons Ltd., New York, **2007**.

[151] K. A. Campbell, E. Yikilmaz, C. V. Grant, W. Gregor, A. F. Miller, R. D. Britt, *J. Am. Chem. Soc.* **1999**, *121*, 4714.

[152] M. Zheng, S. V. Khangulov, G. C. Dismukes, V. V. Barynin, *Inorg. Chem.* **1994**, *33*, 382.

[153] P. J. Pessiki, S. V. Khangulov, D. M. Ho, G. C. Dismukes, *J. Am. Chem. Soc.* **1994**, *116*, 891.

[154] S. V. Khangulov, P. J. Pessiki, V. V. Barynin, D. E. Ash, G. C. Dismukes, *Biochemistry* **1995**, *34*, 2015.

[155] R. G. Evelo, S. Styring, A. W. Rutherford, A. J. Hoff, *Biochim. Biophys. Acta* **1989**, *973*, 428.

[156] J. M. Peloquin, R. D. Britt, *Biochim. Biophys. Acta* **2001**, *1503*, 96.

[157] G. Bernat, F. Morvaridi, Y. Feyziyev, S. Styring, *Biochemistry* **2002**, *41*, 5830.

[158] S. Peterson, K. A. Ahrling, S. Styring, *Biochemistry* **1999**, *38*, 15223.

[159] K. A. Campbell, M. R. Lashley, J. K. Wyatt, M. H. Nantz, R. D. Britt, *J. Am. Chem. Soc.* **2001**, *123*, 5710.

[160] K. O. Schäfer, R. Bittl, F. Lendzian, V. Barynin, T. Weyhermüller, K. Wieghardt, W. Lubitz, *J. Phys. Chem. B* **2003**, *107*, 1242.

[161] G. Berggren, A. Thapper, P. Huang, P. Kurz, L. Eriksson, S. Styring, M. F. Anderlund, *Dalton Trans.* **2009**, 10044.

[162] P. Huang, P. Kurz, S. Styring, *Appl. Magn. Reson.* **2007**, *31*, 301.

[163] T. A. Stich, S. Lahiri, G. Yeagle, M. Dicus, M. Brynda, A. Gunn, C. Aznar, V. J. DeRose, R. D. Britt, *Appl. Magn. Reson.* **2007**, *31*, 321.

[164] T. Weyhermüller, T. K. Paine, E. Bothe, E. Bill, P. Chaudhuri, *Inorg. Chim. Acta* **2002**, *337*, 344.

[165] D. L. Hughes, D. J. Lowe, M. Y. Mohammed, C. J. Pickett, N. M. Pinhal, *J. Chem. Soc. Dalton Trans.* **1990**, 2021.

[166] W. Levason, C. A. McAuliffe, B. J. Sayle, *J. Chem. Soc. Dalton Trans.* **1976**, 1177.

[167] P. M. Boorman, C. D. Garner, F. E. Mabbs, *J. Chem. Soc. Dalton Trans.* **1975**, 1299.

[168] P. E. Hoggard, *Struct. Bond.* **2004**, *106*, 37.

[169] AOMX, *An Angular Overlap Model Computer Program*, H. Adamsky, Theoretical Chemistry, Heinrich-Heine-Universität Düsseldorf, **1995**.

[170] H. Adamsky, T. Schönherr, M. Atanasov, *Comprehensive Coordination Chemistry II, Vol. 1*, Lever, A. B. P., Ed.; Elsevier, Oxford, **2004**.

[171] B. Hartke, *Theoretische Chemie I*, Vorlesungsskript, Christian-Albrechts-Universität zu Kiel, **2004**.

[172] A. D. Becke, *Journal of Chemical Physics* **1993**, *98*, 5648.

[173] C. T. Lee, W. T. Yang, R. G. Parr, *Phys. Rev. B* **1988**, *37*, 785.

[174] B. Miehlich, A. Savin, H. Stoll, H. Preuss, *Chem. Phys. Lett.* **1989**, *157*, 200.

[175] A. D. Becke, *Phys. Rev. A* **1988**, *38*, 3098.

[176] J. P. Perdew, *Phys. Rev. B* **1986**, *33*, 8822.

[177] J. P. Perdew, *Phys. Rev. B* **1986**, *34*, 7406.

[178] T. H. Dunning, Jr., P. J. Hay, *Modern Theoretical Chemistry*, Ed. H. F. Schaefer III (Plenum), New York, **1976**.

[179] P. J. Hay, W. R. Wadt, *Journal of Chemical Physics* **1985**, *82*, 270.

[180] P. J. Hay, W. R. Wadt, *Journal of Chemical Physics* **1985**, *82*, 299.

[181] W. R. Wadt, P. J. Hay, *Journal of Chemical Physics* **1985**, *82*, 284.

[182] M. Seth, M. Krykunov, T. Ziegler, J. Autschbach, A. Banerjee, *J. Chem. Phys.* **2008**, *128*, 144105.

[183] M. Seth, M. Krykunov, T. Ziegler, J. Autschbach, *J. Chem. Phys.* **2008**, *128*, 234102.

[184] M. Seth, T. Ziegler, *Advances in Inorganic Chemistry: Theoretical and Computational Inorganic Chemistry, Vol 62* **2010**, *62*, 41.

[185] G. te Velde, F. M. Bickelhaupt, E. J. Baerends, C. F. Guerra, S. J. A. van Gisbergen, J. G. Snijders, T. Ziegler, *J. Comput. Chem.* **2001**, *22*, 931.

[186] A. V. Butcher, J. Chatt, *J. Chem. Soc. (A)* **1971**, 2356.

[187] R. L. Ake, M. Gouterman, *Theor. Chim. Acta* **1969**, *15*, 20.

[188] L. J. Boucher, V. W. Day, *Inorg. Chem.* **1977**, *16*, 1360.

[189] P. J. McCarthy, R. J. Hovey, K. Ueno, A. E. Martell, *J. Am. Chem. Soc.* **1955**, *77*, 5820.

[190] M. P. Hendrich, P. G. Debrunner, *Biophys. J.* **1989**, *56*, 489.

[191] H. Miyasaka, R. Clerac, T. Ishii, H. C. Chang, S. Kitagawa, M. Yamashita, *J. Chem. Soc. Dalton Trans.* **2002**, 1528.

[192] S. Biswas, K. Mitra, B. Adhikary, C. R. Lucas, *Trans. Met. Chem.* **2005**, *30*, 586.

[193] P. Bhowmik, H. P. Nayek, M. Corbella, N. Aliaga-Alcalde, S. Chattopadhyay, *Dalton Trans.* **2011**, *40*, 7916.

[194] Q. Scheifele, C. Riplinger, F. Neese, H. Weihe, A. L. Barra, F. Juranyi, A. Podlesnyak, P. L. W. Tregenna-Piggott, *Inorg. Chem.* **2008**, *47*, 439.

[195] A. Bencini, I. Ciofini, M. G. Uytterhoeven, *Inorg. Chim. Acta* **1998**, *274*, 90.

[196] J. Krahmer. *PhD Thesis*, Christian-Albrechts-Universität zu Kiel, **2011**.

[197] M. Brorson, C. J. H. Jacobsen, C. M. Jensen, I. Schmidt, J. Villadsen, *Inorg. Chim. Acta* **1996**, *247*, 189.

[198] S. Stoll, A. Schweiger, *J. Magn. Reson.* **2006**, *178*, 42.

[199] H. Broda, unpublished work, Christian-Albrechts-Universität zu Kiel, **2011**.

[200] Y. Alias, S. K. Ibrahim, M. A. Queiros, A. Fonseca, J. Talarmin, F. Volant, C. J. Pickett, *J. Chem. Soc. Dalton Trans.* **1997**, 4807.

[201] D. T. Dubin, *J. Biol. Chem.* **1960**, *235*, 783.

[202] M. J. Frisch, G. W. Trucks, H. B. S. Schlegel, G. E.; Robb, M. A.; Cheeseman, J. R.; Montgomery, Jr., J. A.; Vreven, T.; Kudin, K. N.; Burant, J. C.; Millam, J. M.; Iyengar, S. S.; Tomasi, J.; Barone, V.; Mennucci, B.; Cossi, M.; Scalmani, G.; Rega, N.; Petersson, G. A.; Nakatsuji, H.; Hada, M.; Ehara, M.; Toyota, K.; Fukuda, R.; Hasegawa, J.; Ishida, M.; Nakajima, T.; Honda, Y.; Kitao, O.; Nakai, H.; Klene, M.; Li, X.; Knox, J. E.; Hratchian, H. P.; Cross, J. B.; Bakken, V.; Adamo, C.; Jaramillo, J.; Gomperts, R.; Stratmann, R. E.; Yazyev, O.; Austin, A. J.; Cammi, R.; Pomelli, C.; Ochterski, J. W.; Ayala, P. Y.; Morokuma, K.; Voth, G. A.; Salvador, P.; Dannenberg, J. J.; Zakrzewski, V. G.; Dapprich, S.; Daniels, A. D.; Strain, M. C.; Farkas, O.; Malick, D. K.; Rabuck, A. D.; Raghavachari, K.; Foresman, J. B.; Ortiz, J. V.; Cui, Q.; Baboul, A. G.; Clifford, S.; Cioslowski, J.; Stefanov, B. B.; Liu, G.; Liashenko, A.; Piskorz, P.; Komaromi, I.; Martin, R. L.; Fox, D. J.; Keith, T.; Al-Laham, M. A.; Peng, C. Y.; Nanayakkara, A.; Challacombe, M.; Gill, P. M. W.; Johnson, B.; Chen, W.; Wong, M. W.; Gonzalez, C.; Pople, J. A., *Gaussian 03, Revision C.02*, Gaussian, Inc., Wallingford CT, **2004**.

[203] GaussView Version 5.0, R. Dennington, T. Keith, J. Millam, *Semichem Inc.*, Shawnee Mission KS, **2009**.

[204] A. R. Allouche, *Journal of Computational Chemistry* **2011**, *32*, 174.

# Danksagung

An erster Stelle bedanke ich mich herzlich bei Prof. Dr. Felix Tuczek für die intensive Betreuung, und die konstruktive Begleitung dieser Arbeit, sowie für die vielen wertvollen Anregungen und die geduldigen Hilfestellungen, besonders zum theoretischen Hintergrund der MCD-Spektroskopie.

Ganz besonderer Dank gilt Dr. Philipp Kurz und Hans-Martin Berends, v.a. für ihre Unterstützung und bei den MCD- und EPR-Messungen. Ohne ihre tatkräftige Mithilfe und ihren moralischen Beistand wären die aufwendigen und z. T. abenteuerlichen MCD-Messungen nicht möglich gewesen. Darüber hinaus danke ich ihnen natürlich auch für die vielen Diskussionen, Anregungen und Gespräche, auch über die künstliche Photosynthese hinaus.

Großer Dank geht auch an Florian Paulat, der uns mit dem MCD-Spektrometer und den experimentellen Feinheiten der MCD-Spektroskopie vertraut gemacht hat.

Ausdrücklich bedanke ich mich bei Arne Klinkebiel, der im Rahmen seines F2-Praktikums eine umfangreiche Komplexbibliothek synthetisiert hat, die im Folgenden als Grundlage für die MCD-Messungen an einkernigen Mangankomplexen diente, aber auch bei Hannah Lutterbek (F2) und Claudia Stapelfeld (F3) sowie Marcel Richert (Abschlussarbeit).

Des weiteren danke ich Uschi Cornelissen, Stefanie Pehlke und Marianne Karbstein für die Durchführung der Elementaranalysen, die Aufnahme zahlreicher Raman-Spektren sowie ihre Hilfe bei spektroskopischen Fragestellungen.

Bei den Arbeitskreisen Tuczek und Kurz bedanke ich mich für die nette und unkomplizierte Arbeitsatmosphäre während der letzten fünf Jahre. Besonders bedanke ich mich bei Henning Broda, Jan Krahmer und Sven Meyer für die Probenvorbereitung bei den Molybdän-EPR- und MCD-Messungen und die Bereitstellung der benötigten UV/Vis- und IR-/Raman-Spektren, sowie bei Henning für die Bereitstellung des [Mo(O)$Cl_3$*dppe*]-Komplexes.

Ich bedanke mich außerdem bei der GDCh für die großzügigen Reisestipendien.

Zuletzt danke ich Thomas dafür, dass er immer für mich da war. Manchmal.

# Lebenslauf


Anne Westphal

geboren am 09.10.1981 in Sömmerda

Anschrift: Holtenauer Straße 252
24106 Kiel

E-Mail: Anne_Westphal@gmx.de

Staatangehörigkeit: deutsch


**Schule und Hochschulausbildung**

| | |
|---|---|
| 2001 | Abitur am Städtischen Marie-Therese-Gymnasium, Erlangen |
| 2001/02 | Freiwilliges Soziales Jahr im ADS Gerd-Lausen-Haus (Mutter-Kind-Klinik) in Rantum/Sylt |
| WS 2002/03 | Beginn des Chemie-Studiums an der Christian-Albrechts-Universität zu Kiel |
| 10/2004 | Diplom-Vorprüfung |
| 10/2006 | Diplom-Hauptprüfung |
| 06/2007 | Abschluss der Diplomarbeit (Prof. Dr. Felix Tuczek, Institut für Anorganische Chemie der Universität Kiel)<br><br>Titel: „Strategien zur Synthese photoaktiver Liganden für Modellkomplexe zur Modellierung der O-O-Bindungsbildungs-reaktion nach dem Vorbild der photosyntheti-chen Wasseroxidation“ |
| seit 08/2007 | Promotion bei Prof. Dr. Felix Tuczek am Institut für Anorganische Chemie der Christian-Albrechts-Universität, Kiel |

## Konferenzbeiträge

**Vortrag:**

| | |
|---|---|
| 10/2009 | 12. Norddeutsches Doktorandenkolloquium, Oldenburg |
| 02/2010 | 6. Koordinationschemie-Treffen, Mainz |
| 11/2010 | Anorganisch-Chemisches Kolloquium, Institut für Anorganische Chemie, Kiel |

**Poster:**

| | |
|---|---|
| 10/2008 | 14. Vortragstagung der Wöhlervereinigung, München/Garching |
| 02/2009 | 5. Koordinationschemie-Treffen, Erlangen |
| 09/2009 | GDCh-Wissenschaftsforum Chemie 2009, Frankfurt am Main |
| 06/2010 | $10^{th}$ European Biological Inorganic Chemistry Conference (EuroBIC), Thessaloniki/Griechenland |
| 10/2010 | 13. Norddeutsches Doktorandenkolloquium, Greifswald |

# Eidesstattliche Erklärung

Hiermit erkläre ich an Eides statt, dass die vorliegende Arbeit, abgesehen von der Beratung durch meinen Betreuer Prof. Dr. Felix Tuczek, in Inhalt und Form meine eigene Arbeit ist. Sie wurde unter Einhaltung der Regeln der guten wissenschaftlichen Praxis der Deutschen Forschungsgemeinschaft angefertigt.

Die Arbeit wurde weder in Auszügen noch in ganzer Form an anderer Stelle im Rahmen eines Prüfungsverfahrens vorgelegt. Sie wurde in ihrer Gesamtheit nicht veröffentlicht oder zur Veröffentlichung eingereicht.

Kiel, den

Anne Westphal